Electronic Supplementary Material (ESI) for Chemical Society Reviews.

Electronic Supplementary Information (ESI) to accompany:

Uphill Diffusion in Multicomponent Mixtures

Rajamani Krishna*

Van ‘t Hoff Institute for Molecular Sciences, University of Amsterdam, Science Park 904,

1098 XH Amsterdam, The Netherlands

*email: r.krishna@contact.uva.nl

Table of Contents

1. Preamble 3
2. Diffusion in *n*-component fluid mixtures: Fick, Maxwell-Stefan, and Onsager formalisms 4
3. Characteristics and estimation of diffusivities 11
4. Uphill diffusion in ternary gas mixtures: Two-bulb experiment of Duncan and Toor 17
5. Uphill diffusion in ternary gas mixtures: The Loschmidt tube experiment of Arnold and Toor 23
6. Diffusion of heliox in the lung airways 25
7. Separating azeotropes by partial condensation in the presence of inert gas 26
8. Phase stability in binary liquid mixtures: influence on diffusion 27
9. Diffusivities in ternary liquid mixtures in regions close to phase splitting 32
10. Equilibration trajectories in ternary liquid mixtures 39
11. Spontaneous emulsification, and the Ouzo effect 44
12. Serpentine trajectories, spinodal decomposition, and spontaneous emulsification 45
13. Aroma retention in drying of food liquids 52
14. Uphill diffusion in mixtures of glasses, metals, and alloys 52
15. Crossing boundaries in azeotropic distillation 55
16. Coupling effects in diffusion of electrolytes 58
17. Reverse osmosis 61
18. The Soret Effect 62
19. Separations using micro-porous crystalline materials: General considerations 63
20. Fick, Onsager, and Maxwell-Stefan formulations for diffusion inside micro-porous crystalline materials 65
21. Overshoots in transient uptake of binary mixtures in microporous materials 74
22. Overshoot phenomena in transient mixture permeation across microporous membranes 85
23. Notation 88
24. References 102
25. Caption for Figures 110

1. Preamble

This Electronic Supporting Information (ESI) accompanying our Tutorial Review *Uphill Diffusion in Multicomponent Mixtures* provides detailed derivations of the Maxwell-Stefan, and Onsager flux relations, along with solutions to the model equations describing transient equilibration processes. All the necessary data inputs, and calculation methodologies are provided in the ESI. Procedures for estimation of diffusivities are discussed. This should enable the interested reader to reproduce all the calculations and results presented and discussed here.

For ease of reading, this ESI is written as a stand-alone document; as a consequence, there is some overlap of material with the main manuscript.

Also uploaded as ESI are video animations:

(1) MD simulations showing N_2 molecule jumping, lengthwise, across 4 Å window of LTA-4A zeolite

(2) MD simulations showing CH_4 molecule jumping across 4 Å window of LTA-4A zeolite

(3) Transient development of component loadings of N_2 and CH_4 along the radius of a LTA-4A crystal; this animation demonstrates temporal and spatial overshoots.

(4) Transient development of component loadings of N_2 and O_2 along the radius of a CMS particle; this animation demonstrates temporal and spatial overshoots.

(5) Transient development of component loadings of n-hexane (nC6) and 2-methylpentane (2MP) along the radius of a MFI crystal; this animation demonstrates temporal and spatial overshoots.

(6) Transient development of component loadings of N_2 and CH_4 along the radius of a LTA-4A crystal; during both the adsorption and desorption phases. This animation demonstrates asymmetry in the adsorption and desorption phases.

2. Diffusion in *n*-component fluid mixtures: Fick, Maxwell-Stefan, and Onsager formalisms

The quantitative description of diffusion of mixtures of molecules is important to chemists, physicists, biologists, and engineers. For a binary mixture of components 1 and 2 the flux of component 1, J_1, is defined with respect to a chosen reference velocity u. For most of the examples we shall treat in this Tutorial Review, it is convenient to use the molar average mixture velocity u

$$u = x_1 u_1 + x_2 u_2 + \cdots x_n u_n \tag{1}$$

The molar diffusion flux J_1 is commonly related to its composition (mole fraction) gradient $\frac{dx_1}{dz}$ in the form

$$J_1 = -c_t D_{12} \frac{dx_1}{dz} \tag{2}$$

The linear relation (2) was posited in 1855 by Adolf Fick, a physiologist working as an anatomy demonstrator in Zürich, in analogy to the corresponding laws of conduction of heat and electricity. The coefficient D_{12} in Equation (2) is the Fick diffusivity. Most commonly, the diffusion flux is directed downhill, i.e. $J_1/(-dx_1/dz) > 0$. The simplest extension of Equation (2) to *n*-component mixtures is to assume that each flux is dependent on its own composition gradient

$$J_i = -c_t D_i \frac{dx_i}{dz}; \quad i = 1,2,...n \tag{3}$$

where D_i is the "effective" Fick diffusivity of component *i* in the *n*-component mixture. To describe uphill diffusion, we need to use more rigorous formulations of multicomponent diffusion, as we discuss below.

In his classic paper published in 1945 entitled *Theories and Problems of Liquid Diffusion*, Onsager[1] wrote *The theory of liquid diffusion is relatively undeveloped… It is a striking symptom of the common ignorance in this field that not one of the phenomenological schemes which arc fit to describe the general case of diffusion is widely known*. In the Onsager formalism for *n*-component mixtures, the diffusion fluxes J_i are postulated as being linearly dependent on the driving forces that are taken to be the chemical potential gradients, $\frac{d\mu_i}{dz}$. The fluxes J_i are defined with respect to the chosen molar average reference velocity frame u

$$J_i \equiv c_i(u_i - u); \quad i = 1,2,..n \tag{4}$$

The molar fluxes N_i in the laboratory fixed reference frame are related to the diffusion fluxes J_i by

$$N_i \equiv \quad c_i u_i = J_i + x_i N_t; \quad N_t = \sum_{i=1}^{n} N_i \tag{5}$$

Only n-1 of the fluxes J_i are independent because the diffusion fluxes sum to zero

$$\sum_{i=1}^{n} J_i = 0 \tag{6}$$

Also, only (n-1) of the chemical potential $\frac{d\mu_i}{dz}$ are independent, because of the Gibbs-Duhem relationship

$$x_1 \frac{d\mu_1}{dz} + x_2 \frac{d\mu_2}{dz} + \cdots x_n \frac{d\mu_n}{dz} = 0 \tag{7}$$

It is convenient therefore to choose the (n-1) independent chemical potential gradients $\frac{d(\mu_i - \mu_n)}{dz}$ as driving forces for diffusion. In (n-1) dimensional matrix notation, the Onsager formulation is written as

$$(J) = -c_t[L]\frac{1}{RT}\left(\frac{d(\mu - \mu_n)}{dz}\right) \tag{8}$$

The units of the elements L_{ij} are the same as those for Fick diffusivities, i.e. m^2 s^{-1}. The matrix of Onsager coefficients $[L]$ is symmetric because of the Onsager Reciprocal Relations (ORR)[2]

$$L_{ij} = L_{ji} \tag{9}$$

For insightful and robust discussions on the validity of the Onsager relations, see Truesdell.[3]

In proceeding further, we define a (*n*-1) dimensional matrix [*H*], that is the Hessian of the molar Gibbs free energy, *G*

$$H_{ij} = \frac{1}{RT}\frac{\partial^2 G}{\partial x_i \partial x_j} = \frac{1}{RT}\frac{\partial^2 G}{\partial x_i \partial x_i} = H_{ji}; \quad i,j = 1,2\ldots n-1 \tag{10}$$

where *G*, the molar Gibbs free energy for the *n*-component mixture, is the sum of two contributions

$$G = G^{ex} + RT\sum_{i=1}^{n} x_i \ln(x_i); \quad G^{ex} = RT\sum_{i=1}^{n} x_i \ln(\gamma_i) \tag{11}$$

where γ_i is the activity coefficient of component *i*. Equation (11) can also be written in terms of the μ_i, that is the chemical potential or partial molar Gibbs free energy:

$$G = \sum_{i=1}^{n} x_i \mu_i = RT\sum_{i=1}^{n} x_i \ln(\gamma_i x_i) \tag{12}$$

When carrying out the partial differentiations of *G*, required in equation (10), it is important to note that all *n* of the mole fractions cannot be varied independently. So, we re-write equation (12), in terms of the *n*-1 independent mole fractions

$$G = \sum_{i=1}^{n} x_i \mu_i = \sum_{i=1}^{n-1} x_i \left(\mu_i - \mu_n\right) + \mu_n \tag{13}$$

In view of equations (10), and (13), we obtain

$$H_{ij} = \frac{1}{RT}\frac{\partial\left(\mu_i - \mu_n\right)}{\partial x_j} = \frac{1}{RT}\frac{\partial\left(\mu_j - \mu_n\right)}{\partial x_i} = H_{ji}; \quad i,j = 1,2\ldots n-1 \tag{14}$$

Combining equations (8), and (14) we get

$$(J) = -c_t [L][H]\frac{d(x)}{dz} \tag{15}$$

The second law of thermodynamics dictates that the rate of entropy production must be positive definite

$$\sigma = -\frac{1}{T}\sum_{i=1}^{n}\frac{d\mu_i}{dz}J_i = -\frac{1}{T}\sum_{i=1}^{n-1}\frac{d(\mu_i - \mu_n)}{dz}J_i \geq 0 \tag{16}$$

Substituting the Onsager equations (8) for the diffusion fluxes

$$\sigma = \sum_{i=1}^{n-1}\sum_{j=1}^{n-1}L_{ij}\frac{d(\mu_i - \mu_n)}{dz}\frac{d(\mu_j - \mu_n)}{dz} \geq 0 \tag{17}$$

Equation (17) implies that the Onsager matrix $[L]$ be positive definite, i.e.

$$|L| \geq 0; \quad \text{second law of thermodynamics} \tag{18}$$

If we define a $(n\text{-}1) \times (n\text{-}1)$ dimensional Fick diffusivity matrix $[D]$

$$(J) = -c_t[D]\frac{d(x)}{dz} \tag{19}$$

we obtain the inter-relationship

$$[D] = [L][H] \tag{20}$$

Equation (20) underscores the direct influence of mixture thermodynamics on the Fick diffusivites D_{ij}. It is worthy of note that the Fick diffusivity matrix $[D]$, which is a product of two symmetric matrices, $[L]$ and $[H]$ is not symmetric.

For stable single phase fluid mixtures, we must have $|H| \geq 0$. Also, in view of the second law of thermodynamics we have $|L| \geq 0$. In view of equation (20), the condition of phase stability translates to

$$|D| \geq 0; \quad |L| \geq 0; \quad |H| \geq 0; \quad \text{phase stability} \tag{21}$$

Equation (21) implies that all the eigenvalues of the Fick matrix $[D]$ are positive definite. It is interesting to note that thermodynamic stability considerations do not require the diagonal elements D_{ii} to be positive definite. If recourse is made to the kinetic theory of gases, it can be shown that the diagonal elements D_{ii} are individually positive definite for mixtures of ideal gases. The off-diagonal elements $D_{ij}(i \neq j)$ can be either positive or negative, even for ideal gas mixtures. Indeed, the sign of $D_{ij}(i \neq j)$ also depends on the component numbering.

In Section 8, we examine the characteristics of thermodynamic influences in mixtures that are potentially unstable.

The Onsager approach does not offer any clues about the estimation of the elements of $[L]$ using information on the diffusivities of the binary pairs in the *n*-component mixtures. From a practical point of view it is much more convenient to adopt a different formalism that has its origins in the pioneering works of James Clerk Maxwell[4] and Josef Stefan.[5] The Maxwell-Stefan formulation is best appreciated by first considering diffusion in a ternary mixture of *ideal gases*. We write the composition gradient driving forces as linear functions of the fluxes N_i in the following manner

$$\begin{aligned}
-\frac{dx_1}{dz} &= \frac{x_2 N_1 - x_1 N_2}{c_t Đ_{12}} + \frac{x_3 N_1 - x_1 N_3}{c_t Đ_{13}}; \\
-\frac{dx_2}{dz} &= \frac{x_1 N_2 - x_2 N_1}{c_t Đ_{12}} + \frac{x_3 N_2 - x_2 N_3}{c_t Đ_{23}} \\
-\frac{dx_3}{dz} &= \frac{x_1 N_3 - x_3 N_1}{c_t Đ_{13}} + \frac{x_2 N_3 - x_3 N_2}{c_t Đ_{23}}
\end{aligned} \tag{22}$$

Maxwell preceded Stefan in his analysis of multicomponent diffusion and the formulation should properly be termed the Maxwell-Stefan (M-S) instead of Stefan-Maxwell formulation as it is sometimes referred to in the literature. It is interesting to note that Stefan was aware of Maxwell's work but apparently found it difficult to follow. Stefan commented *Das Studium der Maxwell'schen Abhandlung ist nicht leicht*. Equations (22) are entirely consistent with the kinetic theory of gases.[6]

Only two of the Equations (22) are independent because the mole fraction gradients sum to zero

$$\frac{dx_1}{dz} + \frac{dx_2}{dz} + \frac{dx_3}{dz} = 0 \tag{23}$$

Equations (22) after appropriate linearization, were solved independently in 1964 by Herbert Toor[7, 8] and Warren E. Stewart.[9] The exact analytical solutions to the M-S Equations (22) were made available only much later in 1976;[10] the computational details are provided by Taylor and Krishna.[11]

For n-component non-ideal fluid mixtures, the M-S are written in the following manner

$$-\frac{1}{RT}\frac{d\mu_i}{dz}=\sum_{\substack{j=1\\j\neq i}}^{n}\frac{x_j\left(u_i-u_j\right)}{Đ_{ij}};\quad i=1,2,\ldots n \tag{24}$$

By multiplying both sides of equation (24) by x_i after introducing the expressions for fluxes $N_i \equiv c_i u_i = J_i + x_i N_t;\quad N_t=\sum_{i=1}^{n} N_i$ we obtain

$$-\frac{x_i}{RT}\frac{d\mu_i}{dz}=\sum_{\substack{j=1\\j\neq i}}^{n}\frac{x_jN_i-x_iN_j}{c_tĐ_{ij}}=\sum_{\substack{j=1\\j\neq i}}^{n}\frac{x_jJ_i-x_iJ_j}{c_tĐ_{ij}};\quad i=1,2,\ldots n \tag{25}$$

where the second equality arises from application of equations (5), and (6). The $\frac{x_i}{RT}\frac{d\mu_i}{dz}$ is the generalization of the mole fraction gradients, used as driving forces in Equations (22). Indeed, for ideal gas mixtures, equation (25) simplify to yield Equations (22).

The ORR imply that the M-S pair diffusivities are symmetric

$$Đ_{ij}=Đ_{ji};\quad i,j=1,2...n \tag{26}$$

Insertion of the Maxwell-Stefan diffusion eq. (24) into (16) we obtain on re-arrangement[12]

$$\sigma=\frac{1}{2}c_tR\sum_{i=1}^{n}\sum_{j=1}^{n}\frac{x_ix_j}{Đ_{ij}}\left|u_i-u_j\right|^2\geq 0 \tag{27}$$

For mixtures of ideal gases for which the $Đ_{ij}$ are independent of composition the positive definite condition (27) can only be satisfied if

$$Đ_{ij}\geq 0;\quad \text{(ideal gas mixtures)} \tag{28}$$

Equation (28) was first derived by Hirschfelder, Curtiss and Bird.[6] For non-ideal liquid mixtures the $Đ_{ij}$ are composition dependent in general and a result analogous to eq. (28) cannot be derived.

It is helpful to express the left member of equation (25) in terms of the mole fraction gradients by introducing an (n-1) × (n-1) matrix of thermodynamic factors $[\Gamma]$:

$$\frac{x_i}{RT}\frac{d\mu_i}{dz} = \sum_{j=1}^{n-1}\Gamma_{ij}\frac{dx_j}{dz}; \quad \Gamma_{ij} = \delta_{ij} + x_i\frac{\partial \ln \gamma_i}{\partial x_j}; \quad i, j = 1,2\ldots n-1 \tag{29}$$

For non-ideal ternary liquid mixtures, the elements of $[\Gamma]$ can be calculated from Van Laar, Wilson, UNIQUAC or NRTL models describing phase equilibrium thermodynamics.[11, 13]

We also define a $(n\text{-}1) \times (n\text{-}1)$ matrix of inverse diffusivities $[B]$ whose elements are given by

$$B_{ii} = \frac{x_i}{Đ_{in}} + \sum_{\substack{k=1\\k\neq i}}^{n}\frac{x_k}{Đ_{ik}}; \quad B_{ij(i\neq j)} = -x_i\left(\frac{1}{Đ_{ij}} - \frac{1}{Đ_{in}}\right); \quad i, j = 1,2...n-1 \tag{30}$$

For a ternary mixture we get

$$\begin{gathered} B_{11} = \frac{x_1}{Đ_{13}} + \frac{x_2}{Đ_{12}} + \frac{x_3}{Đ_{13}}; \quad B_{12} = -x_1\left(\frac{1}{Đ_{12}} - \frac{1}{Đ_{13}}\right); \\ B_{21} = -x_2\left(\frac{1}{Đ_{12}} - \frac{1}{Đ_{23}}\right); \quad B_{22} = \frac{x_2}{Đ_{23}} + \frac{x_1}{Đ_{12}} + \frac{x_3}{Đ_{23}} \end{gathered} \tag{31}$$

Combining equations (25), (29), and (30), we can re-cast equation (25) into (*n*-1) dimensional matrix notation

$$(J) = -c_t[B]^{-1}[\Gamma]\frac{d(x)}{dz} \tag{32}$$

Comparing equations (15), (19), and (32), we get the inter-relationship between Fick, M-S and Onsager coefficients

$$[L][H] = [D] = [B]^{-1}[\Gamma] \tag{33}$$

Specifically, for a ternary mixture

$$\begin{bmatrix} D_{11} & D_{12} \\ D_{21} & D_{22} \end{bmatrix} = \frac{1}{B_{11}B_{22} - B_{12}B_{21}}\begin{bmatrix} \frac{x_2}{Đ_{23}} + \frac{x_1}{Đ_{12}} + \frac{x_3}{Đ_{23}} & x_1\left(\frac{1}{Đ_{12}} - \frac{1}{Đ_{13}}\right) \\ x_2\left(\frac{1}{Đ_{12}} - \frac{1}{Đ_{23}}\right) & \frac{x_1}{Đ_{13}} + \frac{x_2}{Đ_{12}} + \frac{x_3}{Đ_{13}} \end{bmatrix}\begin{bmatrix} \Gamma_{11} & \Gamma_{12} \\ \Gamma_{21} & \Gamma_{22} \end{bmatrix} \tag{34}$$

Equation (34) simplifies to yield

$$\begin{bmatrix} D_{11} & D_{12} \\ D_{21} & D_{22} \end{bmatrix} = \frac{\begin{bmatrix} Đ_{13}\left(x_1 Đ_{23} + (1-x_1) Đ_{12}\right) & x_1 Đ_{23}\left(Đ_{13} - Đ_{12}\right) \\ x_2 Đ_{13}\left(Đ_{23} - Đ_{12}\right) & Đ_{23}\left(x_2 Đ_{13} + (1-x_2) Đ_{12}\right) \end{bmatrix}}{x_1 Đ_{23} + x_2 Đ_{13} + x_3 Đ_{12}} \begin{bmatrix} \Gamma_{11} & \Gamma_{12} \\ \Gamma_{21} & \Gamma_{22} \end{bmatrix} \tag{35}$$

The values of the Fick and Onsager diffusivities are dependent on the choice of the reference velocity frame, that has been chosen in the foregoing set of expressions as the molar average mixture velocity. For converting the diffusivities from one reference velocity frame to another, explicit expressions are provided in Taylor and Krishna.[11] An important advantage of the M-S formulation, is that the pair diffusivities $Đ_{ij}$ are independent of the choice of the reference velocity frame. Further discussions of the characteristic differences between the Onsager, M-S and Fickian formulations are available in Taylor and Krishna.[11]

Experimental data are invariably on the Fick diffusivity matrix, $[D]$. The procedure for determination of the M-S $Đ_{ij}$ is outlined below. The first step, is to determine the elements of the matrix $[B]$ from $[D][\Gamma]^{-1} = [B]^{-1}; \quad [B] = [\Gamma][D]^{-1}$. For a ternary mixture, the M-S $Đ_{ij}$ can be determined explicitly using the following relations that are derived by Krishna and van Baten,[14] :

$$Đ_{13} = \frac{1}{B_{11} + \frac{x_2 B_{12}}{x_1}} \tag{36}$$

$$Đ_{12} = \frac{1}{B_{11} - \frac{(x_1 + x_3)}{x_1} B_{12}} = \frac{1}{B_{22} - \frac{(x_2 + x_3)}{x_2} B_{21}} \tag{37}$$

$$Đ_{23} = \frac{1}{B_{22} + \frac{x_1 B_{21}}{x_2}} \tag{38}$$

3. Characteristics and estimation of diffusivities

For ideal gas mixtures, the matrix of thermodynamic factors is the identity matrix

$$\Gamma_{ij} = \delta_{ij}; \quad i, j = 1,2 \ldots n-1 \tag{39}$$

and this simplification reduces Equations (25) to Equations (22); consequently

$$\left[D\right] = \left[B\right]^{-1}; \quad \text{ideal gas mixture} \tag{40}$$

For an ideal gas mixture, the binary pair diffusivities $Đ_{ij}$ are independent of composition, and can be estimated from correlations such as that of Fuller et al.[15] which has its origins in the kinetic theory of gases. For an ideal gas mixtures, Equation (40) allows the calculation of the Fick matrix from information on the M-S diffusivities of the constituent binary pairs, $Đ_{ij}$.

For a ternary gas mixture, Equation (40) yields the following expressions for the four elements of $\left[D\right]$

$$\begin{bmatrix} D_{11} & D_{12} \\ D_{21} & D_{22} \end{bmatrix} = \frac{\begin{bmatrix} Đ_{13}\left(x_1 Đ_{23} + (1-x_1)Đ_{12}\right) & x_1 Đ_{23}\left(Đ_{13} - Đ_{12}\right) \\ x_2 Đ_{13}\left(Đ_{23} - Đ_{12}\right) & Đ_{23}\left(x_2 Đ_{13} + (1-x_2)Đ_{12}\right) \end{bmatrix}}{x_1 Đ_{23} + x_2 Đ_{13} + x_3 Đ_{12}} \tag{41}$$

If the binary pair diffusivities are all equal to one another (= $Đ$), then we have the simplification

$$\begin{bmatrix} D_{11} & D_{12} \\ D_{21} & D_{22} \end{bmatrix} \approx \begin{bmatrix} Đ & 0 \\ 0 & Đ \end{bmatrix}; \quad \text{identical pair diffusivities in ideal gas mixture} \tag{42}$$

Conversely, when the binary pair diffusivities are significantly different from one another, then the off-diagonal elements have large magnitudes. Equation (41) also shows that the component numbering alters the sign of the cross-coefficients; negative cross-coefficients are nothing to be alarmed about as they occur routinely *even for ideal gas mixtures*.

Let us now examine how the Fick diffusivities can be estimated for non-ideal fluid mixtures.

For binary liquid mixtures $n = 2$, the (n-1) dimensional matrix equations (29), and (33) simplify to yield

$$D_{12} = Đ_{12}\Gamma = L_{12}H = \frac{L_{12}}{x_1 x_2}\Gamma; \quad \Gamma = \left(1 + \frac{\partial \ln \gamma_1}{\partial \ln x_1}\right) \tag{43}$$

In the pioneering papers by Darken[16, 17] the following expression is postulated for the composition dependence of the Fick diffusivity D_{12}

$$D_{12} = \left(x_2 D_{1,self} + x_1 D_{2,self}\right)\left(1 + \frac{\partial \ln \gamma_1}{\partial \ln x_1}\right) \tag{44}$$

where $D_{1,\mathrm{self}}$ and $D_{2,\mathrm{self}}$ are *tracer*, or *self*- diffusivities of components 1 and 2, respectively, in the binary mixture.

Darken[16, 17] was one of the first to recognize the need to use activity gradients as proper driving forces when setting up the phenomenological relations to describe diffusion. The thermodynamic factor Γ is also referred to as the "Darken correction factor". Combining equations (43) and (44) we obtain the following expression for the composition dependence of the M-S diffusivity $Đ_{12}$ for a binary mixture

$$Đ_{12} = x_2 D_{1,self} + x_1 D_{2,self} \tag{45}$$

The $D_{1,\mathrm{self}}$ and $D_{2,\mathrm{self}}$ are more easily accessible, both experimentally[18-20] and from Molecular Dynamics (MD) simulations,[14] than the $Đ_{12}$.

The pure component $Đ_{\mathrm{ii}}$ are related to the $D_{\mathrm{i,self}}$ in the mixture by

$$Đ_{11} = D_{1,self}^{x_1 \to 1} = Đ_{12}^{x_1 \to 1}; \quad Đ_{22} = D_{2,self}^{x_2 \to 1} = Đ_{12}^{x_2 \to 1} \tag{46}$$

Therefore, the Darken equation (45) may be re-written in terms of the pure component $Đ_{\mathrm{ii}}$ as follows

$$Đ_{12} = x_2 Đ_{11} + x_1 Đ_{22} = x_2 D_{1,self} + x_1 D_{2,self} \tag{47}$$

A somewhat more accurate interpolation formula is the empirical Vignes relation[14, 21]

$$Đ_{12} = \left(Đ_{12}^{x_1 \to 1}\right)^{x_1} \left(Đ_{12}^{x_2 \to 1}\right)^{x_2} = \left(Đ_{11}\right)^{x_1} \left(Đ_{22}\right)^{x_2} \tag{48}$$

Generally speaking, the factoring out of the effects of non-ideal mixture thermodynamics (by use of $\frac{D_{12}}{\Gamma} = Đ_{12}$) results in a milder variation of the M-S diffusivity as compared to the Fick diffusivity. The Vignes formula (48) offers the possibility of interpolation using data at either ends of the composition scale. To verify this, Figures 1a, and 1b present comparison of the Fick, and M-S, and Onsager diffusivities for (a) acetone (1) – water (2), and (b) ethanol (1) – water (2) mixtures along with the estimations using equation (48). We see that that the interpolation formula is of good accuracy. Further examination of the validity of the Vignes interpolation formula in available in published works.[11, 22-26]

The Onsager diffusivity is related to the M-S diffusivity by equation (33) which simplifies for binary mixtures to

$$L_{12} = x_1 x_2 Đ_{12} = \frac{D_{12}}{\Gamma} \tag{49}$$

The L_{12} vanishes at either ends of the composition scale (cf. Figure 1) and this characteristic makes it less desirable for use in practical applications.[11, 12, 27-29]

For diffusion in *n*-component non-ideal liquid mixtures, the matrix of Fick diffusivities $[D]$ has significant non-diagonal contributions caused by (a) differences in the binary pair M-S diffusivities, $Đ_{ij}$, and (b) strong coupling introduced by the matrix of thermodynamic factors $[\Gamma]$.

The experimental data of Cullinan and Toor,[30] for the elements of the Fick diffusivity matrix [*D*] for acetone(1)/benzene(2)/CCl_4(3) mixtures show that the off-diagonal elements are not insignificant in relation to the diagonal elements; see plots in Figure 2.

Let us now examine whether we can estimate the elements of the Fick diffusivity matrix [*D*] for acetone(1)/benzene(2)/CCl_4(3) mixtures using data on the infinite dilution diffusivity values. For this purpose we need to examine diffusivities in each of the binary pairs. Figure 3 presents the experimental data on the Fick diffusivities for (a) acetone(1)/benzene(2), (b) acetone(1)/CCl_4(3), and (c) benzene (2)/ CCl_4(3) mixtures as a function of composition. Also shown in Figure 3 are the M-S diffusivities, calculated from $Đ_{12} = \frac{D_{12}}{\Gamma}$. The benzene/$CCl_4$ mixtures are ideal, and consequently $\Gamma \approx 1; \quad Đ_{12} \approx D_{12}$. For acetone/benzene mixtures the Vignes interpolation formula (48) is of reasonable accuracy, whereas for acetone/CCl_4, the M-S diffusivity does not accurately follow the composition dependence prescribed by equation (48). On the basis of the diffusivity data of the three binary pairs, we determine the following six M-S diffusivity values at either ends of the composition ranges

$$\begin{aligned}
&Đ_{12}^{x_1\to 1} = 4.15; \quad Đ_{12}^{x_2\to 1} = 2.75; \quad \text{for acetone(1)/benzene(2) binary mixture} \\
&Đ_{13}^{x_1\to 1} = 3.57; \quad Đ_{13}^{x_3\to 1} = 1.7; \quad \text{for acetone(1)/CCl}_4\text{(3) binary mixture} \\
&Đ_{23}^{x_2\to 1} = 1.91; \quad Đ_{23}^{x_3\to 1} = 1.42 \quad \text{for benzene(2)/CCl}_4\text{(3) binary mixture}
\end{aligned} \tag{50}$$

Taylor and Krishna[11] have suggested the following extension of the Vignes interpolation formula for applying to ternary mixtures

$$\begin{aligned}
&Đ_{12} = \left(Đ_{12}^{x_1\to 1}\right)^{x_1}\left(Đ_{12}^{x_2\to 1}\right)^{x_2}\left(Đ_{12}^{x_3\to 1}\right)^{x_3}; \quad Đ_{12}^{x_3\to 1} = \sqrt{\left(Đ_{12}^{x_1\to 1}Đ_{12}^{x_2\to 1}\right)} \\
&Đ_{13} = \left(Đ_{13}^{x_1\to 1}\right)^{x_1}\left(Đ_{13}^{x_2\to 1}\right)^{x_2}\left(Đ_{13}^{x_3\to 1}\right)^{x_3}; \quad Đ_{13}^{x_2\to 1} = \sqrt{\left(Đ_{13}^{x_1\to 1}Đ_{13}^{x_3\to 1}\right)} \\
&Đ_{23} = \left(Đ_{23}^{x_1\to 1}\right)^{x_1}\left(Đ_{23}^{x_2\to 1}\right)^{x_2}\left(Đ_{23}^{x_3\to 1}\right)^{x_3}; \quad Đ_{23}^{x_3\to 1} = \sqrt{\left(Đ_{23}^{x_2\to 1}Đ_{23}^{x_3\to 1}\right)}
\end{aligned} \tag{51}$$

The procedure for estimation of the Fick diffusivity matrix $[D]$ is explained in a step-by-step manner in Example 4.2.6 of Taylor and Krishna[11] for one of the nine experimental data sets for acetone(1)/benzene(2)/CCl_4(3) mixtures. The estimations use the combination of equations (35), (50), and (51). The same procedure was employed for the entire data set plotted in Figure 2. The estimated values are compared with the experimental values for each of the four elements in Figure 4. We observe that the diagonal elements D_{11} and D_{22} are predicted fairly well, as is to be expected. However, the estimations of the off-diagonal elements D_{12} and D_{21} are somewhat poorer. Nevertheless, the estimations of the cross-coefficients are of the right order of magnitude and sign.

The accuracy of the estimation of the Fick diffusivity matrix [D] is crucially dependent on the accuracy of the calculations of the the thermodynamic factor matrix $[\Gamma]$. In order to demonstrate this Figure 5a presents a plot of the ratio $\frac{|D|^{1/2}}{|\Gamma|^{1/2}}$ as a function of the mole fraction of acetone in acetone(1)/benzene(2)/CCl_4(3) mixtures. The square root of determinants $|D|$, and $|\Gamma|$ are representative of the “magnitudes” of [D], and $[\Gamma]$ respectively. The ratio $\frac{|D|^{1/2}}{|\Gamma|^{1/2}}$ can be viewed as the “magnitude” of the Maxwell-Stefan diffusivity in the *ternary* mixture. The ratio $\frac{|D|^{1/2}}{|\Gamma|^{1/2}}$ appears to show a simple dependence on the mole fraction of acetone, quite similar to that observed for the variation of the M-S diffusivity in acetone/benzene, and acetone/CCl_4 mixtures; see Figure 3.

Figure 5b presents data on $\frac{|D|^{1/2}}{|\Gamma|^{1/2}}$ as a function of the mole fraction of acetone for acetone(1)/benzene(2)/methanol(3) mixtures. We again note that factoring out the thermodynamic influences yields much milder, well-behaved, composition dependences.

A fairly comprehensive evaluation and discussion of the procedures for estimation of $[D]$ is contained in the paper by Rehfeldt and Stichlmair, [31] and in the dissertation of Rehfeldt.[32] Rather than repeat their results here, we present a re-analysis of the data of Rehfeldt[31, 32] for the Fick diffusivity matrix $[D]$ for (a) methanol(1)/1-butanol(2)/1-propanol, (b) acetone(1)/water(2)/1-propanol(3), (c) acetone(1)/1-butanol(2)/1-propanol(3), and (d) 1-propanol(1)/1-chlorobutane(2)/n-heptane(3) mixtures at 298 K in Figure 6. The ratio $\frac{|D|^{1/2}}{|\Gamma|^{1/2}}$ is plotted in Figure 6 as a function of the mole fraction of component 1 in four different mixtures. For the first three mixtures we see that the ratio $\frac{|D|^{1/2}}{|\Gamma|^{1/2}}$ shows a mild dependence on the composition, emphasizing that the "factoring out" of thermodynamic influences remains the key to proper estimation of $[D]$. For the 1-propanol(1)/1-chlorobutane(2)/n-heptane(3) mixtures there is considerable scatter in the $\frac{|D|^{1/2}}{|\Gamma|^{1/2}}$ data at low concentrations of 1-propanol(1); this scatter is attributable to either scatter in the diffusivity measurements or inaccuracies in the calculations of $[\Gamma]$.

Experimental data on Fick diffusivity matrix in Cu(1)/Ag(2)/Au(3) alloys, are reported in the thesis of Ziebold;[33] their data are summarized, for convenience, in Table 3.[33] The analysis of multicomponent iffusion in alloys is almost exclusively based on the Onsager/Fick formulation, and not the Maxwell-Stefan formulation. Indeed, it would be fair to comment that the advantages of the use of the M-S formulations, over the Onsager formulation, are not adequately recognized by researchers working in diffusion in metals, alloys, ceramics and glasses. Using the data in Table 3, along with the thermodynamic correction factors reported in Table 10 of Ziebold[33] we calculated the ratio $\frac{|D|^{1/2}}{|\Gamma|^{1/2}}$ and plotted this as a function of the atom fraction of Cu(1); see Figure 7. We see that the diffusivity data appears to show a simple dependence of $\frac{|D|^{1/2}}{|\Gamma|^{1/2}}$ on composition. The message that we wish to convey is that the adoption of the M-S formulation for mixture diffusion in alloys will lead to considerable simplifications.

There is a need for the development of improved procedures for estimation of the Fick diffusivity matrix $[D]$. A reasonable engineering approach would be to assume that the Fick diffusivity matrix is simply a scalar times the matrix of thermodynamic factors $[\Gamma]$. The value of the scalar diffusivity can be taken as ratio $\frac{|D|^{1/2}}{|\Gamma|^{1/2}}$, i.e. $[D]=\frac{|D|^{1/2}}{|\Gamma|^{1/2}}[\Gamma]$.

4. Uphill diffusion in ternary gas mixtures: Two-bulb experiment of Duncan and Toor

With the foregoing background on the flux relations, let us analyze, and model, the two-bulb diffusion experiments of Duncan and Toor[34] with ternary $H_2(1)/N_2(2)/CO_2(3)$ gas mixtures. The experimental set-up consisted of a two bulb diffusion cells, pictured in Figure 8. The two bulbs were connected by means of an 86 mm long capillary tube. At time t = 0, the stopcock separating the two composition environments at the center of the capillary was opened and diffusion of the three species was allowed to take place. From the information given in the paper by Duncan and Toor,[34] it is verifiable that the diffusion inside the capillary tube is in the bulk diffusion regime. Furthermore, the pressure differences between the two bulbs are negligibly small implying the absence of viscous flow. Since the two bulbs are sealed there is no net transfer flux out of or into the system, i.e. we have conditions corresponding to equimolar diffusion:

$$u = 0; \quad N_1 + N_2 + N_3 = 0 \tag{52}$$

The initial compositions (mole fractions in the two bulbs, Bulb A and Bulb B, are

$$\begin{aligned}&\text{Bulb A}: x_1 = 0.00000; x_2 = 0.50086; x_3 = 0.49914\\&\text{Bulb B}: x_1 = 0.50121; x_2 = 0.49879; x_3 = 0.00000\end{aligned} \tag{53}$$

The driving forces for the three components are: $\Delta x_1 = 0.50121; \quad \Delta x_2 = -0.00021; \quad \Delta x_3 = -0.4991$.

The composition trajectories for each of the three diffusing species in either bulb has been presented in Figures 9, 10, and 11. We note that despite the fact that the driving force for nitrogen is practically zero, it does transfer from one bulb to the other, exhibiting over-shoot and under-shoot phenomena when approaching equilibrium. The transient equilibration trajectories of H_2, and CO_2 are “normal”, with their compositions in the two bulbs approaching equilibrium in a monotonous manner.

Let us first examine what happens to H_2(1), and CO_2(3). The composition - time trajectories are as expected; H_2 diffuses from Bulb B to Bulb A and the two composition sets approach each other, albeit slowly. CO_2 diffuses from Bulb A to Bulb B in the expected, normal, fashion. The diffusion behavior of these two species H_2, and CO_2 may be termed to be Fickian, i.e. down their respective composition gradients; there is nothing extraordinary about the equilibration characteristics of either H_2, or CO_2.

If we examine the composition - time trajectory of N_2, we observe several curious phenomena. Initially the compositions of nitrogen in the two bulbs are almost identical and therefore at this point the composition gradient driving force for N_2 is practically zero. However it was observed experimentally by Duncan and Toor[34] that the diffusion of N_2 does take place decreasing the composition of Bulb A while the composition of N_2 in Bulb B increases; this is contrary to the Fickian expectations for we have

$$\frac{dx_2}{dz} \approx 0;: \quad J_2 \neq 0; \quad t \approx 0 \tag{54}$$

The Bulb A composition continues to decrease during the time interval $0 < t < t_1$; this diffusion of nitrogen is in an up-hill direction, i.e.

$$\frac{J_2}{-\frac{dx_2}{dz}} < 0; \quad 0 < t < t_1 \tag{55}$$

Uphill diffusion of N_2 continues to take place until the time $t = t_1$ is reached when the composition profiles in either bulb tend to plateau. This plateau implies that the diffusion flux of N_2 is zero at this point despite the fact that there is a large driving force existing. At $t = t_1$ we have

$$\frac{dx_2}{dz} \neq 0;\therefore \quad J_2 = 0; \quad t = t_1 \tag{56}$$

Beyond the point $t = t_1$, the diffusion behavior of N_2 is "normal", i.e. the composition of nitrogen in Bulb B with a higher concentration decreases while the composition of nitrogen in Bulb A with the lower concentration increases.

Toor[7] in a classic paper had anticipated these curious phenomena and assigned the following names to them:

Osmotic diffusion; this is the phenomenon observed at $t = 0$ and described by eq. (54), namely diffusion of a component despite the absence of a driving force.

Uphill, or reverse, diffusion; this phenomenon is observed for N_2 in the time interval $0 < t < t_1$ and described by eq. (55): diffusion of a component in a direction opposite to that dictated by its driving force.

Diffusion barrier: this phenomenon is observed at $t = t_1$ and is described by eq. (56): in this case, a component diffusion flux is zero despite a finite driving force.

Figure 12b presents a plot of the normalized flux of nitrogen $\frac{N_2\delta}{c_t} = \frac{J_2\delta}{c_t}$ (y-axis) vs the mole fraction differences between bulbs A and B for the experiment of Duncan and Toor.[34]

It should be clear that the use of the Fick formulation, Equation (3), will be totally inadequate to describe the anomalies described above because in order to rationalize the experimental observations we must demand the following behavior of the Fick diffusivity for N_2(component 2):

- $D_2 \to \infty$ at the *osmotic diffusion* point; cf. eq. (54),
- $D_2 < 0$ in the region where *uphill diffusion* occurs, cf. eq. (55), and
- $D_2 = 0$ at the *diffusion barrier*, cf. eq. (56).

It must be emphasized that this unusual behavior of the Fick diffusivity for N_2 has been observed experimentally for an *ideal* gas mixture at *constant temperature and pressure* conditions and for a situation corresponding to *equimolar diffusion*, $u = 0; \quad N_1 + N_2 + N_3 = 0$.

The behaviors of hydrogen and carbon dioxide are "normal"; the fluxes and the driving forces have the same sign; see Figures 12a, and 12c.

Figures 13a, and 13b depict the dependence of the flux J_i on its composition (mole fraction) gradient $-\frac{dx_i}{dz}$ for (a) binary mixture and (b) ternary mixture. The differences between binary and ternary mixture diffusion is evident.

Let us now rationalize the curious experimental characteristics with the help of the M-S Equations (22). The M-S diffusivities for the three binary pairs at $T = 308.3$ K are

$$\begin{aligned}
Đ_{12} &= 8.33\times10^{-5} \quad \text{m}^2\ \text{s}^{-1}\\
Đ_{13} &= 6.8\times10^{-5} \quad \text{m}^2\ \text{s}^{-1}\\
Đ_{23} &= 1.68\times10^{-5} \quad \text{m}^2\ \text{s}^{-1}
\end{aligned} \tag{57}$$

The compositions in the two bulbs equilibrate after several hours to $x_{1,\text{eq}} = 0.25$, $x_{2,\text{eq}} = 0.5$ and $x_{3,\text{eq}} = 0.25$. At this equilibrium composition the elements of the Fick diffusivity matrix $[D]$ can be calculated using Equation (41); the result is

$$[D] = \begin{bmatrix} 7.68 & -0.11 \\ -3.83 & 2.16 \end{bmatrix} \times 10^{-5} \quad \text{m}^2\ \text{s}^{-1} \tag{58}$$

In the Duncan-Toor two-bulb experiments, $J_i = N_i$ because we have equimolar diffusion. Let us estimate the flux of N_2: $J_2 = -c_t D_{21}\frac{dx_1}{dz} - c_t D_{22}\frac{dx_2}{dz}$ in Bulb A during the initial stages of the experiment. The composition gradients $\frac{dx_i}{dz}$ can be calculated from the differences between the initial Bulb A composition and the equilibrium composition, $\frac{dx_i}{dz} = \frac{\Delta x_i}{\delta} = \frac{(x_{i,eq} - x_{i,A})}{\delta}$ where δ is the length of the capillary tube connecting the two bulbs and so $J_2 = -\frac{c_t}{\delta}(D_{21}\Delta x_1 + D_{22}\Delta x_2)$, and $J_2 = -\frac{c_t}{\delta}(-3.83\times\Delta x_1 + 2.16\times\Delta x_2)\times10^{-5}$. Initially, $\Delta x_2 = 0$ (cf. Figure 11), but the N_2 flux remains non-zero and equals $-\frac{c_t}{\delta}(-3.83\times\Delta x_1)\times10^{-5}$. Since the driving force $\Delta x_1 = 0.25$, this causes a large positive flux for N_2, directed from Bulb A to B, causing its composition in Bulb A to decrease. Between $t = 0$ and $t = t_1$ the direction of nitrogen transport is against its intrinsic gradient; this is reverse or uphill diffusion, witnessed in in Figure 12. At the point $t = t_1$ we have $J_2 = -\frac{c_t}{\delta}(-3.83\times\Delta x_1 + 2.16\times\Delta x_2)\times10^{-5} = 0$ despite the existence of a significant driving force Δx_2; N_2 experiences a diffusion "barrier". Beyond the point $t = t_1$, the diffusion behavior of N_2 is "normal", directed from Bulb B to Bulb A.

The occurrence of the phenomena of reverse or uphill diffusion observed in the experiments by Duncan and Toor[34] is not in violation of the second law of thermodynamics; the second law requires that the total rate of entropy produced by all diffusing species should be positive definite and equation (16) simplifies for ideal gas mixtures to

$$\sigma = -R\sum_{i=1}^{n} J_i \frac{1}{x_i}\frac{dx_i}{dz} \geq 0; \quad \text{(ideal gas mixtures)} \qquad (59)$$

Equation (59) allows a component k in the multicomponent mixture to consume entropy by undergoing uphill diffusion, i.e. $-\frac{J_k}{\frac{dx_k}{dz}} < 0$, provided the other components produce entropy at such a rate that the overall rate of entropy production σ remains positive definite. Put another way, the other components $(i \neq k)$ pump component k uphill.

On a triangular composition diagram in Figure 10, the phenomenon of uphill diffusion manifests itself in a serpentine equilibration path. The continuous solid lines (in red and green) in Figure 10 are obtained from the following analytic solution, written in two-dimensional matrix form

$$\begin{pmatrix} x_1 - x_{1,eq} \\ x_2 - x_{2,eq} \end{pmatrix} = \exp\left[-\beta \begin{bmatrix} D_{11} & D_{12} \\ D_{21} & D_{22} \end{bmatrix} t \right] \begin{pmatrix} x_{10} - x_{1,eq} \\ x_{20} - x_{2,eq} \end{pmatrix} \tag{60}$$

where β is the cell constant. The initial conditions are, respectively, for Bulb A

$$t = 0; \quad \begin{pmatrix} x_1 \\ x_2 \end{pmatrix} = \begin{pmatrix} x_{10} \\ x_{20} \end{pmatrix} = \begin{pmatrix} 0.00000 \\ 0.50086 \end{pmatrix}; \quad \text{Bulb A} \tag{61}$$

and Bulb B

$$t = 0; \quad \begin{pmatrix} x_1 \\ x_2 \end{pmatrix} = \begin{pmatrix} x_{10} \\ x_{20} \end{pmatrix} = \begin{pmatrix} 0.50121 \\ 0.49879 \end{pmatrix}; \quad \text{Bulb B} \tag{62}$$

Equation (60) can be evaluated explicitly using the matrix calculus procedures described in Appendix A of Taylor and Krishna.[11]

The dashed (blue) lines in Figure 10 are the model calculations taking the Fick diffusivity to be diagonal

$$[D] = \begin{bmatrix} 7.76 & 0 \\ 0 & 2.08 \end{bmatrix} \times 10^{-5} \quad \text{m}^2\ \text{s}^{-1} \tag{63}$$

with the diagonal elements as the eigenvalues of $[D] = \begin{bmatrix} 7.68 & -0.11 \\ -3.84 & 2.16 \end{bmatrix} \times 10^{-5} \quad \text{m}^2\ \text{s}^{-1}$. These equilibration paths are monotonous, and there are no transient overshoots. This provides confirmation that the overshoots and undershoots have their origins in the coupled nature of the diffusion process.

The two eigenvalues of the Fick matrix are $D_{eig,1} = 7.76\times10^{-5}$ m^2 s^{-1}, and $D_{eig,2} = 2.08\times10^{-5}$ m^2 s^{-1}; each eigenvalue has an associated eigenvector; these are dubbed "fast" and "slow" eigenvectors.

The fast and slow eigenvectors are described by

$$(e_1) = \begin{pmatrix} 1 \\ -\dfrac{D_{11} - D_{eig,1}}{D_{12}} \end{pmatrix}; \quad (e_2) = \begin{pmatrix} 1 \\ -\dfrac{-D_{21}}{D_{22} - D_{eig,2}} \end{pmatrix}.$$

See Taylor and Krishna[11] for details on the calculations of the eigenvectors. It is to be noted that the expression for (e_2) provided in Equation (5.6.16) Taylor and Krishna[11] has a typographical error. However, the calculations presented in Example 5.6.1 are correct and the correct formula was used.

The initial transience is dominated by the fast eigenvector, while the approach toward equilibrium is governed by the slow eigenvector. The trajectories following the fast and slow eigenvectors are indicated in Figure 14.

5. Uphill diffusion in ternary gas mixtures: The Loschmidt tube experiment of Arnold and Toor

Arnold and Toor[35] report experimental data on the transient equilibration of $CH_4(1)/Ar(2)/H_2(3)$ gas mixtures of two different compositions in the top and bottom compartments of a Loschmidt tube; see Figures 15, 16, and 17. The driving forces for the three components are: $\Delta x_1 = -0.515; \quad \Delta x_2 = 0.024; \quad \Delta x_3 = 0.491$. We note that the driving force for Ar is significantly lower than that of its two partners. The transient equilibration processes for CH_4, and H_2 are "normal", inasmuch as their equilibration are monotonous see Figure 16a, and 17. The equilibration of Ar, however, shows an overshoot (in bottom compartment) and an undershoot (in top compartment). Such over- and under-shoots are not anticipated by Equation (3) when using a constant value for the diffusivity D_i. In the ternary composition space, the equilibration follows a serpentine, i.e. curvilinear, trajectory; see Figure 16b. The use of Equation (3), with constant D_i anticipates a linear equilibration path in composition space, distinctly at variance with the experimental observations.

The modelling of the Loschmidt diffusion experiments of Arnold and Toor[35] with $CH_4(1)/Ar(2)/H_2(3)$ gas mixtures proceeds along similar lines as for the Duncan-Toor two-bulb experiments. For the ternary gas mixture, the binary pair M-S diffusivities at $T = 307$ K are

$$\begin{aligned} Đ_{12} &= 2.16\times10^{-5} \quad \mathrm{m^2\ s^{-1}} \\ Đ_{13} &= 7.72\times10^{-5} \quad \mathrm{m^2\ s^{-1}} \\ Đ_{23} &= 8.33\times10^{-5} \quad \mathrm{m^2\ s^{-1}} \end{aligned} \tag{64}$$

The two-dimensional Fick diffusivity matrix can be calculated at the equilibrated compositions $x_{1,\mathrm{eq}} = 0.2575$, $x_{2,\mathrm{eq}} = 0.4970$ and $x_{3,\mathrm{eq}} = 0.2455$:

$$[D] = \begin{bmatrix} 4.44 & 1.83 \\ -3.64 & 6.3 \end{bmatrix} \times 10^{-5} \quad \mathrm{m^2\ s^{-1}} \tag{65}$$

The continuous solid lines (red and green) in Figures 15, 16, and 17 are the model calculations as presented in Example 5.5.1 of Taylor and Krishna.[11] The serpentine composition trajectory is properly captured by the assumption of a constant Fick matrix of diffusivities with elements given in equation (65).The coupled diffusion model calculations correctly captures the overshoot and undershoot phenomena observed in the experiments. Such over- and under-shoots are ascribable to the coupling effects in diffusion. In order to verify this, we also carried out model calculations in which the Fick diffusivity matrix is taken to be diagonal

$$[D] = \begin{bmatrix} 8.11 & 0 \\ 0 & 2.63 \end{bmatrix} \times 10^{-5} \quad \mathrm{m^2\ s^{-1}} \tag{66}$$

with the diagonal elements that are eigenvalues of $[D] = \begin{bmatrix} 4.44 & 1.83 \\ -3.64 & 6.3 \end{bmatrix} \times 10^{-5} \quad \mathrm{m^2\ s^{-1}}$. We note that the corresponding transient equilibration of Ar (indicated by the dashed lines in Figure 17) anticipates a monotonous equilibration path, without over- and under-shoots.

6. Diffusion of heliox in the lung airways

In diffusion processes in lung airways, normally at least four gases are involved O_2, CO_2, N_2 and H_2O vapor; the Maxwell-Stefan equations (22) are commonly used to model pulmonary gas transport.[36] The transport of the fresh breathed-in air towards the acini of human beings with chronic obstructive bronchopneumopathy, such as asthma, is rendered difficult due to bronchoconstriction and other factors.[37, 38] Such patients need some respiratory support to allow the oxygen to be transported through the proximal bronchial tree and then diffused in the distal one. One such support system consists of the inhalation of a mixture of heliox (20% O_2; 80% He), that facilitates the transport of oxygen. One important reason for the efficacy of Heliox is the facility with which O_2 diffuses into the lung airways.

Let us model the uptake of O_2 from the Left (subscript L) compartment (O_2 = 20 %; He = 80 %) into air contained in the Right (subscript R) compartment (O_2 = 20 %; N_2 = 80 %); see Figure 18.

For the ternary $O_2(1)/N_2(2)/He(3)$ gas mixture, the binary pair M-S diffusivities at T = 298 K are

$$\begin{aligned} Đ_{12} &= 2.187\times10^{-5} \quad \text{m}^2\ \text{s}^{-1} \\ Đ_{13} &= 7.907\times10^{-5} \quad \text{m}^2\ \text{s}^{-1} \\ Đ_{23} &= 7.407\times10^{-5} \quad \text{m}^2\ \text{s}^{-1} \end{aligned} \tag{67}$$

The two-dimensional Fick diffusivity matrix can be calculated at the equilibrated compositions $x_{1,\text{eq}}$ = 0.2, $x_{2,\text{eq}}$ = 0.4 and $x_{3,\text{eq}}$ = 0.4

$$[D] = \begin{bmatrix} 4.629 & 1.535 \\ 2.991 & 6.006 \end{bmatrix} \times 10^{-5} \quad \text{m}^2\ \text{s}^{-1} \tag{68}$$

The transient diffusion between the Left and Right compartments can be modelled as inter-diffusion between two semi-infinite slabs. The analytic solution for a binary mixture (with components 1, and 2), with a constant Fick diffusivity D_{12} is

$$x_1 = \frac{1}{2}\left(x_{1L} + x_{1R}\right) + \frac{1}{2} erf\left[-\frac{z}{\sqrt{4D_{12}t}}\right]\left(x_{1L} - x_{1R}\right) \tag{69}$$

where x_1 is the mole fraction of component 1 at any position z, and time t, x_{1L} and x_{1R} are the initial compositions in the left and right compartments, respectively. For a ternary mixture, the analytic solution is the matrix generalization of Equation (69)

$$\begin{pmatrix} x_1 \\ x_2 \end{pmatrix} = \frac{1}{2}\begin{pmatrix} x_{1L} + x_{1,R} \\ x_{2L} + x_{2,R} \end{pmatrix} + \frac{1}{2} erf\left[-\frac{z}{\sqrt{4t}} \begin{bmatrix} D_{11} & D_{12} \\ D_{21} & D_{22} \end{bmatrix}^{-1/2} \right] \begin{pmatrix} x_{1L} - x_{1R} \\ x_{2L} - x_{2R} \end{pmatrix} \quad (70)$$

The matrix functions, and calculations, can be carried out explicitly by use of the Sylvester's theorem, as explained in detail in Appendix A of Taylor and Krishna;[11] the solutions yield the continuous solid lines (indicated in red) in Figure 18.

Coupled diffusion leads to serpentine diffusion trajectories, suggesting that O_2 experiences uphill transport. If we ignore coupling effects, we obtain a linear equilibration trajectory shown by the dashed lines in Figure 18.

The transient uptake of O_2, monitored at the position z = -0.5 m, shows a substantial overshoot; see Figure 19. Such an O_2 overshoot is desirable as it results in faster ingress into the patient's lungs.

The use of a diagonal matrix of Fick diffusivities

$$[D] = \begin{bmatrix} 2.855 & 0 \\ 0 & 2.264 \end{bmatrix} \times 10^{-5} \quad \mathrm{m^2\ s^{-1}} \quad (71)$$

leads to a monotonous equilibration, as shown by the dashed lines in Figure 19. Indeed, the transfer of oxygen hardly occurs. In other words, uphill transport is an important part of the heliox therapy.

Bres and Hatzfeld[36] present experimental data for $O_2(1)/N_2(2)/He(3)$ mixture diffusion to support the O_2 overshoot observed in Figure 19.

7. Separating azeotropes by partial condensation in the presence of inert gas

If we condense a 2-propanol(1)/water (2) vapor mixture of azeotropic composition the composition of the condensed liquid will be identical and no separation can be achieved because there is no driving force for diffusion. If the condensation of the vapor mixture is conducted in the presence of a third component such as nitrogen that is inert (i.e. does not condense), the situation changes because we now have to reckon with diffusion in a ternary vapor mixture 2-propanol(1)/water(2)/nitrogen(3); cf. Figure 20. In this ternary vapor mixture, the M-S diffusivities of the binary pairs at 313 K are

$$\begin{aligned} Đ_{12} &= 1.393\times10^{-5} \quad \text{m}^2\ \text{s}^{-1} \\ Đ_{13} &= 1.046\times10^{-5} \quad \text{m}^2\ \text{s}^{-1} \\ Đ_{23} &= 2.554\times10^{-5} \quad \text{m}^2\ \text{s}^{-1} \end{aligned} \tag{72}$$

For 85% inert in the vapor mixture, the matrix of Fick diffusivities is calculated to be

$$[D] = \begin{bmatrix} 1.06 & -0.065 \\ 0.032 & 2.34 \end{bmatrix} \times 10^{-5} \quad \text{m}^2\ \text{s}^{-1} \tag{73}$$

The condensation of the vapor mixture will result in a liquid composition that is different from the azeotropic composition; this is because of the higher mobility of water molecules in the vapor phase. This is evident because of the significantly larger value of D_{22} than D_{11}. Furthermore, the contribution of the cross-term, $D_{21}\Delta x_1$ will serve to enhance the contribution of $D_{22}\Delta x_2$. The net result is that the condensate will be higher in water content than the azeotropic mixture; see Example 8.3.2 of Taylor and Krishna[11] for further calculation details. The experiments of Fullarton and Schlunder[39] confirm that this concept of harnessing diffusion coupling effects is of potential use in practice.

8. Phase stability in binary liquid mixtures: influence on diffusion

Non-ideal mixture thermodynamics has a strong influence on diffusion of liquid mixtures in the vicinity of phase transition regions. Let us consider diffusion in binary liquid mixtures exhibiting either an upper critical solution temperature (UCST), or a lower critical solution temperature (LCST), exemplified by (a) methanol (1) /n-hexane (2), (b) triethylamine (1) / water (2), and (c) n-hexane (1)/ nitrobenzene (2) mixtures; see Figure 21.

To understand the diffusion characteristics of binary liquid mixtures near UCST and LCST, we need to examine the mixture thermodynamics in more detail, starting with the calculations of the Gibbs free energy

$$\frac{G}{RT}=\frac{G^{ex}}{RT}+\left(x_1\ln x_1+x_2\ln x_2\right);\quad \frac{G^{ex}}{RT}=\left(x_1\ln\gamma_1+x_2\ln\gamma_2\right) \tag{74}$$

As illustration, Figure 22a presents calculations for $\frac{G}{RT}$ for methanol – *n*-hexane mixtures at various temperatures in the range 260 K – 320 K. At the two highest temperatures, 310 K, and 320 K the variation of $\frac{G}{RT}$ with composition is monotonic. For temperatures lower than 310 K, we note two minima, corresponding to

$$\frac{\partial G}{\partial x_1}=0 \tag{75}$$

From the data on the vanishing of the first derivative $\frac{\partial G}{\partial x_1}$ (cf. Figure 22b), we can determine the compositions of the two liquid phases that are in equilibrium with each other. The two points thus obtained at various values of *T*, yields the binodal curve (indicated in green) in Figure 22d. The vanishing of the second derivative of the Gibbs free energy

$$\frac{\partial^2 G}{\partial x_1^2}=0 \tag{76}$$

delineates the limits of phase instability; this defines the spinodal curve. The second derivative of the Gibbs free energy is simply related to the thermodynamic factor,

$$\frac{1}{RT}\frac{\partial^2 G}{\partial x_1^2}=H=\frac{\Gamma}{x_1x_2} \tag{77}$$

where Γ, defined by (29), reduces for $n = 2$ to

$$\Gamma=\left(1+\frac{\partial\ln\gamma_1}{\partial\ln x_1}\right) \tag{78}$$

For the derivation of equation (77), see Appendix D of Taylor and Krishna.[11] The calculations of $\frac{\partial^2 G}{\partial x_1^2} = 0$ in Figure 22c yields the points that lie on the spinodal curve (indicated in red). The UCST represents the confluence of the binodal and spinodal curves; the UCST for this system is determined to be 308 K. For any (x_1, T) conditions outside the region delineated by the binodal curve, diffusion acts in a manner to smear out concentration gradients and fluctuations. For any (x_1, T) conditions within the spinodal region, we have phase separation, i.e. de-mixing. The region between the binodal and spinodal envelopes is meta-stable.

In order to quantify the influence of phase instability on diffusion, we calculate the thermodynamic factor Γ using the NRTL equation.[40] Figure 23a presents calculations of the Γ for methanol – n-hexane mixtures at 303.15 K, 305.65 K, 307.75 K, 310.65 K, and 313.15 K, as a function of the mole fraction of methanol, x_1. We note that there is an order of magnitude decrease of Γ as $x_1 \to 0.5$. For the lower temperatures of 303.15 K, 305.65 K, 307.75 K, liquid-liquid phase splitting (demixing) takes place for a range of liquid compositions for which $\Gamma < 0$. At highest two temperatures of 313.15 K and 310.7 K, the system forms a homogeneous liquid phase for the entire composition range; at these two temperatures we note that the values of Γ are in the range of 0.03 – 0.05. It may be anticipated that the strong composition and temperature dependence of Γ will leave their imprint on the characteristics of the Fick diffusivities. This expectation is fulfilled by the experimental data reported by Clark and Rowley[40] for the Fick diffusivity D_{12} for methanol – n-hexane mixtures at five different temperatures 303.15 K, 305.65 K, 307.75 K, 310.65 K, and 313.15 K; see Figure 23b.

The molecular dynamic (MD) simulation results of Krishna and van Baten[23] for D_{12} are in good agreement with the experimental data of Clark and Rowley[40] at each of the five temperatures; see Figure 24.

The MD data on the M-S diffusivity exhibits a much milder composition dependence. Indeed, an important advantage of the M-S diffusivity is that its composition dependence is “better behaved” as compared to the Fick diffusivity. To emphasize this point, Figure 25 compares the experimental Fick diffusivities, D_{12} for methanol – n-hexane mixtures at 313.15 K with the values of $Đ_{12}$, calculated using $Đ_{12} = \frac{D_{12}}{\Gamma}$. We note that the variation in the values of $Đ_{12}$ is only by a factor of two, compared to the factor twenty variation in D_{12}. Also shown are the calculations of $Đ_{12}$ using the Vignes interpolation formula (48).

The Onsager coefficients, L_{12} calculated using Equation (49), vanishes at either end of the composition scale, and is just as "badly behaved" as the Fick D_{12}.

Let us now turn our attention to diffusion in triethylamine(1)/water(2) mixtures whose critical composition is $x_1 = 0.073$, with an LCST = 291.5 K. Haase and Siry[41] have experimentally determined the Fick diffusivities, D_{12}, for $x_1 = 0.073$ and varying temperatures; see Figure 26a. The data show that the value of D_{12} decreases by about one order of magnitude as T approaches UCST = 291.5 K. Figure 26b presents the data on the thermodynamic correction factor Γ as a function of x_1 at temperatures $T =$ 277.15 K, $T = 283.15$, and $T = 291.15$ K. For $x_{1C} = 0.073$, we note an order of magnitude decrease in Γ as T increases from 277.15 K, to $T = 291.15$ K. We conclude, therefore, that the decrease in D_{12} with increasing T is primarily ascribable to the reduction in the value of Γ.

At the spinodal composition, the Fick diffusivity must vanish

$$\frac{1}{RT}\frac{\partial^2 G}{\partial x_1^2} = H = \frac{\Gamma}{x_1 x_2} = 0; \quad D_{12} = 0 \tag{79}$$

In the experiments reported by Vitagliano et al.[42], the Fick diffusivities, D_{12}, for triethylamine (1)/water (2) mixtures, measured at two different temperatures 292.15 K, and 293.15 K, both slightly above the value of UCST = 291.5 K; see Figure 27. The diffusivities were measured at varying compositions approaching the spinodal curve from either side of the spinodal curves. Their data clearly demonstrate that the diffusivities vanish at spinodal composition, in agreement with the expectations of Equation (79).

The diffusivity of urea, and glycine in water plummets to vanishingly low values as the spinodal compositions are reached;[43, 44] see Figures 28a,b. A lucid discussion on diffusion near spinodal points is given by Cussler.[45] The proper driving force for the description of crystallization kinetics is the chemical potential difference between the supersaturated solution (the transferring state) and the crystal (the transferred state), $\frac{\mu_i - \mu_{i,eq}}{RT} = \ln\left(\frac{a_i}{a_{i,eq}}\right)$, where $a_i = \gamma_i x_i$ is the solute activity.[46, 47]

The data on Fick diffusivity[41, 48, 49] of n-hexane (1) / nitrobenzene (2) mixtures as a function of ($T - T_c$) with T_c = UCST = 292.56 K are shown in Figure 29. The Fick diffusivity tends to vanish as the UCST value is approached.

The region between the spinodal curve (indicated by the red line) and the binodal curve (indicated by the green line) is a meta-stable region that offers the possibility of nucleation. Figure 30 shows a schematic of the nucleation and growth process. The top and bottom rows represent two adjacent local regions in the solution. Four different events in the nucleation process are sketched in the four columns. The circles represent the concentration (composition) of component 2. In Event 1, we assume that the mixture is brought into the meta-stable region and that the compositions are uniform in the two adjacent regions. A small concentration fluctuation, pictured as Event 2, will be dissipated by downhill diffusion along the arrows indicated. The net result will be a return to the conditions as sketched in Event 1, for a uniform mixture. A large fluctuation (Event 3) causes the formation of a nucleus (containing pure component 2) of a critical size, indicated by the large circle. Downhill diffusion in the regions surrounding the nucleus will serve to equalize the concentrations surrounding the nucleus; the nucleus itself does not participate in the diffusion process. The net result is that the nucleus grows in size, and the result is depicted in Event 4.

For visualization of the nucleation and growth, see the following videos on YouTube

https://www.youtube.com/watch?v=uYMVN9tDvus

https://www.youtube.com/watch?v=54g-ac6VV1w

https://www.youtube.com/watch?v=A12AEInRYTc

Diffusion in regions corresponding to the demixing region characterized by $\Gamma < 0$, needs special attention. We expect negative values of the Fick diffusivity and, as a consequence, uphill diffusion. In binary systems, diffusion is always downhill of the chemical potential gradient; it can go uphill of the concentration gradient. Such phenomena are observed for mixtures of metallic alloys and polymeric solutions; in such cases uphill diffusion leads to spinodal decomposition.[50]

Figure 31 shows a schematic of the spinodal decomposition process. The top and bottom rows represent two adjacent local regions in the solution. Four different events in the process are sketched in the four columns. The circles represent the concentration (composition) of component 2. In Event 1, we assume that the mixture is brought into the unstable region and that creates a higher concentration in the top region, and a slightly lower concentration in the bottom region. In the unstable region, the Fick diffusivity is negative, and therefore uphill diffusion occurs. Uphill diffusion has the effect of accentuating the segregation process, resulting in Event 3 in which the concentrations in the top and bottom rows are further apart. The segregation continues until the components 1 and 2 are separated into two separate phases. Clearly, the driver for spinodal decomposition is the phenomenon of uphill diffusion.

For visualization of the spinodal decomposition by solution of the Cahn-Hilliard[51, 52] equation, see the following videos on YouTube

https://www.youtube.com/watch?v=52ZDH9mzDtc

https://www.youtube.com/watch?v=CrGatXppcrc

https://www.youtube.com/watch?v=bjhWdTfDUbM

https://www.youtube.com/watch?v=yKLrAXBmpwU

https://www.youtube.com/watch?v=wHYfOAOt3vE

https://www.youtube.com/watch?v=uSapRdGvCDw

9. Diffusivities in ternary liquid mixtures in regions close to phase splitting

Let us first consider phase stability in ternary liquid mixtures that can undergo phase separation yielding two liquid phase phases that are in equilibrium with each other. Figure 32 is a schematic showing liquid/liquid phase equilibrium for a hypothetical ternary liquid mixture. The binodal and spinodal curves converge at the plait point. The region between the spinodal and binodal envelopes is meta-stable (indicated in yellow). Let us consider ternary liquid mixtures of two different compositions A and B that are brought into contact (cf. Figure 32). The average mixture composition (M) falls within in the two-phase region. Each of the mixtures A and B will equilibrate to the compositions at the two ends of the tie-line corresponding to the mixture composition M; these compositions are different from those of A and B. The technology of liquid-liquid extraction is essentially based on the separation that is effected as a consequence of the fact that phase equilibration yields compositions that are distinctly different from the starting ones A and B. The design and development of liquid-liquid extraction processes is crucially dependent on our ability to describe (a) liquid-liquid phase equilibrium thermodynamics, and (b) composition trajectories and fluxes in both the adjoining phases as these approach equilibrium or stationary states.

We now examine the influence of phase stability on diffusion in four different non-ideal ternary mixtures:

glycerol(1)/acetone(2)/water(3) mixtures

water(1)/chloroform(2)/acetic-acid(3) mixtures

water(1)/2-propanol(2)/cyclohexane(3) mixtures

acetone/water/ethylacetate mixtures

In each case we carefully examine the experimental data to draw a variety of conclusions.

Let us begin with the system glycerol(1)/acetone(2)/water(3) for which the liquid-liquid phase equilibrium diagram has been provided by Krishna et al.[13] The experimental data on the binodal curve, and the tie lines are shown in Figure 33. The composition of the plait point is $x_{\mathrm{glycerol}}= 0.1477$, $x_{\mathrm{acetone}}= 0.4163$ and $x_{\mathrm{water}}= 0.4360$. Furthermore, Krishna et al[13] provide the NRTL parameters describing phase equilibrium that will be used later to calculate the thermodynamic correction factors.

The phase stability is dictated by the determinant of the Hessian matrix of the Gibbs free energy, $\left|H\right|$. The spinodal curve is defined by solving $\left|H\right| = 0$.

With the help of the NRTL parameters, the spinodal curve can be determined as shown in Figure 33. At the plait point, the binodal and spinodal curves converge.

Outside the region delineated by the spinodal curve, we have $\left|H\right| > 0$. Also, in view of the second law of thermodynamics (cf. equation (18)), we have $\left|L\right| > 0$. In view of equation (33), the condition of phase stability translates to Equation (21) which implies that both the eigenvalues of the Fick matrix [D] are positive definite.

Within the region delineated by the spinodal curve, we require

$$\left|H\right| < 0; \quad \left|D\right| < 0; \quad \text{phase instability} \tag{80}$$

Equation (80) implies that one of eigenvalues of the Fick diffusivity matrix [D] must be negative. Uphill diffusion must occur within the region of phase instability. The region between the binodal and spinodal curves is meta-stable. At the plait point, and along the spinodal curve we must have

$$\left|D\right| = 0; \quad \left|H\right| = 0; \quad \text{spinodal curve} \tag{81}$$

The thermodynamic factor $\left[\Gamma\right]$ is related to the Hessian matrix

$$\begin{gathered}
\begin{bmatrix} H_{11} & H_{12} \\ H_{21} & H_{22} \end{bmatrix} = \frac{1}{x_3} \begin{bmatrix} \dfrac{(1-x_2)}{x_1} & 1 \\ 1 & \dfrac{(1-x_1)}{x_2} \end{bmatrix} \begin{bmatrix} \Gamma_{11} & \Gamma_{12} \\ \Gamma_{21} & \Gamma_{22} \end{bmatrix}; \\
\begin{bmatrix} \Gamma_{11} & \Gamma_{12} \\ \Gamma_{21} & \Gamma_{22} \end{bmatrix} = \begin{bmatrix} (1-x_1)x_1 & -x_1x_2 \\ -x_1x_2 & (1-x_2)x_2 \end{bmatrix} \begin{bmatrix} H_{11} & H_{12} \\ H_{21} & H_{22} \end{bmatrix}
\end{gathered} \tag{82}$$

So, the determinant of $\left[\Gamma\right]$ also vanishes along the spinodal curve, and at the plait point, i.e. $\left|\Gamma\right| = 0$.

With the above background on phase stability, let us examine the data on Fick diffusivities.

Grossmann and Winkelmann[53-55] have reported data on the Fick diffusivity matrix [D] for glycerol(1)/acetone(2)/water(3) mixtures at 75 different compositions, in the acetone-rich and water-rich regions as indicated in Figure 33. As illustration, at x_1= 0.18, x_2 = 0.22, x_3 = 0.6, $\left[D\right] = \begin{bmatrix} 0.294 & 0.127 \\ 0.148 & 0.213 \end{bmatrix} \times 10^{-9}$ $\text{m}^2\ \text{s}^{-1}$, signaling strong diffusional coupling. The matrix of thermodynamic factors at the composition x_1= 0.18, x_2 = 0.22, x_3 = 0.6 is calculated to be $[\Gamma]=\begin{bmatrix} 1.83 & 0.73 \\ 0.478 & 0.444 \end{bmatrix}$. Thermodynamic coupling effects contribute to large off-diagonal elements of the matrix of Fick diffusivities $[D]$.

Figure 34a presents plots showing the dependence of the elements of $[\Gamma]$ for glycerol(1)/acetone(2)/water(3) mixtures on the mole fractions of glycerol, x_1. The strong thermodynamic coupling is particularly evident when we compare the relative magnitudes of Γ_{21} with respect to the diagonal elements Γ_{22}. Figures 34b and 34c are plots of the determinants $|\Gamma|$ and $|H|$ as a function of the mole fraction of glycerol. We note that as the plait point (x_{glycerol}= 0.1477, x_{acetone}= 0.4163 and x_{water}= 0.4360), both $|\Gamma|$ and $|H|$ tend to vanish because of phase stability considerations; see equation (81).

Figure 35 presents the entire set of experimental data of Grossmann and Winkelmann[53-55] for the elements of the Fick diffusivity matrix [D] for glycerol(1)/acetone(2)/water(3) mixtures, as a function of the mole fractions of acetone, x_2, and water, x_3. We note that the ratio $\frac{D_{21}}{D_{22}}$ approaches values of about 2.5 for high concentrations of acetone; this is largely due to the influence of $\frac{\Gamma_{21}}{\Gamma_{22}}$ as witnessed in Figure 34. A further point to underscore is that the off-diagonal elements can be negative for certain composition regions; negative off-diagonal elements are not forbidden by the second law of thermodynamics, as noted earlier.

Figure 35 provides evidence that the determinant $|D|$ vanishes at the plait point (x_{glycerol}= 0.1477, x_{acetone}= 0.4163 and x_{water}= 0.4360). At a composition x_{glycerol}= 0.16, x_{acetone}= 0.372 and x_{water}= 0.468, that is close to the plait point, Grossmann and Winkelmann[53-55] report the values: $[D]=\begin{bmatrix} 0.4221 & 0.2801 \\ 0.2464 & 0.2129 \end{bmatrix}\times 10^{-9}$ m^2 s^{-1} which yields $|D| = 0.0208\times 10^{-18}$ m^4 s^{-2}. Figure 36 presents a 3D plot of the values of the determinant as a function of the mole fraction of glycerol, and acetone. We see that as the composition approaches the composition of the plait point, the value of the determinant $|D|$ tends to vanish, i.e. $|D| = 0$. Also shown in Figure 36 are the corresponding values of the determinant of $[\Gamma]$. The data confirm that the situation $|D| = 0$ at the plait point has its origin in the requirement $|\Gamma| = 0$, prescribed by thermodynamic stability considerations. The same information is obtained from Figure 37a that plots the determinant $|D|$ as a function of the mole fraction of glycerol, x_1.

The vanishing of the determinant $|D|$ implies that one of the eigenvalues (say, the 2nd one) of the Fick diffusivity matrix [D] is zero, while the other eigenvalue (the 1st one) remains positive definite. Figures 37b, and 37c present plots of the two eigenvalues as a function of the mole fraction of glycerol, x_1, and acetone, x_2, in the liquid mixture. In the Section 10 we shall discuss the implications of the vanishing of 2nd eigenvalue.

Figure 38a presents the values of the ratios D_{12}/D_{11}, and D_{21}/D_{22} of the Fick diffusivity matrix [D] for glycerol(1)/acetone(2)/water(3) mixtures plotted as a function of the determinant $|D|$. We note that as the determinant tends to vanish, D_{12}/D_{11}, and D_{21}/D_{22} tends to increase. In order to demonstrate that coupling effects of the Fick diffusivity matrix [D] is primarily caused by thermodynamic effects, Figure 38a compares the ratios D_{12}/D_{11}, and Γ_{12}/Γ_{11} as a function of the determinant $|D|$. The inter-relation between the two sets is evident.

In order to demonstrate the well-behavedness of the M-S diffusivities, Figure 39a presents a plot of the ratio $\frac{|D|^{1/2}}{|\Gamma|^{1/2}}$ for glycerol(1)/acetone(2)/water(3) mixtures, plotted as a function of the mole fractions of acetone, x_2, and water x_3. The square root of determinants $|D|$, and $|\Gamma|$ are representative of the "magnitudes" of [D], and $[\Gamma]$ respectively. The ratio $\frac{|D|^{1/2}}{|\Gamma|^{1/2}}$ can be viewed as the "magnitude" of the

Maxwell-Stefan diffusivity in the *ternary* mixture. The variation of $\frac{|D|^{1/2}}{|\Gamma|^{1/2}}$ appears to be strongly dependent on the composition of acetone in the mixture. To confirm this, Figure 39b plots $\frac{|D|^{1/2}}{|\Gamma|^{1/2}}$ as a function of the mole fraction of acetone, x_2. We note that the entire data set appears to fall within a narrow band; these results are analogous to those presented earlier in Figure 5, and Figure 6 for acetone(1)/benzene(2)/CCl_4(3), acetone(1)/benzene(2)/methanol(3), methanol(1)/1-butanol(2)/1-propanol, acetone(1)/water(2)/1-propanol(3), acetone(1)/1-butanol(2)/1-propanol(3), and 1-propanol(1)/1-chlorobutane(2)/n-heptane(3) mixtures.

As the second illustration, Figure 40 shows the experimental data for liquid/liquid equilibrium in water(1)/chloroform(2)/acetic-acid(3) mixtures. The binodal curve is indicated in green. The spinodal curve is indicated by the red line.

The experimental data of Vitagliano et al.[56] for Fick diffusivity matrix [D] of water(1)/chloroform(2)/acetic-acid(3) mixtures at six different compositions (cf. Figure 40) also confirm the expectations of Equations (21), and (81). We note that values of the determinant $|D|$ progressively decreases in magnitude as the compositions become increasingly poorer in acetic acid. At the plait point (composition: $x_1 = 0.375$, $x_2 = 0.261$ and $x_3 = 0.364$) the matrix of Fick diffusivities determined by Vitagliano et al.[56] by extrapolation of their data is $[D] = \begin{bmatrix} 0.92 & 0.40 \\ 0.37 & 0.161 \end{bmatrix} \times 10^{-9} \quad \mathrm{m^2\ s^{-1}}$. It can be confirmed that determinant vanishes, i.e. $|D| = 0$.

The classic experiments of Vitagliano et al.[56] that were published in 1978 were supplemented by more recent measurements in 2007 by Buzatu et al.[57] for Fick diffusivity matrix [D] of water(1)/chloroform(2)/acetic-acid(3) mixtures at five different compositions; see Figure 41.

The two sets of experimental data of Vitagliano et al.[56] and Buzatu et al.[57] are combined and analyzed in Figure 42.

Figure 42a shows a plot of the determinant $|D|$ as a function of $(1 - x_3)$ for water(1)/chloroform(2)/acetic-acid(3) mixtures. The results show that the determinant $|D|$ reduces in magnitude as the compositions approach the two-phase region.

Figure 42b shows a plot of the determinant $|\Gamma|$ as a function of $(1- x_3)$. As the plait point is approached, the determinant $|\Gamma|$ tends to vanish.

Figure 42c presents a plot of the ratio $\frac{|D|^{1/2}}{|\Gamma|^{1/2}}$ as a function of $(1- x_3)$. The square root of determinants $|D|$, and $|\Gamma|$ are representative of the "magnitudes" of $[D]$, and $[\Gamma]$ respectively. The ratio $\frac{|D|^{1/2}}{|\Gamma|^{1/2}}$ can be viewed as the "magnitude" of the Maxwell-Stefan diffusivity in the *ternary* mixture. The ratio $\frac{|D|^{1/2}}{|\Gamma|^{1/2}}$ appears to show a simple dependence on the mole fraction of acetone, quite similar to that observed for the variation of the M-S binary mixtures; see Figure 3.

Figure 42d plots the ratios Γ_{12}/Γ_{11}, and Γ_{21}/Γ_{22} as a function of the determinant $|\Gamma|$. This shows that the influence of thermodynamic coupling is increased as the spinodal curve is approached.

Figure 42e shows the ratios D_{12}/D_{11}, and D_{21}/D_{22} of the Fick diffusivity matrix $[D]$ as a function of the determinant $|D|$. We note that as the determinant tends to vanish, D_{12}/D_{11} increases to values in excess of unity. The lowering the magnitude of $|D|$ as the plait point is approached, also signifies an increase in the importance of coupling effects. It is clear that the coupling effects have their roots in non-ideal solution thermodynamics.

The data in Figure 38 and Figure 42 lead us to conclude that the condition $|D| = 0$ implies the strongest possible diffusional coupling effect.

Clark and Rowley[58] report experimental data for the determinant of the Fick diffusivity matrix $[D]$ for water(1)/2-propanol(2)/cyclohexane(3) mixtures as $(T - T_c)$ where T is the temperature at which the diffusivities are measured, and critical temperature T_c = 303.67 K; see Figure 43. The elements of the Fick matrix of diffusivities were measured at a constant composition corresponding to that at the plait point at 303.67 K: x_1 = 0.367, x_2= 0.389, x_3= 0.244. Examination of the values of the Fick diffusivity matrix (also indicated in Figure 43a), we see that the coupling effects get increasingly stronger as T_c is approached; concomitantly the determinant $|D|$ gets progressively smaller in magnitude.

Figure 44 shows the phase equilibrium diagram for acetone/water/ethylacetate mixtures at 293 K. Pertler[59] reports the values of the elements of the Fick diffusivity matrix in both the ethylacetate-rich and water-rich regions. In each of these two cases, he adopts a different numbering for the components. For the ethylacetate-rich region, the values of the Fick diffusivity matrix $[D]$ are reported using the component number acetone(1)/water(2)/ethylacetate(3); the values are plotted in Figure 44. Particularly noteworthy is the extremely large negative value of D_{21}. The large negative value of D_{21} is caused by the corresponding large negative value of Γ_{21}, as is evident in the plot on the right upper side of Figure 44. We will see in Section 11, that the strong coupling effects engendered by this large negative value of D_{21} will leave its imprint on the equilibration trajectory.

Figure 45 presents the experimental data of Pertler[59] for the elements of the Fick diffusivity matrix in the water-rich region of the phase diagram; these values correspond to the component numbering: acetone(1)/ethylacetate(2)/water(3). The negative value of D_{12} is caused by the corresponding large negative value of Γ_{12}, as is evident in the plot on the left upper side of Figure 45.

10. Equilibration trajectories in ternary liquid mixtures

In homogeneous single-phase regions, uphill diffusion can occur as a result of sizable magnitudes of cross-coefficients of the Fick diffusivity matrix. To demonstrate this let us consider inter-diffusion of water(1)/chloroform(2)/acetic-acid(3) mixtures that ensues when two different compositions (in the left and right compartments in Figure 46) are brought in contact. The initial composition of the left compartment is: $x_{1,L}$ = 0.48, $x_{2,L}$= 0.1 and $x_{3,L}$ = 0.42. The initial composition of the right compartment is: $x_{1,R}$ = 0.2, $x_{2,R}$ = 0.38 and $x_{3,R}$ = 0.42. The composition at equilibrium is $x_{1,eq}$ = 0.34, $x_{2,eq}$ = 0.24 and

$x_{3,\mathrm{eq}} = 0.42$. We note that there is no driving force for the transfer of acetic acid, component 3. The transient equilibration process is described by the coupled two-dimensional matrix equation

$$\begin{pmatrix} x_1 \\ x_2 \end{pmatrix} = \frac{1}{2}\begin{pmatrix} x_{1L} + x_{1,R} \\ x_{2L} + x_{2,R} \end{pmatrix} + \frac{1}{2} erf\left[-\frac{z}{\sqrt{4t}} \begin{bmatrix} D_{11} & D_{12} \\ D_{21} & D_{22} \end{bmatrix}^{-1/2} \right] \begin{pmatrix} x_{1R} - x_{1L} \\ x_{2R} - x_{2L} \end{pmatrix} \tag{83}$$

At the equilibrated composition at equilibrium is $x_{1,\mathrm{eq}} = 0.34$, $x_{2,\mathrm{eq}} = 0.24$ and $x_{3,\mathrm{eq}} = 0.42$, Vitagliano et al;[56] report the Fick diffusivity matrix as $[D] = \begin{bmatrix} 0.309 & 0.368 \\ 0.344 & 0.939 \end{bmatrix} \times 10^{-9}$ m^2 s^{-1}; $|D| = 0.164 \times 10^{-18}$ m^4 s^{-2}. For the chosen set of input parameters, the importance of diffusion couplings can be gauged from the values of $\frac{D_{12}(x_{2R} - x_{2L})}{D_{11}(x_{1R} - x_{1L})} = -1.2$; $\frac{D_{21}(x_{1R} - x_{1L})}{D_{22}(x_{2R} - x_{2L})} = -0.367$; these values indicate that the influence of diffusion coupling is indeed significant. As a consequence of coupling effects, the equilibration of acetic acid displays overshoots and undershoots; see Figure 46. In the ternary composition space, the equilibration trajectory follows a serpentine path, as depicted in the ternary plot in Figure 46.

Serpentine trajectories are also obtained for equilibration in glycerol(1)/acetone(2)/water(3) mixtures; this is illustrated by the set of two simulations shown in Figure 47.

Let us examine the first of these sets of simulations (for the equilibrium composition $x_1 = 0.1$, $x_2 = 0.432$, $x_3 = 0.468$), in more detail in order to gain insights into the phenomena of uphill diffusion. Figure 48a shows the equilibration trajectory in 2D composition (mole fraction) space. The serpentine trajectory indicates uphill diffusion for glycerol. The uphill transport of glycerol is also clearly evident when we plot the compositions of each component as a function of the dimensionless distance coordinate $\frac{z}{\sqrt{4D_{ref}t}}$ where the value of the chosen reference diffusivity $D_{ref} = 10^{-9}$ m^2 s^{-1}; see Figure 48b. This plot clearly indicates that uphill diffusion is only experienced by glycerol, and not by either acetone or water. The NRTL parameters describing phase equilibrium for this system are available from the work of Krishna et al.[13] Using the NRTL parameters we determined the activity coefficient, γ_i, for each of the component during the transient equilibration process. For each component we determined the activity, a_i,, defined as

$$a_i = \gamma_i x_i \tag{84}$$

Figure 48c shows the plot of the activity trajectory in 2D space. The thermodynamic activity shows a monotonous equilibration trajectory. This is an important result which indicates that glycerol diffusion is not uphill of its activity driving force. To further strengthen this finding, Figure 48d compares the profiles of mole fraction and activity, as a function of the dimensionless distance coordinate. The activity of glycerol does not show any overshoots or undershoots.

It is often true that uphill diffusion in condensed phases is witnessed in *composition* space; it does not occur in *activity* space.

Figure 49a presents the results for the serpentine trajectories obtained with simulations with the equilibrium composition: $x_1= 0.18$, $x_2 = 0.22$, $x_3 = 0.6$. The same trajectory when plotted in 2D activity space exhibits a monotonous equilibration; see Figure 49b. The comparison of the transience for acetone, expressed in both mole fractions and activity plotted against the dimensionless coordinate $\frac{z}{\sqrt{4D_{ref}t}}$ is shown in Figure 49c. There is no overshoot or undershoot in the activity profiles for acetone.

Now let us consider the situation in which initial compositions in the left and right chambers are such that the equilibrium composition is the plait point of water(1)/chloroform(2)/acetic-acid(3). The initial composition of the left compartment is: $x_{1,L} = 0.5$, $x_{2,L} = 0.136$ and $x_{3,L} = 0.364$. The initial composition of the right compartment is: $x_{1,R} = 0.25$, $x_{2,R} = 0.386$ and $x_{3,R} = 0.364$. The average composition is determined to be $x_1 = 0.375$, $x_2 = 0.261$ and $x_3 = 0.364$, corresponding to the plait point. We note that there is no driving force for the transfer of acetic acid, component 3. From the data of Vitagliano et al.[56] the Fick diffusivity matrix is $\left[D\right] = \begin{bmatrix} 0.92 & 0.40 \\ 0.37 & 0.161 \end{bmatrix} \times 10^{-9}$ $\mathrm{m^2\ s^{-1}}$. For the chosen set of input parameters, we obtain $\frac{D_{12}(x_{2R}-x_{2L})}{D_{11}(x_{1R}-x_{1L})}=-0.434$; $\frac{D_{21}(x_{1R}-x_{1L})}{D_{22}(x_{2R}-x_{2L})}=-2.3$; these values indicate strong coupling. However, we have a unique situation due to the vanishing of the determinant, $|D|=0$; one of the eigenvalues of Fick diffusivity matrix [D] also vanishes. Consequently, the equilibration of all three components must relax along the eigenvector corresponding to the non-zero eigenvalue $D_{eig,1}=1.08\times10^{-9}$ $\mathrm{m^2\ s^{-1}}$; for more detailed discussions see Krishna et al.[60] and Taylor and Krishna.[11] The equilibration trajectories are given by the set of uncoupled equations

$$x_i=\frac{1}{2}(x_{iL}+x_{iR})+\frac{1}{2}erf\left[-\frac{z}{\sqrt{4D_{eig,1}t}}\right](x_{iL}-x_{iR});\quad i=1,2,3 \tag{85}$$

These trajectories are linear in the composition space, and do not display any over- or under-shoots for acetic acid; see Figure 50. It is paradoxical that the composition trajectories are constrained to follow a linear trajectory despite strong coupling effects.

We now consider published experimental data to verify the serpentine trajectories witnessed in Figures 46, 47, 48, 49, and 50.

Krishna et al.[60] have reported experimental data on the equilibration paths followed in glycerol(1)/acetone(2)/water(3) mixtures that provide confirmation of curvilinear equilibration trajectories. In one on the sets of experiments conducted in a Lewis stirred cell, the initial compositions of the two liquid phases are: Glycerol-rich phase in the bottom cell: $x_{1,0}$ = 0.85, $x_{2,0}$ = 0.0,and $x_{3,0}$ = 0.15; Acetone-rich phase in the top cell: $x_{1,0}$ = 0.0, $x_{2,0}$ = 0.77 and $x_{3,0}$ = 0.23. The mixture composition ends up in the region of phase instability; see Figure 51. Consequently, each of the two phases must equilibrate to the corresponding points at the two ends of the tie-line. The equilibrium compositions at the end of the tile line are for the Glycerol-rich phase: $x_{1,\mathrm{eq}}$ = 0.552, $x_{2,\mathrm{eq}}$ = 0.164 and $x_{3,\mathrm{e}}$ = 0.284; Acetone-rich phase: $x_{1,\mathrm{eq}}$ = 0.042, $x_{2,\mathrm{eq}}$ = 0.894 and $x_{3,\mathrm{eq}}$ = 0.064.

In the experiments each of the two equilibration trajectories were monitored experimentally; these are shown (red circles in the glycerol-rich phase, and green squares in the acetone-rich phase) in Figure 51.

Each of the two phases exhibits one half of a serpentine path. Let us analyze each of the equilibration paths in more detail.

Krishna et al.[60] develop a model to capture the equilibration trajectories that consists of solving a set of two coupled matrix differential equations in either phase. The solution yields the following relation

$$\begin{pmatrix} x_{1,eq} - x_1 \\ x_{2,eq} - x_2 \end{pmatrix} = \exp\left[-\beta \begin{bmatrix} D_{11} & D_{12} \\ D_{21} & D_{22} \end{bmatrix} t \right] \begin{pmatrix} x_{1,eq} - x_{1,0} \\ x_{2,eq} - x_{2,0} \end{pmatrix} \tag{86}$$

where β is the cell constant for the Lewis stirred cell.

The equilibration paths in the glycerol-rich phase are well described by the following values of the Fick matrix of diffusivities that are obtained by extrapolation of the diffusivity data of Grossmann and Winkelmann[53, 54]

$$[D] = \begin{bmatrix} 0.33 & 0.04 \\ 0.1 & 0.35 \end{bmatrix} \times 10^{-9} \quad \mathrm{m^2\ s^{-1}} \tag{87}$$

The comparison of the experimentally determined equilibration trajectories with the model calculations for the glycerol-rich phase are shown in in Figure 52. The curvilinear equilibration trajectory is ascribable to the coupling between species diffusion, evidenced by the non-zero off-diagonal elements.

For the acetone-rich phase, the comparison of the experimentally determined equilibration trajectories with the model calculations are shown in Figure 53; here, the model calculations use Fick diffusivity values using the data of Grossmann and Winkelmann[53, 54] for guidance in extrapolation

$$[D] = \begin{bmatrix} 2.4 & 0.1 \\ 1 & 1.1 \end{bmatrix} \times 10^{-9} \quad \mathrm{m^2\ s^{-1}} \tag{88}$$

Figure 54 presents the simulation results for the equilibration trajectory followed in acetone(1)/ethylacetate(2)/water(3) mixtures when two mixtures of compositions (in mass tractions) ω_1=0.01, ω_2=0.01, ω_3=0.98, and ω_1=0.17, ω_2=0.1, ω_3=0.73 are allowed to equilibrate to yield the final equilibrated value ω_1=0.09, ω_2=0.055, ω_3=0.855. The values of the Fick diffusivity used in the calculations corresponds to the third point in the water-rich data set of Pertler[59]: $[D]=\begin{bmatrix}0.179 & -0.287\\ 0.316 & 0.764\end{bmatrix}\times 10^{-9}\quad \mathrm{m^2\ s^{-1}}$. We note that the trajectory followed is serpentine in shape. The experimental data obtained by Haeberl and Blass[61] (shown in the inset to Figure 54) confirms that the equilibration tends to "hug" the binodal curve rather than follow a straight-line equilibration path.

A unique situation occurs for equilibration near the region of the plait point. The data of Grossmann and Winkelmann[53, 54] when extrapolated to the plait point suggest the set of values $[D]=\begin{bmatrix}0.42 & 0.35\\ 0.3 & 0.24\end{bmatrix}\times 10^{-9}\quad \mathrm{m^2\ s^{-1}}$; $|D|=0$. As a consequence one of the eigenvalues of Fick diffusivity matrix [D] must vanish and the equilibration of all components must relax along the eigenvector corresponding to the non-zero eigenvalue $D_{eig,1}=0.67\times 10^{-9}\quad \mathrm{m^2\ s^{-1}}$

$$\left(x_{i,eq}-x_i\right)=\exp(-\beta D_{eig,1}t)\left(x_{i,eq}-x_{i,0}\right);\quad i=1,2,3 \tag{89}$$

In the ternary composition space, the trajectory is linear, not serpentine, despite the significant coupling effects that are implicit in the condition $|D|=0$. The linear trajectory is confirmed by one set of experimental data of Krishna et al.[60] wherein the initial compositions in the two compartments lie on the tangent to the plait point; the equilibration paths are shown in Figure 55.

11. Spontaneous emulsification, and the Ouzo effect

When the diffusion trajectory in either, or both, of the liquid phases enters the meta-stable region we may experience spontaneous emulsification,[62-64] and the Ouzo effect.[65-67] Let us briefly discuss the Ouzo effect.

The aniseed-based alcoholic beverage variously called Ouzo (in Greece), Anis del Mono (in Spain), Pastis (in France), Sambuca (in Italy), and Raki (in Turkey), consists of a three component mixture of ethanol (≈45 vol%), water (55 vol%) and an essential oil called trans-anethol (≈ 0.1%). It is commonly consumed with the addition of three to five volumes of water to one volume of Ouzo. Figure 56 presents a phase equilibrium diagram for the ternary mixture of trans-anethol/ethanol/water. Diffusion of water into the ethanol/trans-anethol phase results in super-saturation of oil phase; the diffusion trajectory leads into the meta-stable region (in the bottom left corner) in which the oil spontaneously nucleates into tiny droplets.[68] The tiny 1 nm sized droplets scatter light, causing the drink to appear milky white.

For visualization of the Ouzo effect, watch the following videos on YouTube

https://www.youtube.com/watch?v=GxyWncY3O2g

https://www.youtube.com/watch?v=t5jbxh0C0UU

Vitale and Katz[67] have coined the generic term "Ouzo effect" to describe such a process of creating meta-stable liquid-liquid dispersions. Since no input of mechanical energy is involved, this offers an energy-efficient method of producing nanospheres and nanoparticles.[68] The Ouzo effect is distinct from spinodal decomposition that occurs when the metal-stable state separates into two liquid phases.[69]

What is the trajectory followed during the equilibration process when water is added to Ouzo? To answer this question let us zoom in on the bottom left corner of the phase diagram; see Figure 57. In the classic paper by Ruschak and Miller,[63] linear equilibration trajectories are used to predict spontaneous emulsification. If we assume a linear equilibration process (dashed line), then the binodal envelope is not penetrated, and no emulsification can occur; see Figure 57. The only possibility that the binodal envelope can be entered is if the equilibration trajectory follows a curvilinear path. We investigate this possibility in detail in the following section.

12. Serpentine trajectories, spinodal decomposition, and spontaneous emulsification

Figure 58 depicts the phase equilibrium diagram for the ternary system toluene(1)/ethanol(2)/water(3). This is one of the systems used by Ruschak and Miller[63] to explain the conditions required for spontaneous emulsification. Consider inter-diffusion of pure water and mixture of composition E, in the homogenous single phase region. A linear equilibration path (shown by the dashed line) must necessarily traverse the meta-stable zone that lies between the binodal and spinodal envelopes. An entry into the meta-stable zone is a pre-requisite to the possible eventuality of spontaneous emulsification. Consider inter-diffusion of two homogenous mixtures of compositions A and B, both in the homogeneous region, just above the binodal curve. A linear equilibration process (shown by the dashed line) shall remain in the homogeneous single-phase region; no spontaneous emulsification is possible. For A/B inter-diffusion process, if a serpentine trajectory is followed, as sketched schematically, then the unstable liquid-liquid phase splitting is entered and spinodal decomposition will occur. Consider inter-diffusion of mixtures of compositions C and D. The linear equilibration trajectory (shown by the dashed line) is at a tangent to the binodal curve, but remains in the single-phase region. For C/D inter-diffusion process, a serpentine trajectory will foray into the meta-stable region and spontaneous emulsification may occur. Since serpentine trajectories are not budgetted for in the Ruschak-Miller analysis, spontaneous emulsification will be ruled out *a priori*.

We examine the feasibility of forays into meta-stable regions of the phase diagram by examining the equilibration trajectories in nine different mixtures:

water(1)/chloroform(2)/acetic-acid(3)

acetone(1)/water(2)/ethylacetate(3)

water(1)/2-propanol(2)/cyclohexane(3)

water(1)/acetone(2)/toluene(3)

toluene(1)/ethanol(2)/water(3)

water(1)/caprolactam(2)/toluene(3)

water(1)/caprolactam(2)/benzene (3)

toluene(1)/propionic-acid (2)/water(3)

ethylacetate(1)/propionic-acid (2)/water(3)

Let us start by examining the diffusion trajectories for water(1)/chloroform(2)/acetic-acid(3) mixtures. We performed simulations in which the initial composition of the left compartment is: $x_{1,\mathrm{L}} = 0.55$, $x_{2,\mathrm{L}} = 0.1$ and $x_{3,\mathrm{L}} = 0.35$; the initial composition of the right compartment is: $x_{1,\mathrm{R}} = 0.13$, $x_{2,\mathrm{R}} = 0.38$ and $x_{3,\mathrm{R}} = 0.49$. The composition at equilibrium is $x_{1,\mathrm{eq}} = 0.34$, $x_{2,\mathrm{eq}} = 0.24$ and $x_{3,\mathrm{eq}} = 0.42$. The average composition corresponds to the fifth data set of Vitagliano et al;[56] for that reason we take the values of the Fick diffusivity matrix as $[D]=\begin{bmatrix}0.309 & 0.368\\ 0.344 & 0.939\end{bmatrix}\times 10^{-9}$ m^2 s^{-1}; $|D|=0.164\times 10^{-18}$ m^4 s^{-2}. For the chosen set of parameters, the importance of diffusion couplings can be gauged from the values of $\frac{D_{12}(x_{2R}-x_{2L})}{D_{11}(x_{1R}-x_{1L})}=-0.79$; $\frac{D_{21}(x_{1R}-x_{1L})}{D_{22}(x_{2R}-x_{2L})}=-0.55$; these values indicate that the influence of diffusion coupling is not negligible. We note that composition trajectory in the left chamber has forayed into the meta-stable region; see Figure 59. A linear equilibration trajectory, shown by the dashed lines in Figure 59, remains in the homogeneous single-phase region.

The two eigenvalues of the Fick matrix are $D_{eig,1}=1.1\times 10^{-9}$ m^2 s^{-1}, and $D_{eig,2}=0.15\times 10^{-9}$ m^2 s^{-1}; each eigenvalue has an associated eigenvector; these are dubbed "fast" and "slow" eigenvectors because of the relative magnitudes. Figure 60 indicates the actual diffusion trajectory, along with the fast and slow eigenvectors; see Taylor and Krishna[11] for details on the calculations of the eigenvectors. We note that the initial transience is dominated by the fast eigenvector, while the approach toward equilibrium is governed by the slow eigenvector.

For the second example, Figure 61 shows the equilibration trajectory followed by a small perturbation in acetone(1)/water(2)/ethylacetate(3) mixtures at 293 K. The composition (in mass tractions) of the mixture at equilibrium is, ω_1=0.2, ω_2=0.05, ω_3=0.75. The values of the Fick diffusivity used in the calculations $[D]=\begin{bmatrix}1.371 & 0.298\\ -17.47 & 6.016\end{bmatrix}\times 10^{-9}$ m^2 s^{-1} corresponds to the sixth point in the data set of Pertler.[59] We note that overshoot in the water concentration has entered into the meta-stable zone, opening up the possibility of emulsification.

The composition profiles plotted against the dimensionless coordinate $\frac{z}{\sqrt{4D_{ref}t}}$ are also plotted in Figure 61. We note that overshoots and undershoots are experienced by both water and ethylacetate. This is quite unusual and arises from the extremely large negative value of D_{21}.

Figure 62 presents the equilibration trajectories in water(1)/2-propanol(2)/cyclohexane(3) mixtures for the equilibrium composition x_1= 0.36, x_2 = 0.4, x_3 = 0.24, that lies just above the plait point at the critical temperature T_c = 303.67, i.e. x_1 = 0.367, x_2= 0.389, x_3= 0.244. The equilibration trajectories are calculated at four different temperatures, 303.75 K, 304.15 K, 304.65 K, 396.65 K. At all four temperatures, the equilibration trajectories penetrate the binodal curve. The closer the temperature is to the critical temperature, T_c = 303.67 K, the deeper is the penetration. As a consequence, we should expect phase splitting should ensue in all the four cases; straight-line equilibration trajectories would not anticipate phase splitting in any of the four scenarios.

Let us examine the trajectory followed during equilibration of homogenous mixtures of two different compositions for the system water(1)/acetone(2)/toluene(3). The composition of the equilibrated mixture is chosen to be $x_{1,\mathrm{eq}}$ = 0.2, $x_{2,\mathrm{eq}}$ = 0.61 and $x_{3,\mathrm{eq}}$ = 0.19, which point lies just above the binodal curve. The M-S diffusivities of the binary pairs are estimated as

$$\begin{array}{lll} Đ_{12}^{x_1\to 1} = 5.2; & Đ_{12}^{x_2\to 1} = 1.3; & \text{for water(1)/acetone(2) binary mixture} \\ Đ_{13}^{x_1\to 1} = 0.5; & Đ_{13}^{x_3\to 1} = 1; & \text{for water(1)/toluene(3) binary mixture} \\ Đ_{23}^{x_2\to 1} = 0.5; & Đ_{23}^{x_3\to 1} = 2; & \text{for acetone(2)/toluene(3) binary mixture} \end{array}$$

. At the average composition, the matrix of thermodynamic factors is calculated from phase equilibrium thermodynamics: $[\Gamma] = \begin{bmatrix} -0.009 & -0.403 \\ 0.323 & 1.2 \end{bmatrix}$. Using a combination of equations (35), and (51), we estimate the matrix of Fick diffusivities $[D] = \begin{bmatrix} -0.19 & -1.29 \\ 0.574 & 2.38 \end{bmatrix} \times 10^{-9}$ m^2 s^{-1}. It is particularly noteworthy that the Γ_{11}, and D_{11} are both negative; thermodynamic stability only requires that the determinants of $[\Gamma]$ and $[D]$ be positive definite. Using this diffusivity estimate, we calculated the diffusion trajectory. We note that the serpentine trajectory has just not managed to penetrate the binodal envelope; see Figure 63.

As the fifth, and final example we consider inter-diffusion of toluene(1)/ethanol(2)/water(3) mixtures; the composition (in mole tractions) of the mixture at equilibrium $x_{1,\mathrm{eq}}$ = 0.012, $x_{2,\mathrm{eq}}$ = 0.208 and $x_{3,\mathrm{eq}}$ = 0.78, which point already lies in the meta-stable zone between the binodal and spinodal envelopes. The M-S diffusivities of the binary pairs are estimated as

$$\begin{array}{ll} \text{Đ}_{12}^{x_1\to 1}=1.0; \quad \text{Đ}_{12}^{x_2\to 1}=0.5; & \text{for toluene(1)/ethanol(2) binary mixture} \\ \text{Đ}_{13}^{x_1\to 1}=1.0; \quad \text{Đ}_{13}^{x_3\to 1}=0.5; & \text{for toluene(1)/water(3) binary mixture} \\ \text{Đ}_{23}^{x_2\to 1}=1.7; \quad \text{Đ}_{23}^{x_3\to 1}=1.64 & \text{for ethanol(2)/water(3) binary mixture} \end{array}$$

. At the average composition, the matrix of thermodynamic factors is calculated from phase equilibrium thermodynamics: $[\Gamma]=\begin{bmatrix} 0.686 & -0.114 \\ -1.655 & 0.333 \end{bmatrix}$. Using a combination of equations (35), and (51), we estimate the matrix of Fick diffusivities $[D]=\begin{bmatrix} 0.6 & -0.1 \\ -2.6 & 0.53 \end{bmatrix}\times 10^{-9}$ m^2 s^{-1}. Using this diffusivity estimate, we calculated the diffusion trajectory. We note that the serpentine trajectory has penetrated the spinodal envelope and entered unstable region; see Figure 64; this implies phase splitting. A further noteworthy point is that the trajectory in the lower left corner attains negative values for the toluene mole fraction. Therefore, it is entirely possible that this predicted trajectory is unrealizable in practice.

To set the background for the next two mixtures water(1)/caprolactam(2)/toluene(3) and water(1)/caprolactam(2)/benzene (3) we shall investigate, we provide the following quote from the PhD dissertation of Bollen;.[70] This dissertation can be downloaded from http://dissertations.ub.rug.nl/faculties/science/1999/a.m.bollen/ .

The idea that emulsification might be a mass transfer driven process stems from problems in the industrial extraction of caprolactam from water. Caprolactam is the main feedstock for the manufacture of nylon-6,6, and there are several processes for its industrial manufacturing. In one of these processes, which is used by DSM in the Netherlands, the stream leaving the reactor is an aqueous solution of caprolactam. Caprolactam is extracted from this stream with benzene in a rotating disk contactor (RDC). In the top of the extraction column, where the reactor stream is fed, a very fine dispersion forms in the benzene phase, which hinders the separation of the two phases. This, in turn, negatively influences the purity of the product.

Let us examine the trajectory followed during equilibration of homogenous mixtures of two different compositions for the system water(1)/caprolactam(2)/toluene(3). The composition of the equilibrated mixture is chosen to be $x_{1,\mathrm{eq}} = 0.64$, $x_{2,\mathrm{eq}} = 0.2725$ and $x_{3,\mathrm{eq}} = 0.0875$, which point lies on the binodal curve. At the average composition, the matrix of thermodynamic factors is calculated from phase equilibrium thermodynamics: $\left[\Gamma\right]=\begin{bmatrix}-0.176 & -1.52\\ 0.42 & 2.10\end{bmatrix}$. We assume that the matrix of Fick diffusivities is the product of a scalar diffusivity 10^{-9} m^2 s^{-1} multiplied by $\left[\Gamma\right]$; i.e. $\left[D\right]=\begin{bmatrix}-0.176 & -1.52\\ 0.42 & 2.10\end{bmatrix}\times 10^{-9}$ m^2 s^{-1}. Using this estimate, we calculated the equilibration trajectory. We note that the serpentine trajectory has penetrated the binodal envelope; see Figure 65. This indicates the spontaneous emulsification is feasible.

Let us examine the trajectory followed during equilibration of homogenous mixtures of two different compositions for the system water(1)/caprolactam(2)/benzene (3) for the equilibrium composition. The composition of the equilibrated mixture is chosen to be x_1= 0.125, x_2 = 0.165, x_3 = 0.71 which point lies on the binodal curve. At the average composition, the matrix of thermodynamic factors is calculated from phase equilibrium thermodynamics: $\left[\Gamma\right]=\begin{bmatrix}0.591 & -0.925\\ -0.878 & 2.11\end{bmatrix}$. We assume that the matix of Fick diffusivities is the product of a scalar diffusivity 10^{-9} m^2 s^{-1} multiplied by $\left[\Gamma\right]$; i.e. $\left[D\right]=\begin{bmatrix}0.591 & -0.925\\ -0.878 & 2.11\end{bmatrix}\times 10^{-9}$ m^2 s^{-1}. Using this estimate, we calculated the equilibration trajectory. We note that the serpentine trajectory has penetrated the binodal envelope; see Figure 66. This indicates the spontaneous emulsification is feasible.

Let us examine the trajectory followed during equilibration of homogenous mixtures of two different compositions for the system toluene(1)/propionic-acid (2)/water(3). The composition of the equilibrated mixture is chosen to be $x_{1,\mathrm{eq}}$ = 0.475, $x_{2,\mathrm{eq}}$ = 0.4 and $x_{3,\mathrm{eq}}$ = 0.285, which point lies on the binodal curve. At the average composition, the matrix of thermodynamic factors is calculated from phase equilibrium thermodynamics: $\left[\Gamma\right]=\begin{bmatrix}0.3267 & -0.2963\\ 0.1806 & 1.1958\end{bmatrix}$. We assume that the matrix of Fick diffusivities is the product of a scalar diffusivity 10^{-9} m^2 s^{-1} multiplied by $\left[\Gamma\right]$; i.e.

$[D]=\begin{bmatrix} 0.3267 & -0.2963 \\ 0.1806 & 1.1958 \end{bmatrix}\times 10^{-9}$ m^2 s^{-1}. Using this estimate, we calculated the equilibration trajectory. We note that the serpentine trajectory has penetrated the binodal envelope; see Figure 67. This indicates the spontaneous emulsification is feasible.

Let us examine the trajectory followed during equilibration of homogenous mixtures of two different compositions for the system ethylacetate(1)/propionic-acid(2)/water(3). The composition of the equilibrated mixture is chosen to be $x_{1,eq} = 0.675$, $x_{2,eq} = 0.13$ and $x_{3,eq} = 0.195$, which point lies on the binodal curve. At the average composition, the matrix of thermodynamic factors is calculated from phase equilibrium thermodynamics: $[\Gamma]=\begin{bmatrix} -0.0358 & -1.7447 \\ 0.5700 & 3.6379 \end{bmatrix}$. We assume that the matrix of Fick diffusivities is the product of a scalar diffusivity 10^{-9} m^2 s^{-1} multiplied by $[\Gamma]$; i.e. $[D]=\begin{bmatrix} -0.0358 & -1.7447 \\ 0.5700 & 3.6379 \end{bmatrix}\times 10^{-9}$ m^2 s^{-1}. Using this estimate, we calculated the equilibration trajectory. We note that the serpentine trajectory has penetrated the binodal envelope; see Figure 68. This indicates the spontaneous emulsification is feasible.

Another consequence of curvilinear equilibration trajectories is experienced in the immersion precipitation process for membrane preparation.[71, 72] Figure 69 shows the equilibration trajectories when a 10% solution of Cellulose Acetate (CA) in acetone is immersed in a bath of pure water; the trajectories at three different times, $t = 10$ s, $t = 25$ s, and $t = 50$ s are depicted. We note the curvilinear trajectory at $t = 50$ s has entered the meta-stable region. This foray into the meta-stable region impacts on the membrane structure.[71, 72]

For experimental evidence of curvilinear trajectories followed during membrane preparation, see Prakash et al.[73] and Shojaie et al.[74, 75]

Within the spinodal envelope (the grey region in Figure 58), spinodal decomposition and phase separation occurs.[69] As discussed with the aid of Figure 31, uphill diffusion is involved in the spinodal decomposition process.

13. Aroma retention in drying of food liquids

During drying of food liquids such as orange juice and coffee, it is essential to retain the presence of volatile aroma compounds whilst removing water. A food liquid typically consists of aroma, water and sugar or coffee extract. Consider acetone to represent a model aroma compound with malto-dextrin representing the sugar compound. With decreasing water concentrations there is a strong decrease in the diffusion coefficients both for acetone and water, with a much stronger decrease of acetone diffusivity; see Figure 70a. At water concentrations lower than 15 wt % the ratio $D_{\mathrm{acetone}}/D_{\mathrm{water}}$ becomes so small that the system can be considered impermeable to acetone; see Figure 70b. In spray drying operation it is essential to ensure a rapid decrease of water concentration at the outer surface of the food liquid droplet and if the surface water is very quickly lowered to below 15 wt %, aroma retentions up to 100 % are possible.[76] Rigorous modelling of the drying of food liquids, demands the use of the Maxwell-Stefan equations (25).

14. Uphill diffusion in mixtures of glasses, metals, and alloys

The proper description of multicomponent diffusion in metals, glasses, steels, alloys, and composites is important in a wide variety of processes such as bonding, cladding, controlled heat treatments, and surface modification.[77]

One of the very first experimental evidence of uphill diffusion is available in the classic experiments reported by Darken, [17] who was one of the first to recognize the need to use activity gradients as proper driving forces when setting up the phenomenological relations to describe diffusion The following three quotes from his 1949 paper also serve as learning points for this tutorial review

"*the driving force in an isothermal diffusion process may be regarded as the gradient of the chemical potential,*",

"*for a system with more than two components it is no longer necessarily true that a given element tends to diffuse toward a region of lower concentration even within a single phase region*", and "*departure from the behavior of an ideal solution may be so great that the concentration gradient and the chemical potential gradient, or activity gradient, may be of different sign, thus giving rise to uphill diffusion*".

Two austenite bars of different compositions (0.48% C, 3.8% Si), and (0.45% C, 0.05% Si) are welded together. The Carbon in the high-Si bar has a significantly higher chemical potential or activity than the bar with the lower Si content. After Carbon was allowed to diffuse for 13 days at 1323 K, most of the C diffused into the low-Si bar; see Figure 71. The over- and under-shoots in the %C are adequately modelled by equations that are based on the work of Kirkaldy[78]

$$\begin{pmatrix} x_1 \\ x_2 \end{pmatrix} = \frac{1}{2}\begin{pmatrix} x_{1L} + x_{1,R} \\ x_{2L} + x_{2,R} \end{pmatrix} + \frac{1}{2} erf\left[-\frac{z - z_0}{\sqrt{4t}} \begin{bmatrix} D_{11} & D_{12} \\ D_{21} & D_{22} \end{bmatrix}^{-1/2} \right] \begin{pmatrix} x_{1L} - x_{1R} \\ x_{2L} - x_{2R} \end{pmatrix} \tag{90}$$

with the values of the Fick diffusivity matrix

$$[D] = \begin{bmatrix} 480 & 34 \\ 0 & 2.3 \end{bmatrix} \times 10^{-13} \quad \text{m}^2\ \text{s}^{-1} \tag{91}$$

The position $z = z_0$ is the interface, also called the Matano plane.

Figure 72 shows the transient equilibration of a diffusion couple consisting of Cu(1)/Ag(2)/Au(3) mixtures. The atom fractions at equilibrium are $x_1 = 0.475$, $x_2 = 0.175$, $x_3 = 0.35$. The trajectories are calculated with the values of the Fick diffusivity matrix $[D] = \begin{bmatrix} 2.3 & 1.11 \\ 1.8 & 3.1 \end{bmatrix} \times 10^{-14}\ \text{m}^2\ \text{s}^{-1}$ using the diffusivity data of Ziebold[33] that are provided in Table 3 as guideline. We note that Ag(2) displays pronounced overshoot and undershoot phenomena that is also confirmed in the experiments of Ziebold[33] with Sample 3.

To illustrate the diffusional characteristics of multicomponent glasses, let us consider a set of experiments reported by Varshneya and Cooper.[79] Two glass slabs with different compositions of $K_2O/SrO/SiO_2$ were brought into contact at time t=0 and the transient concentration distributions determined. The wt% of each component is measured on either side of the Matano plane ($z = z_0 = 0$), measured at t = 4.55 h after the start of the experiment are shown in Figure 73a. The over- and undershoots in the SrO concentrations are adequately modelled by equation (90), wherein the matrix of Fick diffusivities have the values

$$[D]=\begin{bmatrix} 1 & -0.267 \\ -1.22 & 0.33 \end{bmatrix}\times 10^{-13} \quad \mathrm{m^2\ s^{-1}} \tag{92}$$

Figure 73b shows a 3D trajectory plot of the wt% K_2O vs wt% SrO vs wt% SiO_2. The equilibration trajectory is serpentine in shape, and is clearly attributable to the coupled characteristics of the matrix of Fick diffusivities $[D]$.

If the matrix of Fick diffusivities is assumed to be diagonal with elements

$$[D]=\begin{bmatrix} 1 & 0 \\ 0 & 1 \end{bmatrix}\times 10^{-13} \quad \mathrm{m^2\ s^{-1}} \tag{93}$$

the corresponding equilibration trajectories are indicated by the dashed lines in Figures 73b. We note that the transient equilibration becomes monotonic for the uncoupled diffusion process.

Let us examine the experimental data of Vielzeuf and Saúl[80] for inter-diffusion of Fe/Mg/Ca mixtures in garnet, a precious stone consisting of a deep red vitreous silicate mineral. A diffusion "couple" with two different compositions are brought into contact at time t = 0; see Figure 74. The driving forces for the three components are (in atom fractions): $\Delta x_1 = -0.15; \quad \Delta x_2 = 0.01; \quad \Delta x_3 = 0.14$. The composition profiles on either side of the interface marker (z = 0, the Matano plane) are monitored at various time intervals. The composition profiles at t = 100 h (cf. Figure 74a) shows spatial over- and under-shoot in the composition profile for Mg, whose driving force is significantly lower than that of the two partner atoms. In ternary composition space, the equilibration trajectory is serpentine in shape; see Figure 74b.

The modelling of the experimental data Vielzeuf and Saúl[80] for inter-diffusion of Fe/Mg/Ca mixtures in garnet proceeds along similar lines to the foregoing examples. The overshoot in the equilibration of Mg is adequately modelled using the values of the Fick diffusivity matrix

$$[D]=\begin{bmatrix} 5.86 & -1.02 \\ -5.5 & 1.18 \end{bmatrix}\times 10^{-19} \quad \mathrm{m^2\ s^{-1}} \tag{94}$$

in equation (90); see Figure 75a. Use of the diagonal matrix

$$[D]=\begin{bmatrix}3 & 0\\ 0 & 3\end{bmatrix}\times 10^{-19} \quad \mathrm{m^2\ s^{-1}} \tag{95}$$

leads to monotonous equilibration trajectories indicated by the dashed line in Figure 75b.

The non-monotonous equilibration trajectory observed for SrO in Figure 73, and Mg in Figure 75 signal the occurrence of uphill diffusion; such phenomena are of importance in the processing of ceramics, cements, alloys, steels, and composites.[77, 81]

For multi-component mixtures ($n \geq 3$), uphill diffusion often occurs even when the phase is stable. Also, the diffusion flux may also be directed uphill, against the chemical potential gradient. In sharp contrast, in binary systems ($n = 2$), uphill diffusion occurs only in case of phase instability. In binary systems, diffusion is most commony downhill of the chemical potential, or activity, gradient; it can go uphill of the concentration gradient in unstable regions.

15. Crossing boundaries in azeotropic distillation

Distillation is the most widely used separation process in the chemical process industries. Design and simulation procedures for distillation are commonly based on the equilibrium stage model, developed by Sorel more than a hundred years ago.[82] Departures from thermodynamic equilibrium between the vapor and liquid phases on a distillation tray (see schematic in Figure 76), are commonly accounted for in practice by introducing the Murphree component efficiencies

$$E_{i,MV} = \frac{y_{iL} - y_{iE}}{y_i^* - y_{iE}}; \quad i = 1,2,...n \tag{96}$$

where y_{iE}, and y_{iL} are, respectively, the vapor phase mole fractions, entering and leaving a tray, and y_i^* is the vapor composition in thermodynamic equilibrium with the liquid leaving the tray. For a tray in thermodynamic equilibrium, the component efficiencies are 100% for each component. Mass transfer resistances on either side of the vapor/liquid interface reduce the component efficiencies to values below 100%. For binary distillation, the Murhpree component efficiencies are bounded, i.e.

$0 \le E_{1,MV} = E_{2,MV} \le 1$. For multicomponent distillation, with the number of species $n \ge 3$, coupled diffusion effects in either vapor or liquid phases cause the component efficiencies to be distinctly different from one another, $E_{1,MV} \ne E_{2,MV} \ne E_{3,MV}$. Phenomena such as osmotic diffusion, diffusion barrier, and uphill diffusion (cf. Figure 13b) result in Murphree component efficiencies that are unbounded ($E_{i,MV} \to \pm\infty$), zero ($E_{i,MV} = 0$), or negative ($E_{i,MV} < 0$); this has been demonstrated in several experimental studies.[27, 83-90]

Consider distillation of water(1)/ethanol(2)/acetone(3) mixtures. The pure component boiling points are: water = 373.2 K; ethanol = 351.6 K; acetone = 329.7 K; water/ethanol azeotrope = 351.4 K (composition of azeotrope = 12% water, 88% ethanol). Ethanol is the component with the intermediate boiling point. Consequently, the transfer of ethanol is from the liquid to the vapor phase near the top of the distillation column, approaching the condenser. However, ethanol transfers from the vapor to the liquid phase near the bottom of the column approaching the reboiler. This implies that the driving force for transfer of ethanol, $\left(y_2^* - y_{2E}\right)$, must necessarily change sign from the bottom to the top of the column. At some intermediate position, we may also have the situation corresponding to $\left(y_2^* - y_{2E}\right) = 0$. In one set of experimental results of Springer et al.[84] in the laboratory set-up shown in Figure 77a, the values of $\left(y_2^* - y_E\right)$ are plotted in Figure 77b. We note that the ethanol driving force is negative for Stages 2 – 9, $\left(y_2^* - y_E\right) \approx 0$ for Stage 10, and $\left(y_2^* - y_{2E}\right) > 0$ for Stage 11; see Figure 77b. The values of the $E_{2,MV}$ for ethanol is negative on Stage 10; on Stage 11, $E_{i,MV} > 1$; see Figure 77c. This implies reverse or uphill diffusion on stages 10 and 11; the transfer of ethanol is dictated by the driving forces of the other two components $\left(y_1^* - y_{1E}\right)$, and $\left(y_3^* - y_{3E}\right)$, that are both finite.[84]

Unequal component efficiencies, $E_{1,MV} \ne E_{2,MV} \ne E_{3,MV}$, influence the composition trajectories followed by the vapor and liquid phase along the distillation column. Generally speaking, residue curve maps provide a good indication of the composition trajectories along the distillation column in which all the component efficiencies are equal to one another $E_{1,MV} = E_{2,MV} = E_{3,MV}$. Figure 78a shows the residue curve maps (blue lines) for the water(1)/ethanol(2)/acetone(3) distillation. The thick black line is the distillation boundary; this boundary cannot normally be crossed during distillation.[91]

Consider the experimentally determined composition trajectories for total reflux operations, implying $x_i = y_i$, starting with the condenser composition $x_1 = 0.03$, $x_2 = 0.48$ and $x_3 = 0.49$, that corresponds to conditions to the left of the distillation boundary; see Figure 78b. Also shown are the simulation results for the trajectories calculated by the Equilibrium (EQ) stage model (continuous green line, $E_{1,MV} = E_{2,MV} = E_{3,MV} = 1$) and the Non-Equillibrium (NEQ) stage model (continuous red line, properly accounting for the resistances to transfer in both vapor and liquid phases, resulting in $E_{1,MV} \neq E_{2,MV} \neq E_{3,MV}$). The NEQ model is able to follow the experimentally observed column trajectories much better than the EQ model; the differences in the column composition trajectories are due to differences in the component Murphree efficiencies.

Consider now the experimentally determined composition trajectories in Figure 78c starting with the condenser composition $x_1 = 0.035$, $x_2 = 0.272$ and $x_3 = 0.693$, that is close to the distillation boundary on the left hand side. We note that the experimental data indicates that the boundary is crossed. The NEQ model is able to retrace this boundary-crossing trajectory, and correctly predicts that the column gets progressively richer in water as we proceed down the column to the reboiler. The EQ model anticipates that the column gets enriched in ethanol as the reboiler is approached, staying on the left side of the boundary. Springer et al.[86] present a total of six experimental runs that demonstrate boundary crossing possibilities; in every case, the NEQ predicts the right behavior.

For heterogeneous azeotropic distillation of water/ethanol/cyclohexane, and water/acetone/toluene (cf. Figure 79), the experimental data Springer et al.[85] also show boundary crossing effects, that are adequately described by NEQ models. It is to be noted that the NEQ model in such cases needs to have the capability of handling vapor/liquid(1)/liquid(2) transfers.[85, 92]

For design of distillation columns with a specified purity requirements at the top, the use of the more realistic NEQ model may demand significantly increased number stages.[82] The ChemSep software includes a rigorous implementation the NEQ model for absorption, and distillation processes.[82] This software is available for download at

http://www.chemsep.com/

16. Coupling effects in diffusion of electrolytes

For transport of ionic species in electrolyte solutions, we need to consider the electrostatic potential gradient as an additional driving force for transport. An important advantage of the M-S formulation is that the contribution of the electrostatic potential gradient needs to be added to the left member of equations (25)

$$-\frac{x_i}{RT}\frac{d\mu_i}{dz} - x_i z_i \frac{\mathrm{F}}{RT}\frac{d\Phi}{dz} = \sum_{\substack{j=1 \\ j\neq i}}^{n} \frac{x_j N_i - x_i N_j}{c_t Đ_{ij}}; \quad i = 1,2,\ldots n \tag{97}$$

where z_i is the charge on species i, and F is the Faraday constant. The species n is usually water (W), that is usually present in significantly large quantities, and can often be considered stagnant, $N_W = c_W u_W = 0$. For dilute aqueous solutions of electrolytes, the ion-ion interactions can often be neglected, and also $\frac{x_i}{RT}\frac{d\mu_i}{dz} \approx \frac{dx_i}{dz}$. With these assumptions and simplifications, equations (97) reduce to the Nernst-Planck equation for the flux of individual ionic species

$$N_i = -Đ_{iw}\frac{dc_i}{dz} - c_i z_i Đ_{iw}\frac{\mathrm{F}}{RT}\frac{d\Phi}{dz}; \quad i = 1,2,\ldots n-1 \tag{98}$$

where the $Đ_{iw}$ in equation (98) are the ionic diffusivities. If there is no flow of current, this results in the electroneutrality constraint

$$\sum_{i=1}^{n-1} z_i \mathrm{F} N_i = 0 \tag{99}$$

Combining equations (98), and (99), we obtain the following expression for the diffusion potential that is engendered due to ionic diffusion

$$\frac{d\Phi}{dz} = -\frac{\sum_{i=1}^{n-1} z_i Đ_{iw} \frac{dc_i}{dz}}{\frac{F}{RT}\sum_{i=1}^{n-1} c_i z_i^2 Đ_{iw}} \tag{100}$$

The effective diffusivities of ionic species *i* is

$$D_{i,eff} \equiv -\frac{N_i}{\frac{dc_i}{dz}} = Đ_{iw} + \frac{c_i z_i Đ_{iw} \frac{F}{RT}\frac{d\Phi}{dz}}{\frac{dc_i}{dz}} \tag{101}$$

The diffusion potential has the effect of influencing the motion of each of the ionic species. The second term on the right of equation (101) serves either to accelerate or decelerate each species, depending on the species charges, z_i, and mobilities.

As illustration, consider the experimental results of Vinograd and McBain[93] in a two-compartment diffusion cell, shown schematically in Figure 80. The bottom compartment contained pure water while the top one contained an aqueous electrolyte solution. Diffusion takes place through the pores of a sintered glass disk that separated the two compartments. In one set of experiments, the top compartment contained an aqueous solution of HCl and $BaCl_2$, the composition of which was varied. On complete ionization the mixture consists of the ionic species H^+, Cl^-, Ba^{2+} and un-ionized H_2O. By monitoring the concentrations of the three ionic species as a function of time, Vinograd and McBain[93] obtained the effective ionic diffusivities D_i for H^+, Cl^- and Ba^{2+}. The experimentally observed ionic diffusivities are shown in Figure 80 as function of the square root of the ratio of the initial ionic concentrations of H^+ and Ba^{2+} in the top compartment $\sqrt{c_{H+}/c_{Ba2+}}$. With increasing values of $\sqrt{c_{H+}/c_{Ba2+}}$, it is observed that both D_{H+} and D_{Ba2+} decrease while D_{Cl-} increases. During the start of the diffusion process, the highly mobile H^+ diffuses ahead of its companion ions into the pure water compartment, creating an excess of positive charge. This induces a diffusion potential $d\Phi/dz$ which acts in such a way as to maintain electro-neutrality. The consequence is that the Cl^- experiences an extra electrostatic "pull", enhancing its effective diffusivity value. The electrical potential gradient also serves to retard the motion of the positive ions H^+ and Ba^{2+} or in other words these ions experience a "push" in a direction opposite to that dictated by their composition gradient driving forces. For $\sqrt{c_{\mathrm{H+}}/c_{\mathrm{Ba2+}}}$ =2 the electrostatic "push" on Ba^{2+} is such as to result in a vanishing value for $D_{\mathrm{Ba2+}}$. The continuous solid lines in Figure 80 are the calculations of the effective diffusivities according to equation (101); further computational details are provided in Example 2.4.2 of Taylor and Krishna.[11] For $\sqrt{c_{\mathrm{H+}}/c_{\mathrm{Ba2+}}}$ > 2, negative values of $D_{\mathrm{Ba2+}}$ are obtained, signifying that uphill diffusion is feasible.

It should also be clear from Equation (100) that the sign of diffusion potential is dictated by the concentration gradients of the individual ions and is therefore dependent on the signs (i.e. directions) of the concentration gradients. This directional influence of the diffusion potential is illustrated clearly by the experiments of Kraaijeveld and Wesselingh[94] for external mass transfer limited ion exchange. Exchanging Na^{+} within the ion exchange bead with H+ from the bulk chloride solution proceeds at a significantly higher rate than for the reverse exchange process; see Figure 81. Analogous asymmetric exchange kinetics is found for the $\mathrm{Ca}^{2+}/\mathrm{H}^{+}/\mathrm{Cl}^{-}$ system.[94] The details of the modelling of diffusion in ion-exchange processes is available in Wesselingh and Krishna.[25]

Yang and Pintauro[95] report an interesting set of experimental data for transient transport of H^{+}, Na^{+}, and Cs^{+} ions across a Nafion cation exchange membrane separating the acid and salt compartments; see Figure 82. The HSO_4^{-} and SO_4^{2-} ions cannot cross the membrane. The H^{+} ions transfer from the acid to the salt compartment. Both Na^{+}, and Cs^{+} ions transfer from the salt to the acid compartment. Due to the significantly higher mobility of the H^{+} ions, there is a significant influence of the diffusion potential $\frac{d\Phi}{dz}$ that tends to accelerate the motion of the Na^{+}, and Cs^{+} ions during the initial stages of the transience. Since the concentration driving force of Cs^{+} ions is very small, the initial transience is strongly dictated by the diffusion potential $\frac{d\Phi}{dz}$; this results in the observed overshoot in the transient equilibration of Cs^{+}.

17. Reverse osmosis

The best known example of uphill diffusion is in the reverse osmosis (RO) process for desalination in which fresh water is recovered from saline water by use of a polyamide film membrane that rejects salt, and only allows water to permeate; see Figure 83. The transport of water occurs from the compartment with salt water (typically 98% water), on the left of the membrane to a region with nearly 100% pure water, on the right side. Uphill transport of water is achieved by application of a pressure differential across the membrane that must exceed the osmotic pressure of 2.7 MPa.[25] Both concentration and pressure gradients dictate the net flux of water across the RO membrane; equation (2) does not provide an adequate description of inter-membrane transport.

In reverse osmosis, the driving force for transport across the polyamide membrane layer must additionally account for the contribution of the pressure gradients. The expression for the flux of water across the membrane (see schematic in Figure 83) is obtained by modifying equation (25) as follows

$$-\frac{x_w}{RT}\frac{d\mu_w}{dz}-\frac{1}{RT}\overline{V}_w\frac{dp}{dz}=\frac{N_w}{c_t Đ_{wM}} \tag{102}$$

where $\overline{V_w}$ is the partial molar volume. In equation (102), we ignore diffusional interactions between water and salt. Furthermore, ignoring thermodynamic non-ideality effects, we can re-write Equation (102) in the following form for a membrane of thickness δ

$$-\frac{\Delta x_w}{\delta}-\frac{1}{RT}\overline{V}_w\frac{\Delta p}{\delta}=\frac{N_w}{c_t Đ_{wM}} \tag{103}$$

In desalination operations, the upstream compartment will typically have 2 mole % salt and the downstream compartment will be practically salt-free. Therefore, the driving force for water transport $\Delta x_w = 1.0 - 0.98 = 0.02$. If no additional pressure is applied to the upstream compartment, the pressure difference at equilibrium, corresponding to $N_w = 0$, is called the osmotic pressure

$$\Delta p = \Pi = -\frac{RT\Delta x_w}{\overline{V}_w} \tag{104}$$

Typically, T = 298 K, and $\overline{V_w} = 1.8\times10^{-5}$ m^3 mol^{-1}; the osmotic pressure is 2.75 MPa. In order to drive water from the left to right in Figure 83, we need to apply Δp values exceeding 2.75 MPa. In desalination operations we have uphill diffusion of water by application of an additional driving force. Further details on the modelling of transport phenomena in reverse osmosis is provided by Wesselingh and Krishna.[25]

In electro-osmosis, water is dragged uphill by electrostatic potential gradients; see Wesselingh and Krishna.[25]

18. The Soret Effect

The Soret effect, also called thermal diffusion, is the tendency of a mixture of two or more components to separate due to a temperature gradient. In 1879 Charles Soret discovered that a salt solution contained in a tube with the two ends at different temperatures did not remain uniform in composition; the salt was more concentrated near the cold end than near the hot end of the tube; for a review of the history and applications see Platten.[96]

One usually writes for the mass flux of the reference chemical compound in a binary mixture

$$J_1 = -\rho_t D_{12}\frac{d\omega_1}{dz} - \rho_t D_T \omega_1 (1-\omega_1)\frac{dT}{dz} \tag{105}$$

The first term in the right hand side of Equation (105) is Fick's law of diffusion, with the mass fraction ω_1 of the reference component 1 and D_{12} the Fick diffusivity; the second term describes the Soret effect or thermo-diffusion effect, proportional to the temperature gradient $\frac{dT}{dz}$, with D_T the thermo-diffusion coefficient. Since the thermo-diffusion effect does not exist in pure fluids one, the factor $\omega_1(1-\omega_1)$ is included in the right member of Equation (105). Even so, D_T remains concentration dependent, exactly as the Fick diffusivity D_{12}. Thus the second term in the right hand side of Equation (105) describes mass separation due to a temperature gradient, whereas the first describes homogenization by Fickian diffusion. The two terms are thus of opposite sign, and when they are of equal intensity, we are in steady-state conditions

$$J_1 = -\rho_t D_{12} \frac{d\omega_1}{dz} - \rho_t D_T \omega_1 \left(1-\omega_1\right) \frac{dT}{dz} = 0 \tag{106}$$

implying

$$\frac{d\omega_1}{dz} = -\frac{D_T}{D_{12}} \omega_1 \left(1-\omega_1\right) \frac{dT}{dz} \tag{107}$$

and the Soret coefficient S_T is defined as

$$S_T = \frac{D_T}{D} = -\frac{1}{\omega_1 \left(1-\omega_1\right)} \frac{\frac{d\omega_1}{dz}}{\frac{dT}{dz}} \tag{108}$$

The Soret coefficient S_T may be positive or negative depending on the sign of D_T or on the sense of migration of the reference component 1 to the cold or to the hot regions. In absolute value an order of magnitude for usual organic mixtures or aqueous solutions is S_T = 0.001 to 0.01 K^{-1}. Typically, the value of the mass fraction difference between the hot and cold ends $\Delta\omega_1 \approx 0.01$, often smaller. But even if the separation remains small, the Soret effect has some practical implications. For example, Huang et al.[97] demonstrate the use of thermal diffusion for fractionation of isotopes of Fe, Ca, and Mg from silicate melts.

Coupling between the salinity and temperature gradients often cause double-diffusive convection, and salt fingers that are of importance in oceanography and geology.[98]

19. Separations using micro-porous crystalline materials: General considerations

A wide variety of ordered crystalline porous materials is used in several applications in separation applications.[99-102] These include zeolites (crystalline aluminosilicates), carbon nanotubes (CNTs), metal-organic frameworks (MOFs), zeolitic imidazolate frameworks (ZIFs), covalent organic frameworks (COFs), periodic mesoporous organosilicas organosilicas (PMOs), SBA-16, and MCM-41. The characteristic pore dimensions of these structures are either in the *micro*-porous (d_p < 2 nm), or *meso*-porous ranges (2 nm < d_p < 50 nm). The main focus of our attention will be on micro-porous crystalline materials.

A number of different channel topologies and connectivities are encountered in zeolites, MOFs, COFs, and ZIFs; these can be divided into five broad classes;

1. One-dimensional (1D) channels (e.g. AFI, LTL, TON, $Fe_2(BDP)_3$, MgMOF-74, MIL-47, MIL-53(Cr), BTP-COF); see Figure 84.
2. 1D channels with side pockets (e.g. MOR, FER); see Figure 85.
3. Intersecting channels (e.g. MFI, BEA, BOG, Zn(bdc)dabco, Co(bdc)dabco); see Figure 86.
4. Cages separated by narrow windows (e.g. LTA, CHA, DDR, ZIF-8); see Figure 87.
5. Cavities with large windows (e.g. FAU, IRMOF-1, CuBTC, MOF-177); see Figure 88.

Further details on the structure, landscape, pore dimensions on a very wide variety of micro-porous materials are available in the published literature.[103-105]

The technologies used in industrial separations are either pressure swing adsorption (PSA) units (exemplified in Figure 89), or membrane permeation devices (see schematic in Figure 90).

The operations of fixed bed adsorption units are intrinsically transient in nature, i.e. the gas (or fluid) phase concentrations vary both with distance along the adsorber, z, and time, t.[104, 106-108] Most commonly, the separation performance of PSA adsorbers is dictated by mixture adsorption equilibrium. Intra-particle diffusion limitations cause distended breakthrough characteristics and usually lead to diminished separation effectiveness. There are however some examples, as we shall examine later, where diffusional influences act in a manner so as to enhance separations. At the other extreme, we could have a situation in which diffusional effects over-ride the influence of adsorption equilibrium and is the prime driver for separation. For separation of $O_2(1)$ /$N_2(2)$ mixture using LTA-4A, LTA-5A, or NaX, the adsorption selectivity is in favor of N_2 due to the larger permanent quadrupole of N_2 compared to that of O_2. This implies that an adsorption based process would selectively adsorb N_2, and pure O_2

can be produced in the adsorption phase of PSA operations.[109, 110] For production of purified N_2, it is desirable to selectively adsorb O_2. This selectivity towards O_2 can be achieved by choosing LTA-4A zeolite. Diffusion limitations are severe in LTA-4A because the window regions are partially blocked by the cations (see Na^+ locations in the window regions shown in Figure 89). Due to its smaller cross-sectional dimension, 3.1 Å for O_2, compared to 3.3 Å for N_2, the inter-cage hopping of O_2 occurs at a rate that is about 100 times higher than that of N_2. The significantly lower diffusivity of N_2 has the consequence that purified N_2 breaks through earlier in a fixed bed adsorber; see simulated breakthroughs in Figure 89.

By contrast to PSA units, the separation performance of membrane devices (see schematic in Figure 90) is always influenced by intra-crystalline diffusion, in addition to adsorption equilibrium.[111, 112]

We now examine the modelling of intra-crystalline diffusion, and the significance of coupling effects.

20. Fick, Onsager, and Maxwell-Stefan formulations for diffusion inside micro-porous crystalline materials

In contrast to the treatment of diffusion in bulk fluid mixtures for which the reference frame is chosen as the molar average velocity of the mixture (cf. Equation (4)), the molar fluxes for diffusion in microporous crystalline materials are defined with respect to the material framework, i.e. $N_i = J_i$.[29, 107] In development of flux relations it is tacitly assumed that the framework material is the $(n+1)th$ component of the mixture. *Unary* diffusion inside the pores is comparable in characteristics to diffusion in *binary* fluid mixtures. Put another way, the "dimensionality" of the diffusion is increased by unity when we write the flux relations for diffusion inside pores. Binary mixture diffusion in microporous materials is described by 2 × 2 dimensional matrix equations, much in the same way as bulk liquid phase diffusion in ternary mixtures.

For unary diffusion, the Fickian formulation relates the component flux N_i, expressed as the number of moles of species *i* transported per m^2 surface of *crystalline material* per second, to the gradient of the molar loadings, q_i

$$N_i = -\rho D_i \frac{dq_i}{dz} \tag{109}$$

where ρ is the framework density. Equation (109) defines the Fick diffusivity D_i, also termed "transport" diffusivity.[99] The Fick diffusivity D_i can be determined by fitting transient uptake data and from chromatographic experiments.[113]

For a binary mixture consisting of species 1 and 2, each of the component fluxes N_1 and N_2, is influenced by the gradients in the molar loadings, $\frac{dq_1}{dz}$, and $\frac{dq_2}{dz}$ of *both* species in the mixture. In the Fick formulation for binary mixtures, diffusion coupling effects are accounted for by defining a matrix of Fick diffusivities $\begin{bmatrix} D_{11} & D_{12} \\ D_{21} & D_{22} \end{bmatrix}$:

$$\begin{pmatrix} N_1 \\ N_2 \end{pmatrix} = -\rho \begin{bmatrix} D_{11} & D_{12} \\ D_{21} & D_{22} \end{bmatrix} \begin{pmatrix} \frac{dq_1}{dz} \\ \frac{dq_2}{dz} \end{pmatrix}; \quad \text{Fick formulation} \tag{110}$$

A major shortcoming of the Fickian formulation (110) is that the diagonal elements of $\begin{bmatrix} D_{11} & D_{12} \\ D_{21} & D_{22} \end{bmatrix}$ cannot be related simply to the data for unary Fick diffusivities of components 1 and 2, i.e. D_1 and D_2. The ratios D_{12}/D_{11}, and D_{21}/D_{22} reflect the extent of "coupling" in the species fluxes. Such couplings have two different origins, and to distinguish between these it is necessary to adopt the Maxwell-Stefan mixture diffusion formulations that use chemical potential gradients, $\frac{d\mu_1}{dz}$ and $\frac{d\mu_2}{dz}$, are used as driving forces of intra-crystalline diffusion.

In the Onsager formulation, the fluxes are linearly related to the chemical potential gradients by defining a matrix of Onsager coefficients $[L]$

$$\begin{pmatrix} N_1 \\ N_2 \end{pmatrix} = -\frac{\rho}{RT} \begin{bmatrix} L_{11} & L_{12} \\ L_{21} & L_{22} \end{bmatrix} \begin{pmatrix} \frac{d\mu_1}{dz} \\ \frac{d\mu_2}{dz} \end{pmatrix}; \quad \text{Onsager formulation} \tag{111}$$

The Onsager Reciprocal Relations[29] prescribes the symmetry relation

$$L_{12} = L_{21} \tag{112}$$

The Onsager formulation suffers from the major disadvantage that the diagonal elements L_{11} and L_{22} cannot be identified with the corresponding values L_1, and L_2 for unary transport of species 1 and 2.[29]

The most convenient formulation for diffusion inside porous materials is afforded by the Maxwell-Stefan (M-S) equations, which for *n*-component diffusion inside micro-porous crystalline can be written as[29, 103, 105, 114-116]

$$-\rho \frac{q_i}{RT}\frac{d\mu_i}{dz} = \sum_{\substack{j=1 \\ j \neq i}}^{n} \frac{x_j N_i - x_i N_j}{Đ_{ij}} + \frac{N_i}{Đ_i}; \quad i = 1,2,..n \tag{113}$$

where q_i are molar loadings of the *adsorbed* species. The fluxes N_i defined in Equations (113) are expressed in terms of the number of moles of species *i* transported per m^2 of the *surface of material* per second.

In Equations (113) the $Đ_i$ is the M-S diffusivities of species *i*, portraying the interaction between component *i* in the mixture with the surface, or wall of the structure. An important advantage of the M-S formulation is that $Đ_i$ can be identified with the values for unary species *i*; there are however exceptional circumstances where this advantage does not hold.[117, 118]

The x_i in Equations (113) represent the component mole fractions in the adsorbed phase within the pores and calculated from

$$x_i = q_i / q_t; \quad 1,2,.....n \tag{114}$$

where q_t is the *total* mixture loading:

$$q_t = \sum_{i=1}^{n} q_i \tag{115}$$

The $Đ_{ij}$ are M-S exchange coefficients representing interaction between component *i* with component *j*. At the molecular level, the $Đ_{ij}$ reflect how the facility for transport of species *i correlates* with that of species j. For micro-porous crystalline materials, the magnitudes of $Đ_{ij}$ are a fraction of the corresponding M-S diffusivity for the binary fluid mixture.[21, 111, 119] The stronger the degree of confinement within the pores, the lower is the fraction. For meso-porous materials the guest molecules are not strongly constrained and, as a consequence, the $Đ_{ij}$ can be identified with that of the diffusivity of the *binary* fluid mixture of the pair *i-j*.[21, 111, 119] Indeed, for mesoporous materials, Equations (113) are essentially equivalent to the Dusty Gas Model (DGM).[120] In the DGM, the $Đ_i$ are calculated with the help of the Knudsen formula, but the limitations of this assumption for strongly adsorbing species has been underscored in several recent investigations.[118, 121, 122]

The Onsager reciprocal relations prescribe the symmetry constraint

$$Đ_{ij} = Đ_{ji} \tag{116}$$

By defining an n-dimensional square matrix $[B]$ with elements

$$B_{ii} = \frac{1}{Đ_i} + \sum_{\substack{j=1 \\ j \neq i}}^{n} \frac{x_j}{Đ_{ij}}; \quad B_{ij} = -\frac{x_i}{Đ_{ij}}; \quad i,j = 1,2....n \tag{117}$$

we can recast equation (113) into the following form

$$-\rho \frac{q_i}{RT}\frac{d\mu_i}{dz} = \sum_{j=1}^{n} B_{ij} N_j; \quad i = 1,2,..n \tag{118}$$

The chemical potential gradients $d\mu_i/dz$ can be related to the gradients of the molar loadings, q_i, by defining thermodynamic correction factors Γ_{ij}

$$\frac{q_i}{RT}\frac{d\mu_i}{dz} = q_i \frac{d\ln f_i}{dz} = \sum_{j=1}^{n} \Gamma_{ij}\frac{dq_j}{dz}; \quad \Gamma_{ij} = \frac{q_i}{f_i}\frac{\partial f_i}{\partial q_j}; \quad i,j = 1,....n \tag{119}$$

Let us now examine the two special cases of unary and binary systems.

For unary diffusion of component i, the Maxwell-Stefan relations simplify to yield

$$N_i = -\rho D_i \frac{dq_i}{dz} = -\rho Đ_i \Gamma_i \frac{dq_i}{dz}; \quad \Gamma_i = \frac{q_i}{f_i}\frac{\partial f_i}{\partial q_i}; \quad \text{unary system} \tag{120}$$

where the commonly used Fick diffusivity of species *i* is related to the unary Maxwell-Stefan diffusivity

$$D_i = Đ_i \Gamma_i; \quad \text{unary system} \tag{121}$$

The influence of the thermodynamic correction factor is analogous to that for binary diffusion in fluid mixtures; cf. equation (43). If the adsorption isotherm is described by a single-site Langmuir isotherm, the thermodynamic factor is

$$\Gamma_i = \left(\frac{1}{1-\theta_i} \right); \quad \text{single - site Langmuir isotherm} \tag{122}$$

Figure 91a presents a calculation of the thermodynamic factor Γ_i, for single-site Langmuir isotherm, plotted as a function of the fractional occupancy, θ_i. The thermodynamic factor Γ_i always exceeds unity and we have the hierarchy $D_i \geq Đ_i$. At pore saturation, we have $\theta_i \to 1; \quad \Gamma_i \to \infty$, and it is therefore convenient to calculate the *inverse* thermodynamic factor $1/\Gamma_i$ which decreases linearly with θ_i; see Figure 91b.

The thermodynamic factor Γ_i has a direct influence on the transient adsorption/desorption processes. During the adsorption phase, the influence of increasing Γ_i is to accelerate the component uptake. However, during the desorption phase, Γ_i decreases progressively, and the process becomes progressively slower. One of the first studies to demonstrate the asymmetry in the adsorption and desorption kinetics was that of Garg and Ruthven[123] for C_2H_6 in LTA-4A. They showed that desorption is a slower process than transient uptake; for a quantitative analysis of the experimental data of Garg and Ruthven;[123] see the simulations presented in the Supporting Material accompanying the paper by Krishna.[104]

For transient unary uptake within a crystal, the radial distribution of molar loadings, q_i, within a spherical crystallite, of radius r_c, is obtained from a solution of a set of differential equations describing the uptake

$$\frac{\partial q_i(r,t)}{\partial t} = -\frac{1}{\rho}\frac{1}{r^2}\frac{\partial}{\partial r}\left(r^2 N_i\right) \tag{123}$$

At any time *t*, during the transient approach to thermodynamic equilibrium, the spatially averaged molar loading within the crystallite r_c is obtained by integration of the radial loading profile

$$\overline{q}_i(t) = \frac{3}{r_c^3}\int_0^{r_c} q_i(r,t) r^2 dr \tag{124}$$

The $\overline{q}_i(t)$ can be compared directly with experimental transient uptake data. An analytical solution to equation (123) is only possible for the special case in which the Fick D_i can be considered to be independent of the loading. In this case, the expression for fractional approach to equilibrium is[113]

$$\frac{\left(\overline{q}_i(t) - q_i(r_c,0)\right)}{\left(q_i(r_c,t=\infty) - q_i(r_c,0)\right)} = 1 - \frac{6}{\pi^2}\sum_{m=1}^{\infty}\frac{\exp(-m^2\pi^2 \frac{D_i}{r_c^2} t)}{m^2} \tag{125}$$

Equation (125) allows data on transient uptake to be fitted to obtain an average value of the Fick diffusivity D_i that is representative of the range of loadings encountered in the experiment.

Figure 92 shows the experimental data for transient adsorption and desorption profiles for C_2H_6 in LTA-4A zeolite. The adsorption branch can be fitted with D_i/r_c^2 = 1.1×10^{-3} s^{-1}, while the desorption branch yields a lower value D_i/r_c^2 = 6×10^{-4} s^{-1}. The asymmetry in the adsorption and desorption kinetics is not easy to interpret on the basis of the Fick formulation.

The inverse thermodynamic factor, $1/\Gamma_i$, decreases linearly with fractional occupancy (cf. Figure 91b). Both the adsorption and desorption cycles can be fitted with $Đ_i/r_c^2$ = 2×10^{-4} s^{-1}. This implies that that the asymmetry in the adsorption and desorption transience has their origin in the characteristics of $1/\Gamma_i$; the slower desorption kinetics is attributable to the decrease in Γ_i during the desorption phase.

Experimental data of Niessen and Karge[124] for transient adsorption/desorption of *p*-xylene in MFI zeolite (H-ZSM-5) at 375 K are shown in Figure 93. Niessen and Karge[124] found that data for the desorption phase could be fitted with a Fick diffusivity that is a factor 16 lower than the fitted diffusivity for the adsorption phase. The differences in the diffusivities are easy to rationalize by the Maxwell-Stefan equations, and the influence of the thermodynamic correction factor Γ_i.

There are many cases, however, in which the simple Langmuir isotherm model does not adequately capture the isotherm characteristics. For the adsorption of methanol and ethanol in ZIF-8, for example, the adsorption isotherms (cf. Figure 94a) show steep characteristics.[117] The steepness of the isotherms can only be properly captured by using the dual-site Langmuir-Freundlich isotherm

$$q_i = q_{i,A,sat} \frac{b_{i,A} f_i^{\nu_{i,A}}}{1 + b_{i,A} f_i^{\nu_{i,A}}} + q_{i,B,sat} \frac{b_{i,B} f_i^{\nu_{i,B}}}{1 + b_{i,B} f_i^{\nu_{i,B}}} \tag{126}$$

with at least one of the exponents ν_i exceeds unity; the fits are shown by the continuous solid lines. Analytic differentiation of equation (126) yields Γ_i. As saturation is approached $\Gamma_i \to \infty$, and so it is much more convenient to plot the inverse thermodynamic factor, $\frac{1}{\Gamma_i}$ as a function of the loading; see Figure 94b. We note that the $\frac{1}{\Gamma_i}$ exceeds unity for a range of loadings; this signifies the molecular clustering effects.[117, 125-129] Such effects are akin to the steep decrease in the thermodynamic factors observed for methanol/*n*-hexane mixtures in the composition range corresponding to liquid-liquid phase splitting; cf. Figures 25, and 26.

For the range of loadings in which $\frac{1}{\Gamma_i} > 1$, the Fick diffusivity is lower than the M-S diffusivity, i.e. $D_i \le Đ_i$. This trend is confirmed by the experimental data of Chmelik et al.[130] for the unary Fick and M-S diffusivities of methanol, and ethanol in ZIF-8; see Figures 94c, and 94d.

For a binary mixture, the Maxwell-Stefan diffusion equations are[29, 103, 105, 114-116]

$$\begin{aligned} -\rho \frac{q_1}{RT}\frac{d\mu_1}{dz} &= \frac{x_2 N_1 - x_1 N_2}{Đ_{12}} + \frac{N_1}{Đ_1}; \\ -\rho \frac{q_2}{RT}\frac{d\mu_2}{dz} &= \frac{x_1 N_2 - x_2 N_1}{Đ_{12}} + \frac{N_2}{Đ_2} \end{aligned} \tag{127}$$

For a binary mixture, the chemical potential gradients can be related to the gradients in molar loadings

$$\frac{1}{RT}\begin{pmatrix} q_1 \frac{d\mu_1}{dz} \\ q_2 \frac{d\mu_2}{dz} \end{pmatrix} = \begin{bmatrix} \Gamma_{11} & \Gamma_{12} \\ \Gamma_{21} & \Gamma_{22} \end{bmatrix} \begin{pmatrix} \frac{dq_1}{dz} \\ \frac{dq_2}{dz} \end{pmatrix} = \begin{pmatrix} \Gamma_{11}\frac{dq_1}{dz} + \Gamma_{12}\frac{dq_2}{dz} \\ \Gamma_{21}\frac{dq_1}{dz} + \Gamma_{22}\frac{dq_2}{dz} \end{pmatrix} \tag{128}$$

The elements Γ_{ij} can be determined from models describing mixture adsorption equilibrium, relating the component molar loadings q_1 and q_2, to the partial gas phase fugacities f_1 and f_2. The off-diagonal elements of the matrix $\begin{bmatrix} \Gamma_{11} & \Gamma_{12} \\ \Gamma_{21} & \Gamma_{21} \end{bmatrix}$ can have magnitudes significantly larger than unity.

For the simple case in which each species is described by a single-site Langmuir isotherm for either component in the binary mixture

$$q_i = \frac{q_{i,sat} b_i f_i}{1 + b_i f_i}; \quad \text{single - component Langmuir isotherm} \tag{129}$$

the partial gas phase fugacities are related to the component loadings by the mixed-gas Langmuir model:

$$\frac{q_i}{q_{i,sat}} = \theta_i = \frac{b_i f_i}{1 + b_1 f_1 + b_2 f_2}; \quad i = 1,2; \quad \text{mixed - gas Langmuir} \tag{130}$$

Differentiation of equation (130) yields

$$\begin{bmatrix} \Gamma_{11} & \Gamma_{12} \\ \Gamma_{21} & \Gamma_{22} \end{bmatrix} = \frac{1}{1 - \theta_1 - \theta_2} \begin{bmatrix} 1 - \theta_2 & \frac{q_{1,sat}}{q_{2,sat}}\theta_1 \\ \frac{q_{2,sat}}{q_{1,sat}}\theta_2 & 1 - \theta_1 \end{bmatrix}; \quad \text{mixed - gas Langmuir model} \tag{131}$$

While, the mixed-gas Langmuir model is commonly used for describing mixture adsorption; in the more general case we need to use the Ideal Adsorbed Solution Theory (IAST) developed by Myers and Prausnitz.[131] Equation (131) also implies that the $\begin{bmatrix} \Gamma_{11} & \Gamma_{12} \\ \Gamma_{21} & \Gamma_{21} \end{bmatrix}$ reduces to the identity matrix at low occupancies; this scenario is likely to be valid, as an approximation, for operations at lower pressures and/or higher temperatures.

For a binary mixture ($n = 2$) the square matrix $[B]$ is

$$[B] = \begin{bmatrix} \frac{1}{Đ_1} + \frac{x_2}{Đ_{12}} & -\frac{x_1}{Đ_{12}} \\ -\frac{x_2}{Đ_{12}} & \frac{1}{Đ_2} + \frac{x_1}{Đ_{12}} \end{bmatrix} \tag{132}$$

The inverse of the square matrix $[B]$ can be obtained explicitly

$$[B]^{-1} = \frac{1}{1 + \frac{x_1 Đ_2}{Đ_{12}} + \frac{x_2 Đ_1}{Đ_{12}}} \begin{bmatrix} Đ_1\left(1 + \frac{x_1 Đ_2}{Đ_{12}}\right) & \frac{x_1 Đ_1 Đ_2}{Đ_{12}} \\ \frac{x_2 Đ_1 Đ_2}{Đ_{12}} & Đ_2\left(1 + \frac{x_2 Đ_1}{Đ_{12}}\right) \end{bmatrix} \tag{133}$$

Equations (127), and (128) can be combined to yield explicit expression for the fluxes

$$\begin{pmatrix} N_1 \\ N_2 \end{pmatrix} = -\frac{\rho}{1 + \frac{x_1 Đ_2}{Đ_{12}} + \frac{x_2 Đ_1}{Đ_{12}}} \begin{bmatrix} Đ_1\left(1 + \frac{x_1 Đ_2}{Đ_{12}}\right) & \frac{x_1 Đ_1 Đ_2}{Đ_{12}} \\ \frac{x_2 Đ_1 Đ_2}{Đ_{12}} & Đ_2\left(1 + \frac{x_2 Đ_1}{Đ_{12}}\right) \end{bmatrix} \begin{bmatrix} \Gamma_{11} & \Gamma_{12} \\ \Gamma_{21} & \Gamma_{22} \end{bmatrix} \begin{pmatrix} \frac{dq_1}{dz} \\ \frac{dq_2}{dz} \end{pmatrix} \tag{134}$$

Comparison with the Fick formulation (110), we find the following explicit expression for the matrix of Fick diffusivities $[D]$

$$\begin{bmatrix} D_{11} & D_{12} \\ D_{21} & D_{22} \end{bmatrix} = \frac{\rho}{1 + \frac{x_1 Đ_2}{Đ_{12}} + \frac{x_2 Đ_1}{Đ_{12}}} \begin{bmatrix} Đ_1\left(1 + \frac{x_1 Đ_2}{Đ_{12}}\right) & \frac{x_1 Đ_1 Đ_2}{Đ_{12}} \\ \frac{x_2 Đ_1 Đ_2}{Đ_{12}} & Đ_2\left(1 + \frac{x_2 Đ_1}{Đ_{12}}\right) \end{bmatrix} \begin{bmatrix} \Gamma_{11} & \Gamma_{12} \\ \Gamma_{21} & \Gamma_{22} \end{bmatrix} \tag{135}$$

Equation (134) demonstrates that there are two different factors that contribute to strong coupling in mixture diffusion. Values of $Đ_i/Đ_{12}$ in the range of 2 to 20 imply strong correlation effects; this results in significant contribution of the off-diagonal elements in the first right member of Equation (134). Often, but not always, strong correlation effects cause slowing-down of more-mobile-less-strongly-adsorbed molecules by tardier-more-strongly-adsorbed-partner species. Such is the case, for example, for diffusion of CO_2/H_2 mixtures in structures as MgMOF-74 and NaX zeolite.[111] Correlation effects generally act to reduce the propensity for overshoots, and uphill diffusion.

Values of $Đ_i/Đ_{12} << 1$, imply negligible influence of correlations; in this case, the first members on the right of Equations (127) can be ignored, yielding

$$\begin{pmatrix} N_1 \\ N_2 \end{pmatrix} = -\rho \begin{bmatrix} Đ_1 & 0 \\ 0 & Đ_2 \end{bmatrix} \begin{bmatrix} \Gamma_{11} & \Gamma_{12} \\ \Gamma_{21} & \Gamma_{22} \end{bmatrix} \begin{pmatrix} \frac{dq_1}{dz} \\ \frac{dq_2}{dz} \end{pmatrix}; \quad \text{negligible correlations} \tag{136}$$

Extensive Molecular Dynamics (MD) simulations have shown that correlation effects are of negligible importance for mixture diffusion across cage type zeolites such as ZIF-8, CHA, LTA, DDR, ERI that consist of cages separated by windows in the 3.4 Å – 4.2 Å size range;[103, 105, 111, 132] molecules jump one-at-a-time across the narrow windows, and the assumption of negligible correlations is justified. Indeed, in all the analyses presented below, we use equations (136) to model overshoots in transient binary mixture diffusion.

21. Overshoots in transient uptake of binary mixtures in microporous materials

Let us begin by considering the separation of $N_2(1)/CH_4(2)$ mixtures that is important in the context of natural gas upgrading. For transportation purposes, the pipeline specifications usually demand that the amount of N_2 in natural gas is less than about 3%, because the presence of N_2 reduces the heating value. For purification of natural gas streams, that is commonly available at high pressures, it is desirable to use adsorbents in pressure swing adsorption (PSA) units that are selective to N_2 that is present in quantities that are often as high as 20%. For most known adsorbents, the adsorption selectivity favors CH_4. One practical solution to this problem is to rely on diffusion selectivities by using microporous materials that have significantly higher diffusivities of N_2, compared to that of CH_4.[133, 134]

The earliest study demonstrating the possibility of utilizing diffusion selectivities for separating $N_2(1)/CH_4(2)$ mixtures is contained in the classic paper of Habgood[135] that presents experimental data on transient uptake of $N_2(1)/CH_4(2)$ mixtures in crystallites of LTA-4A. His data measured at 194 K with partial pressures p_1 =50.9 kPa and p_2 =49.1 kPa are shown in Figure 95. The N_2(1)/CH_4(2) mixture constitutes a combination of more-mobile-less-strongly-adsorbed-N_2 and tardier-more-strongly-adsorbed-CH_4. Nitrogen is a "pencil-like" molecule (4.4 Å × 3.3 Å) that can hop length-wise across the narrow windows; the "spherical" CH_4 (3.7 Å) is much more severely constrained and has a diffusivity that is 22 times lower than that of N_2. But N_2 has an adsorption strength that is a factor 2.2 lower than that of CH_4. During the initial stages of the transient uptake, the pores of LTA-4A are predominantly richer in the more mobile N_2, but this is displaced by the more strongly-adsorbed-but-tardier CH_4 molecules at longer times. This results in an overshoot in the N_2 uptake in the experimental data. Note that the maximum loading of N_2 is about a factor 2.5 times that of the final equilibrated uptake. Put another way, supra-equilibrium loadings are attained for N_2 during a short time interval in the early stages of the transient uptake.

Based on his experimental results for transient uptake, Habgood filed a patent claiming that natural gas could be upgraded by removing the faster diffusing nitrogen using 4A zeolite and a kinetically controlled separation process at a low sub-ambient temperature.

Let us now model the transient uptake process. The windows separating adjacent cages of LTA-4A zeolite are about 4 Å in size; each of the constituent species hops across the windows one-at-a-time. Put another way, the jumps are not correlated, and equations (136) can be used to describe intra-crystalline diffusion within crystals.

The calculations of the elements of the matrix of thermodynamic factors Γ_{ij} for N_2(1)/CH_4(2) mixture within LTA-4A crystals demonstrate the significance of the off-diagonal elements at higher loadings; see Figure 96a. We note that for total mixture loadings, $q_t = q_1 + q_2$ less than 0.5 mol kg^{-1}, the off-diagonal elements of the matrix $\begin{bmatrix} \Gamma_{11} & \Gamma_{12} \\ \Gamma_{21} & \Gamma_{21} \end{bmatrix}$ are less than about 0.1. However, for $q_t > 1.5$ mol kg^{-1}, the off-diagonal elements approach values close to that of the diagonal elements. In other words, thermodynamic coupling effects become increasingly important as the loadings increase.

Let us see whether equations (136) are capable of reproducing the observed experimental overshoots. For transient mixture uptake within a crystal, the radial distribution of molar loadings, q_i, within a spherical crystallite, of radius r_c, is obtained from a solution of a set of differential equations describing the uptake

$$\frac{\partial q_i(r,t)}{\partial t} = -\frac{1}{\rho}\frac{1}{r^2}\frac{\partial}{\partial r}\left(r^2 N_i\right); \quad i = 1,...n \tag{137}$$

At any time t, during the transient approach to thermodynamic equilibrium, the spatially averaged molar loading within the crystallite r_c is obtained by integration of the radial loading profile

$$\overline{q}_i(t) = \frac{3}{r_c^3}\int_0^{r_c} q_i(r,t) r^2 dr; \quad i = 1,2,...n \tag{138}$$

The $\overline{q}_i(t)$ can be compared directly with experimental transient uptake data of Habgood.[135]

The continuous solid lines in Figure 97 are the calculations of the Maxwell-Stefan model using the flux equations (136); this model successfully captures the overshoot in the uptake of the more mobile N_2.

The dashed lines in Figure 97 are the simulations in which the matrix of thermodynamic factors is assumed to be the identity matrix

$$\begin{pmatrix} N_1 \\ N_2 \end{pmatrix} = -\rho \begin{bmatrix} Đ_1 & 0 \\ 0 & Đ_2 \end{bmatrix} \begin{pmatrix} \frac{\partial q_1}{\partial r} \\ \frac{\partial q_2}{\partial r} \end{pmatrix} \tag{139}$$

Neglect of thermodynamic coupling results in uptake profiles that do not exhibit an overshoot in N_2 uptake. The simulation results presented in Figures 97 confirm that thermodynamic coupling is the cause of the N_2 overshoot.

In order to demonstrate that the N_2 overshoot has its origins in the influence of the thermodynamic factors, Figure 96b presents calculations of the elements of the matrix of thermodynamic factors Γ_{ij} calculated from the transient uptake simulations, as a function of time. We note that off-diagonal element Γ_{12} is significantly higher than the value of the diagonal element Γ_{22} during the interval $5 < t^{1/2} < 25$ for which the N_2 overshoot manifests. Figure 96c presents calculations of the thermodynamically "corrected" loadings $q_1\mu_1/RT = \Gamma_{11}q_1 + \Gamma_{12}q_2$, and $q_2\mu_2/RT = \Gamma_{21}q_1 + \Gamma_{22}q_2$ as a function of $t^{1/2}$. It is observed that the equilibration of N_2, measured in terms of corrected loadings, does not exhibit an overshoot and approaches equilibrium in a monotonic manner.

A further point to note from the data on the thermodynamic factor in Figure 96a is that the influence of thermodynamic coupling should decrease as the loadings are decreased during desorption. This would suggest that the transient desorption of $N_2(1)/CH_4(2)$ mixture in LTA-4A crystals should have a different character. In order to verify this, Figure 98a presents simulations of transient desorption process for $N_2(1)/CH_4(2)$ mixture in LTA-4A crystals, exposed to binary gas mixtures at 194 K. The initial crystal is brought to equilibrium by exposure to gas phase partial pressures p_1 =50.9 kPa; p_2 = 49.1 kPa. At time $t = 0$, the bulk gas is exposed to conditions such that $p_1 = p_2 = 0$. We note that the desorption of both the components occurs monotonously. Figure 98b compares the composition trajectories for the adsorption (green line) and desorption cycles (red line). It is evident that the trajectories have markedly different characteristics. There is no experimental data to verify the asymmetry witnessed in Figure 98.

In order to demonstrate the possibility of purifying natural gas by exploiting diffusion selectivity principles, Figure 99 presents the transient breakthroughs of a 10/90 $N_2(1)/CH_4(2)$ mixture in a fixed bed adsorber packed with LTA-4A operating at a total pressure of 100 kPa and 194 K. We note that the the more strongly adsorbed is rejected in nearly pure form during the earlier stages of the transient breakthrough.

By tuning the size of the microporous channels and using ETS-4 as adsorbent, both adsorption and diffusion characteristics favor the selective uptake of N_2 from $N_2(1)/CH_4(2)$ mixtures.[133, 134, 136] The transient uptake data of Majumdar et al.[134] for Ba-ETS-4 are shown in Figures 100a, and 100b for (a) 10/90, and (b) 50/50 mixtures show overshoots in the uptake of the more mobile N_2. The experimentally observed overshoots for N_2 result from thermodynamic coupling effects.[104]

Figure 101 shows simulations of the transient uptake of O_2/N_2 mixture in LTA-4A crystals exposed to a total pressure of 200 kPa and 298 K. The windows of LTA-4A, of nominal size 0.4 nm, are partially blocked due to the cations, as noted in Figure 101. The partial blocking of the window regions, reduces the effective cross-section available for inter-cage hopping of O_2, and N_2. Due to its smaller cross-sectional dimension, 3.1 Å for O_2, compared to 3.3 Å for N_2, the intra-crystalline diffusivity of O_2 is about 100 times higher than that of N_2. The simulations of transient uptake using flux equations (136) with $Đ_{O2}/r_c^2 = 2\times10^{-3}$ s^{-1}; $Đ_{O2}/Đ_{N2} = 100$ result in slight overshoot of the O_2 loading. The significantly lower diffusivity of N_2 has the consequence that purified N_2 breaks through earlier in a fixed bed adsorber; see simulated breakthroughs in fixed beds in Figure 89.

Diffusion selectivity in favor of O_2 is also achievable by use of Carbon Molecular Sieve (CMS).[137] The experimental data of Chen et al.[138] for transient uptake of O_2/N_2 mixture in CMS shows an overshoot for the more mobile O_2; see Figure 102a. The experimentally observed O_2 overshoot is properly captured using the flux equations (136) with the ratio of diffusivities $Đ_{O2}/Đ_{N2} = 36.8$, based on the data provided by Chen et al.[138] The composition trajectories followed during adsorption and desorption cycles are not symmetric; see Figure 102b.

Purity levels up to 99.9995% N_2 are achievable in PSA processes using either LTA-4A or CMS. This nitrogen purity level can also be ensured by cryogenic systems, but they are considerably more complex. However, it is essential to stress that PSA processes can recover only oxygen or nitrogen as relatively pure streams, but not both from the same process at the same time.

For co-adsorption of a mixture of CH_4 and C_2H_6 in LTA-4A, the more mobile CH_4 is found to exhibit an overshoot in the experiments reported by Carlson and Dranoff;[139] see Figure 103. In this mixture we have a combination of more-mobile-less-strongly-adsorbed-CH_4 and tardier-more-strongly-adsorbed-C_2H_6. The experimentally observed overshoot for CH_4 results from thermodynamic coupling effects.[104]

The separation of alkene/alkane mixtures is important in practice, as we shall discuss in detail in a later section. Here, we consider the transient uptake of propene/propane mixtures in two different structures, ZIF-8 and CHA, that have cages separated by narrow windows. For both ZIF-8 and CHA, the adsorption strength of the saturated propane is higher than that of propene, whereas the diffusivities are significantly higher for the unsaturated propene. Figures 104, and 105 present simulations of transient uptake of propene(1)/propane(2) within crystals of ZIF-8, and CHA. In both cases the more mobile propene exhibits a maximum in the uptake. The overshoot is significantly lower for ZIF-8 for which $Đ_1/Đ_2$ = 125.[140] The extent of overshoot is significantly higher for CHA for which the ratio of diffusivities of propene to propane, $Đ_1/Đ_2$ = 5000.[141] For both materials, neglect of thermodynamic coupling yields a monotonic approach to equilibrium for both species; see the dashed lines in Figures 104, and 105.

The overshoot phenomenon for transient uptake within crystals is particularly prominent for mixtures for which the differences in both mobilities and adsorption strengths are significantly large. This is best illustrated by the experimental data of Saint-Remi et al.[142] for transient uptake of ethanol/1-propanol mixtures within SAPO-34, that is the structural analog of CHA zeolite; see Figure 106a. The more mobile ethanol is found to exhibit a pronounced maximum in the uptake transience. For uptake of methanol/1-propanol mixture, the more mobile methanol also exhibits a sharp maximum in the experimental uptake data reported by Saint-Remi et al.[142]; see Figure 106b. The overshoots in the uptakes of the shorter alcohol can be confirmed by simulations of transient mixture uptake in CHA zeolite.[104] The experimentally observed overshoot for ethanol and propanol results from thermodynamic coupling effects; this has been shown in the simulation results.[104] A further point that needs to be stressed is that for the mixture uptakes in Figure 106, both adsorption and diffusion favor the alcohol with the shorter chain length; this is counter-intuitive

The transient mixture uptake simulations also indicate that there is an overshoot in the intra-crystalline loading of the shorter alcohol. This is illustrated in Figure 107 that presents data on the radial profiles of the loadings of ethanol and 1-propanol within CHA crystal, for ethanol/1-propanol mixture uptake at times $t = 10^2$ s, $t = 10^3$ s, $t = 10^4$ s, and $t = 5\times10^4$ s. The component loading of ethanol displays a maximum close to surface of the crystal during the initial stages of the transient uptake process.

The breakthrough experimental data of Remy et al.[143] for separation of ethanol/1-propanol in a fixed bed adsorber packed with SAPO-34 are shown in Figure 108b. The component that is eluted first from the adsorber is the alcohol with the longer chain length. Both adsorption and diffusion serve to strengthen each other; this synergy results in enhanced separations.

When the total pressure surrounding a crystalline adsorbent is increased or decreased, this does not imply that both components will, correspondingly, increase and decrease, respectively. In order to illustrate this aspect, Figures 109a,b presents simulation results for transient adsorption/desorption kinetics for ethanol/1-propanol mixture in CHA, subjected to a step increase (2 kPa to 2 MPa), or step decrease (2 MPa to 2 kPa) in total pressure. In the adsorption phase, we note that the loading of ethanol increases, while that of 1-propanol decreases; see Figure 109a. The reverse scenario holds for the desorption cycle; see Figure 109b. This is because, 1-propanol has the higher adsorption strength in the Henry regime.[144] But entropy effects favor the shorter 1-alcohol at pore saturation conditions. The adsorption/desorption kinetics, at first sight, give the impression of counter-current diffusion. In the composition space, the adsorption and desorption cycles follow different paths; see Figure 109c.

The experimental data of Kärger and Bülow[145] for transient uptake of n-heptane(1)/benzene(2) mixture in NaX zeolite at 359 K shows an overshoot in the uptake of the more mobile n-heptane; see Figure **110**. Benzene is much more strongly adsorbed due to electrostatic interactions with the Na^+ cations. The stronger binding energy of benzene makes the mobility of benzene significantly lower than that of the non-polar n-heptane.[146] The windows separating the adjacent cages of NaX are about 7.4 Å, and correlations effects meed to be taken into consideration for quantitative modelling, and the appropriate flux expressions (134), including correlations are required.[104, 111, 147] However, correlation effects are not responsible for overshoots, as these tend to "iron out" differences between the species mobilities and mitigate against overshoots. The overshoot of the n-heptane uptake is purely ascribable to the off-diagonal elements of $\begin{bmatrix} \Gamma_{11} & \Gamma_{12} \\ \Gamma_{21} & \Gamma_{21} \end{bmatrix}$; this is confirmed by detailed simulation data.[104]

The experimental data of Niessen and Karge[124, 148] for transient uptake of benzene(1)/ethylbenzene(2), and benzene(1)/*p*-xylene(2) mixtures in MFI zeolite (H-ZSM-5) show overshoots in the benzene uptake; see Figure **111** and Figure 112. The experimentally observed overshoots for benzene results from thermodynamic coupling effects; this has been demonstrated by detailed simulation data.[104]

Titze et al.[149] have monitored the transient uptake of n-hexane(nC6)/2-methylpentane(2MP) mixtures in MFI crystal using Infra-Red Microscopy (IRM). Figure 113a shows the experimental data for Run 1 in which MFI crystals are exposed to an equimolar gas phase mixture at a total pressure of 2.6 Pa. The transient equilibration of nC6 displays a pronounced overshoot. The essential features of the transient uptake can be adequately simulated by the flux equations (136) taking $Đ_1/r_c^2$ = 0.016 s^{-1}; $Đ_2/r_c^2$ = 1.6×10^{-4} s^{-1}; the simulation results are shown by the continuous solid lines in Figure 113a.Particularly noteworthy is that the experimentally observed overshoot of nC6 uptake is adequately reflected in the simulations. The total mixture loading at which the maximum in the nC6 uptake occurs is $\Theta_t \approx 4$ molecules/uc. As shown in Figure 113b, the value of $(\Gamma_{12}\ \Theta_2/\Gamma_{11}\ \Theta_1)$ exhibits a maximum at $\Theta_t \approx 4$ molecules/uc. The inescapable conclusion is that the maximum in $(\Gamma_{12}\ \Theta_2/\Gamma_{11}\ \Theta_1)$ is directly contributory to the maximum in the corresponding uptake in the simulations. Indeed, to confirm that the characteristics of the matrix $\begin{bmatrix}\Gamma_{11} & \Gamma_{12}\\ \Gamma_{21} & \Gamma_{21}\end{bmatrix}$ causes the overshoot, we carried out simulations in which this thermodynamic correction factor is assumed to be the identity matrix, and the simplified equation (139) apply; with this model there is no overshoot in the transient uptake of nC6; see Figure 113b.

Interestingly, the transient overshoot of nC6 also implies spatial overshoots of nC6 loading within the MFI crystal. Figure 114 presents simulations of the radial profiles of the loadings of nC6 and 2MP within MFI crystal for conditions corresponding to Run 1 monitored at times: t = 5 s, t = 10.2 s, t = 50.6 s, and t = 832 s. For times t = 5 s, t = 10.2 s, we note that the nC6 loadings exhibit overshoots in the uptake of nC6, with values exceeding that at the surface, $r = r_c$. At long times, the compositions are uniform in the radial direction.

Another consequence of thermodynamic coupling, is that adsorption and desorption cycles are not symmetric. To demonstrate this, Figure 115 presents a comparison of adsorption and desorption cycles for transient uptake of nC6(1)/2MP(2) mixtures in MFI zeolite at 298 K. In the adsorption phase: initial partial pressures $p_1 = p_2 = 0$ Pa; final partial pressures $p_1 = p_2 = 1.3$ Pa. In the desorption cycle: initial partial pressures $p_1 = p_2 = 1.3$ Pa; final partial pressures $p_1 = p_2 = 0$ Pa. The diffusivity inputs are the same as in Run 1 of Titze et al.[149] The continuous solid lines include thermodynamic coupling effects as described by Titze et al.[149] We note that the trajectories followed in composition space are not symmetric. The dashed lines are simulations in which the thermodynamic coupling effects are ignored; this makes the composition trajectories to be symmetric. The off-diagonal elements of matrix $\begin{bmatrix} \Gamma_{11} & \Gamma_{12} \\ \Gamma_{21} & \Gamma_{21} \end{bmatrix}$ are responsible for introducing asymmetry in the adsorption and desorption cycles.

Now, we address the question: Is it possible to obtain *undershoots* for a component during desorption? In order to demonstrate this possibility, Figure 116 presents simulation results for transient adsorption/desorption kinetics for equimolar nC6/2MP gas mixtures in MFI zeolite. In the adsorption phase, the bulk gas phase is subjected to a step increase in total pressure from 0.4 Pa to 4 Pa. In the desorption cycle, the bulk gas phase is subjected to a step decrease in total pressure from 4 Pa to 0.4 Pa. The continuous solid lines include thermodynamic coupling effects as described by Titze et al.[149] In the desorption phase, nC6 exhibits a slight *under*shoot, whereas during the adsorption phase, nC6 experiences an *over*shoot. There is no experimental verification of such undershoot phenomena in the published literature. The dashed lines are simulations in which the thermodynamic coupling effects are ignored; in these simulations both overshoot and undershoot disappear. Furthermore, we note that thermodynamic coupling effects introduces an asymmetry in the equilibration trajectories in composition space; the off-diagonal elements of matrix $\begin{bmatrix} \Gamma_{11} & \Gamma_{12} \\ \Gamma_{21} & \Gamma_{21} \end{bmatrix}$ are responsible for introducing the asymmetry. Conversely, the assumption that the thermodynamic factor matrix is the identity matrix results in composition trajectories that are symmetric for the adsorption/desorption cycles.

Figure 117 presents simulations of the transient adsorption/desorption of n-butane(nC4)/iso-butane(iC4) mixtures in MFI. The linear *n*-butane has a mobility that is about 1-2 orders of magnitude higher than that of the branched isomer because of subtle configurational differences; this has been established PFG NMR experiments of Fernandez et al.[150] Configurational-entropy effects also serve to prefer the adsorption of the linear isomer.[149] There is synergy between adsorption and diffusion, analogous to that for nC6/2MP uptake. The continuous solid lines in Figure 117 are simulation results that include the influence of thermodynamic coupling. We note that the more mobile nC4 exhibits an overshoot during the adsorption cycle. If the thermodynamic coupling effects are ignored, this overshoot disappears. Furthermore, we note that the inclusion of thermodynamic coupling effects introduces an asymmetry in the composition trajectories that are followed during the adsorption and desorption phases. The neglect of thermodynamic coupling effects makes the composition trajectories symmetric for adsorption/desorption cycles.

The experimental data of Niessen and Karge[124] for transient adsorption/desorption of benzene(1)/*p*-xylene(2) mixtures in MFI zeolite (H-ZSM-5) at 395 K provide confirmation of the asymmetry in transient adsorption/desorption cycles. The MFI zeolite is first initialized by exposure to pure benzene at a pressure of 115 Pa; the partial pressure of benzene in the gas phase is held constant at 115 Pa through the experiment. At time $t = 0$, the partial pressure of p-xylene is increased to 115 Pa. At time $t = 400$ s, the partial pressure of p-xylene is decreased to 0 Pa. Figure 118a shows the component loadings during transient adsorption/desorption process. A visual inspection reveals that the adsorption of p-xylene occurs faster that its desorption. Niessen and Karge[124] found the fitted Fick diffusivity values (ignoring all coupling effects) for either component in the adsorption cycle to be about 9 times higher than for the desorption cycle. Figure 118b compares the adsorption and desorption trajectories in composition space. The two trajectories are not symmetric.

Another consequence of thermodynamic coupling effects is that counter-current uptake of mixtures is not asymmetric. In order to demonstrate this, Figure 119 presents transient counter-current uptake of nC6(1)/2MP(2) mixtures in MFI zeolite. Two scenarios are simulated: (a) initial partial pressures $p_1 =$

1.3 Pa, $p_2 = 0$ Pa; final partial pressures $p_1 = 0$ Pa, $p_2 = 1.3$ Pa; (b) initial partial pressures $p_1 = 0$ Pa, $p_2 = 1.3$ Pa; final partial pressures $p_1 = 1.3$ Pa, $p_2 = 0$ Pa. The diffusivity inputs are the same as in Run 1 of Titze et al.[149] The continuous solid lines include thermodynamic coupling effects as described by Titze et al.[149] We note that the trajectories followed in composition space are not symmetric. The dashed lines are simulations in which the thermodynamic coupling effects are ignored; this makes the composition trajectories to be symmetric. The off-diagonal elements of matrix $\begin{bmatrix} \Gamma_{11} & \Gamma_{12} \\ \Gamma_{21} & \Gamma_{21} \end{bmatrix}$ are responsible for introducing asymmetry in the trajectories followed in the two scenarios.

The overshoot of nC6 also manifests for uptake of a gas phase 5-component nC6/2MP/3MP/22DMB/23DMB mixture in MFI zeolite. The component loadings during transient uptake for simulations that include thermodynamic coupling using the flux equations (136) are shown in Figure 120a. We note that the most mobile nC6 exhibits a sharp maximum during the early stages of the transience. The significantly higher nC6 loading within the crystal during the early stages of the transience contributes to a later breakthrough of nC6 in fixed bed adsorbers. If thermodynamic coupling effects are ignored, the component loadings exhibit a monotonous approach to equilibrium; see Figure 120b.

We now address the question: Is it possible to obtain *overshoots* for more than one component during transient equilibration? Figure 121a presents transient uptake inside MFI crystal exposed to a gas phase 4-component CH_4/ C_2H_6/ C_3H_8/ nC_4H_{10} mixture at a total pressure of 100 kPa and 300 K. These uptake simulations include thermodynamic coupling using the flux relations Equation (136). We note that the three lighter alkanes CH_4, C_2H_6, and C_3H_8 display overshoots in the uptake. When thermodynamic coupling effects are ignored, and uncoupled flux equation (139) used, all the overshoots disappear; see Figure 121b.

22. Overshoot phenomena in transient mixture permeation across microporous membranes

Thermodynamic coupling effects often lead to unusual phenomena such as overshoots in the flux of the more mobile partners during transient mixture permeation across microporous membranes.

The transient permeation fluxes *N*i are obtained by solving the set of partial differential equations

$$\frac{\partial q_i(z,t)}{\partial t} = -\frac{1}{\rho}\frac{\partial}{\partial z}\left(N_i\right) \tag{140}$$

where z is the distance coordinate along the direction of membrane thickness. The appropriate flux expressions for the permeation fluxes *N*i to be used for ZIF-8, LTA, DDR, CHA, and SAPO-34 membranes are Equation (136). For other microporous membrane layers made of MFI, FAU, MIL-53 we need additionally to account for correlation effects and use Equation (134). The boundary conditions are the partial pressures and component molar loadings at the upstream (z = 0) and downstream ($z = \delta$) faces of the membrane; see schematic in Figure 90.

$$\begin{aligned} z = 0; &\quad p_i = p_{i0}; \quad q_i = q_{i0} \\ z = \delta; &\quad p_i = p_{i\delta}; \quad q_i = q_{i\delta} \end{aligned} \tag{141}$$

Depending on the M-S diffusivities $Đ_1$ and $Đ_2$ and the mixture adsorption equilibrium, the use of either Equation (136) or Equation (134) in Equation (140) could lead to an overshoot in the flux of the more mobile species during approach to steady-state.

Consider the transient permeation of propene(1) and propane(2) across a ZIF-8 membrane. The steady-state permeation experiments of Pan et al.[151] show that the permeation is selective to propene because of subtle differences in the bond angles and bond lengths; the inter-cage hopping of propene across the 3.3 Å (flexible) windows of ZIF-8 occurs about 125 times faster than the saturated propane. The Langmuir adsorption constant of propane is 1.07 times higher than that of propene. The separation selectivity is dictated by diffusivities, not by adsorption. Figures 122 present the fluxes of propene(1) and propane(2) for permeation across ZIF-8 membrane using two different simulation scenarios. Simulations taking thermodynamic coupling effects into account, using Equation (136) (cf. Figure 122a) show an overshoot in the flux of the more mobile propene. Neglect of thermodynamic coupling effects (cf. Figure 122a), using equation (139), shows that the fluxes of both propene and propane show a monotonous approach to steady-state. It is important to stress that while neglect of thermodynamic coupling has a significant influences on the transient permeation, the ratio of the fluxes at steady-state are practically identical.

Geus et al.[152] report experimental data on transient permeation CH_4/nC_4H_{10} mixture across MFI (cf. Figure 123); the flux of the more mobile CH_4 exhibits a pronounced maximum.

In order to demonstrate that the overshoot in the flux of the more mobile CH_4 is due to thermodynamic coupling effects, Figure 124a presents the simulations for transient permeation of $CH_4/C_2H_6/C_3H_8/nC_4H_{10}$ mixture across an MFI membrane using the flux relations Equation (136). We note that the three lighter alkanes CH_4, C_2H_6, and C_3H_8 display overshoots in the permeation fluxes. All these overshoots disappear when permeation simulations ignore thermodynamic coupling and use uncoupled flux equation (139); see Figure 124b.

The experimental data of Bakker[153] for transient permeation H_2/n-C_4H_{10} mixture across MFI membrane shows a maximum in the flux of the more mobile H_2; see Figure 125. Since the mobility of H_2 is about two orders of magnitude higher than that of n-C_4H_{10}, the overshoot in the H_2 flux is very prominent.

For permeation of nC6/2MP, and nC6/23DMB mixture across an MFI membrane, Matsufuji et al.[154] have reported transient data showing overshoots in the nC6 flux during transient approach to steady-state; see Figures 126a, and 126b.

The experimental data of Matsufuji et al.[155] for transient permeation of (a) 50/50 m-xylene/p-xylene, and (b) 24/50/25 p-xylene/m-xylene/o-xylene mixtures across MFI membrane show a maximum in the flux of p-xylene which is the most mobile of the three xylene isomers; see Figures 127a, and 127b.

In Figure 11 of their paper, Kolvenbach et al.[156] have reported experimental data on permeation of benzene/p-xylene mixtures across an MFI membrane. They observed overshoots in the benzene flux during the early stages of the transience in experiments at 313 K, and 343 K. However, the benzene overshoot was seen to disappear at 403 K. Their experimental results suggest the conclusion that thermodynamic coupling effects are the root cause of the benzene overshoots at 313 K, and 343 K at which thermodynamic coupling effects are significant. With increasing temperatures, the component loadings are significantly lower; this results in smaller magnitudes of the off-diagonal elements of $\begin{bmatrix} \Gamma_{11} & \Gamma_{12} \\ \Gamma_{21} & \Gamma_{21} \end{bmatrix}$ due to significantly lower fractional occupancies; see Equation (131); indeed in the limit of vanishing occupancies, $\begin{bmatrix} \Gamma_{11} & \Gamma_{12} \\ \Gamma_{21} & \Gamma_{21} \end{bmatrix}$ reduces to the identity matrix and no overshoots are possible. We carried out simulations for transient mixture permeation using the pure component isotherms and the *T*-dependent diffusivities in Figure 6 of Kolvenbach et al.[156] The results presented in Figures 128a, b, and c are in qualitative agreement with the experiments of Kolvenbach et al.[156]. As in the experiments, the benzene overshoots are observed at 313 K, and 343 K but disappears at 403 K.

23. Notation

a_{i}	component activity, dimensionless
$[B]$	matrix of inverse M-S coefficients, m^{-2} s
c_{i}	molar concentration of species *i*, mol m^{-3}
c_{t}	total molar concentration of mixture, mol m^{-3}
$Đ_{\mathrm{i}}$	Maxwell-Stefan diffusivity for guest-framework interaction in pore, m^{2} s^{-1}
$Đ_{\mathrm{ij}}$	M-S exchange coefficient, m^{2} s^{-1}
$Đ_{12}$	M-S diffusivity for binary pair 1-2, m^{2} s^{-1}
$D_{\mathrm{i}}^{\mathrm{T}}$	thermal diffusion coefficient of component *i*, m^{2} s^{-1}
D_{12}	Fick diffusivity for binary mixture, m^{2} s^{-1}
$[D]$	Fick diffusivity matrix, m^{2} s^{-1}
$\lvert D \rvert$	Determinant of the Fick diffusivity matrix, m^{4} s^{-2}
D_{i}	Fick diffusivity of species *i* in porous material, m^{2} s^{-1}
$D_{\mathrm{i,self}}$	self-diffusivity of species *i*, m^{2} s^{-1}
f_{i}	partial fugacity of species *i*, Pa
f_{t}	total fugacity of bulk fluid mixture, Pa
F	Faraday constant, 9.65×10^{4} C mol^{-1}
G	Gibbs free energy, J mol^{-1}
G^{ex}	Excess Gibbs free energy, J mol^{-1}
$[H]$	Hessian of the Gibbs free energy defined by equation (10), dimensionless
J_{i}	molar diffusion flux of species *i* with respect to u, mol m^{-2} s^{-1}
L	length of packed bed adsorber, m
$[L]$	Onsager diffusivity matrix, m^{2} s^{-1}
M_{i}	molar mass of species *i*, kg mol^{-1}
n	number of species in the mixture, dimensionless
N_{i}	molar flux of species *i* in laboratory fixed reference frame, mol m^{-2} s^{-1}
N_{t}	molar flux of total mixture in laboratory fixed reference frame, mol m^{-2} s^{-1}
p_{i}	partial pressure of species *i* in mixture, Pa

p_t	total system pressure, Pa
q_i	component molar loading of species *i*, mol kg^{-1}
$q_{i,sat}$	molar loading of species *i* at saturation, mol kg^{-1}
q_t	total molar loading in mixture, mol kg^{-1}
$\overline{q}_i(t)$	*spatially averaged* component molar loading of species *i*, mol kg^{-1}
r	radial direction coordinate, m
r_c	radius of crystallite, m
R	gas constant, 8.314 J mol^{-1} K^{-1}
t	time, s
T	absolute temperature, K
x_i	mole fraction of component *i* in bulk fluid phase, dimensionless
y_i	mole fraction of component *i* in bulk vapor phase, dimensionless
u	molar average mixture velocity, m s^{-1}
$\overline{V}_i$	partial molar volume of species *i,* m^3 mol^{-1}
z	direction coordinate, m
z_0	position of Matano plane, m
z_i	charge on species *i*, dimensionless

Greek letters

β	cell constant, dimension depends on the context
δ	length of diffusion path or thickness of membrane, m
δ_{ij}	Kronecker delta, dimensionless
γ_i	activity coefficient of component *i*, dimensionless
ϕ	fractional pore volume, dimensionless
Γ_{ij}	thermodynamic factors, dimensionless
$[\Gamma]$	matrix of thermodynamic factors, dimensionless
μ_i	molar chemical potential, J mol^{-1}
Π	osmotic pressure, Pa
θ_i	fractional occupancy of species *i*, dimensionless

Θ_i	loading of species *i*, molecules per unit cell
$\Theta_{i,sat}$	saturation loading of species *i*, molecules per unit cell
Θ_t	total molar loading of mixture, molecules per unit cell
ρ	framework density, kg m^{-3}
σ	rate of entropy production, J m^{-3} s^{-1} K^{-1}
τ	time, dimensionless
Φ	electrostatic potential, V
ω_i	mass fraction of species *i*, dimensionless

Subscripts

A	referring to site A
B	referring to site B
i	referring to component *i*
n	referring to component *n*
t	referring to total mixture
T	thermal diffusion

Superscripts

T	thermal diffusion

Table 1. NRTL parameters for acetone(1)/benzene(2)/carbon-tetrachloride(3) at 298 K. These parameters are from Example 3.3.1 of Taylor and Krishna.[11]

	τ_{ij}	τ_{ji}	$\alpha_{ij} = \alpha_{ji}$
	dimensionless	dimensionless	dimensionless
acetone(1)/benzene(2)	-0.4605	0.76432	0.2
acetone(1)/carbon-tetrachloride(3)	-0.4279	1.5931	0.2
benzene(2)/carbon-tetrachloride(3)	-0.51821	0.7338	0.2

Table 2. NRTL parameters for acetone(1)/benzene(2)/methanol(3) at 298 K. The parameters have been retrieved from the web.

	τ_{ij}	τ_{ji}	$\alpha_{ij} = \alpha_{ji}$
	dimensionless	dimensionless	dimensionless
acetone(1)/benzene(2)	0.9247	-0.3826	0.3
acetone(1)/methanol(3)	0.3418	0.3827	0.3
benzene(2)/methanol(3)	0.5701	1.283	0.4

Table 3. Experimentally determined values of the Fick diffusivity matrix, expressed in units of 10^{-14} m^2 s^{-1}, as a function of the atom fractions of Cu, x_1, and Ag, x_2. These data at T = 998 K are from Table 8 of Ziebold.[33]

x_1	x_2	D_{11}	D_{12}	D_{21}	D_{22}
0.021	0.869	1.2	0.07	-0.6	0.42
0.059	0.845	1.7	0.04	0.19	1.4
0.138	0.781	0.74	-0.28	0.81	1.6
0.036	0.727	2.3	0.7	0	0.63
0.112	0.719	2.1	0.5	0.21	1.3
0.073	0.593	1.2	0.28	0.83	0.76
0.075	0.586	1	0.22	0.96	0.91
0.14	0.457	1.9	1.1	2.1	2.4
0.131	0.34	0.99	0.09	1.7	1.3
0.351	0.18	2.5	1.6	2.8	4
0.351	0.042	3	1.7	0.57	2.8
0.418	0.03	3.1	0.75	0.29	2
0.446	0.025	3.2	0.73	0.81	3.3
0.585	0.048	2.3	0.53	0.81	3
0.603	0.129	2.3	1.11	1.8	3.1
0.629	0.095	2.4	1.04	1.9	3.6
0.666	0.027	1.8	0.2	0.18	1.5
0.663	0.007	2.1	2.4	0.04	1.8
0.798	0.059	1.11	0.28	0.42	1.5
0.81	0.039	0.93	0.2	0.17	1.4
0.816	0.024	0.73	-0.01	0.11	1.3
0.886	0.03	0.61	-0.03	0.08	0.93
0.901	0.021	0.43	-0.21	0.04	0.85

Table 4. NRTL parameters for methanol(1)-hexane(2) at various temperatures. The parameters are from Clark and Rowley.[40]

$$\tau_{ij} = \frac{A_{ij}}{T}; \quad A_{ij} = B_{ij} + C_{ij}T$$

$$\alpha_{ij} = \alpha_{ji} = 0.2$$

	12	21
B_{ij}	1606.53	1540.7
C_{ij}	-4.2156	-3.7096

Table 5. NRTL parameters for glyercol(1)/acetone(2)/water(3) at 298 K. These parameters are from Krishna et al.[13]

	τ_{ij}	τ_{ji}	$\alpha_{ij} = \alpha_{ji}$
	dimensionless	dimensionless	dimensionless
glycerol(1)/acetone(2)	0.868	2.467	0.2
glycerol(1)/water(3)	-1.29	-1.52	0.2
acetone(2)/water(3)	-0.665	2.095	0.2

Table 6. UNIQUAC parameters for water(1)/chloroform(2)/acetic-acid(3) at 298 K. These parameters are from Pertler.[59] These parameters needed re-adjustment in order to match the experimental solubility data of Othmer and Ku.[157] The following are the adjusted values used in the calculations.

	r_i	q_i
	dimensionless	dimensionless
water(1)	0.92	1.4
chloroform(2)	2.87	2.41
acetic-acid(3)	2.2024	2.072

	τ_{ij}	τ_{ji}
	dimensionless	dimensionless
water(1)/chloroform(2)	0.4285	0.229
water(1)/acetic-acid(3)	1.274	1.312
chloroform(2)/acetic-acid(3)	1.388	0.885

Table 7. UNIQUAC parameters for water(1)/acetone(2)/ethyl-acetate(3) at 298 K. These parameters are from Pertler.[59]

	r_i	q_i
	dimensionless	dimensionless
water(1)	0.92	1.4
acetone(2)	2.5735	2.336
ethyl-acetate(3)	3.4786	3.116

	τ_{ij}	τ_{ji}
	dimensionless	dimensionless
water(1)/acetone(2)	1.328	0.488
water(1)/ ethyl-acetate(3)	0.7705	0.2538
acetone(2)/ethyl-acetate(3)	1.3068	0.827

Table 8. NRTL parameters for toluene(1)/ethanol(2)/water(3) at 298 K. The toluene/water parameters are from Wang et al.[158] The remaining parameters are from the DECHEMA Dortmund data bank; the ethanol/toluene τ_{ji} has been modified to match experimental binodal data.[159, 160]

	τ_{ij}	τ_{ji}	$\alpha_{ij} = \alpha_{ji}$
	dimensionless	dimensionless	dimensionless
toluene(1)/ethanol(2)	1.938	0.6	0.529
toluene(1)/water(3)	15.219	7.529	0.2
ethanol(2)/water(3)	-0.0978	2.096	0.293

Table 9. UNIQUAC parameters for water(1)/acetone(2)/toluene(3) at 298 K. These parameters are from the DECHEMA Dortmund data bank. The water/toluene parameters are estimated from published experimental data.

	r_i	q_i
	dimensionless	dimensionless
water(1)	0.92	1.4
acetone(2)	2.5735	2.336
toluene(3)	3.9228	2.968

	τ_{ij}	τ_{ji}
	dimensionless	dimensionless
water(1)/acetone(2)	1.34	0.26
water(1)/ toluene(3)	0.555	0.0344
acetone(2)/toluene(3)	1.61	0.4

Table 10. UNIQUAC parameters for water(1)/caprolactam(2)/toluene(3). at 298.15 K. These parameters are from Table 1, Chapter 7 of the PhD dissertation of Bollen.[70]

	r_i	q_i
	dimensionless	dimensionless
water(1)	0.92	1.4
caprolactam(2)	4.6106	3.724
toluene(3)	3.9928	2.968

	τ_{ij}	τ_{ji}
	dimensionless	dimensionless
water(1)/caprolactam(2)	0.1027043	3.647516849
water(1)/ toluene(3)	0.2563201	0.0964476
caprolactam(2)/toluene(3)	0.3324973	1.4351863

Table 11. UNIQUAC parameters for water(1)/caprolactam(2)/benzene(3) at 298.15 K. These parameters are from Table 1, Chapter 7 of the PhD dissertation of Bollen.[70]

	r_i	q_i
	dimensionless	dimensionless
water(1)	0.92	1.4
caprolactam(2)	4.6106	3.724
benzene(3)	3.1878	2.4

	τ_{ij}	τ_{ji}
	dimensionless	dimensionless
water(1)/caprolactam(2)	1.5339381	1.7321924
water(1)/ benzene(3)	0.3259823	0.1101953
caprolactam(2)/benzene(3)	1.4594085	0.8758174

Table 12. UNIQUAC parameters for toluene(1)/water(2)/propionic-acid(2)/water(3) at 298.15 K. These parameters are from Table 6 of Kim and Park.[161] However, there is some uncertainty about the units of the energy parameters listed in Table 6 because the units are not specified. Furthermore, equation (16) of Kim and Park[161] appears to contain a typo. Due to the combination of the uncertainties, our binodal curve do not correspond with the experimental data. Therefore, the calculations presented here must be viewed as being consistent for a partially miscible (hypothetical) mixture for which the following set of UNIQUAC parameters are valid.

	r_i	q_i
	dimensionless	dimensionless
toluene(1)	3.9928	2.968
Propionic-acid(2)	2.9	2.58
water(3)	0.92	1.4

	τ_{ij}	τ_{ji}
	dimensionless	dimensionless
toluene(1) / propionic-acid (2)	1.08985977	0.86688385
toluene(1)/ water(3)	0.81980947	0.3296506
Propionic-acid (2)/ water(3)	1.21111669	0.61226107

Table 13. UNIQUAC parameters for ethylacetate(1)/propionic-acid(2)/water(3) at 298.15 K. These parameters are from Table 6 of Kim and Park.[161] However, there is some uncertainty about the units of the energy parameters listed in Table 6 because the units are not specified. Furthermore, equation (16) of Kim and Park[161] appears to contain a typo. Due to the combination of the uncertainties, our binodal curve do not correspond with the experimental data. Therefore, the calculations presented here must be viewed as being consistent for a partially miscible (hypothetical) mixture for which the following set of UNIQUAC parameters are valid.

	r_i	q_i
	dimensionless	dimensionless
ethylacetate(1)	3.4786	3.116
Propionic-acid(2)	2.9	2.58
water(3)	0.92	1.4

	τ_{ij}	τ_{ji}
	dimensionless	dimensionless
ethylacetate (1)/ propionic-acid (2)	0.94875404	2.69011546
ethylacetate (1)/ water(3)	0.19953302	0.33562196
Propionic-acid (2)/ water(3)	3.28217216	1.9470615

Table 14. 1-site Langmuir-Freundlich parameters for ethene, ethane, propene and propane in ZIF-8. The *T*-dependent parameters are obtained by fitting the combined sets of pure component isotherm data of Li et al.[140] and Böhme et al.[162] determined for a variety of temperatures in the range 273 K to 408 K.

$$q = q_{sat}\frac{bp^{\nu}}{1+bp^{\nu}} \; b_A = b_0 \exp\left(\frac{E}{RT}\right)$$

	q_{sat} mol kg^{-1}	b_0 Pa$^{-\nu}$	E kJ mol^{-1}	ν dimensionless
ethene	12	9.37×10^{-11}	21.5	1.08
ethane	12	8.55×10^{-11}	23.2	1.08
propene	5.2	4.57×10^{-11}	33.9	1
propane	5.2	1.39×10^{-10}	31.3	1

24. References

(1) Onsager, L. Theories and Problems of Liquid Diffusion, *Annals N.Y. Acad. Sci.* **1945**, *46*, 241-265.

(2) de Groot, S. R.; Mazur, P. Non-Equilibrium Thermodynamics; North-Holland Publishing Co.: Amsterdam, 1962.

(3) Truesdell, C. A. Rational Thermodynamics; McGraw-Hill: New York, 1969.

(4) Maxwell, J. C. On the dynamical theory of gases, *Phil. Trans. Roy. Soc.* **1866**, *157*, 49-88.

(5) Stefan, J. Über das Gleichgewicht und die Bewegung insbesondere die Diffusion von Gasgemengen, *Sitzber. Akad. Wiss. Wien.* **1871**, *63*, 63-124.

(6) Hirschfelder, J. O.; Curtiss, C. F.; Bird, R. B. Molecular theory of gases and liquids; Second Corrected Printing, John Wiley: New York, USA, 1964.

(7) Toor, H. L. Diffusion in Three-Component Gas Mixtures, *A.I.Ch.E.J.* **1957**, *3*, 198-207.

(8) Toor, H. L. Solution of the Linearised Equations of Multi-component Mass Transfer, *A.I.Ch.E.J.* **1964**, *10*, 448-465.

(9) Stewart, W. E.; Prober, R. Matrix Calculation of Multi-component Mass Transfer in Isothermal Systems, *Ind. Eng. Chem., Fundam.* **1964**, *3*, 224-235.

(10) Krishna, R.; Standart, G. L. A multicomponent film model incorporating a general matrix method of solution to the Maxwell-Stefan equations, *A.I.Ch.E.J.* **1976**, *22*, 383-389.

(11) Taylor, R.; Krishna, R. Multicomponent mass transfer; John Wiley: New York, 1993.

(12) Standart, G. L.; Taylor, R.; Krishna, R. The Maxwell-Stefan formulation of irreversible thermodynamics for simultaneous heat and mass transfer, *Chem. Eng. Commun.* **1979**, *3*, 277-289.

(13) Krishna, R.; Low, C. Y.; Newsham, D. M. T.; Olivera Fuentes, C. G.; Paybarah, A. Liquid Liquid Equilibrium in the System Glycerol Water Acetone at 25 ^{o}C, *Fluid Phase Equilib.* **1989**, *45*, 115-120.

(14) Krishna, R.; van Baten, J. M. The Darken relation for multicomponent diffusion in liquid mixtures of linear alkanes. An investigation using Molecular Dynamics (MD) simulations, *Ind. Eng. Chem. Res.* **2005**, *44*, 6939-6947.

(15) Fuller, E. N.; Schettler, P. D.; Giddings, J. C. A new method for prediction of binary gas-phase diffusion coefficients, *Ind. Eng. Chem.* **1966**, *58*, 19-27.

(16) Darken, L. S. Diffusion, Mobility and Their Interrelation through Free Energy in Binary Metallic Systems, *Trans. AIME* **1948**, *175*, 184-201.

(17) Darken, L. S. Diffusion of Carbon in Austenite with a Discontinuity in Composition, *Trans. AIME* **1949**, *180*, 430-438.

(18) Shieh, J. C.; Lyons, P. A. Transport Properties of Liquid n-Alkanes, *J. Phys. Chem.* **1969**, *73*, 3258-3264.

(19) Bidlack, D. L.; Anderson, D. K. Mutual diffusion in the system hexane-hexadecane, *J. Phys. Chem.* **1964**, *68*, 206-208.

(20) Helbaek, M.; Hafskjold, B.; Dysthe, D. K.; Sorland, G. H. Self-diffusion coefficients of methane or ethane mixtures with hydrocarbons at high pressure by NMR, *J. Chem. Eng. Data* **1996**, *41*, 598-603.

(21) Krishna, R.; van Baten, J. M. Unified Maxwell-Stefan description of binary mixture diffusion in micro- and meso- porous materials, *Chem. Eng. Sci.* **2009**, *64*, 3159-3178.

(22) Liu, X.; Bardow, A.; Vlugt, T. J. H. Multicomponent Maxwell-Stefan Diffusivities at Infinite Dilution, *Ind. Eng. Chem. Res.* **2011**, *50*, 4776-4782.

(23) Krishna, R.; van Baten, J. M. MD simulations of diffusivities in methanol – n-hexane mixtures near the liquid-liquid phase splitting region, *Chem Eng Technol* **2006**, *29*, 516-519.

(24) Krishna, R.; van Baten, J. M. Validating the Darken relation for diffusivities in fluid mixtures of varying densities by use of MD simulations, *Chem Eng Technol* **2006**, *29*, 761-765.

(25) Wesselingh, J. A.; Krishna, R. Mass transfer in multicomponent mixtures; Delft University Press: Delft, 2000.

(26) Hsu, Y.-D.; Chen, Y.-P. Correlation of the mutual diffusion coefficients of binary liquid mixtures, *Fluid Phase Equilibr.* **1998**, *152*, 149-168.

(27) Krishna, R.; Standart, G. L. Mass and energy transfer in multicomponent systems, *Chem. Eng. Commun.* **1979**, *3*, 201-275.

(28) Krishna, R. A Unified Theory of Separation Processes Based on Irreversible Thermodynamics, *Chem. Eng. Commun.* **1987**, *59*, 33-64.

(29) Krishna, R.; van Baten, J. M. Onsager coefficients for binary mixture diffusion in nanopores, *Chem. Eng. Sci.* **2008**, *63*, 3120-3140.

(30) Cullinan, H. T.; Toor, H. L. Diffusion in the Three-Component Liquid System: Acetone-Benzene Carbon Tetrachloride, *J. Phys. Chem.* **1965**, *69*, 3941-3949.

(31) Rehfeldt, S.; Stichlmair, J. Measurement and prediction of multicomponent diffusion coefficients in four ternary liquid systems, *Fluid Phase Equilib.* **2010**, *290*, 1-14.

(32) Rehfeldt, S. Mehrkomponentendiffusion in Flüssigkeiten, Technische Universität München, München, 2009.

(33) Ziebold, T. O. Ternary Diffusion in Copper-Silver-Gold Alloys, Massachusetts Institute of Technology, Cambridge, Massachusetts, 1965.

(34) Duncan, J. B.; Toor, H. L. An Experimental Study of Three Component Gas Diffusion, *A.I.Ch.E.J.* **1962**, *8*, 38-41.

(35) Arnold, K. R.; Toor, H. L. Unsteady Diffusion in Ternary Gas Mixtures, *A.I.Ch.E.J.* **1967**, *13*, 909-914.

(36) Bres, M.; Hatzfeld, C. Three-Gas Diffusion - Experimental and Theoretical Study, *Pflügers Arch.* **1977**, *371*, 227-233.

(37) Boudin, L.; Götz, D.; Grec, B. Diffusion Models of Multicomponent Mixtures in the Lung, ESAIM: Proceedings, 90-103, 2010. http://dx.doi.org/10.1051/proc/2010008.

(38) Chevrolet, J.-C. Helium oxygen mixtures in the intensive care unit, *Critical Care* **2001**, *5*, 179–181.

(39) Fullarton, D.; Schlünder, E. U. Diffusion Distillation - A New Separation .Process for Azeotropic Mixtures - Part I: Selectivity and Transfer Efficiency, *Chem. Eng. Process.* **1986**, *20*, 255-263.

(40) Clark, W. M.; Rowley, R. L. The mutual diffusion coefficient of methanol - n-hexane near the consolute point, *A.I.Ch.E.J.* **1986**, *32*, 1125-1131.

(41) Haase, R.; Siry, M. Diffusion im kritischen entmischungsgebiet binärer flüssiger systeme, *Z. Phys. Chem.* **1968**, *57*, 56-73.

(42) Vitagliano, V.; Sartorio, R.; Chiaravalle, E.; Ortona, O. Diffusion and Viscosity in Water-Triethylamine Mixtures at 19 and 20 "C, *J. Chem. Eng. Data* **1980**, *25*, 121-124.

(43) Myerson, A. S.; Senol, D. Diffusion Coefficients near the Spinodal Curve, *A.I.Ch.E.J.* **1984**, *30*, 1004-1006.

(44) Chang, Y. C.; Myerson, A. S. Diffusivity of Glycine in Concentrated Solutions and Supersaturated Aqueous Solutions, *A.I.Ch.E.J.* **1986**, *32*, 1567-1569.

(45) Cussler, E. L. Diffusion: Mass Transfer in Fluid Systems; 3rd Edition, Cambridge University Press: Cambridge, 2007.

(46) Garside, J. Industrial Crystallization from Solution, *Chem. Eng. Sci.* **1985**, *40*, 3-26.

(47) Louhi-Kultanen, M.; Kallas, J.; Partanen, J.; Sha, Z.; Oinas, P.; Palosaari, S. The influence of multicomponent diffusion on crystal growth in electrolyte solutions , *Chem. Eng. Sci.* **2001**, *56*, 3505-3515.

(48) Matos Lopes, M. L. S.; Nieto de Castro, C. A.; Sengers, J. V. Mutual Diffusivity of a Mixture of n-Hexane and Nitrobenzene Near Its Consolute Point, *Int. J. Thermophys.* **1992**, *13*, 283-294.

(49) Wu, G.; Fiebig, M.; Leipertz Messung des bin iren Diffusionskoeffizienten in einem Entmischungssystem mit Hilfe der Photonen-Korrelationsspektroskopie, *Wärme- und Stoffübertragung* **1988**, *22*, 365-371.

(50) Glicksman, M. E. Diffusion in Solids: Field Theory, Solid-state Principles, and Applications; John Wiley: New York, 2000.

(51) Cahn, J. W.; Hilliard, J. E. Free Energy of a Nonuniform System. II. Nucleation in a Two-Component Incompressible Fluid, *J. Chem. Phys.* **1959**, *31*, 688-699.

(52) Cahn, J. W. On Spinodal Decomposition, *J. Chem. Phys.* **1961**, *9*, 795-801.

(53) Grossmann, T.; Winkelmann, J. Ternary Diffusion Coefficients of Glycerol + Acetone + Water by Taylor Dispersion Measurements at 298.15 K, *J. Chem. Eng. Data* **2005**, *50*, 1396-1403.

(54) Grossmann, T.; Winkelmann, J. Ternary Diffusion Coefficients of Glycerol + Acetone + Water by Taylor Dispersion Measurements at 298.15 K. 2. Acetone-Rich Region, *J. Chem. Eng. Data* **2007**, *52*, 336-340.

(55) Grossmann, T.; Winkelmann, J. Ternary Diffusion Coefficients of Glycerol + Acetone + Water by Taylor Dispersion Measurements at 298.15 K. 3. Water-Rich Region, *J. Chem. Eng. Data* **2007**, *52*, 341-344.

(56) Vitagliano, V.; Sartorio, R.; Scala, S.; Spaduzzi, D. Diffusion in a Ternary System and the Critical Mixing Point, *J. Solution Chem.* **1978**, *7*, 605-621.

(57) Buzatu, D.; Buzatu, F. D.; Paduano, L.; Sartorio, R. Diffusion Coefficients for the Ternary System Water + Chloroform + Acetic Acid at 25 °C, *J. Solution Chem.* **2007**, *36*, 1373-1384.

(58) Clark, W. M.; Rowley, R. L. Ternary Liquid Diffusion Coefficients Near Plait Points, *Int. J. Thermophys.* **1986**, *6*, 631-642.

(59) Pertler, M. Die Mehrkomponenten-Diffuson in nicht vollständig mischbaren Flüssigkeiten, Technische Universität München, München, 1996.

(60) Krishna, R.; Low, C. Y.; Newsham, D. M. T.; Olivera-Fuentes, C. G.; Standart, G. L. Ternary mass transfer in liquid-liquid extraction, *Chem. Eng. Sci.* **1985**, *40*, 893-903.

(61) Haeberl, M.; Blass, E. Multicomponent Effects in Liquid-Liquid Extraction, *Chem. Eng. Res. Des., Trans. IChemE.* **1999**, *77*, 647-655.

(62) Jackson, R. Diffusion in Ternary Mixtures with and without Phase Boundaries, *Ind. Eng. Chem., Fundam.* **1977**, *16*, 304-306.

(63) Ruschak, K. J.; Miller, C. A. Spontaneous Emulsification in Ternary Systems with Muss Transfer, *Ind. Eng. Chem., Fundam.* **1972**, *11*, 534-540.

(64) Miller, C. A. Spontaneous Emulsification Produced by Diffusion - A Review, *Colloids Surf.* **1988**, *29*, 89-102.

(65) Sitnikova, N. L.; Sprik, R.; Wegdam, G.; Eiser, E. Spontaneously Formed trans-Anethol/Water/Alcohol Emulsions: Mechanism of Formation and Stability, *Langmuir* **2005**, *21*, 7083-7089.

(66) Lecuyer, C. Water on Earth; John Wiley & Sons, Inc.: Hoboken, USA., 2013.

(67) Vitale, S. A.; Katz, J. L. Liquid Droplet Dispersions Formed by Homogeneous Liquid-Liquid Nucleation: “The Ouzo Effect”, *Langmuir* **2003**, *19*, 4105-4110.

(68) Ganachaud, F.; Katz, J. L. Nanoparticles and Nanocapsules Created Using the Ouzo Effect: Spontaneous Emulsification as an Alternative to Ultrasonic and High-Shear Devices *ChemPhysChem* **2005**, *6*, 209-216.

(69) Ullmann, A.; Gat, S.; Ludmer, Z.; Brauner, N. Phase Separation of Partially Miscible Solvent Systems: Flow Phenomena and Heat and Mass Transfer Applications, *Rev. Chem. Eng.* **2008**, *24*, 159-262.

(70) Bollen, A. M. Collected tales on mass transfer in liquids, Ph.D. Dissertation, Rijksuniversiteit Groningen, Groningen, 1999. http://dissertations.ub.rug.nl/faculties/science/1999/a.m.bollen/

(71) van den Berg, G. B.; Smolders, C. A. Diffusional phenomena in membrane separation processes, *J. Membr. Sci.* **1992**, *73*, 103-118.

(72) Reuvers, A. J.; Smolders, C. A. Formation of membranes by means of immersion precipitation Part II. The mechanism of formation of membranes prepared from the system cellulose acetate - acetone - water, *J. Membr. Sci.* **1987**, *34*, 67-86.

(73) Prakash, S. S.; Francis, L. F.; Scriven, L. E. Microstructure evolution in dry cast cellulose acetate membranes by cryo-SEM, *J. Membr. Sci.* **2006**, *283*, 328-338.

(74) Shojaie, S.; Krantz, W. B.; Greenberg, A. R. Dense polymer film and membrane formation via the dry-cast process Part I. Model development, *J. Membr. Sci.* **1994**, *94*, 255-280.

(75) Shojaie, S.; Krantz, W. B.; Greenberg, A. R. Dense polymer film and membrane formation via the dry-cast process Part II. Model validation and morphological studies, *J. Membr. Sci.* **1994**, *94*, 281-298.

(76) Coumans, W. J.; Kerkhof, P. J. A. M.; Bruin, S. Theoretical and Practical Aspects of Aroma Retention in Spray Drying and Freeze Drying, *Dry. Technol.* **1994**, *12*, 99-149.

(77) Gupta, P. K.; Cooper, A. R. The [*D*] Matrix for Multicomponent Diffusion, *Physica* **1971**, *54*, 39-59.

(78) Kirkaldy, J. S. Diffusion in Multicomponent Metallic Systems, *Canad. J. Phys.* **1957**, *35*, 435-4440.

(79) Varshneya, A. K.; Cooper, A. R. Diffusion in the System K_2O-SrO-SiO_2: III, Interdiffusion Coefficients, *J. Am. Ceram.. Soc.* **1972**, *55*, 312-317.

(80) Vielzeuf, D.; Saúl, A. Uphill diffusion, zero-flux planes and transient chemical solitary waves in garnet, *Contrib. Mineral. Petrol.* **2011**, *161*, 683-702.

(81) Christensen, N. H. Multiphase Ternary Diffusion Couples, *J. Am. Ceram.. Soc.* **1977**, *60*, 293-296.

(82) Taylor, R.; Krishna, R.; Kooijman, H. Real-World Modeling of Distillation, *Chem. Eng. Prog.* **2003**, *99 (7)*, 28-39.

(83) Krishna, R.; Martinez, H. F.; Sreedhar, R.; Standart, G. L. Murphree point efficiencies in multicomponent systems, *Trans. Inst. Chem. Eng.* **1977**, *55*, 178-183.

(84) Springer, P. A. M.; Baur, R.; Krishna, R. Influence of interphase mass transfer on the composition trajectories and crossing of boundaries in ternary azeotropic distillation, *Sep. Purif. Technol.* **2002**, *29*, 1-13.

(85) Springer, P. A. M.; Baur, R.; Krishna, R. Composition trajectories for heterogeneous azeotropic distillation in a bubble-cap tray column: Influence of mass transfer, *Chem. Eng. Res. Des.* **2003**, *81*, 413-426.

(86) Springer, P. A. M.; Buttinger, B.; Baur, R.; Krishna, R. Crossing of the distillation boundary in homogeneous azeotropic distillation: Influence of interphase mass transfer, *Ind. Eng. Chem. Res.* **2002**, *41*, 1621-1631.

(87) Springer, P. A. M.; Krishna, R. Crossing of boundaries in ternary azeotropic distillation: Influence of interphase mass transfer, *Int. Commun. Heat Mass Transf.* **2001**, *28*, 347-356.

(88) Springer, P. A. M.; van der Molen, S.; Baur, R.; Krishna, R. Experimental verification of the necessity to use the Maxwell-Stefan formulation in describing trajectories during azeotropic distillation, *Chem. Eng. Res. Des.* **2002**, *80*, 654-666.

(89) Springer, P. A. M.; van der Molen, S.; Krishna, R. The need for using rigorous rate-based models for simulations of ternary azeotropic distillation, *Comput. Chem. Eng.* **2002**, *26*, 1265-1279.

(90) Baur, R.; Taylor, R.; Krishna, R.; Copati, J. A. Influence of mass transfer in distillation of mixtures with a distillation boundary, *Chem. Eng. Res. Des.* **1999**, *77*, 561-565.

(91) Doherty, M. F.; Malone, M. F. Conceptual Design of Distillation Systems; McGraw-Hill: New York, 2001.

(92) Higler, A.; Chande, R.; Taylor, R.; Baur, R.; Krishna, R. Nonequilibrium Modelling of Three-Phase distillation, *Comput. Chem. Eng.* **2004**, *28*, 2021-2036.

(93) Vinograd, J. R.; McBain, J. W. Diffusion of Electrolytes and Ions in their Mixtures, *J. Am. Chem. Soc.* **1941**, *63*, 2008-2015.

(94) Kraaijeveld, G.; Wesselingh, J. A. The Kinetics of Film-Diffusion-Limited Ion Exchange, *Chem. Eng. Sci.* **1993**, *48*, 467-473.

(95) Yang, Y.; Pintauro, P. N. Multicomponent Space-Charge Transport Model for Ion-Exchange Membranes, *A.I.Ch.E.J.* **2000**, *46*, 1177-1190.

(96) Platten, J. K. The Soret Effect: A Review of Recent Experimental Results, *J. Appl. Mech.* **2006**, *73*, 5-15.

(97) Huang, F.; Chakraborty, P.; Lundstrom, C. C.; Holmden, C.; Glessner, J. J. G.; Kieffer, S. W.; Lesher, C. E. Isotope fractionation in silicate melts by thermal diffusion, *Nature* **2010**, *464*, 396-401.

(98) McDougall, T. J. Double-diffusive convection caused by coupled molecular diffusion, *J. Fluid Mech.* **1963**, *126*, 379-397.

(99) Kärger, J.; Ruthven, D. M.; Theodorou, D. N. Diffusion in Nanoporous Materials; Wiley - VCH: Weinheim, 2012.

(100) Krishna, R.; van Baten, J. M. In Silico Screening of Zeolite Membranes for CO_2 Capture, *J. Membr. Sci.* **2010**, *360*, 323-333.

(101) Krishna, R.; van Baten, J. M. In silico screening of metal-organic frameworks in separation applications, *Phys. Chem. Chem. Phys.* **2011**, *13*, 10593-10616.

(102) Thomas, A. Functional Materials: From Hard to Soft Porous Frameworks, *Angew. Chem. Int. Ed.* **2010**, *49*, 8328 – 8344.

(103) Krishna, R. Diffusion in Porous Crystalline Materials, *Chem. Soc. Rev.* **2012**, *41*, 3099-3118.

(104) Krishna, R. The Maxwell-Stefan Description of Mixture Diffusion in Nanoporous Crystalline Materials, *Microporous Mesoporous Mater.* **2014**, *185*, 30-50.

(105) Krishna, R. Describing the diffusion of guest molecules inside porous structures, *J. Phys. Chem. C* **2009**, *113*, 19756-19781.

(106) Ruthven, D. M.; Farooq, S.; Knaebel, K. S. Pressure swing adsorption; VCH Publishers: New York, 1994.

(107) Krishna, R.; Baur, R. Modelling issues in zeolite based separation processes, *Sep. Purif. Technol.* **2003**, *33*, 213-254.

(108) He, Y.; Krishna, R.; Chen, B. Metal-Organic Frameworks with Potential for Energy-Efficient Adsorptive Separation of Light Hydrocarbons, *Energy Environ. Sci.* **2012**, *5*, 9107-9120.

(109) Farooq, S.; Rathor, M. N.; Hidajat, K. A Predictive Model for a Kinetically Controlled Pressure Swing Adsorption Separation Process, *Chem. Eng. Sci.* **1993**, *48*, 4129-4141.

(110) Farooq, S. Sorption and Diffusion of Oxygen and Nitrogen in Molecular- Sieve RS-10, *Gas Sep. Purif.* **1995**, *9*, 205-212.

(111) Krishna, R.; van Baten, J. M. Investigating the Influence of Diffusional Coupling on Mixture Permeation across Porous Membranes *J. Membr. Sci.* **2013**, *430*, 113-128.

(112) Caro, J.; Noack, M. Zeolite membranes - Recent Developments and Progress, *Microporous Mesoporous Mat.* **2008**, *115*, 215-233.

(113) Ruthven, D. M. Principles of Adsorption and Adsorption Processes; John Wiley: New York, 1984.

(114) Skoulidas, A. I.; Sholl, D. S.; Krishna, R. Correlation effects in diffusion of CH_4/CF_4 mixtures in MFI zeolite. A study linking MD simulations with the Maxwell-Stefan formulation, *Langmuir* **2003**, *19*, 7977-7988.

(115) Chempath, S.; Krishna, R.; Snurr, R. Q. Nonequilibrium MD simulations of difusion of binary mixtures containing short n-alkanes in faujasite, *J. Phys. Chem. B* **2004**, *108*, 13481-13491.

(116) Hansen, N.; Keil, F. J. Multiscale modeling of reaction and diffusion in zeolites: from the molecular level to the reactor, *Soft Mater.* **2012**, *10*, 179-201.

(117) Krishna, R.; van Baten, J. M. Hydrogen Bonding Effects in Adsorption of Water-alcohol Mixtures in Zeolites and the Consequences for the Characteristics of the Maxwell-Stefan Diffusivities, *Langmuir* **2010**, *26*, 10854-10867.

(118) Krishna, R.; van Baten, J. M. Influence of Adsorption Thermodynamics on Guest Diffusivities in Nanoporous Crystalline Materials, *Phys. Chem. Chem. Phys.* **2013**, *15*, 7994-8016.

(119) Krishna, R.; van Baten, J. M. An investigation of the characteristics of Maxwell-Stefan diffusivities of binary mixtures in silica nanopores, *Chem. Eng. Sci.* **2009**, *64*, 870-882.

(120) Mason, E. A.; Malinauskas, A. P. Gas Transport in Porous Media: The Dusty-Gas Model; Elsevier: Amsterdam, 1983.

(121) Krishna, R.; van Baten, J. M. Investigating the validity of the Knudsen prescription for diffusivities in a mesoporous covalent organic framework, *Ind. Eng. Chem. Res.* **2011**, *50*, 7083-7087.

(122) Krishna, R.; van Baten, J. M. Investigating the validity of the Bosanquet formula for estimation of diffusivities in mesopores, *Chem. Eng. Sci.* **2012**, *69*, 684-688.

(123) Garg, D. R.; Ruthven, D. M. Effect of the concentration dependence of diffusivity on zeolitic sorption curves, *Chem. Eng. Sci.* **1972**, *27*, 417-423.

(124) Niessen, W.; Karge, H. G. Diffusion of *p*-xylene in Single and Binary Systems Investigated by FTIR Spectroscopy, *Microporous Mater.* **1993**, *1*, 1-8.

(125) Krishna, R.; van Baten, J. M. Investigating cluster formation in adsorption of CO_2, CH_4, and Ar in zeolites and metal organic frameworks at sub-critical temperatures, *Langmuir* **2010**, *26*, 3981-3992.

(126) Krishna, R.; van Baten, J. M. Highlighting a variety of unusual characteristics of adsorption and diffusion in microporous materials induced by clustering of guest molecules, *Langmuir* **2010**, *26*, 8450-8463.

(127) Krishna, R.; van Baten, J. M. Highlighting Pitfalls in the Maxwell-Stefan Modeling of Water-Alcohol Mixture Permeation across Pervaporation Membranes, *J. Membr. Sci.* **2010**, *360*, 476-482.

(128) Krishna, R.; van Baten, J. M. A molecular dynamics investigation of the unusual concentration dependencies of Fick diffusivities in silica mesopores, *Microporous Mesoporous Mater.* **2011**, *138*, 228-234.

(129) Krishna, R.; van Baten, J. M. A rationalization of the Type IV loading dependence in the Kärger-Pfeifer classification of self-diffusivities, *Microporous Mesoporous Mater.* **2011**, *142*, 745-748.

(130) Chmelik, C.; Bux, H.; Caro, J.; Heinke, L.; Hibbe, F.; Titze, T.; Kärger, J. Mass transfer in a Nanoscale Material Enhanced by an Opposing Flux, *Phys. Rev. Lett.* **2010**, *104*, 085902.

(131) Myers, A. L.; Prausnitz, J. M. Thermodynamics of Mixed Gas Adsorption, *A.I.Ch.E.J.* **1965**, *11*, 121-130.

(132) Krishna, R.; van Baten, J. M. A molecular dynamics investigation of the diffusion characteristics of cavity-type zeolites with 8-ring windows, *Microporous Mesoporous Mater.* **2011**, *137*, 83-91.

(133) Bhadra, S. J.; Farooq, S. Separation of Methane Nitrogen Mixture by Pressure Swing Adsorption for Natural Gas Upgrading, *Ind. Eng. Chem. Res.* **2011**, *50*, 14030-14045.

(134) Majumdar, B.; Bhadra, S. J.; Marathe, R. P.; Farooq, S. Adsorption and Diffusion of Methane and Nitrogen in Barium Exchanged ETS-4, *Ind. Eng. Chem. Res.* **2011**, *50*, 3021-3034.

(135) Habgood, H. W. The Kinetics of Molecular Sieve Action. Sorption of Nitrogen-Methane Mixtures by Linde Molecular Sieve 4A, *Canad. J. Chem.* **1958**, *36*, 1384-1397.

(136) Kuznicki, S. M.; Bell, V. A.; Nair, S.; Hillhouse, H. W.; Jacubinas, R. M.; Braunbarth, C. M.; Toby, B. H.; Tsapatsis, M. A titanosilicate molecular sieve with adjustable pores for size-selective adsorption of molecules, *Nature* **2001**, *412*, 720-724.

(137) Yang, R. T. Adsorbents: Fundamentals and Applications; John Wiley & Sons, Inc.: Hoboken, New Jersey, 2003.

(138) Chen, Y. D.; Yang, R. T.; Uawithya, P. Diffusion of oxygen, nitrogen and their mixtures in Carbon Molecular-Sieve, *A.I.Ch.E.J.* **1994**, *40*, 577-585.

(139) Carlson, N. W.; Dranoff, J. S. Competitive adsorption of methane and ethane on 4A zeolite. Fundamentals of Adsorption; Edited by A.I. Liapis, AIChE: New York, 1986.

(140) Li, K.; Olson, D. H.; Seidel, J.; Emge, T. J.; Gong, H.; Zeng, H.; Li, J. Zeolitic Imidazolate Frameworks for Kinetic Separation of Propane and Propene, *J. Am. Chem. Soc.* **2009**, *131*, 10368-10369.

(141) Khalighi, M.; Chen, Y. F.; Farooq, S.; Karimi, I. A.; Jiang, J. W. Propylene/Propane Separation Using SiCHA, *Ind. Eng. Chem. Res.* **2013**, *52*, 3877-3892.

(142) Saint-Remi, J. C.; Baron, G. V.; Denayer, J. F. M. Non-Uniform Chain Length Dependent Diffusion of Short 1-Alcohols in SAPO-34 in Liquid Phase, *J. Phys. Chem. C* **2013**, *117*, 9758-9765.

(143) Remy, T.; Saint-Remi, J. C.; Singh, R.; Webley, P. A.; Baron, G. V.; Denayer, J. F. M. Adsorption and Separation of C1-C8 Alcohols on SAPO-34, *J. Phys. Chem. C* **2011**, *115*, 8117-8125.

(144) Krishna, R.; van Baten, J. M. Entropy-based Separation of Linear Chain Molecules by Exploiting Differences in the Saturation Capacities in Cage-type Zeolites, *Sep. Purif. Technol.* **2011**, *76*, 325-330.

(145) Kärger, J.; Bülow, M. Theoretical Prediction of Uptake Behaviour in Adsorption Kinetics of Binary Gas Mixtures Using Irreversible Thermodynamics, *Chem. Eng. Sci.* **1975**, *30*, 893-896.

(146) Krishna, R.; van Baten, J. M. Investigating the Relative Influences of Molecular Dimensions and Binding Energies on Diffusivities of Guest Species Inside Nanoporous Crystalline Materials *J. Phys. Chem. C* **2012**, *116*, 23556-23568.

(147) Krishna, R. Multicomponent surface diffusion of adsorbed species - A description based on the generalized Maxwell-Stefan equations, *Chem. Eng. Sci.* **1990**, *45*, 1779-1791.

(148) Karge, H. G. Infrared Spectroscopic Investigation of Diffusion, Co-diffusion and Counter-diffusion of Hydrocarbon Molecules in Zeolites, *C.R. Chim.* **2005**, *8*, 303-319.

(149) Titze, T.; Chmelik, C.; Kärger, J.; van Baten, J. M.; Krishna, R. Uncommon Synergy Between Adsorption and Diffusion of Hexane Isomer Mixtures in MFI Zeolite Induced by Configurational Entropy Effects *J. Phys. Chem. C* **2014**, *118*, 2660-2665.

(150) Fernandez, M.; Kärger, J.; Freude, D.; Pampel, A.; van Baten, J. M.; Krishna, R. Mixture Diffusion in Zeolites Studied by MAS PFG NMR and Molecular Simulation, *Microporous Mesoporous Mater.* **2007**, *105*, 124-131.

(151) Pan, Y.; Li, T.; Lestari, G.; Lai, Z. Effective Separation of Propylene/Propane Binary Mixtures by ZIF-8 Membranes, *J. Membr. Sci.* **2012**, *390-391*, 93-98.

(152) Geus, E. R.; van Bekkum, H.; Bakker, W. J. W.; Moulijn, J. A. High-temperature Stainless Steel Supported Zeolite (MFI) Membranes: Preparation, Module Construction, and Permeation Experiments, *Microporous Mater.* **1993**, *1*, 131-147.

(153) Bakker, W. J. W. Structured systems in gas separation, Ph.D. Dissertation, Delft University of Technology, Delft, 1999.

(154) Matsufuji, T.; Watanabe, K.; Nishiyama, N.; Egashira, Y.; Matsukata, M.; Ueyama, K. Permeation of Hexane Isomers Through an MFI Membrane, *Ind. Eng. Chem. Res.* **2000**, *39*, 2434-2438.

(155) Matsufuji, T.; Nishiyama, N.; Matsukata, M.; Ueyama, K. Separation of Butane and Xylene Isomers with MFI-type Zeolitic Membrane Synthesized by a Vapor-Phase Transport Method, *J. Membr. Sci.* **2000**, *178*, 25-34.

(156) Kolvenbach, R.; Al-Yassir, N.; S.S. Al-Khattaf, S. S.; Gobin, O. C.; Ahn, J. H.; Jentys, A.; Lercher, J. A. A comparative study of diffusion of benzene/p-xylene mixtures in MFI particles, pellets and grown membranes, *Catal. Today* **2011**, *168*, 147-157.

(157) Othmer, D. F.; Ku, P. L. Solubility Data for Ternary Liquid Systems. Acetic Acid and Formic Acid Distributed between Chloroform and Water, *J. Chem. Eng. Data* **1960**, *5*, 42-44.

(158) Wang, H.; Wang, Q.; Xiong, Z.; Chen, C. Liquid–liquid equilibria for ternary system water + toluene + benzaldehyde at (303.2–343.2) K, *Fluid Phase Equilib.* **2014**, *383*, 43-48.

(159) Ruiz, F.; Prats, D.; Gomis, V. Quaternary Liquid-Liquid Equilibrium: Water-Ethanol-ChtoroformToluene at 25 ^{o}C. Experimental Determination and Graphical and Analytical Correlation of Equillbrium Data, *J. Chem. Eng. Data* **1985**, *30*, 412-416.

(160) Washburn, E. R.; Beguin, A. E.; Beckford, O. C. The Ternary System: Ethyl Alcohol, Toluene and Water at 25^{o}, *J. Am. Chem. Soc.* **1939**, *61*, 1694-1695.

(161) Kim, J.-K.; Park, D.-W. Liquid-Liquid Equilibrium for the Ternary Systems of Solvents+Water+Propionic Acid at 25 ^{o}C and Atmospheric Pressure, *Korean J. Chem. Eng.* **2005**, *22*, 256-263.

(162) Böhme, U.; Barth, B.; Paula, C.; Kuhnt, A.; Schwieger, W.; Alexander Mundstock, A.; Caro, J.; Hartmann, M. Ethene/Ethane and Propene/Propane Separation via the Olefin and Paraffin Selective Metal−Organic Framework Adsorbents CPO-27 and ZIF8, *Langmuir* **2013**, *29*, 8592-8600.

(163) Tyn, M. T.; Calus, W. F. Temperature and Concentration Dependence of Mutual Diffusion Coefficients of Some Binary Liquid Systems, *J. Chem. Eng. Data* **1975**, *20*, 310-316.

(164) Königer, A.; Meier, B.; Köhler, W. Measurement of the Soret, diffusion, and thermal diffusion coefficients of three binary organic benchmark mixtures and of ethanol–water mixtures using a beam deflection technique, *Philos. Mag.* **2009**, *89*, 907-923.

(165) Anderson, D. K.; Hall, J. R.; Babb, A. L. Mutual diffusion in non-ideal binary liquid mixtures, *J. Phys. Chem.* **1958**, *62*, 404-408.

(166) Caldwell, C. S.; Babb, A. L. Diffusion in Ideal Binary Liquid Mixtures, *J. Phys. Chem.* **1956**, *60*, 51-56.

(167) Alimadadian, A.; Colver, C. P. A New Technique for the Measurement of Ternary Diffusion Coefficients in Liquid Systems, *Can. J. Chem. Eng.* **1976**, *54*, 208-213.

(168) Krishna, R.; Wesselingh, J. A. The Maxwell-Stefan approach to mass transfer, *Chem. Eng. Sci.* **1997**, *52*, 861-911.

(169) Counsell, J. F.; Everett, D. H.; Munn, R. J. Recent redeterminations of the phase diagram of the system: triethylamine + water, *Pure. Appl. Chem.* **1961**, *2*, 335-338.

(170) Kohler, F.; Rice, O. K. Coexistence Curve of the Triethylamine-Water System, *J. Chem. Phys.* **1957**, *26*, 1614-1618.

(171) D'Agostino, C.; Mantle, M. D.; Gladden, L. F.; Moggridge, G. D. Prediction of mutual diffusion coefficients in non-ideal mixtures from pulsed field gradient NMR data:Triethylamine–water near its consolute point, *Chem. Eng. Sci.* **2012**, *74*, 105-113.

(172) Favvas, A.; Mitropoulos, A. C. What is spinodal decomposition?, *J. Eng. Sci. & Tech. Rev.* **2008**, *1*, 25-27.

(173) Battler, J. R.; Clark, W. M.; Rowley, R. L. Excess Enthalpy and Liqdd-Liquid Equilibrium Surfaces for the Cyclohexane2-Propanoi-Water System from 293.15 to 323,15 K, *J. Chem. Eng. Data* **1985**, *30*, 254-259.

25. Caption for Figures

Figure 1. Comparison of the Fick diffusivities, D_{12}, with the Maxwell-Stefan, $Đ_{12}$, and Onsager, L_{12}, diffusivities for (a) acetone (1) – water (2), and (b) ethanol(1)-water(2) mixtures. The experimental data on D_{12} are from Tyn and Calus,[163] Grossmann and Winkelmann,[53] and Königer et al.[164] The $Đ_{12}$ are obtained by correcting for the thermodynamic factor $Đ_{12} = \frac{D_{12}}{\Gamma}$. The thermodynamic factor is calculated using the NRTL parameters from the Dortmund data bank. Also shown are the calculations using the Vignes interpolation formula (48). The Onsager coefficients L_{12} are calculated using equation (43).

Figure 2. The experimental data of Cullinan and Toor[30], for the elements of the Fick diffusivity matrix [D] for acetone(1)/benzene(2)/carbon tetrachloride (3) mixtures.

Figure 3. Comparison of the Fick and Maxwell-Stefan diffusivities for (a) acetone(1)/benzene(2), (b) acetone(1)/carbon tetrachloride (3), and (c) benzene (2)/carbon tetrachloride (3) mixtures. The Fick diffusivity data are culled from Cullinan and Toor[30], Anderson et al.[165], and Caldwell and Babb.[166] Also shown are the calculations using the Vignes interpolation formula (48).

Figure 4. (a) Comparison of the experimental data of Cullinan and Toor[30] for the elements of the Fick diffusivity matrix [*D*] for acetone(1)/benzene(2)/carbon-tetrachloride(3) mixtures with the estimations using equations (29), and (33). The estimation procedure used here is precisely the same as that outlined in Example 4.2.6 of Taylor and Krishna[11] for one of the nine experimental data sets. The required NRTL parameters for calculation of thermodynamic factors are provided in Table 1.

Figure 5. The ratio $\frac{|D|^{1/2}}{|\Gamma|^{1/2}}$ plotted as a function of the mole fraction of acetone in the (a) acetone(1)/benzene(2)/carbon-tetrachloride(3), and (b) acetone(1)/benzene(2)/methanol(3) mixtures. The Fick diffusivity data for acetone(1)/benzene(2)/methanol(3) mixture are from Alimadadian and Colver;[167] the NRTL parameters are provided in Table 2.

Figure 6. The ratio $\frac{|D|^{1/2}}{|\Gamma|^{1/2}}$ plotted as a function of the mole fraction of component 1 in four different mixtures. Re-analysis of the data of Rehfeldt[31, 32] for the Fick diffusivity matrix [*D*] for (a) methanol(1)/1-butanol(2)/1-propanol, (b) acetone(1)/water(2)/1-propanol(3), (c) acetone(1)/1-butanol(2)/1-propanol(3), and (d) 1-propanol(1)/1-chlorobutane(2)/n-heptane(3) mixtures at 298 K. The calculations of the the thermodynamic factor matrix $[\Gamma]$ are based on the Wilson parameters reported in Table 9.2 of the dissertation of Rehfeldt.[32]

Figure 7. The ratio $\frac{|D|^{1/2}}{|\Gamma|^{1/2}}$ plotted as a function of the atom fraction of Cu(1) in Cu(1)/Ag(2)/Au(3) alloys mixtures. The diffusivity data are provided in Table 3. The data on the thermodynamic correction factors are from Table 10 of Ziebold.[33]

Figure 8. The two-bulb diffusion experiment of Duncan and Toor[34] with $H_2(1)/N_2(2)/CO_2(3)$ gas mixture.

Figure 9. (a) Experimental data of Duncan and Toor[34] on the transient approach to equilibrium in the two-bulb diffusion experiments for $H_2(1)/N_2(2)/CO_2(3)$ mixtures. (b) Equilibration trajectories in composition space, followed in the two bulbs. The dashed line represents the trajectory predicted by uncoupled Fickian formulation.

Figure 10. The composition trajectory in each of the Bulbs A, and B in the two-bulb diffusion experiments for $H_2(1)/N_2(2)/CO_2(3)$ plotted on a triangular composition diagram. The symbols represent the experimental data of Duncan and Toor.[34] The continuous solid lines (red and green) are the model calculations as presented in Example 5.4.1 of Taylor and Krishna.[11] The dashed (blue) line are the model calculations with a diagonal matrix of Fick diffusivities. The Maxwell-Stefan equations, after appropriate linearization, were solved analytically for diffusion of gaseous mixtures independently in 1964 by Professor Herbert Toor (see picture) [7, 8] and Professor Warren Stewart.[9] The exact analytical solutions to the M-S equations was made available only much later in 1976.[10]

Figure 11. Transient approach to equilibrium in the two-bulb diffusion experiments for $H_2(1)/N_2(2)/CO_2(3)$ mixtures. The experimental data of Duncan and Toor[34] are compared with solutions of the Maxwell-Stefan diffusion equations.

Figure 12. Plot of the normalized flux (*y*-axis) vs the mole fraction driving force for (a) hydrogen, (b) nitrogen, and (c) carbon dioxide in the experiment of Duncan and Toor[34] for $H_2(1)/N_2(2)/CO_2(3)$ mixtures.

Figure 13. The dependence of the flux J_i, with respect to the molar average mixture velocity u, on its composition (mole fraction) gradient $\frac{dx_i}{dz}$ for (a) binary mixture and (b) ternary mixture. Adapted from Krishna and Wesselingh.[168]

Figure 14. The composition trajectory in each of the Bulbs A, and B in the two-bulb diffusion experiments for $H_2(1)/N_2(2)/CO_2(3)$ plotted on a triangular composition diagram. Also shown are the fast and slow eigenvectors.

Figure 15. The Loschmidt tube experiment of Arnold and Toor[35] with $CH_4(1)/Ar(2)/H_2(3)$ gas mixture. The composition trajectory in the top and bottom compartments in the Loschmidt diffusion experiments, plotted on a triangular composition diagram. The symbols represent the experimental data of Arnold and Toor for the spatially averaged compositions in the top and bottom tubes.[35] The continuous solid lines (red and green) are the model calculations as presented in Example 5.5.1 of Taylor and Krishna.[11] The dashed (blue) line are the model calculations with a diagonal matrix of Fick diffusivities.

Figure 16. (a) The Loschmidt tube experiment of Arnold and Toor[35] on the transient approach to equilibrium for CH_4(1)/Ar(2)/H_2(3) gas mixtures. The plotted data are spatially averaged compositions in the top and bottom compartments. (b) Equilibration trajectories in composition space, followed in the two tubes. The dashed line represents the trajectory predicted by uncoupled Fickian formulation.

Figure 17.Transient approach to equilibrium in the Loschmidt tube experiment of Arnold and Toor[35] with CH_4(1)/Ar(2)/H_2(3) gas mixture.

Figure 18. Composition trajectories for O_2(1)/N_2(2)/He(3) gas mixture diffusing from Left compartment (O_2 = 20 %; He = 80 %) into air contained in the Right compartment (O_2 = 20 %; N_2 = 80 %).

Figure 19. Transient equilibration of O_2, for O_2(1)/N_2(2)/He(3) gas mixture diffusion, monitored at the position z = -0.5 m.

Figure 20. Condensation of an azeotropic mixture of 2-propanol(1)/water(2) in the presence of an inert gas such as nitrogen (3) results in a condensate which is richer in water than the azeotrope.

Figure 21. (a) Liquid/liquid phase equilibrium for methanol(1)/n-hexane (2) mixtures exhibiting with UCST at 308 K. The calculations of the binodal curve use NRTL parameters from Clark and Rowley.[40] (b) Liquid/liquid phase equilibrium for triethylamine (1) – water (2) mixture exhibiting LCST at 291.5

K. These are experimental data for the binodal and spinodal curves are taken from Counsell et al.[169], Kohler and Rice,[170] and Vitagliano et al.[42] (c) Liquid-liquid equilibrium for n-hexane (1)/ nitrobenzene (2) mixtures with T_c = UCST = 292.56 K.[49]

Figure 22. (a) Calculations of (a) free energy, $\frac{G}{RT}$, (b) first derivative, $\frac{1}{RT}\frac{\partial G}{\partial x_1}$, and (c) second derivative, $\frac{1}{RT}\frac{\partial^2 G}{\partial x_1^2}$ for methanol – *n*-hexane mixtures at various temperatures in the range 260 K – 320 K using NRTL parameters from Clark and Rowley.[40] (d) Binodal and Spinodal curves, determined from (a), (b), and (c).

Figure 23. (a) Calculations of the thermodynamic correction factor Γ for methanol – n-hexane mixtures at 303.15 K, 305.65 K, 307.75 K, 310.65 K, and 313.15 K using NRTL parameters from Table 4. (b) Experimental data of Clark and Rowley[40] for Fick diffusivities, D_{12}, for methanol – n-hexane mixtures at 303.15 K, 305.65 K, 307.75 K, 310.65 K, and 313.15 K. The two sets of Figures are presented with both linear and logarithmic scales on the *y*-axes.

Figure 24. Comparison of the experimental data of Clark and Rowley[40] for Fick diffusivities, D_{12}, for methanol – n-hexane mixtures at (a) 303.15 K, (b) 305.65 K, (c) 307.75 K, (d) 310.65 K, and (e) 313.15 K with corresponding MD simulation results of Krishna and van Baten[23] for the corresponding Fick and M-S diffusivities.

Figure 25. Comparison of the experimental data of Clark and Rowley[40] for Fick diffusivities, D_{12}, with the M-S diffusivities for methanol(1)/n-hexane (2) mixtures, obtained by correcting for the thermodynamic factor $Đ_{12} = \frac{D_{12}}{\Gamma}$. The thermodynamic factor is calculated using NRTL parameters from Table 4. The Onsager coefficients L_{12} calculated using equation (43). Also shown are the calculations using the Vignes interpolation formula (48).

Figure 26. (a) Experimental data of Haase and Siry[41] for the temperature dependence of the Fick diffusivities, D_{12}, for triethylamine(1)/water(2) mixtures, measured at the critical composition x_1 = 0.073. (b) Thermodynamic correction factor Γ for triethylamine(1)/water(2) mixtures at temperatures T = 277.15 K, T = 283.15, and T = 291.15 K; these plots are based on the data of D'Agostino et al.[171]

Figure 27. (a) Liquid/liquid phase equilibrium for triethylamine (1) – water (2) mixture exhibiting LCST at 291.5 K. The experimental data for the binodal and spinodal curves are taken from Counsell et al.,[169] Kohler and Rice,[170] and Vitagliano et al.[42] (b) Experimental data of Vitagliano et al.[42] for Fick diffusivities, D_{12}, for triethyamine(1)/water(2) mixtures, measured at two different temperatures 292.15 K, and 293.15 K, for various compositions on either side of the spinodal curves in (a).

Figure 28. Fick diffusivity of (a) urea, and (b) glycine in aqueous solutions function of molar concentration of solute. Experimental data of Myerson and Senol,[43] and Chang and Myerson.[44]

Figure 29. Fick diffusivity of n-hexane (1) / nitrobenzene (2) mixtures as a function of (T – T_c) with T_c = UCST = 292.56 K. Experimental data of Matos Lopes et al.,[48] Haase and Siry,[41] and Wu et al.[49]

Figure 30. The nucleation and growth process. This sketch is adapted from the paper of Favvas and Mitropoulos.[172]

Figure 31. The spinodal decomposition process.

Figure 32. Schematic showing liquid/liquid phase equilibrium for a hypothetical ternary liquid mixture. The binodal and spinodal curves converge at the plait point. Consider two mixtures of compositions A and B are brought into contact. The average mixture composition (M) falls within in the two-phase region. Each of the mixtures A and B will equilibrate to the compositions at the two ends of the tie-line corresponding to the mixture composition M. The mixture with a composition M will split into two phases at either end of the tie-line.

Figure 33. The phase equilibrium diagram for glycerol(1)/acetone(2)/water(3) mixtures at 298 K.[13] The composition of the plait point is: $x_{\text{glycerol}}= 0.1477$, $x_{\text{acetone}}= 0.4163$ and $x_{\text{water}}= 0.4360$. Also indicated are the 75 compositions for which Grossmann and Winkelmann[53-55] have measured the Fick diffusivity matrix $[D]$ for glycerol(1)/acetone(2)/water(3) mixtures. As indicated, at $x_1= 0.18$, $x_2 = 0.22$, $x_3 = 0.6$, $[D]=\begin{bmatrix} 0.294 & 0.127 \\ 0.148 & 0.213 \end{bmatrix}\times 10^{-9} \quad \text{m}^2 \text{ s}^{-1}$, and $|D| = 0.044\times 10^{-18} \quad \text{m}^4 \text{ s}^{-2}$. The spinodal curve is calculated using the constraint $|H| = 0; \quad \text{spinodal curve}$; for this purpose the phase equilibrium is determined from the NRTL parameters in Table 5.

Figure 34. (a) Calculations of the elements of the Thermodynamic correction factor matrix $[\Gamma]$ for glycerol(1)/acetone(2)/water(3) mixtures, as a function of the mole fractions of glycerol, x_1. In these calculations, the ratio of the mole fraction of acetone to that of water is fixed at $x_2/x_3 = 0.85$. These calculations are based on the use of NRTL parameters as reported by Krishna et al.[13] (b) Calculations of the determinant $|\Gamma|$ as function of the mole fraction of glycerol, x_1. (c) Calculations of the determinant $|H|$ as function of the mole fraction of glycerol, x_1.

Figure 35. The experimental data of Grossmann and Winkelmann[53-55] for the elements of the Fick diffusivity matrix $[D]$ for glycerol(1)/acetone(2)/water(3) mixtures, as a function of the mole fractions of acetone, x_2, and water, x_3. Note, that values of the diffusivities depend on the numbering of the components.

Figure 36. The experimental data of Grossmann and Winkelmann[53-55] for the determinant of the Fick diffusivity matrix $|D|$ for glycerol(1)/acetone(2)/water(3) mixtures, as a function of the mole fraction of glycerol, x_1, and acetone, x_2, in the liquid mixture. The composition of the plait point is: $x_{\mathrm{glycerol}}= 0.1477$, $x_{\mathrm{acetone}}= 0.4163$ and $x_{\mathrm{water}}= 0.4360$. The determinant $|D|$ has the units of 10^{-18} m^4 s^{-2}. The calculations of the determinant of the thermodynamic factor matrix $[\Gamma]$ are also shown alongside.

Figure 37. (a) The experimental data of Grossmann and Winkelmann[53-55] for the determinant of the Fick diffusivity matrix $|D|$ for glycerol(1)/acetone(2)/water(3) mixtures, as a function of the mole fraction of glycerol, x_1, in the liquid mixture. (b, c) Eigenvalues of the Fick diffusivity matrix $[D]$ for

glycerol(1)/acetone(2)/water(3) mixtures, as a function of the mole fraction of glycerol, x_1, and acetone, x_2, in the liquid mixture.

Figure 38. (a) The ratios D_{12}/D_{11}, and D_{21}/D_{22} of the Fick diffusivity matrix $[D]$ for glycerol(1)/acetone(2)/water(3) mixtures plotted as a function of the determinant $|D|$. These experimental data are from Grossmann and Winkelmann[53-55] (b) The ratios D_{12}/D_{11}, and Γ_{12}/Γ_{11} plotted as a function of the determinant $|D|$.

Figure 39. The ratio $\frac{|D|^{1/2}}{|\Gamma|^{1/2}}$ glycerol(1)/acetone(2)/water(3) mixtures, plotted (a) as a function of the mole fractions of acetone, x_2, and water x_3 and (b) only as a function of the mole fraction of acetone, x_2.

Figure 40. Experimental data of Vitagliano et al.[56] for Fick diffusivity matrix $[D]$ of water(1)/chloroform(2)/acetic-acid(3) mixtures at six different compositions. The measured values of the Fick matrix $[D]$, in units of 10^{-9} m^2 s^{-1}, are indicated. The composition of the plait point is x_1 = 0.375, x_2= 0.262, x_3= 0.363. The binodal curve is from the experimental data of Othmer and Ku.[157] The spinodal curve is obtained from the criterion of phase stability; the UNIQUAC parameters are provided in Table 6.

Figure 41. Experimental data of Buzatu et al.[57] for Fick diffusivity matrix $[D]$ of water(1)/chloroform(2)/acetic-acid(3) mixtures at six different compositions. The measured values of the Fick matrix $[D]$, in units of 10^{-9} m^2 s^{-1}, are indicated. The composition of the plait point is x_1 = 0.375, x_2= 0.262, x_3= 0.363.

Figure 42. (a) Plot of the determinant $\left|D\right|$ that has the units of 10^{-18} m^4 s^{-2} as a function of (1- x_3) for water(1)/chloroform(2)/acetic-acid(3) mixtures. (b) Plot of the determinant $\left|\Gamma\right|$ as a function of (1- x_3) for water(1)/chloroform(2)/acetic-acid(3) mixtures. (c) The ratio $\frac{\left|D\right|^{1/2}}{\left|\Gamma\right|^{1/2}}$ plotted as a function of (1- x_3). (d) The ratios Γ_{12}/Γ_{11}, and Γ_{21}/Γ_{22} plotted as a function of the determinant $\left|\Gamma\right|$. (e) The ratios D_{12}/D_{11}, and D_{21}/D_{22} of the Fick diffusivity matrix [D] for water(1)/chloroform(2)/acetic-acid(3) mixtures plotted as a function of the determinant $\left|D\right|$. The experimental data are from Vitagliano et al.[56] and Buzatu et al.[57]

Figure 43. (a) Experimental data of Clark and Rowley[58] for the determinant of the Fick diffusivity matrix $\left|D\right|$ for water(1)/2-propanol(2)/cyclohexane(3) mixtures as ($T - T_c$) where T is the temperature at which the diffusivities are measured, with T_c = 303.67 K. The elements of the Fick matrix of diffusivities were measured at a constant composition of the plait point at 303.67 K: x_1 = 0.367, x_2= 0.389, x_3= 0.244. The measured values of the Fick matrix [D], in units of 10^{-10} m^2 s^{-1}, are also indicated; the corresponding values of the determinant $\left|D\right|$ has the units of 10^{-18} m^4 s^{-2}. (b) Data of Battler et al.[173] for the binodal curves at T = 293.15 K, 303.15 K, and 323.15 K.

Figure 44. Phase equilibrium diagram for acetone/water/ethylacetate mixtures at 293 K. The binodal curve data is from Haeberl and Blass.[61] The spinodal curve is obtained from the criterion of phase stability; the UNIQUAC parameters are provided Table 7. Also indicated are the six experimental values of of Pertler[59] for the elements of the Fick diffusivity matrix in the ethylacetate-rich region of the

phase diagram; these values correspond to the component numbering: acetone(1)/water(2)/ethylacetate(3). The phase diagram is plotted in mass fractions.

Figure 45. Experimental data of Pertler[59] for the elements of the Fick diffusivity matrix in the water-rich region of the phase diagram; these values correspond to the component numbering: acetone(1)/ethylacetate(2)/water(3). The phase diagram is plotted in mass fractions.

Figure 46. Transient inter-diffusion in a diffusion couple consisting of water(1)/chloroform(2)/acetic-acid(3) mixtures. The compositions of the two mixtures in the left and right chambers are indicated; both initial compositions and the final equilibrated compositions are in the homogeneous single phase region. The transient approach to equilibrium is plotted against the dimensionless coordinate $\frac{z}{\sqrt{4D_{ref}t}}$ where the value of the reference diffusivity $D_{ref} = 10^{-9}$ m^2 s^{-1}. The values of the Fick diffusivity matrix is $[D] = \begin{bmatrix} 0.309 & 0.368 \\ 0.344 & 0.939 \end{bmatrix} \times 10^{-9}$ m^2 s^{-1}; $|D| = 0.164 \times 10^{-18}$ m^4 s^{-2}, corresponding to the fifth data set of Vitagliano et al.[56]

Figure 47. Equilibration trajectories in glycerol(1)/acetone(2)/water(3) mixtures at 298 K. The equilibration trajectories were simulated for two cases, with two different equilibrium compositions: (a) $x_1 = 0.18$, $x_2 = 0.22$, $x_3 = 0.6$, and (b) $x_1 = 0.1$, $x_2 = 0.432$, $x_3 = 0.468$. The Fick diffusivity matrix for these two simulations are obtained from the experimental data of Grossmann and Winkelmann[53-55]; these are indicated.

Figure 48. (a) Equilibration trajectories in glycerol(1)/acetone(2)/water(3) mixtures at 298 K for the equilibrium composition x_1= 0.1, x_2 = 0.432, x_3 = 0.468. The plot is in 2D composition space. (b) For the trajectory in (a), the transient approach to equilibrium of each component is plotted against the dimensionless coordinate $\frac{z}{\sqrt{4D_{ref}t}}$ where the value of the reference diffusivity $D_{ref} = 10^{-9}$ m^2 s^{-1}. The Fick diffusivity matrix for this simulation is indicated in Figure 47. (c) Equilibration trajectories plotted in 2D activity space. (d) Transient equilibration of glycerol, expressed in both mole fractions and activities.

Figure 49. (a) Equilibration trajectories in glycerol(1)/acetone(2)/water(3) mixtures at 298 K for the equilibrium composition x_1= 0.18, x_2 = 0.22, x_3 = 0.6. The plot is in 2D composition space. The Fick diffusivity matrix for this simulation is indicated in Figure 47. (b) Equilibration trajectories plotted in 2D activity space. (c) Transient equilibration of glycerol, expressed in both mole fractions and activities, plotted against the dimensionless coordinate $\frac{z}{\sqrt{4D_{ref}t}}$ where the value of the reference diffusivity $D_{ref} = 10^{-9}$ m^2 s^{-1}.

Figure 50. Transient inter-diffusion in water(1)/chloroform(2)/acetic-acid(3) mixtures. The compositions of the two mixtures in the left and right chambers are indicated; both initial compositions and the final equilibrated compositions are in the homogeneous single phase region, at a tangent to the binodal curve. The transient approach to equilibrium is plotted against the dimensionless coordinate $\frac{z}{\sqrt{4D_{ref}t}}$ where the value of the reference diffusivity $D_{ref} = 10^{-9}$ m^2 s^{-1}. The values of the Fick

diffusivity matrix is $\left[D\right]=\begin{bmatrix} 0.92 & 0.40 \\ 0.37 & 0.161 \end{bmatrix}\times 10^{-9}$ m^2 s^{-1}; $\left|D\right|=0$, corresponding to those determined by Vitagliano et al.[56] at the plait point.

Figure 51. Experimental data for the equilibration paths for glycerol(1)/acetone(2)/water(3) mixture measured in a stirred Lewis cell by Krishna et al.[60] The data for the acetone rich phase are shown by the green squares. The data for glycerol-rich phase are shown by red circles. The mixture composition indicated by M on the dashed line connecting the two initial compositions in the acetone-rich and glycerol-rich regions separates into two liquid phases with compositions at either end of the tie-line as indicated. The values of the Fick diffusivity matrices used in the simulations of the equilibration trajectories are also indicated.

Figure 52. Comparison of experimental data (red circles) for the equilibration paths in the glycerol-rich phase for the system glycerol(1)/acetone(2)/water(3) mixture with the model calculations shown by the continuous solid red lines.

Figure 53. Comparison of experimental data (green squares) for the equilibration paths in the acetone-rich phase for the system glycerol(1)/acetone(2)/water(3) mixture with the model calculations shown by the continuous solid green lines.

Figure 54. Equilibration trajectory followed in acetone(1)/ethylacetate(2)/water(3) mixtures at 293 K. Two mixtures of compositions (in mass tractions) ω_1=0.01, ω_2=0.01, ω_3=0.98, and ω_1=0.17, ω_2=0.1, ω_3=0.73 are allowed to equilibrate to yield the final equilibrated value ω_1=0.09, ω_2=0.055, ω_3=0.855. The values of the Fick diffusivity used in the calculations corresponds to the third point in the water-rich data set of Pertler[59]: $[D]=\begin{bmatrix} 0.179 & -0.287 \\ 0.316 & 0.764 \end{bmatrix}\times 10^{-9}$ m^2 s^{-1}. Also shown in the inset are the experimental data points obtained by Haeberl and Blass.[61]

Figure 55. Experimental data of Krishna et al.[60] on the equilibration paths for the system glycerol(1)/acetone(2)/water(3) mixture. The initial compositions in the two compartments lie on the tangent to the plait point (composition: x_{glycerol}= 0.1477, x_{acetone}= 0.4163, x_{water}= 0.4360) parallel to the tie lines.

Figure 56. Phase equilibrium diagram for the ternary mixture of trans-anethol/ethanol/water. The binodal curve data is from Sitnikova et al.[65] Also shown are the typical composition of Ouzo that is three component mixture of ethanol (≈45 vol%), water (55 vol%) and an essential oil called trans-anethol (≈ 0.1%).

Figure 57. Equlibration trajectories followed on addition of water to Ouzo.

Figure 58. Trajectories followed during equilibration of homogenous mixtures of different compositions for the system toluene(1)/ethanol(2)/water(3). The NRTL parameters for toluene(1)/ethanol(2)/water(3) are provided in Table 8. Please note that the compositions are plotted in mass fraction space.

Figure 59. Transient inter-diffusion in a diffusion couple consisting of water(1)/chloroform(2)/acetic-acid(3) mixtures. The values of the Fick diffusivity matrix is $[D]=\begin{bmatrix} 0.309 & 0.368 \\ 0.344 & 0.939 \end{bmatrix}\times 10^{-9} \quad \mathrm{m^2\ s^{-1}}$; $|D| = 0.164\times 10^{-18} \quad \mathrm{m^4\ s^{-2}}$, corresponding to the fifth data set of Vitagliano et al.[56]

Figure 60. The diffusion trajectories followed during equilibration of water(1)/chloroform(2)/acetic-acid(3) mixtures. Also shown by the dashed lines are the "fast" and "slow" eigenvectors. The values of the Fick diffusivity matrix is $[D]=\begin{bmatrix} 0.309 & 0.368 \\ 0.344 & 0.939 \end{bmatrix}\times 10^{-9} \quad \mathrm{m^2\ s^{-1}}$; $|D| = 0.164\times 10^{-18} \quad \mathrm{m^4\ s^{-2}}$, corresponding to the fifth data set of Vitagliano et al.[56]

Figure 61. Equilibration trajectory followed by a small perturbation in acetone(1)/water(2)/ ethylacetate(3) mixtures at 293 K. Two mixtures of compositions (in mass tractions) ω_1=0.17, ω_2=0.05, ω_3=0.78, and ω_1=0.23, ω_2=0.05, ω_3=0.72 are allowed to equilibrate to yield the final equilibrated value ω_1=0.2, ω_2=0.05, ω_3=0.75. The values of the Fick diffusivity used in the calculations corresponds to the sixth point in the ethylacetate-rich data set of Pertler[59]:

$[D]=\begin{bmatrix} 1.371 & 0.298 \\ -17.47 & 6.016 \end{bmatrix}\times 10^{-9}$ m^2 s^{-1}. The transient approach to equilibrium is plotted against the dimensionless coordinate $\frac{z}{\sqrt{4D_{ref}t}}$ where the value of the reference diffusivity $D_{ref}=10^{-9}$ m^2 s^{-1}.

Figure 62. Equilibration trajectories in water(1)/2-propanol(2)/cyclohexane(3) for the equilibrium composition x_1= 0.36, x_2 = 0.4, x_3 = 0.24, that lies just above the plait point for the critical temperature T_c = 303.67 K, i.e. x_1 = 0.367, x_2= 0.389, x_3= 0.244. The equilibration trajectories are calculated at four different temperatures, 303.75 K, 304.15 K, 304.65 K, 396.65 K. The diffusivity values used in these simulations correspond to the experimental data of Clark and Rowley.[58] The measured values of the Fick matrix [D], in units of 10^{-10} m^2 s^{-1}, are also indicated; the corresponding values of the determinant $|D|$ has the units of 10^{-18} m^4 s^{-2}.

Figure 63. Trajectory followed during equilibration of homogenous mixtures of two different compositions for the system water(1)/acetone(2)/toluene(3) with the equilibrium composition $x_{1,eq}$= 0.2, $x_{2,eq}$ = 0.51, $x_{3,eq}$ = 0.1. The UNIQUAC parameters for calculation of the phase equilibrium thermodynamics are provided in Table 9.

Figure 64. Trajectories followed during equilibration of homogenous mixtures of two different compositions for the system toluene(1)/ethanol(2)/water(3) with the equilibrium composition $x_{1,eq}$ = 0.012, $x_{2,eq}$ = 0.208 and $x_{3,eq}$ = 0.78.The NRTL parameters for toluene(1)/ethanol(2)/water(3) are provided in Table 8.

Figure 65. Trajectory followed during equilibration of homogenous mixtures of two different compositions for the system water(1)/caprolactam(2)/toluene(3) for the equilibrium composition $x_{1,\mathrm{eq}}$ = 0.64, $x_{2,\mathrm{eq}}$ = 0.2725 and $x_{3,\mathrm{eq}}$ = 0.0875. The UNIQUAC parameters for calculation of the phase equilibrium thermodynamics are provided in Table 10.

Figure 66. Trajectory followed during equilibration of homogenous mixtures of two different compositions for the system water(1)/caprolactam(2)/benzene (3) for the equilibrium composition x_1= 0.125, x_2 = 0.165, x_3 = 0.71. The UNIQUAC parameters for calculation of the phase equilibrium thermodynamics are provided in Table 11.

Figure 67. Trajectory followed during equilibration of homogenous mixtures of two different compositions for the system for toluene(1)/propionic-acid (2)/water(3) for the equilibrium composition $x_{1,\mathrm{eq}}$ = 0.475, $x_{2,\mathrm{eq}}$ = 0.4 and $x_{3,\mathrm{eq}}$ = 0.285. The UNIQUAC parameters for calculation of the phase equilibrium thermodynamics are provided in Table 12.

Figure 68. Trajectory followed during equilibration of homogenous mixtures of two different compositions for the system for ethylacetate(1)/propionic-acid(2)/water(3) for the equilibrium composition $x_{1,\mathrm{eq}}$ = 0.675, $x_{2,\mathrm{eq}}$ = 0.13 and $x_{3,\mathrm{eq}}$ = 0.195. The UNIQUAC parameters for calculation of the phase equilibrium thermodynamics are provided in Table 13.

Figure 69. Diffusion trajectories during the immersion precipitation process for membrane preparation; adapted from the papers of van den Berg and Smolders,[71] and Reuvers and Smolders.[72] A 10% solution of Cellulose Acetate (CA) in acetone is immersed in a bath of pure water. The transient equilibration trajectories at three different times, t =10 s, t = 25 s, and t = 50 s are depicted.

Figure 70. (a) Effective diffusivity of water and acetone in maltodextrin, and coffee extract solutions as a function of wt% water content. (b) Ratio of diffusivities of acetone and water in aqueous maltodextrin, and coffee extract solutions as function of wt % water content. The graphs are re-drawn using data from Coumans et al.[76]

Figure 71. Experimental data of Darken[17] for inter-diffusion between the left and right austenite bars consisting of C/Si/Fe mixtures. The wt% of each component is measured on either side of the Matano plane, measured at t = 13 days after the start of the experiment are shown. The calculations of the coupled diffusion model are based on the Fick diffusivity matrix determined by Kirkaldy for this experiment.[78]

Figure 72. Transient equilibration of a diffusion couple consisting of Cu(1)/Ag(2)/Au(3) mixtures. The atom fractions at equilibrium are x_1= 0.475, x_2 = 0.175, x_3 = 0.35. The trajectories are calculated with the values of the Fick diffusivity matrix $\left[D\right]=\begin{bmatrix} 2.3 & 1.11 \\ 1.8 & 3.1 \end{bmatrix}\times 10^{-14}\ \text{m}^2\ \text{s}^{-1}$. The transient approach to equilibrium is plotted against the dimensionless coordinate $\frac{z}{\sqrt{4D_{ref}t}}$ where the value of the reference diffusivity $D_{ref} = 10^{-14}\ \text{m}^2\ \text{s}^{-1}$.

Figure 73. (a) Experimental data of Varshneya and Cooper[79] for inter-diffusion between the left and right slabs consisting of $K_2O/SrO/SiO_2$ mixtures. The wt% of each component is measured on either side of the Matano plane, measured at t = 4.55 h after the start of the experiment are shown. (b) Trajectories in 3D composition space.

Figure 74. Experimental data of Vielzeuf and Saúl[80] for inter-diffusion in a diffusion couple consisting of Fe/Mg/Ca mixtures. The atom % of each component is measured on either side of the Matano plane, measured at t = 100 h after the start of the experiment are shown.

Figure 75. (a) Experimental data of Vielzeuf and Saúl[80] for inter-diffusion between the left and right slabs containing Fe/Mg/Ca mixtures. The atom % of each component is measured on either side of the Matano plane, measured at t = 100 h after the start of the experiment are shown as function of the distance. (b) Equilibration trajectories in composition space. The dashed line represents the trajectory predicted by uncoupled Fickian formulation.

Figure 76. Schematic showing vapor/liquid contacting on a distillation tray.

Figure 77. (a) Schematic of a laboratory-scale distillation column used in the experiments of Springer et al.[84, 86] which includes a total condenser (1), a partial reboiler (12), 10 bubble-cap trays (2-11), and 13 draw-off faucets, 9 for vapor samples and 4 for liquid samples. (b) Ethanol driving force $\left(y_2^* - y_E\right)$ on

each stage for the system water(1)/ethanol(2)/acetone(3). (c) Murphree component efficiencies for the system water(1)/ethanol(2)/acetone(3).

Figure 78. (a) Residue curve map for the water(1)/ethanol(2)/acetone(3) system, showing a straight-line distillation boundary and a binary minimum-boiling azeotrope between water and ethanol (large green circle). The pure component boiling points are indicated in green letters: water = 373.2 K; ethanol = 351.6 K; acetone = 329.7 K; water/ethanol azeotrope = 351.4 K. (b, c) Experimental data for (b) Run T2-6, and (c) T2-26 of Springer et al.[86] (blue circles) showing the column composition trajectories for the water(1)/ethanol(2)/acetone(3) system in the column operating at total reflux implying $x_i = y_i$. Also shown in (b, c) are the simulation results showing the trajectories calculated by the Equilibrium (EQ) stage model (continuous green line, $E_{1,MV} = E_{2,MV} = E_{3,MV} = 1$) and the Non-Equillibrium (NEQ) stage model (continuous red line, properly accounting for the resistances to transfer in both vapor and liquid phases, resulting in $E_{1,MV} \neq E_{2,MV} \neq E_{3,MV}$). The solid black line is the distillation boundary.

Figure 79. Experimental data of Springer et al.[85] (red circles) for composition trajectories for distillation of water(1)/acetone(2)/toluene(3) mixtures. The grey shaded areas represent the region in which liquid–liquid phase splitting occurs. The pure component boiling points are indicated in green letters: water = 373.2 K; toluene = 384 K; acetone = 329.7 K; water/toluene azeotrope = 358 K.

Figure 80. Diffusion in mixed ion systems. Experimental data of Vinograd and McBain[93] for ionic diffusivities of H^+, Ba^{++}, and Cl^- in a two-compartment diffusion cell. The continuous solid lines are the

calculations using the Nernst-Planck equation; for further computational details see Example 2.4.2 of Taylor and Krishna.[11]

Figure 81. External mass transfer limited transfer rates to and from ion-exchange particles are direction dependent. Experimental data of Kraaijeveld and Wesselingh.[94]

Figure 82. Experimental data of Yang and Pintauro[95] for the transient concentrations of H^+, Na^+, and Cs^+ in the salt and acid compartments that are separated by a Nafion cation exchange membrane.

Figure 83. Water transport across polyamide-based Reverse Osmosis (RO) membrane. Adapted from Wesselingh and Krishna.[25]

Figure 84. Examples of one-dimensional (1D) channel structures: AFI, MgMOF-74, and MIL-53(Cr)-lp, BTP-COF, and $Fe_2(BDP)_3$.

Figure 85. Examples of 1D channel structures with side pockets: MOR and FER.

Figure 86. Examples of structures consisting of intersecting channels: MFI, and Zn(bdc)dabco.

Figure 87. Structures consisting of cages separated by narrow windows: LTA, CHA, DDR, and ZIF-8.

Figure 88. “Open” structures that consist of cages separated by large windows: IRMOF-1, CuBTC, and FAU.

Figure 89. PSA process for production of purified N_2 by separation of $O_2(1)/N_2(2)$ mixture in a fixed bed adsorber packed with LTA-4A operating at a total pressure of 200 kPa and 298 K. The simulation details are available in the Supplementary Material accompanying the article by Krishna.[104]

Figure 90. Schematic of membrane permeation device. Typically, the micro-porous crystalline layer has a thickness of 25 – 50 μm.

Figure 91. (a) Thermodynamic factor Γ_i, for single-site Langmuir isotherm, plotted as a function of the fractional occupancy. (b) Inverse thermodynamic factor $1/\Gamma_i$, plotted as a function of the fractional occupancy.

Figure 92. Transient adsorption and desorption profiles for C_2H_6 in LTA-4A zeolite at 298 K. Experimental data of Garg and Ruthven.[123]

Figure 93. Experimental data of Niessen and Karge[124] for transient adsorption/desorption of *p*-xylene in MFI zeolite (H-ZSM-5) at 375 K.

Figure 94 Configurational-Bias Monte Carlo (CBMC) simulations[117] of (a) Unary adsorption isotherms, and (b) Inverse thermodynamic factors for adsorption of methanol, and ethanol in ZIF-8. (c, d) Experimental data of Chmelik et al.[130] for the unary Fick and M-S diffusivities of methanol, and ethanol in ZIF-8.

Figure 95. Experimental data of Habgood[135] on transient uptake of $N_2(1)/CH_4(2)$ mixture within LTA-4A crystals, exposed to binary gas mixtures at 194 K and partial pressures p_1 =50.9 kPa; p_2 = 49.1 kPa.

Figure 96. (a) Elements of the matrix of thermodynamic factors Γ_{ij} for $N_2(1)/CH_4(2)$ mixture adsorption in LTA-4A crystals, exposed to equimolar binary gas mixtures. The data is plotted as a function of the total mixture loading, q_t. (b) Elements of the matrix of thermodynamic factors Γ_{ij} calculated from the transient uptake simulations. The data is plotted as a function of $t^{1/2}$. (c) Calculations of $\Gamma_{11}q_1 + \Gamma_{12}q_2$, and $\Gamma_{21}q_1 + \Gamma_{22}q_2$ as a function of $t^{1/2}$. For the calculations on (a), (b), and (c), we use the mixed-gas Langmuir model. The pure component isotherms were fitted to the experimental data using the single-site Langmuir parameters: N_2: $q_{1,sat}$ = 3.6 mol kg^{-1}; b_1 = 9.4×10^{-5} Pa^{-1}; CH_4: $q_{2,sat}$ = 3.6 mol kg^{-1}; b_1 = 2.08×10^{-4} Pa^{-1}.

Figure 97. Comparison of the Maxwell-Stefan model calculations with the experimental data of Habgood[135] on transient uptake of $N_2(1)/CH_4(2)$ mixture within LTA-4A crystals, exposed to binary gas mixtures at 194 K and partial pressures p_1 =50.9 kPa; p_2 = 49.1 kPa. Maxwell-Stefan diffusivities: $Đ_1/r_c^2$ = 1.56×10^{-5} s^{-1}; $Đ_2/r_c^2$ = 7.2×10^{-9} s^{-1}. The continuous solid lines are the calculations using Equation (136). The dashed lines are the calculations using uncoupled flux equation (139).

Figure 98. (a) Simulations of the transient desorption process for $N_2(1)/CH_4(2)$ mixture in LTA-4A crystals, exposed to binary gas mixtures at 194 K. The initial crystal is brought to equilibrium by exposure to gas phase partial pressures p_1 =50.9 kPa; p_2 = 49.1 kPa. At time t = 0, the bulk gas is exposed to conditions such that $p_1 = p_2 = 0$. (b) Comparison of the composition trajectories for the adsorption (green line) and desorption cycles (red line) for transient adsorption/desorption of $N_2(1)/CH_4(2)$ mixture within LTA-4A crystals, exposed to binary gas mixtures at 194 K. Both sets of simulations include thermodynamic coupling effects.

Figure 99. PSA process for separation of 10/90 $N_2(1)/CH_4(2)$ mixture in a fixed bed adsorber packed with LTA-4A operating at a total pressure of 100 kPa and 194 K.

Figure 100. (a, b) Experimental data of Majumdar et al.[134] for transient uptake of (a) 10/90, and (b) 50/50 mixtures of $N_2(1)/CH_4(2)$ mixtures in Ba-ETS-4 at 283 K and total pressure of 0.7 MPa. Note that the y-axes represent the fractional uptake of each component; this is obtained by dividing each of the

component loadings by the final equilibrated loading within the crystal. The experimentally observed overshoots for N_2 result from thermodynamic coupling effects.

Figure 101. Transient uptake of $O_2(1)/N_2(2)$ mixture in LTA-4A crystals exposed to a total pressure of 200 kPa and 298 K. The transient uptake simulations use Equation (136) taking $Đ_{O2}/r_c^2 = 2\times10^{-3}$ s^{-1}; $Đ_{O2}/Đ_{N2} = 100$. The single-site Langmuir parameters for pure component isotherms are: O_2: $q_{1,\mathrm{sat}} = 1.91$ mol kg^{-1}; $b_1 = 5.65\times10^{-7}$ Pa^{-1}; N_2: $q_{2,\mathrm{sat}} = 1.91$ mol kg^{-1}; $b_2 = 1.13\times10^{-6}$ Pa^{-1}. The ratio $b_2/b_1 = 2$. Further simulation details are available in the Supplementary Material accompanying the article by Krishna.[104]

Figure 102. (a) The experimental data of Chen et al.[138] for transient uptake of $O_2(1)/N_2(2)$ mixture in carbon molecular sieve (CMS) at 300 K exposed to binary gas mixtures at partial pressures $p_1 = 109.6$ kPa; $p_2 = 432.56$ kPa. The continuous solid lines are transient uptake simulations use Equation (136) taking $Đ_{O2}/r_c^2 = 3.5\times10^{-4}$ s^{-1}; $Đ_{N2}/r_c^2 = 9.5\times10^{-6}$ s^{-1}; $Đ_{O2}/Đ_{N2} = 36.8$. The single-site Langmuir parameters for pure component isotherms are: O_2: $q_{1,\mathrm{sat}} = 1.9$ mol kg^{-1}; $b_1 = 1.45\times10^{-6}$ Pa^{-1}; N_2: $q_{2,\mathrm{sat}} = 1.4$ mol kg^{-1}; $b_2 = 1.5\times10^{-6}$ Pa^{-1}. (b) Comparison of the adsorption/desorption cycles in composition space.

Figure 103. Experimental data of Carlson and Dranoff[139] on the fractional approach to equilibrium during the co-adsorption of methane and ethane in LTA-4A zeolite. The experimentally observed overshoot for methane result from thermodynamic coupling effects.

Figure 104. Simulations of transient uptake of $C_3H_6(1)/C_3H_8(2)$ within crystals of ZIF-8. The simulations for ZIF-8 are at 303 K using the isotherm parameters specified in Table **14**, along with $Đ_1/r_c^2$ = 1.5×10^{-2} s^{-1}; $Đ_1/Đ_2$ = 125; ratio of single-site Langmuir parameter b_2/b_1 = 1.07. The continuous solid lines are the calculations using Equation (136). The dashed lines are the calculations using uncoupled flux equation (139).

Figure 105. Simulations of transient uptake of $C_3H_6(1)/C_3H_8(2)$ within crystals of CHA. The simulations for CHA are at 353 K and based on the data provided by Khalighi et al.[141]: $Đ_1/r_c^2$ = 1.73×10^{-4} s^{-1}; $Đ_1/Đ_2$ = 5000; ratio of single-site Langmuir parameter b_2/b_1 = 2.67. The continuous solid lines are the calculations using Equation (136). The dashed lines are the calculations using uncoupled flux equation (139).

Figure 106. Experimental data of Saint-Remi et al.[142] for transient uptake of (a) ethanol/1-propanol, and (b) methanol/1-propanol mixtures within SAPO-34, that is the structural analog of CHA zeolite. The experimentally observed overshoot for ethanol, and methanol result from thermodynamic coupling effects; this has been shown in the simulation results presented in the Supplementary Material accompanying the article by Krishna.[104]

Figure 107. Radial profiles of the loadings of ethanol and 1-propanol within CHA crystal, for ethanol/1-propanol mixture uptake, monitored at times $t = 10^2$ s, $t = 10^3$ s, $t = 1\times10^4$ s, and $t = 5\times10^4$ s.

Figure 108. Separation of ethanol/1-propanol mixtures in a fixed bed adsorber packed with SAPO-34. (a) experimental uptake data reported by Saint-Remi et al.[142] within the crystals of SAPO-34. (b) Experimental data of Remy et al.[143] for transient breakthroughs.

Figure 109. (a, b) Transient (a) adsorption, and (b) desorption for ethanol(1)/1-propanol(2) mixture in CHA at 300 K. In (b) initially the crystal is equilibrated by exposing to an equimolar gas phase mixture with partial fugacities of 1 MPa; at time *t* = 0, the bulk gas phase is maintained with partial fugacities of 1 kPa. In (a) the reverse scenario holds. (c) Comparison of the adsorption/desorption composition trajectories. The mixture thermodynamics equilibrium is determined using the IAST.

Figure 110. Experimental data of Kärger and Bülow[145] for transient uptake of n-heptane(1)/benzene(2) mixture in NaX zeolite at 359 K. The experimentally observed overshoot for n-heptane result from thermodynamic coupling effects. Also shown in the portrait or Professor Jörg Kärger who carried out several pioneering experimental studies on diffusion that has paved the way to a better understanding of the motion of molecules within nanoporous materials.

Figure 111. Experimental data of Niessen and Karge[124, 148] for uptake of benzene(1)/ethylbenzene(2) mixture in MFI zeolite (H-ZSM-5). The experimentally observed overshoots for benzene result from thermodynamic coupling effects; this has been shown in the simulation results presented in the Supplementary Material accompanying the article by Krishna.[104]

Figure 112. Experimental data of Niessen and Karge[124, 148] for uptake of benzene(1)/*p*-xylene(2) mixture in MFI zeolite (H-ZSM-5). The experimentally observed overshoots for benzene result from thermodynamic coupling effects.

Figure 113. (a) Comparison of the Maxwell-Stefan model simulation results using Equation (136) with IRM experimental data of Titze et al.[149] for transient uptake of nC6(1)/2MP(2) mixtures in MFI zeolite at 298 K. (b) Calculations of $(\Gamma_{12}\ \Theta_2/\Gamma_{11}\ \Theta_1)$ as a function of the total loading Θ_t. (c) Maxwell-Stefan model simulations using equation (139) in which the matrix of thermodynamic correction factors is assumed to be the identity matrix. The mixture thermodynamics equilibrium is determined using the IAST. Input data simulation of Run 1: $Đ_1/r_c^2 = 0.016\ \mathrm{s}^{-1}$; $Đ_2/r_c^2 = 1.6\times10^{-4}\ \mathrm{s}^{-1}$; $t = 0$; $p_1(r_c,0) = p_2(r_c,0) = 0$ Pa; $t \geq 0$; $p_1(r_c,t) = p_2(r_c,t) = 1.3$ Pa. Further details are provided by Titze et al.[149]

Figure 114. Radial profiles of the loadings of nC6 and 2MP within MFI crystal, for conditions corresponding to Run 1 as specified in the legend to Figure 113, monitored at times: $t = 5$ s, $t = 10.2$ s, $t = 50.6$ s, and $t = 832$ s.

Figure 115. Comparison of adsorption and desorption cycles for transient uptake of nC6(1)/2MP(2) mixtures in MFI zeolite at 298 K. In the adsorption phase: initial partial pressures $p_1 = p_2 = 0$ Pa; final partial pressures $p_1 = p_2 = 1.3$ Pa. In the desorption cycle: initial partial pressures $p_1 = p_2 = 1.3$ Pa; final

partial pressures $p_1 = p_2 = 0$ Pa. The diffusivity inputs are as indicated in the legend to Figure 113. The continuous solid lines using Equation (136) that include thermodynamic coupling effects as described by Titze et al.[149] The dashed lines are simulations using uncoupled flux equation (139).

Figure 116. Transient adsorption/desorption kinetics for nC6/2MP mixture in MFI zeolite at 298 K. In the desorption cycle: initial partial pressures $p_1 = p_2 = 2$ Pa; final partial pressures: $p_1 = p_2 = 0.2$ Pa. In the adsorption cycle: initial partial pressures $p_1 = p_2 = 0.2$ Pa; final partial pressures: $p_1 = p_2 = 2$ Pa. The mixture thermodynamics equilibrium is determined using the RAST; further details are provided by Titze et al.[149] The diffusivity inputs are as indicated in the legend to Figure 113. The continuous solid lines using Equation (136) that include thermodynamic coupling effects as described by Titze et al.[149] The dashed lines are simulations using uncoupled flux equation (139).

Figure 117. Transient uptake of nC4/iC4 mixture in MFI at 298 K using the Maxwell-Stefan model. In the adsorption phase: initial partial pressures $p_1 = p_2 = 0$ Pa; final partial pressures $p_1 = p_2 = 100$ Pa. In the desorption cycle: initial partial pressures $p_1 = p_2 = 100$ Pa; final partial pressures $p_1 = p_2 = 0$ Pa. Input data: $Đ_1/r_c^2 = 0.08$ s^{-1}; $Đ_2/r_c^2 = 4\times10^{-3}$ s^{-1}. The mixture thermodynamics equilibrium is determined using the RAST; the Wilson parameters are tabulated in the Supporting Information accompanying the paper by Titze et al.[149] The continuous solid lines using Equation (136) that include thermodynamic coupling effects, as described by Titze et al.[149] The dashed lines are simulations using uncoupled flux equation (139).

Figure 118. (a) Experimental data of Niessen and Karge[124] for transient adsorption/desorption of benzene(1)/*p*-xylene(2) mixtures in MFI zeolite (H-ZSM-5) at 395 K. The experiments are initialized by exposure to pure benzene at a pressure of 115 Pa; the partial pressure of benzene in the gas phase is held constant at 115 Pa through the experiment. At time $t = 0$, the partial pressure of p-xylene is increased to 115 Pa. At time $t = 400$ s, the partial pressure of p-xylene is decreased to 0 Pa. (b) Comparison of the adsorption and desorption trajectories in composition space.

Figure 119. Transient counter-current uptake of nC6(1)/2MP(2) mixtures in MFI zeolite. Two scenarios are simulated: (i) initial partial pressures $p_1 = 1.3$ Pa, $p_2 = 0$ Pa; final partial pressures $p_1 = 0$ Pa, $p_2 = 1.3$ Pa; (ii) initial partial pressures $p_1 = 0$ Pa, $p_2 = 1.3$ Pa; final partial pressures $p_1 = 1.3$ Pa, $p_2 = 0$ Pa. The diffusivity inputs are as indicated in the legend to Figure 113. The continuous solid lines using Equation (136) that include thermodynamic coupling effects as described by Titze et al.[149] The dashed lines are simulations using uncoupled flux equation (139).

Figure 120. Transient uptake inside MFI crystal exposed to a gas phase 5-component nC6/2MP/3MP/22DMB/23DMB mixture at a total pressure of 100 kPa and 433 K. The partial pressures of the components in the bulk gas phase at the inlet are $p_1 = p_2 = p_3 = p_4 = p_5 = 20$ kPa. Diffusional effects are quantified with $Đ_{nC6}/r_c^2 = 0.002$ s^{-1}; $Đ_{nC6}/Đ_{2MP} = 5$; $Đ_{nC6}/Đ_{3MP} = 5$; $Đ_{nC6}/Đ_{22DMB} = 25$; $Đ_{nC6}/Đ_{23DMB} = 25$. (a) These uptake simulations include thermodynamic coupling using the flux relations Equation (136). (b) These uptake simulations ignore thermodynamic coupling and use uncoupled flux equation (139).

Figure 121. Transient uptake inside MFI crystal exposed to a gas phase 4-component $CH_4/C_2H_6/C_3H_8/nC_4H_{10}$ mixture at a total pressure of 100 kPa and 300 K. The partial pressures of the components in the bulk gas phase at the inlet are p_1 = 85 kPa; p_2 = 11 kPa; p_3 = 3.5 kPa; p_4 = 0.5 kPa. Diffusional effects are quantified with $Đ_{CH4}/r_c^2 = 8\times10^{-5}\ \mathrm{s}^{-1}$; $Đ_{C2H6}/r_c^2 = 1.8\times10^{-5}\ \mathrm{s}^{-1}$; $Đ_{C3H8}/r_c^2 = 6\times10^{-6}\ \mathrm{s}^{-1}$; $Đ_{nC4H10}/r_c^2 = 3.2\times10^{-6}\ \mathrm{s}^{-1}$. (a) These uptake simulations include thermodynamic coupling using the flux relations Equation (136). (b) These uptake simulations ignore thermodynamic coupling and use uncoupled flux equation (139).

Figure 122. Simulation of transient permeation of propene(1)/propane(2) mixture across ZIF-8 membrane at 303 K. The diffusivity data used are from Li et al.:[140] $\rho Đ_1/\delta = 1.39\times10^{-3}$ kg m^{-2} s^{-1}, $\rho Đ_2/\delta = 1.11\times10^{-5}$ kg m^{-2} s^{-1}; $Đ_1/Đ_2$ = 125; ratio of single-site Langmuir parameter b_2/b_1 = 1.07; membrane thickness δ = 5 μm; partial pressures in upstream membrane compartment, $p_1 = p_2$ = 50 kPa. The downstream compartment is placed under vacuum. (a) These membrane permeation simulations include thermodynamic coupling using the flux relations Equation (136). (b) These permeation simulations ignore thermodynamic coupling and use uncoupled flux equation (139). Further simulation details are available in the Supplementary Material accompanying the article by Krishna.[104]

Figure 123. Experimental data of Geus et al.[152] for transient permeation $CH_4/n\text{-}C_4H_{10}$ mixture across MFI membrane. The experimentally observed overshoot for methane flux result from thermodynamic coupling effects

Figure 124. Transient permeation of linear alkanes across MFI membrane. The upstream compartment consists of a gas phase 4-component $CH_4/C_2H_6/C_3H_8/nC_4H_{10}$ mixture at a total pressure of 100 kPa and

300 K. The partial pressures of the components in the bulk gas phase at the inlet are p_1 = 25 kPa; p_2 = 25 kPa; p_3 = 25 kPa; p_4 = 25 kPa. Diffusional effects are quantified with $Đ_{CH4}/\delta^2 = 8\times10^{-1}$ s^{-1}; $Đ_{C2H6}/\delta^2 = 1.8\times10^{-1}$ s^{-1}; $Đ_{C3H8}/\delta^2 = 6\times10^{-2}$ s^{-1}; $Đ_{nC4H10}/\delta^2 = 3.2\times10^{-2}$ s^{-1}. The membrane thickness δ= 5μm. (a) These membrane permeation simulations include thermodynamic coupling using the flux relations Equation (136). (b) These permeation simulations ignore thermodynamic coupling and use uncoupled flux equation (139).

Figure 125. Experimental data of Bakker[153] for transient permeation H_2/n-C_4H_{10} mixture across MFI membrane. The theoretical analysis of this transient mixture permeation behavior is provided by Krishna and Baur.[107] The simulations with the M-S model also correctly predicts the overshoot in the flux of H_2.

Figure 126. (a, b) Experimental data of Matsufuji et al.[154] for transient permeation of (a) nC6(1)/2MP(2), and (b) nC6(1)/23DMB(3) mixtures across MFI membrane. The experimentally observed overshoots for nC6 fluxes result from thermodynamic coupling effects; this has been shown in the simulation results presented in the Supplementary Material accompanying the article by Krishna.[104]

Figure 127. (a, b) Experimental data of Matsufuji et al.[155] for transient permeation of (a) 50/50 m-xylene/p-xylene, and (b) 24/51/25 *p*-xylene/*m*-xylene/*o*-xylene mixtures across MFI membrane at 303 K. The experimentally observed overshoots for p-xylene fluxes result from thermodynamic coupling

effects; this has been shown in the simulation results presented in the Supplementary Material accompanying the article by Krishna.[104]

Figure 128. Transient simulations of benzene/*p*-xylene mixture permeation across MFI membranes at (a) 313 K, (b) 343 K, (c) 403 K. These simulations are based on isotherms and the *T*-dependent diffusivities in Figure 6 of Kolvenbach et al.[156]

ESI Fig. 1

Fick, Onsager, Maxwell-Stefan diffusivities

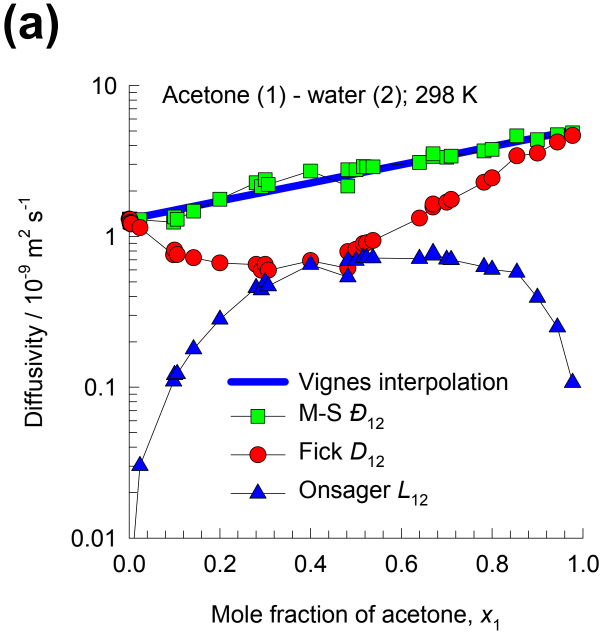

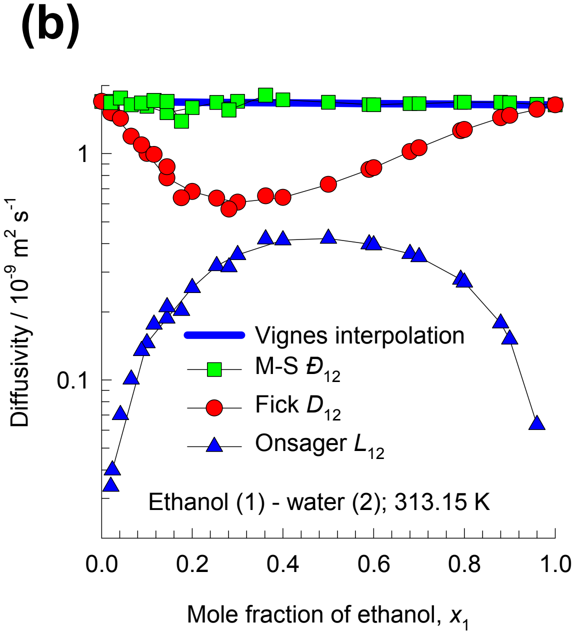

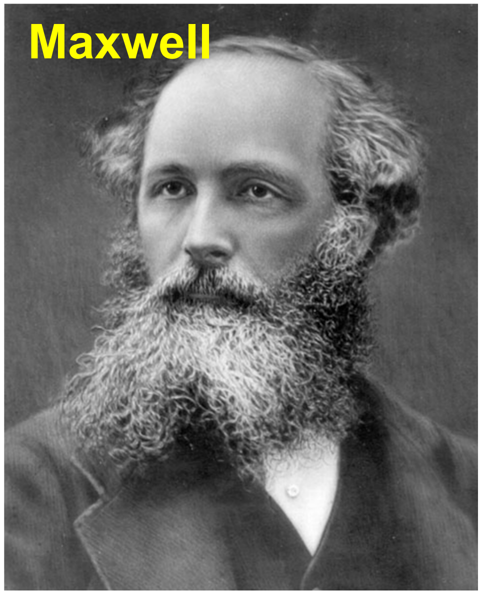

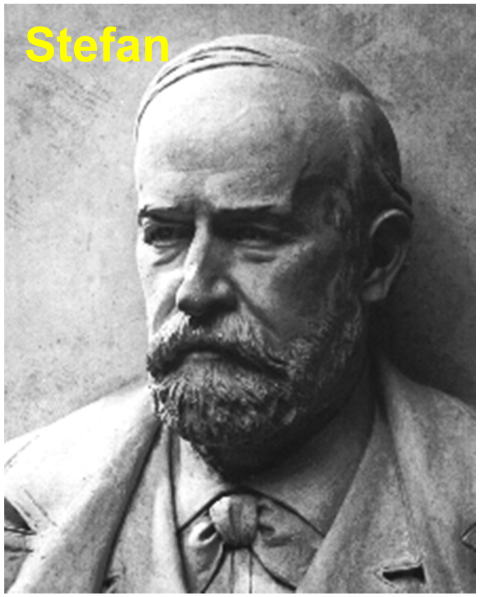

Fick matrix: Acetone/Benzene/CCl_4

ESI Fig. 2

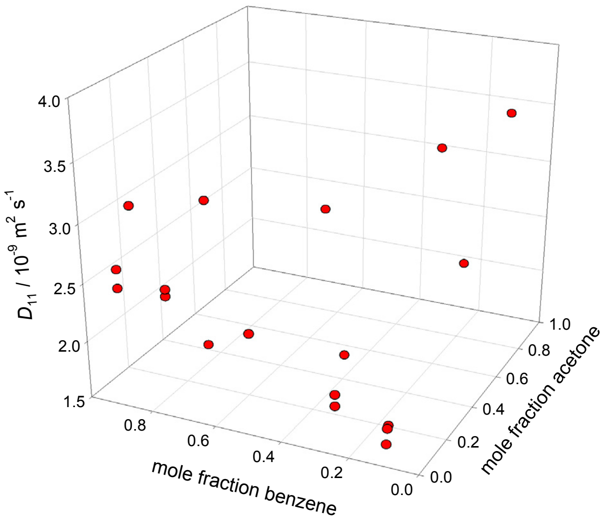

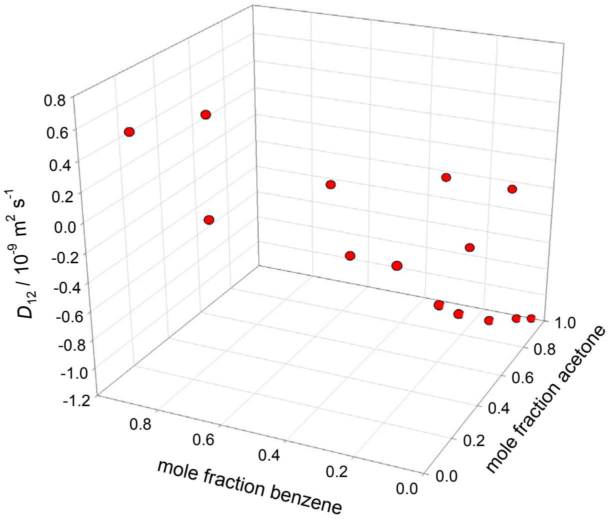

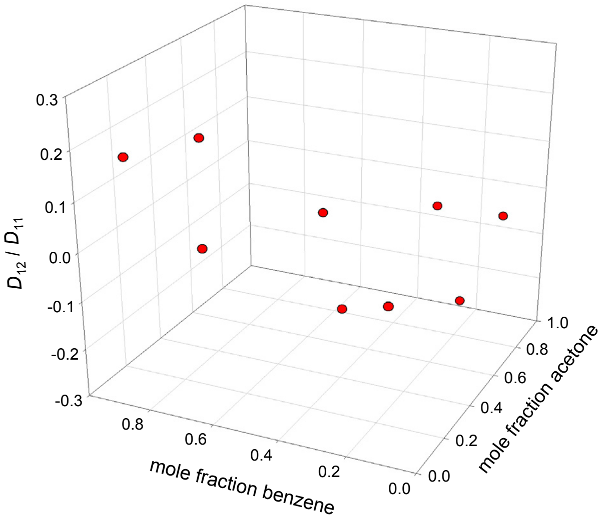

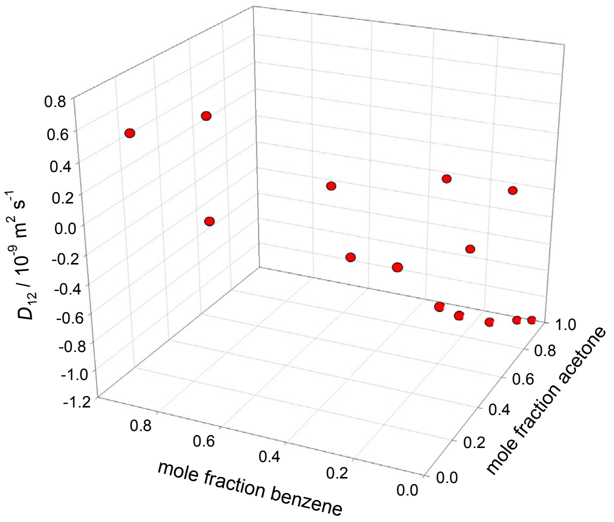

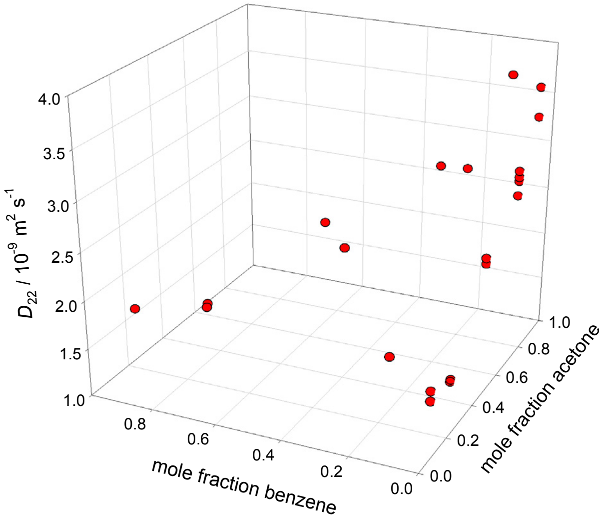

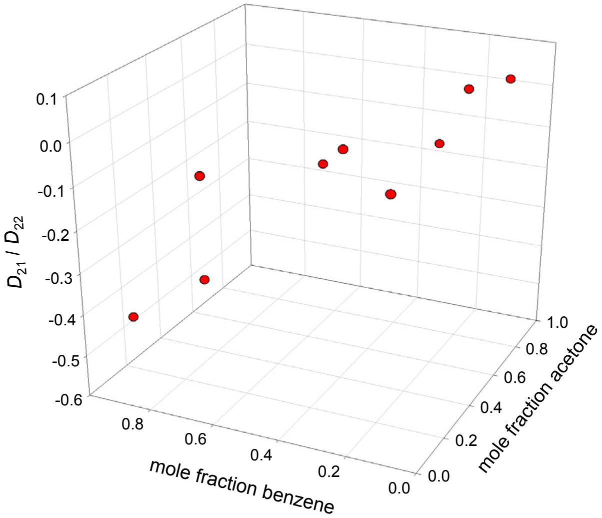

Acetone/Benzene/CCl_4

ESI Fig. 3

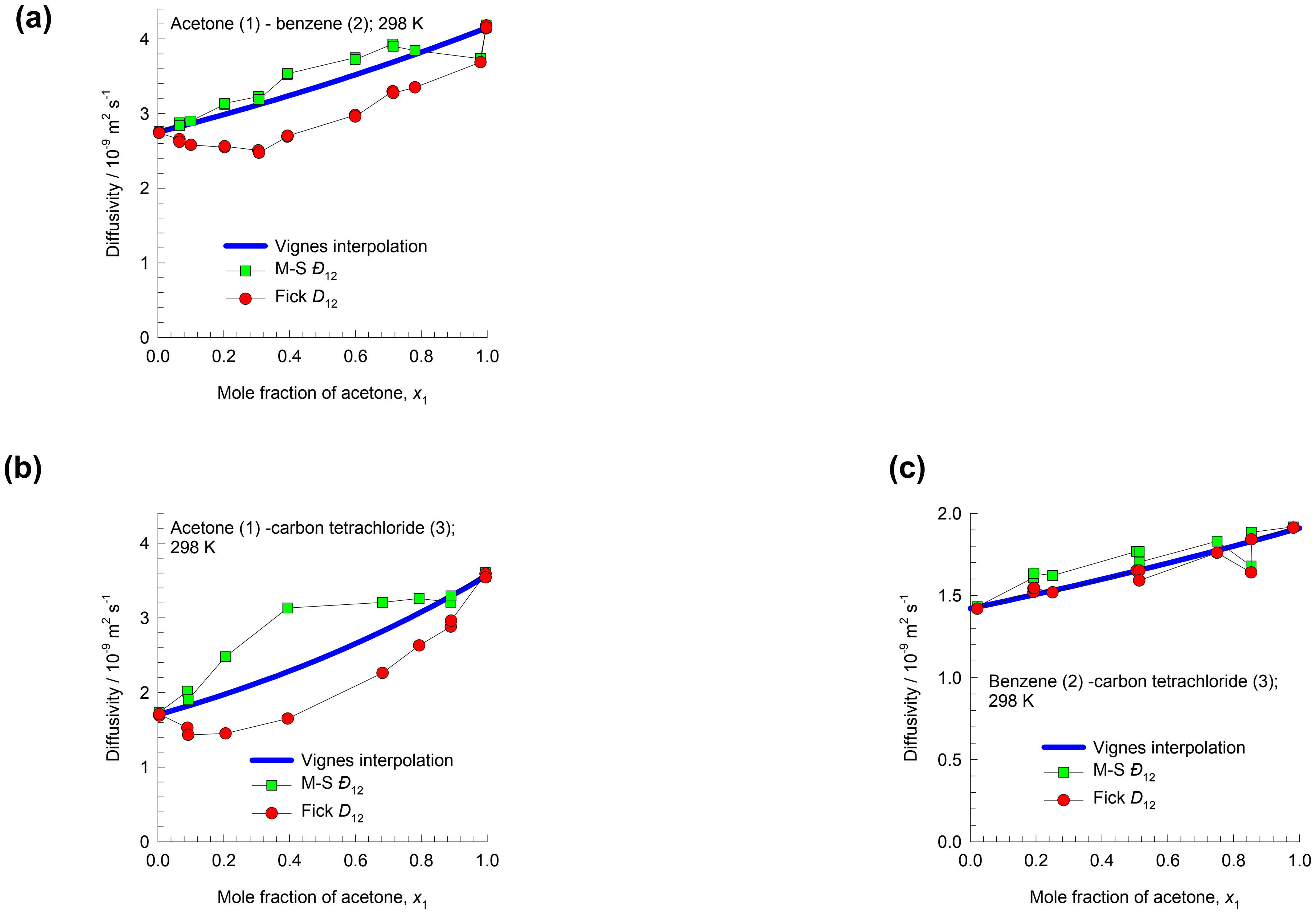

Fick matrix: Acetone/Benzene/CCl_4

ESI Fig. 4

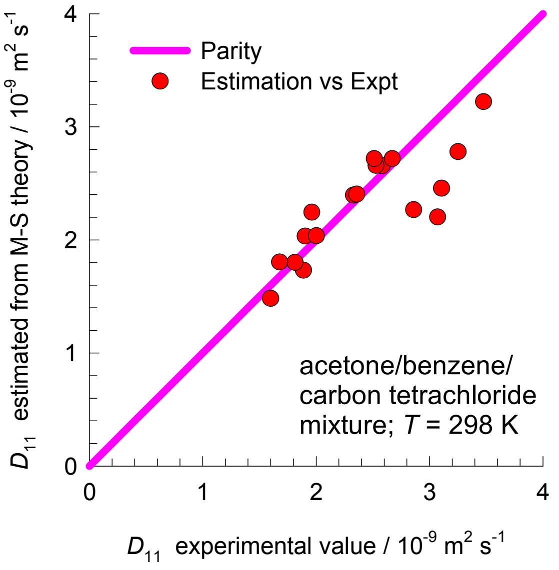

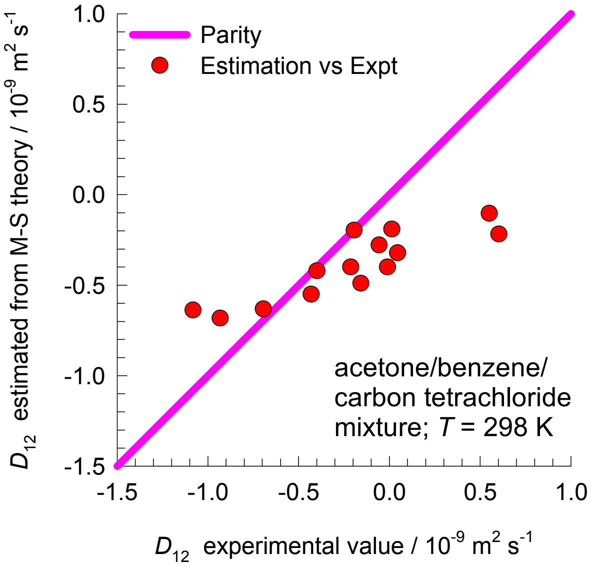

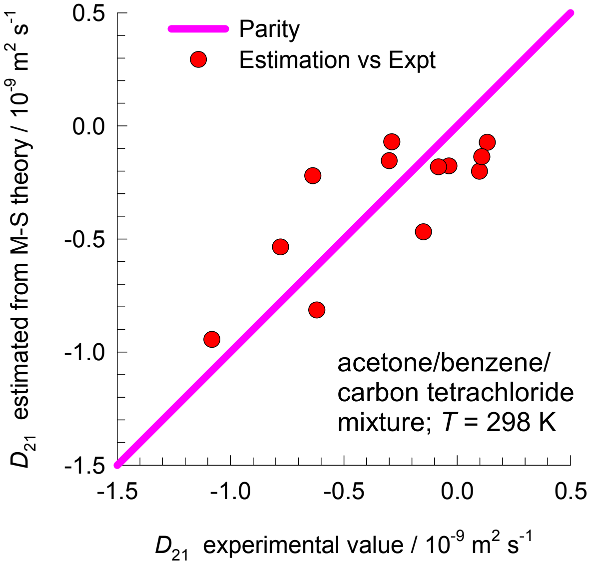

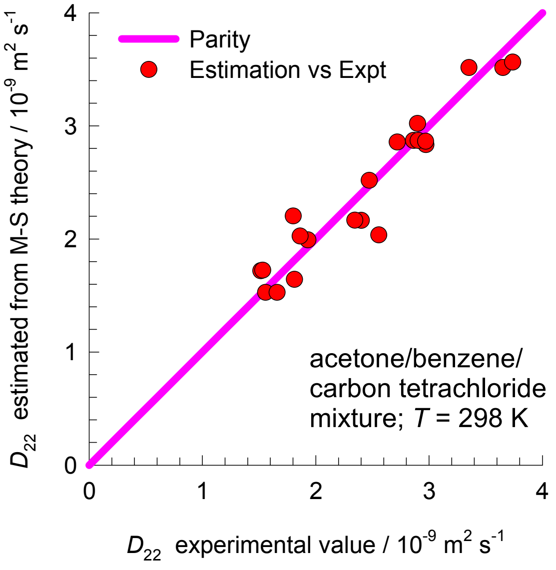

Ratio $|D|^{1/2} / |\Gamma|^{1/2}$

ESI Fig. 5

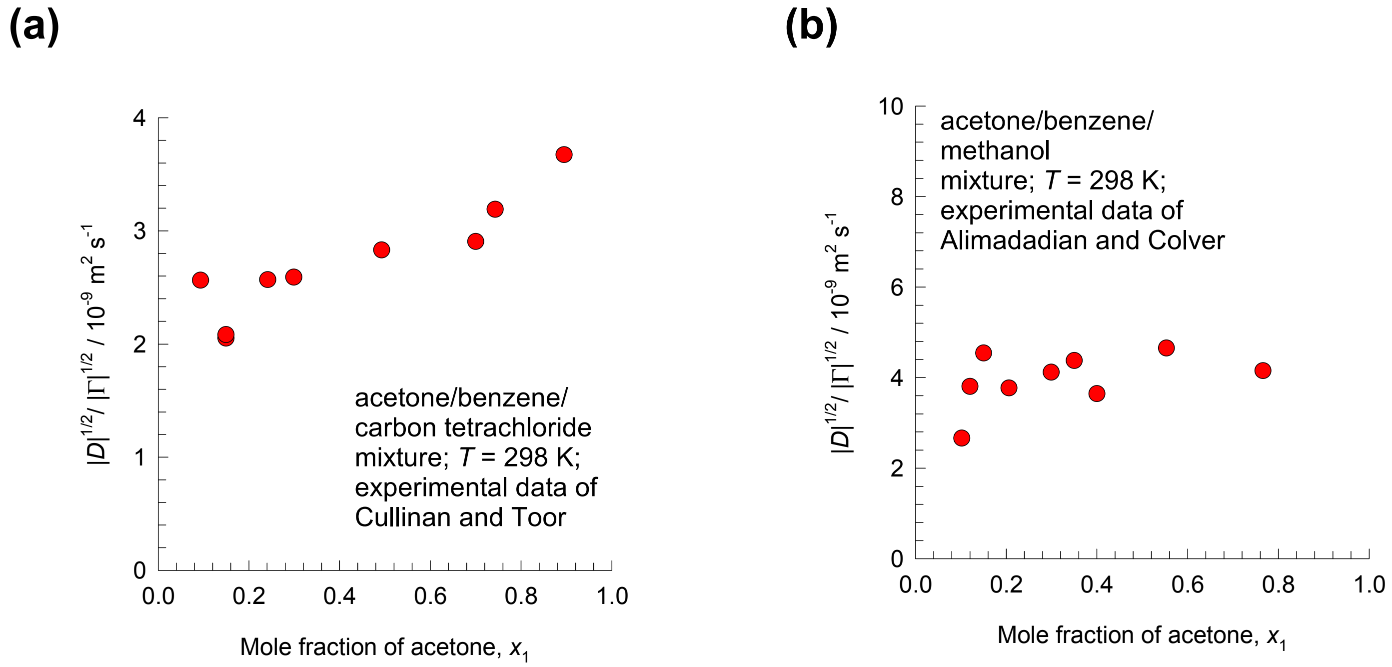

acetone/benzene/carbon tetrachloride mixture; T = 298 K; experimental data of Cullinan and Toor

acetone/benzene/methanol mixture; T = 298 K; experimental data of Alimadadian and Colver

The ratio $\frac{|D|^{1/2}}{|\Gamma|^{1/2}}$

can be viewed as the “magnitude” of the Maxwell-Stefan diffusivity in the *ternary* mixture.

Rehfeldt data: Ratio $|D|^{1/2}/|\Gamma|^{1/2}$

ESI Fig. 6

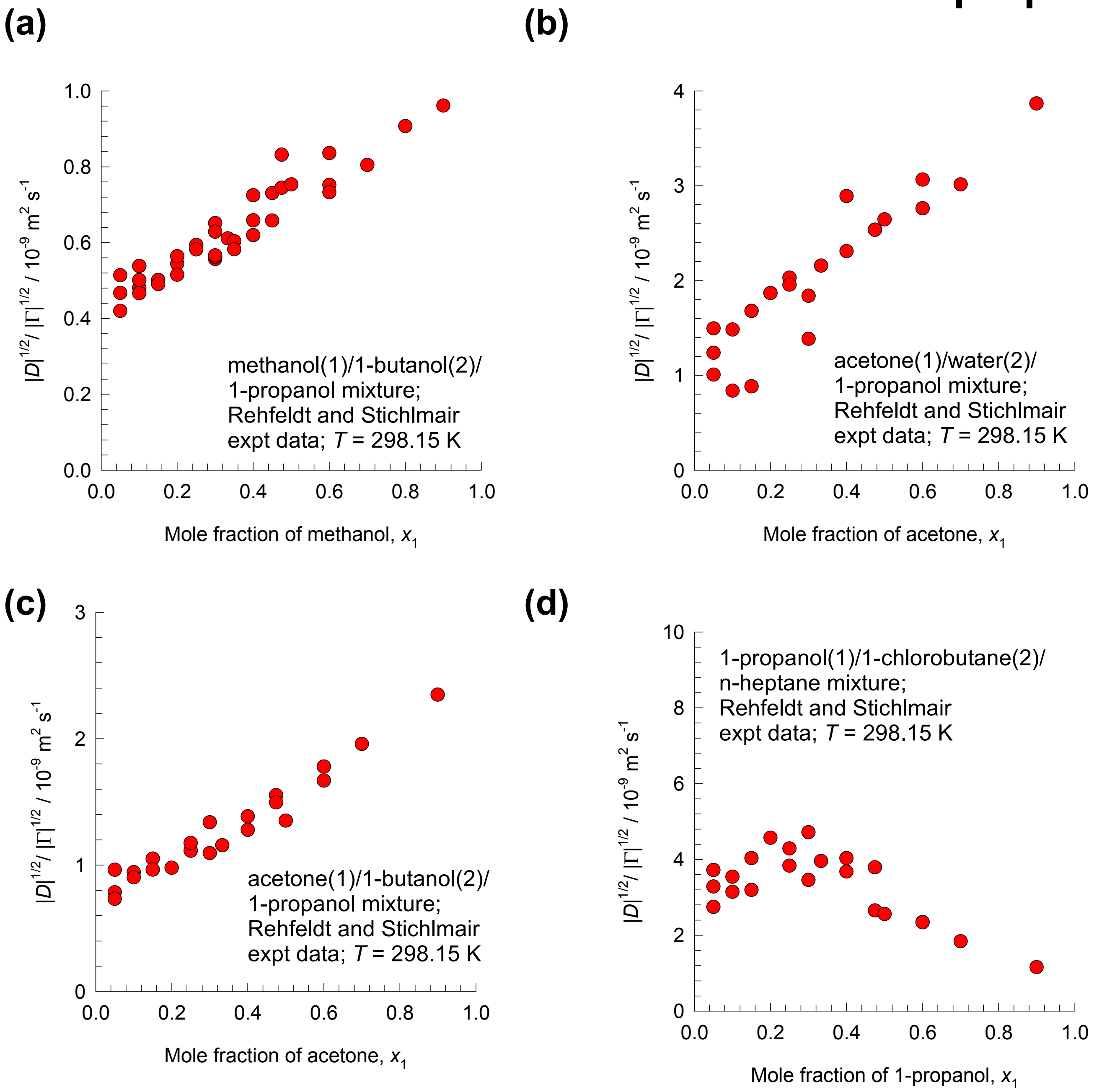

The ratio

$$\frac{|D|^{1/2}}{|\Gamma|^{1/2}}$$

can be viewed as the "magnitude" of the Maxwell-Stefan diffusivity in the *ternary* mixture.

Ziebold data: Ratio $|D|^{1/2} / |\Gamma|^{1/2}$

ESI Fig. 7

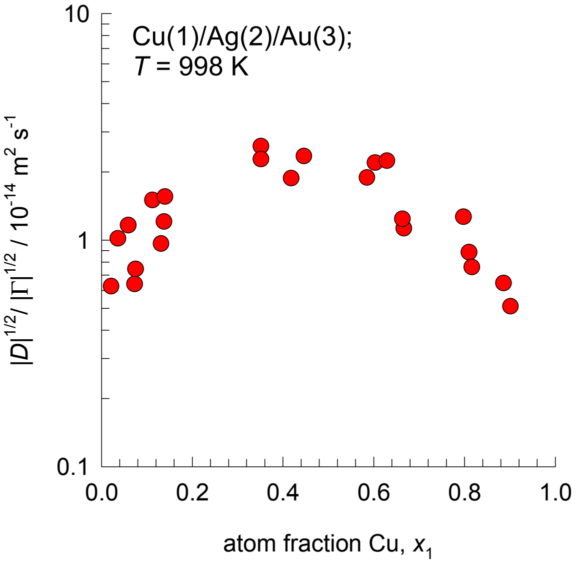

ESI Fig. 8

$H_2/N_2/CO_2$ gas mixture diffusion

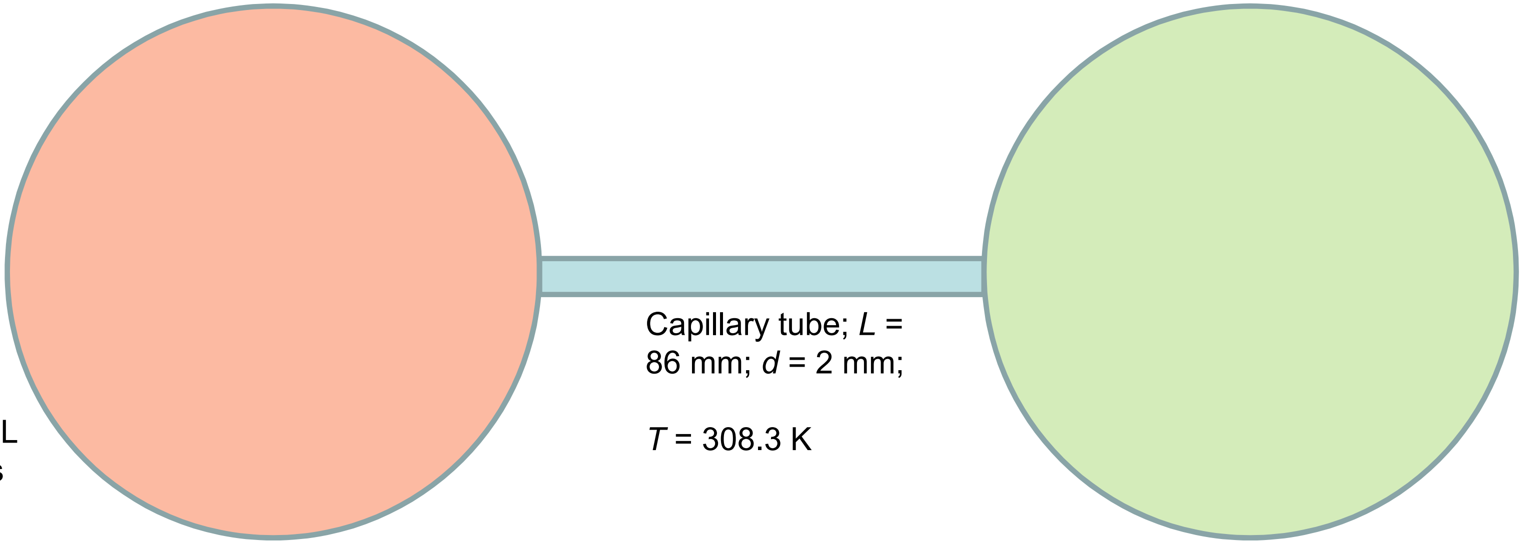

Bulb A

Bulb B

Capillary tube; *L* = 86 mm; *d* = 2 mm;

T = 308.3 K

78 mL
glass
bulb

Initial
Compositions:
H_2 = 0.0
N_2 = 0.50086
CO_2 = 0.49914

Initial
Compositions:
H_2 = 0.50121
N_2 = 0.49879
CO_2 = 0.0

ESI Fig. 9

$H_2/N_2/CO_2$ gas mixture diffusion

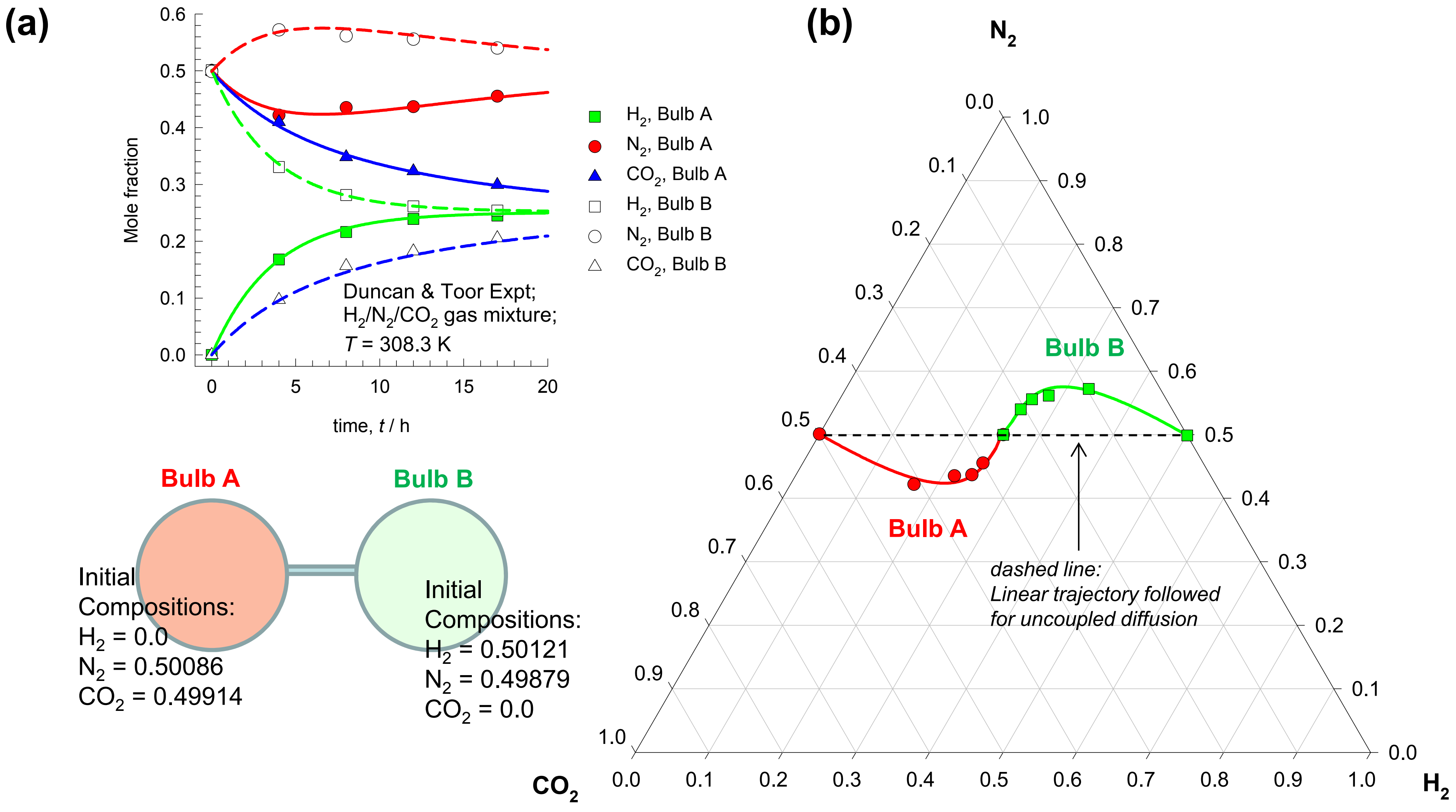

Initial Compositions:
H_2 = 0.0
N_2 = 0.50086
CO_2 = 0.49914

Initial Compositions:
H_2 = 0.50121
N_2 = 0.49879
CO_2 = 0.0

ESI Fig. 10

$H_2/N_2/CO_2$ gas mixture diffusion

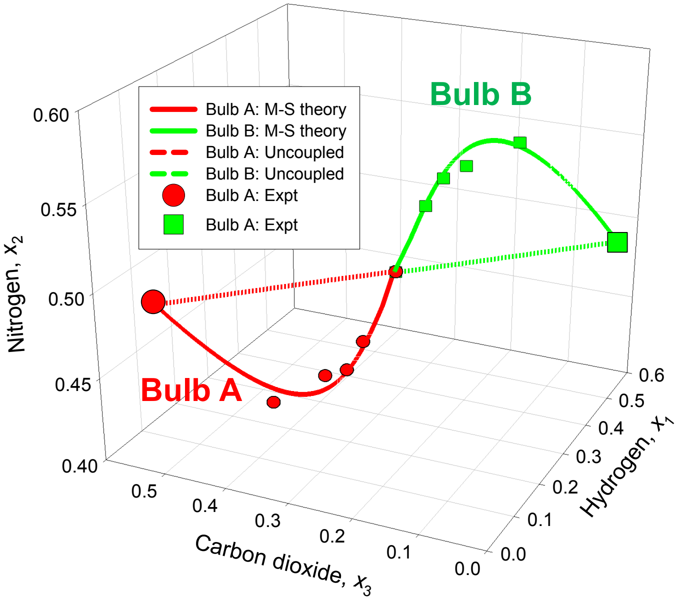

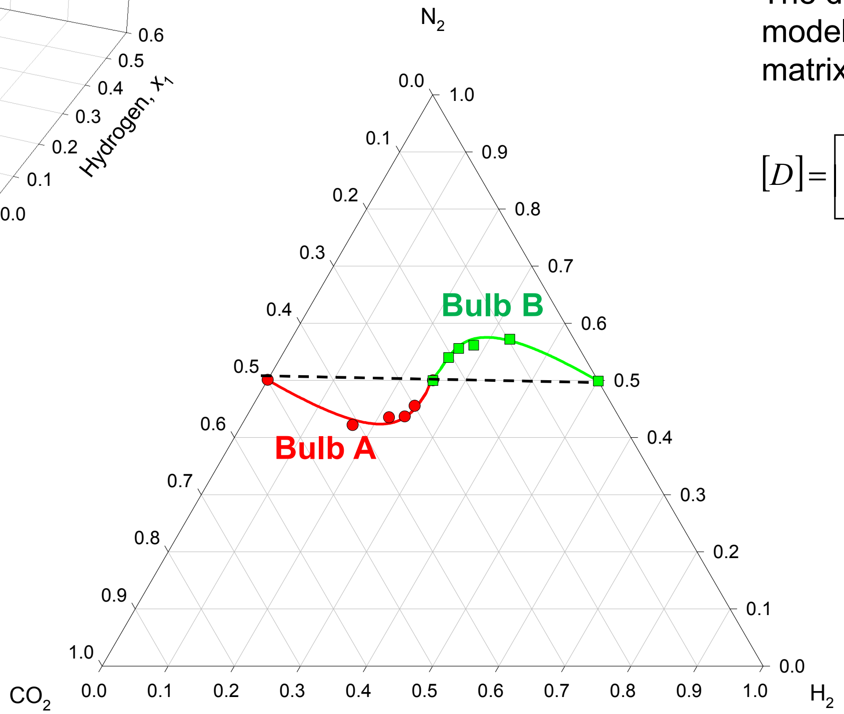

The continuous solid lines (red and green) are the model calculations with

Fick diffusivity matrix

$$[D]=\begin{bmatrix} 7.68 & -0.11 \\ -3.84 & 2.16 \end{bmatrix}\times 10^{-5} \quad \mathrm{m^2\ s^{-1}}$$

The dashed solid lines (blue) are the model calculations using a diagonal Fick matrix

$$[D]=\begin{bmatrix} 7.76 & 0 \\ 0 & 2.08 \end{bmatrix}\times 10^{-5} \quad \mathrm{m^2\ s^{-1}}$$

ESI Fig. 11

$H_2/N_2/CO_2$ gas mixture diffusion

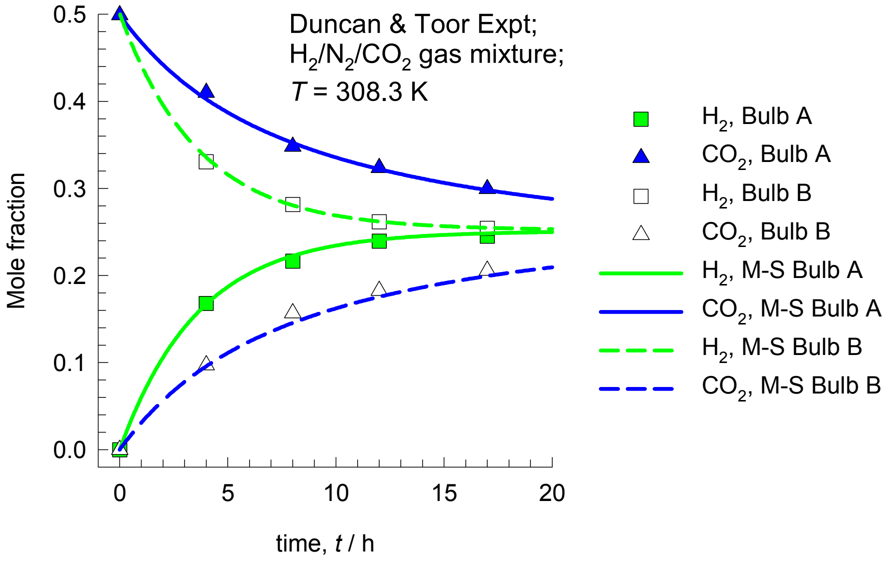

Transient over(under)shoots are captured by Maxwell-Stefan model

$$-\frac{dx_1}{dz}=\frac{x_2N_1-x_1N_2}{c_t Đ_{12}}+\frac{x_3N_1-x_1N_3}{c_t Đ_{13}};$$
$$-\frac{dx_2}{dz}=\frac{x_1N_2-x_2N_1}{c_t Đ_{12}}+\frac{x_3N_2-x_2N_3}{c_t Đ_{23}}$$
$$-\frac{dx_3}{dz}=\frac{x_1N_3-x_3N_1}{c_t Đ_{13}}+\frac{x_2N_3-x_3N_2}{c_t Đ_{23}}$$

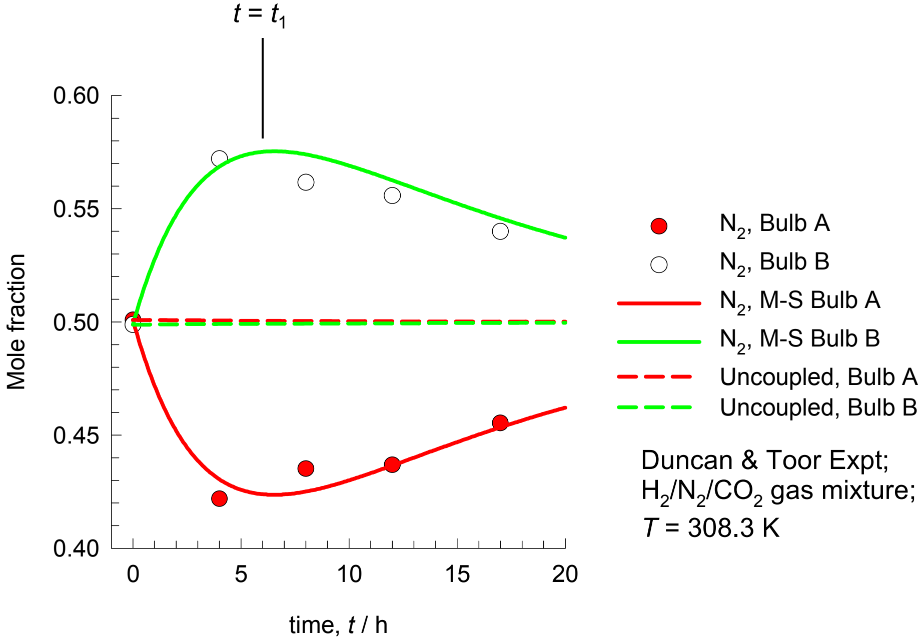

M-S diffusivities

$$Đ_{12} = 8.33\times10^{-5} \quad \mathrm{m^2\ s^{-1}}$$
$$Đ_{13} = 6.8\times10^{-5} \quad \mathrm{m^2\ s^{-1}}$$
$$Đ_{23} = 1.68\times10^{-5} \quad \mathrm{m^2\ s^{-1}}$$

Fick diffusivity matrix

$$[D]=\begin{bmatrix} 7.68 & -0.11 \\ -3.84 & 2.16 \end{bmatrix}\times10^{-5} \quad \mathrm{m^2\ s^{-1}}$$

ESI Fig. 12

(a) Hydrogen flux vs driving force

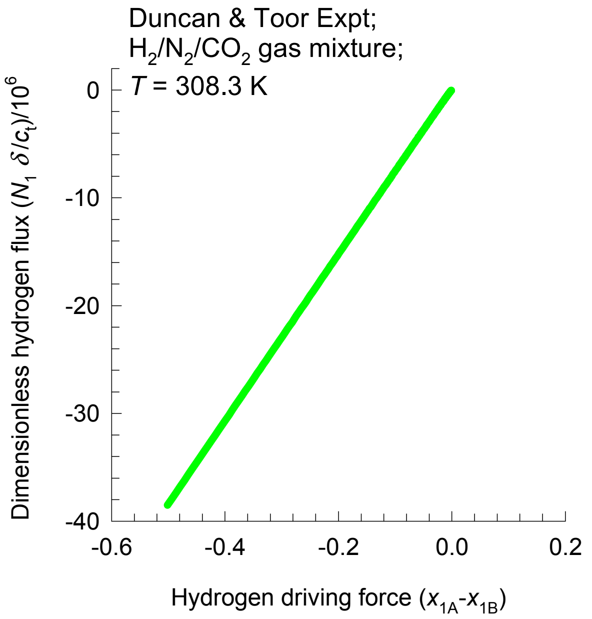

(c) Carbon dioxide flux vs driving force

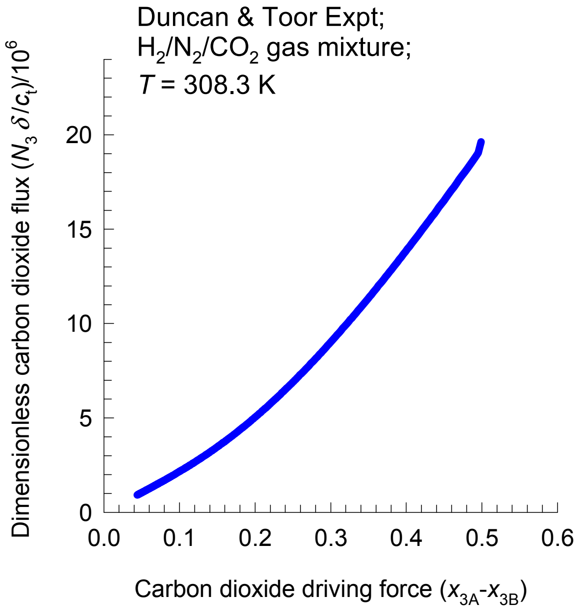

(b) Nitrogen flux vs driving force

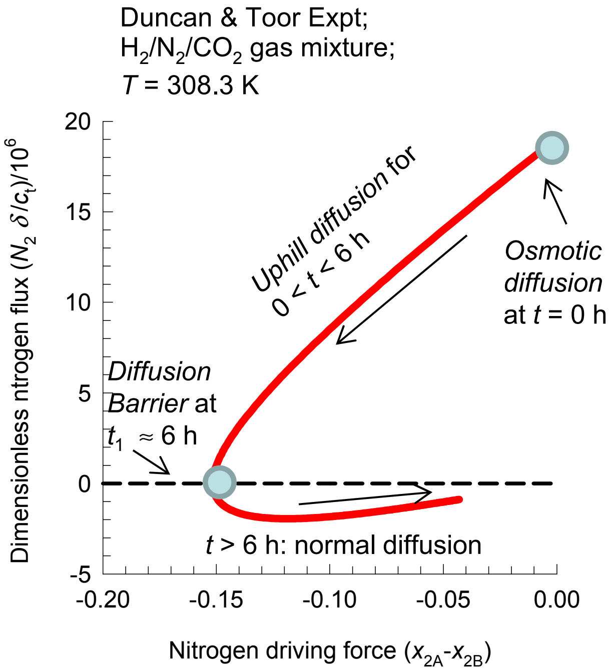

ESI Fig. 13

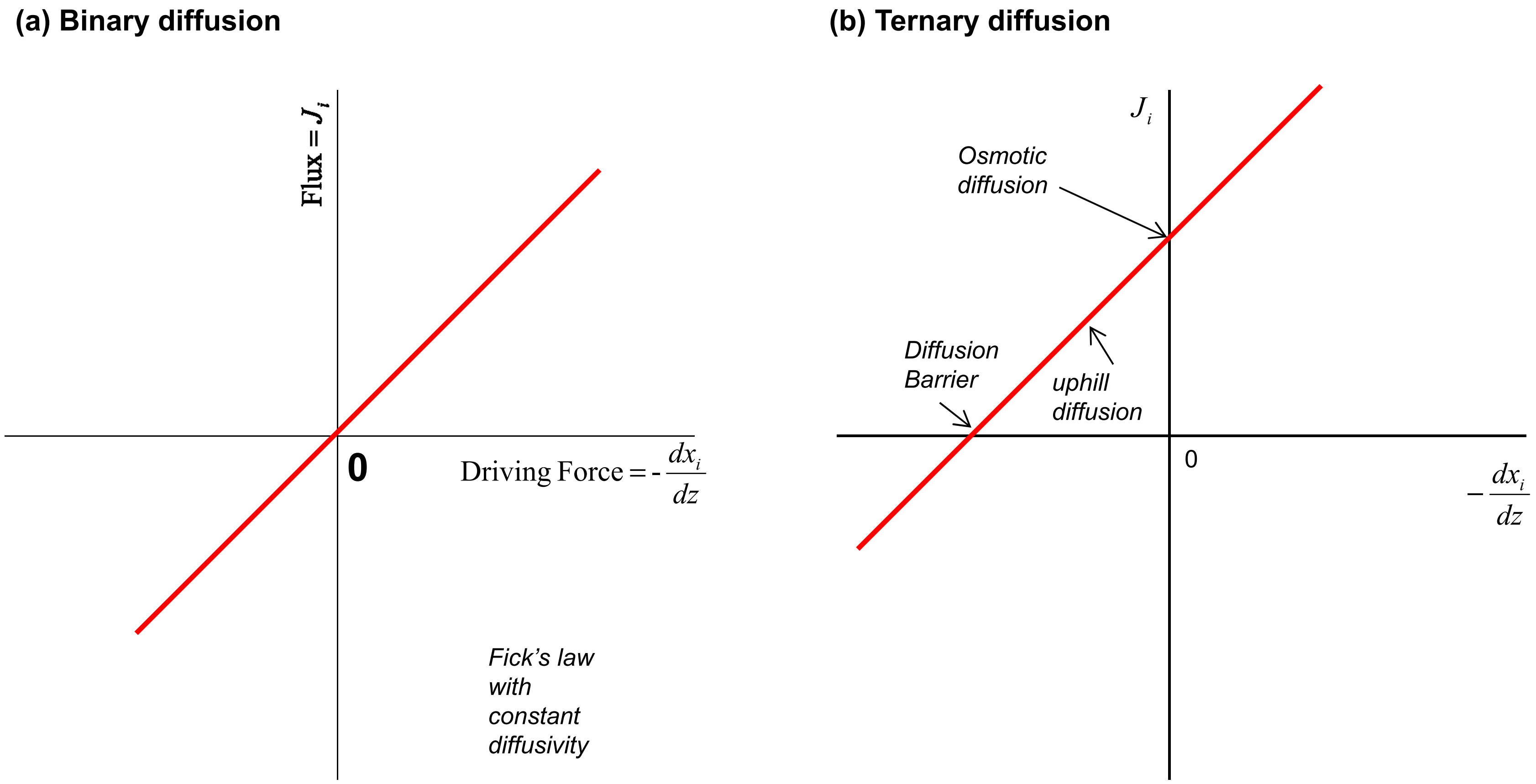

(a) Binary diffusion

(b) Ternary diffusion

ESI Fig. 14

$H_2/N_2/CO_2$ gas mixture diffusion

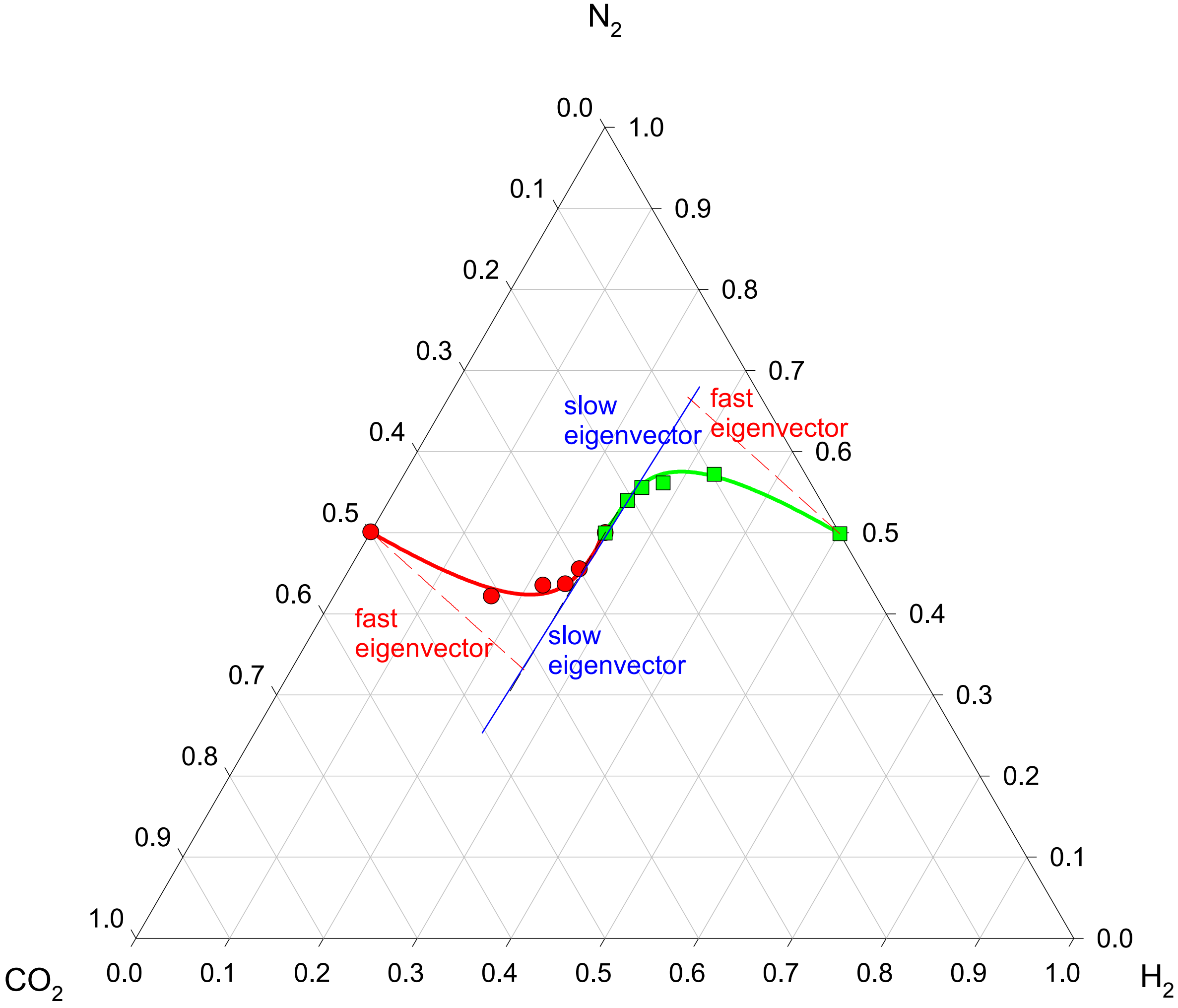

ESI Fig. 15

$CH_4/Ar/H_2$ gas mixture diffusion in Loschmidt tube

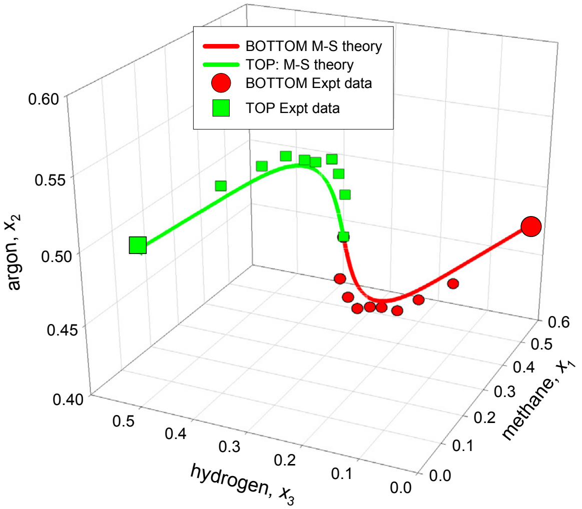

Initial Compositions:
CH_4 = 0.0
Ar = 0.509
H_2 = 0.491

Initial Compositions:
CH_4 = 0.515
Ar = 0.485
H_2 = 0

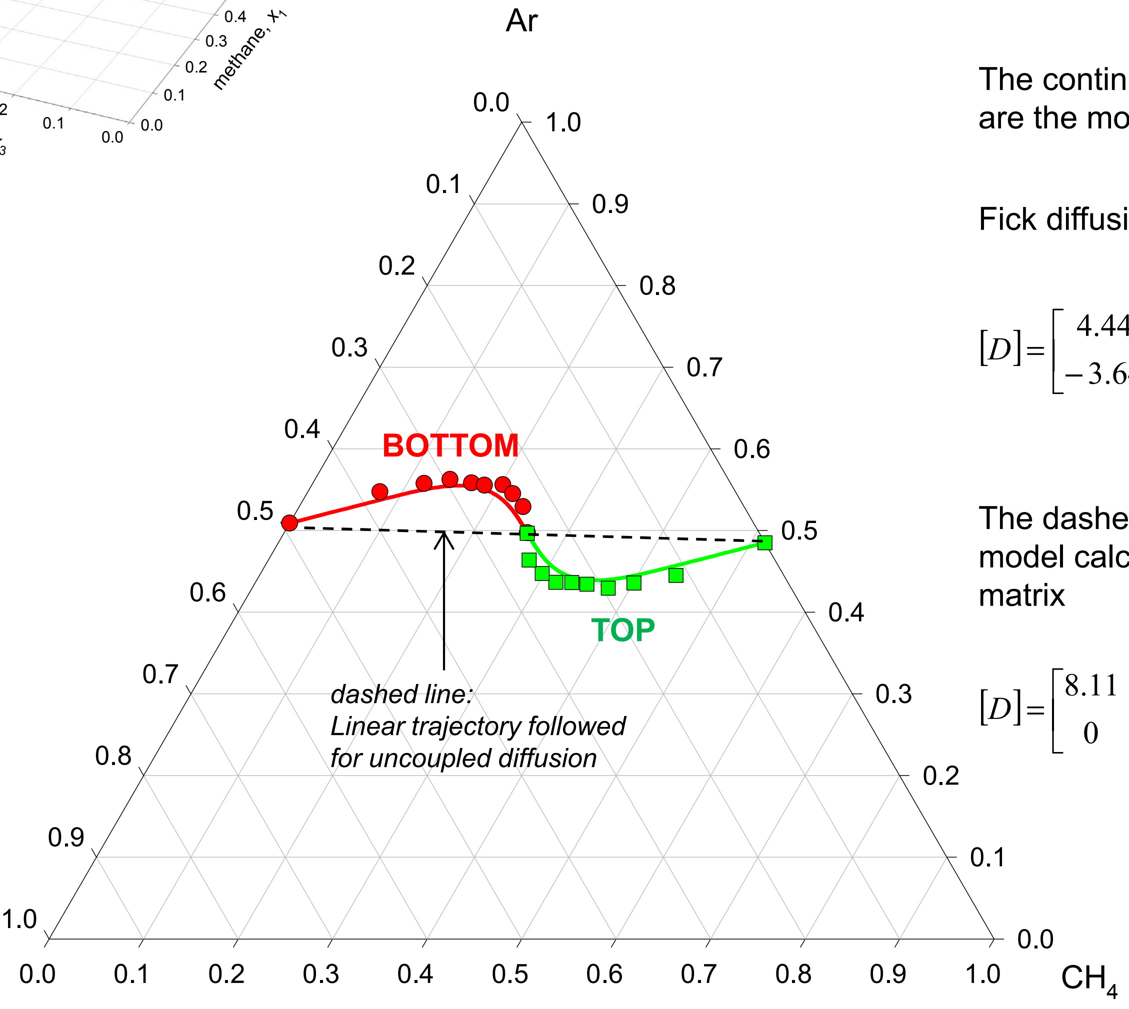

dashed line:
Linear trajectory followed for uncoupled diffusion

The continuous solid lines (red and green) are the model calculations with

Fick diffusivity matrix

$$[D]=\begin{bmatrix} 4.44 & 1.83 \\ -3.64 & 6.3 \end{bmatrix}\times 10^{-5} \quad \mathrm{m^2\ s^{-1}}$$

The dashed solid lines (blue) are the model calculations using a diagonal Fick matrix

$$[D]=\begin{bmatrix} 8.11 & 0 \\ 0 & 2.63 \end{bmatrix}\times 10^{-5} \quad \mathrm{m^2\ s^{-1}}$$

ESI Fig. 16

$CH_4/Ar/H_2$ gas mixture diffusion

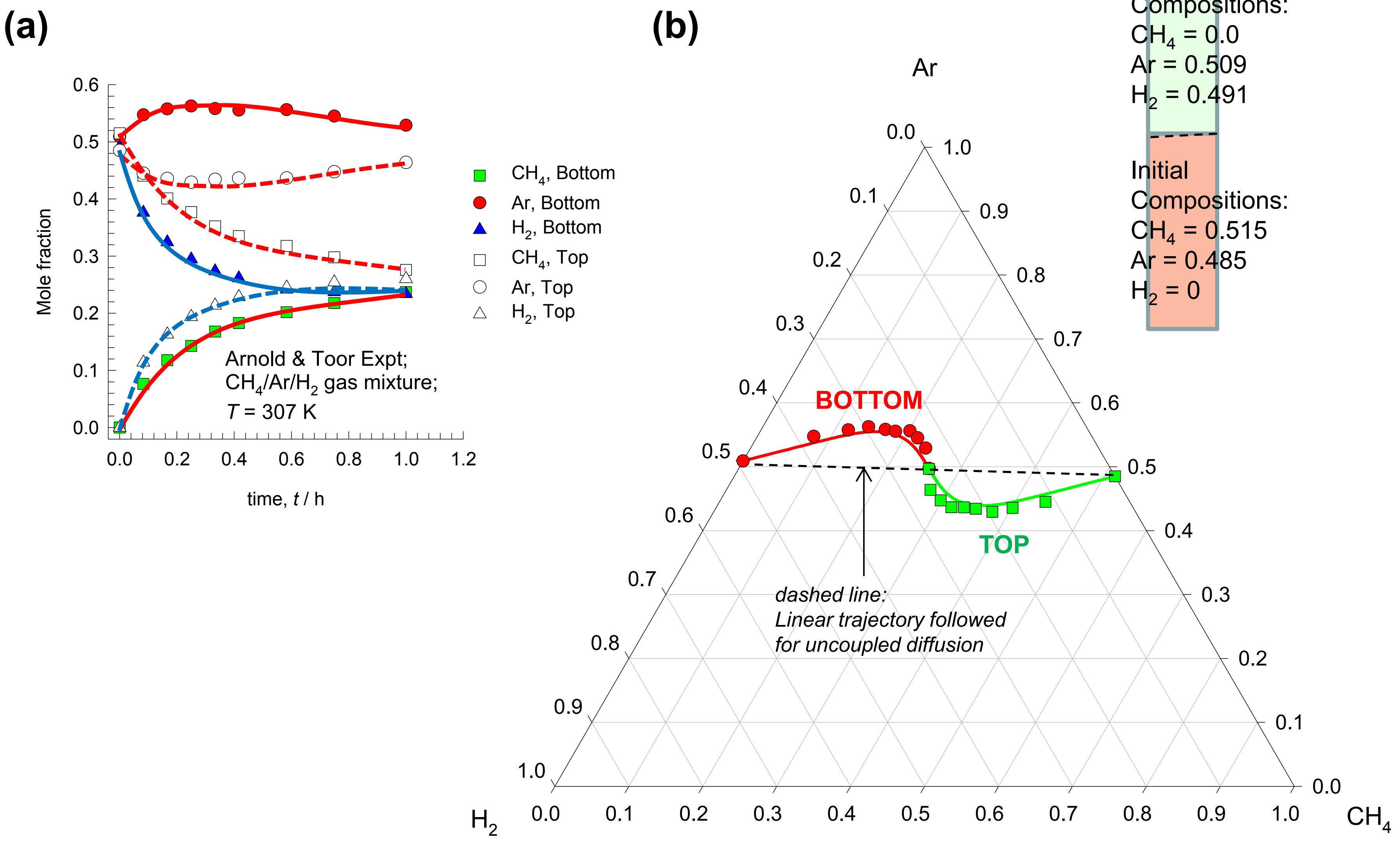

Arnold & Toor Expt;
$CH_4/Ar/H_2$ gas mixture;
T = 307 K

dashed line:
Linear trajectory followed
for uncoupled diffusion

Initial
Compositions:
$CH_4 = 0.0$
$Ar = 0.509$
$H_2 = 0.491$

Initial
Compositions:
$CH_4 = 0.515$
$Ar = 0.485$
$H_2 = 0$

ESI Fig. 17

Transient approaches to Equilibrium

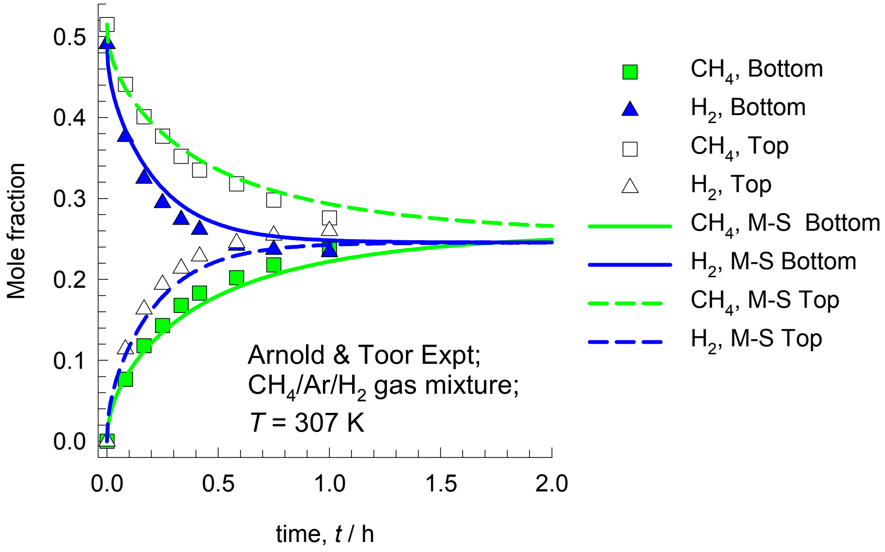

Transient over(under)shoots are captured by taking account of coupling effects

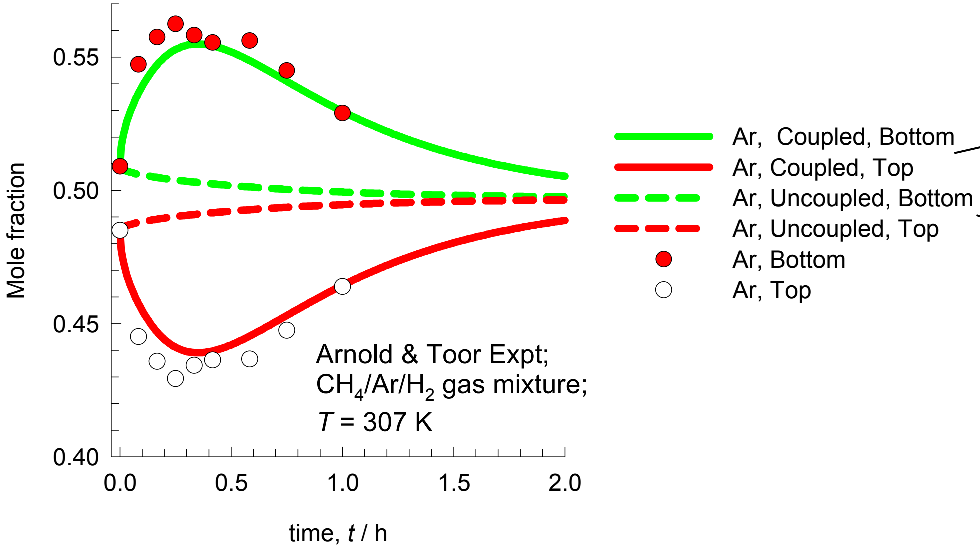

Coupled:

$$[D]=\begin{bmatrix} 4.44 & 1.83 \\ -3.64 & 6.3 \end{bmatrix}\times 10^{-5} \quad \mathrm{m}^2\ \mathrm{s}^{-1}$$

Uncoupled:

$$[D]=\begin{bmatrix} 8.11 & 0 \\ 0 & 2.63 \end{bmatrix}\times 10^{-5} \quad \mathrm{m}^2\ \mathrm{s}^{-1}$$

ESI Fig. 18

$O_2/N_2/He$ gas mixture diffusion

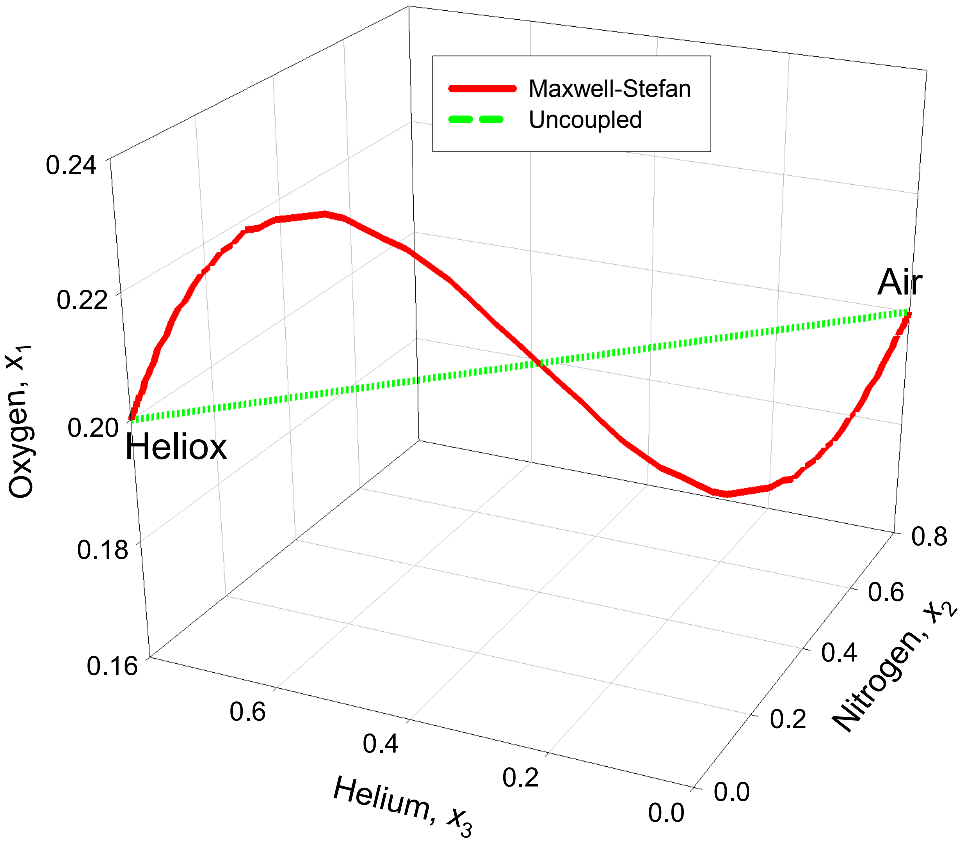

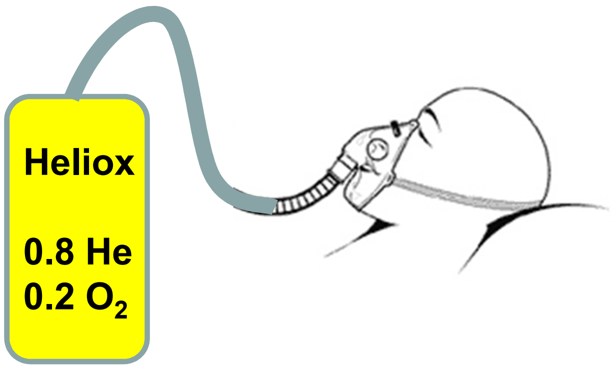

Heliox

0.8 He
0.2 O_2

Air in patient

0.8 N_2
0.2 O_2

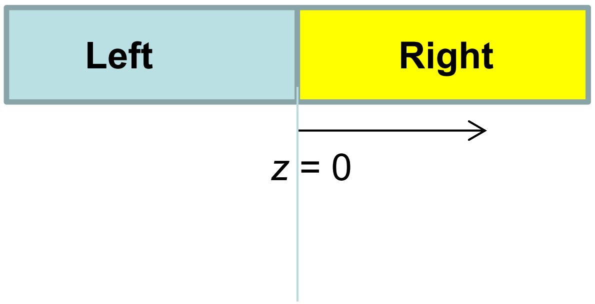

ESI Fig. 19

$O_2/N_2/He$ gas mixture diffusion

Heliox

0.8 He
0.2 O_2

Air in patient

0.8 N_2
0.2 O_2

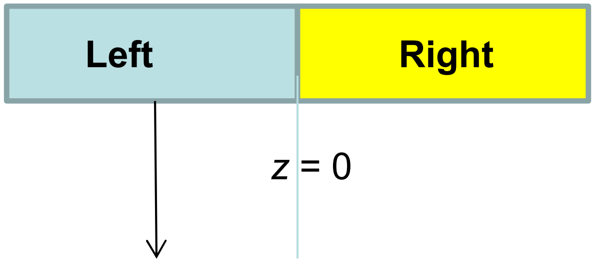

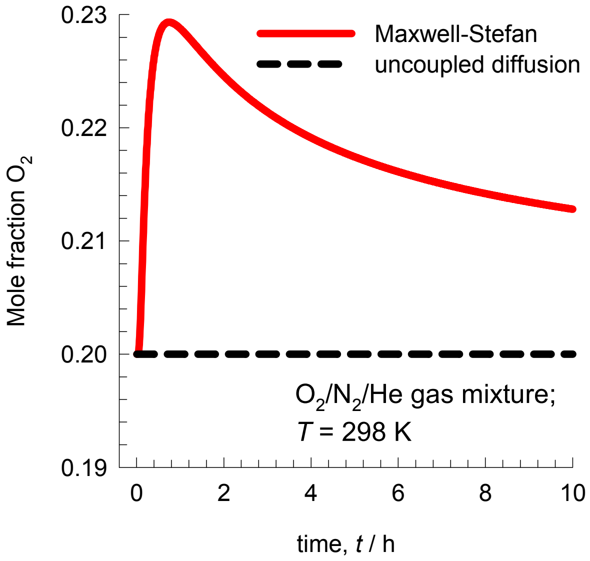

ESI Fig. 20

Breaking azeotropes by partial condensation

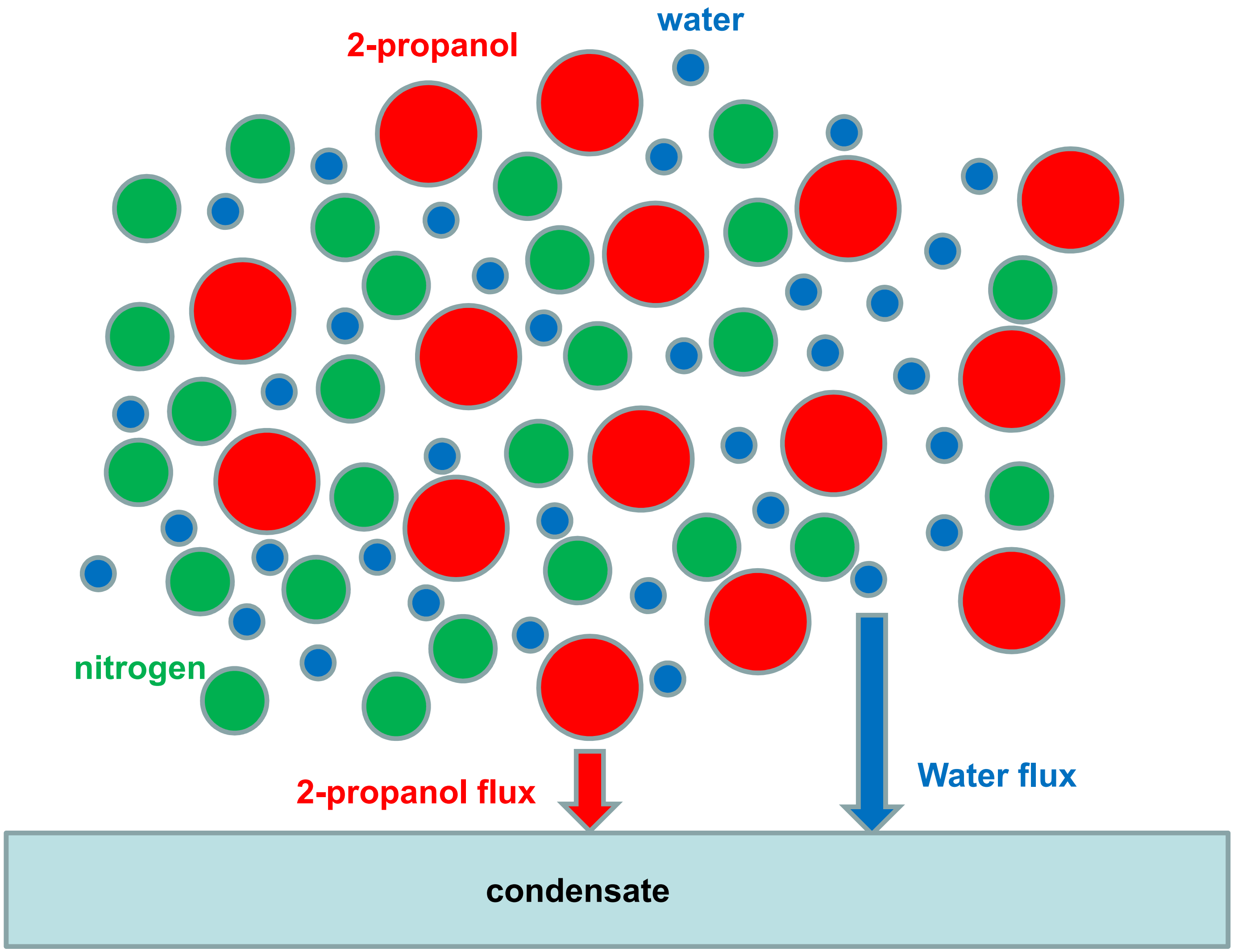

ESI Fig. 21

UCST and LCST

(a) methanol(1)/n-hexane(2)

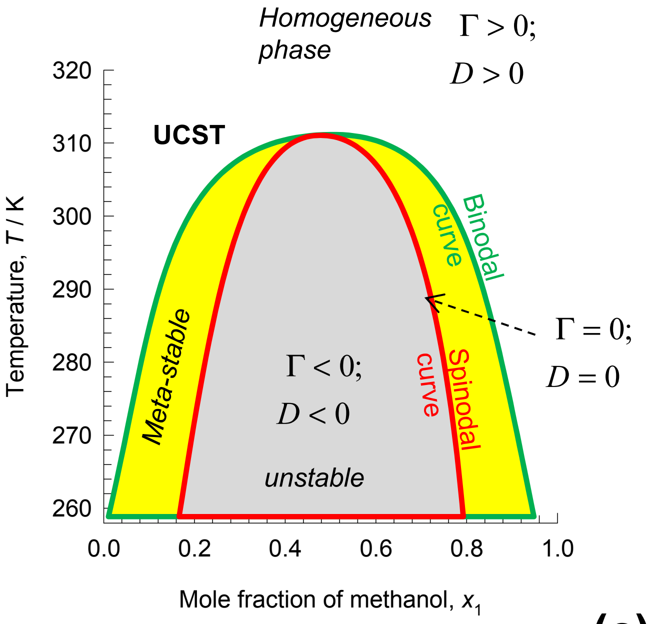

(b) triethylamine(1)/water(2)

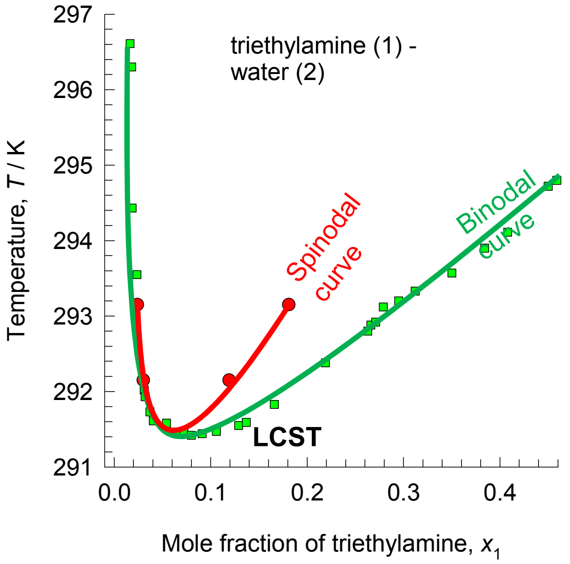

(c) n-hexane(1)/nitrobenzene(2)

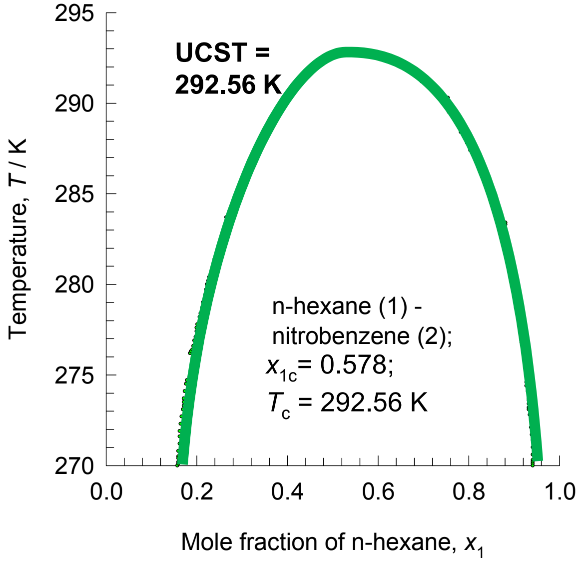

ESI Fig. 22

Binodal and spinodal

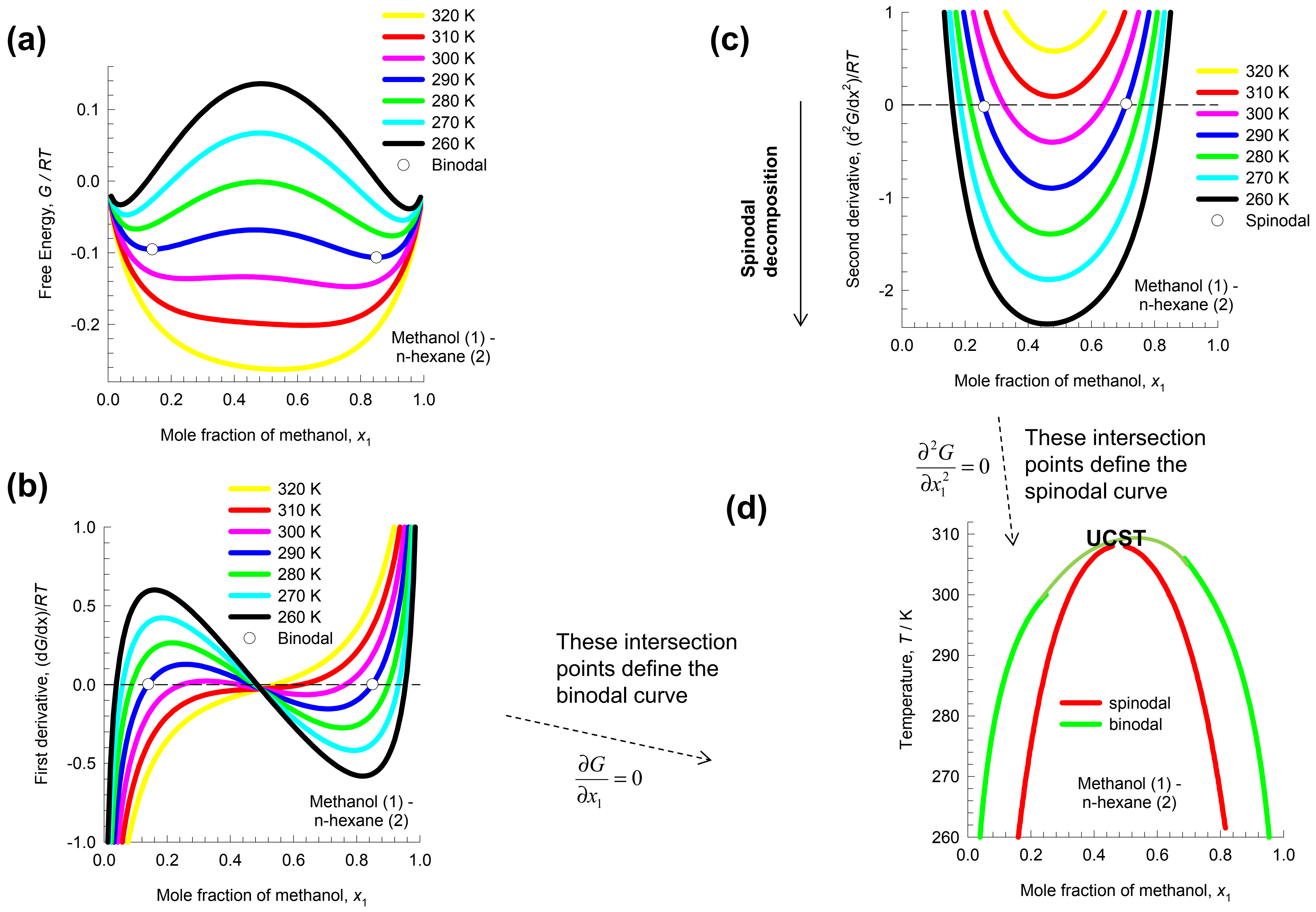

These intersection points define the binodal curve

$$\frac{\partial G}{\partial x_1} = 0$$

$$\frac{\partial^2 G}{\partial x_1^2} = 0$$

These intersection points define the spinodal curve

Methanol/n-hexane mixture diffusion

ESI Fig. 23

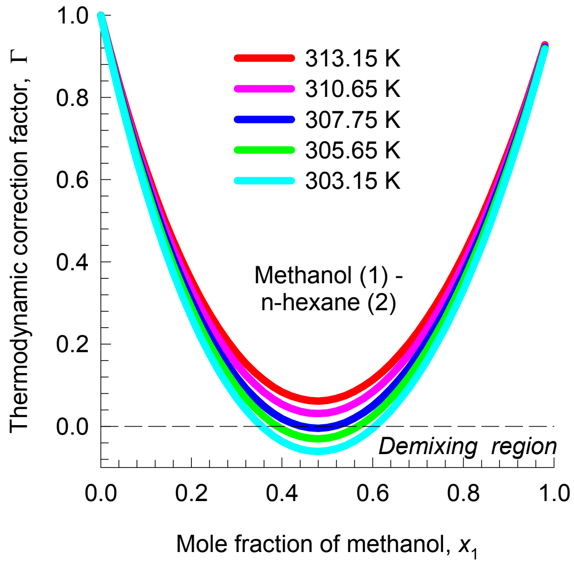

(a)

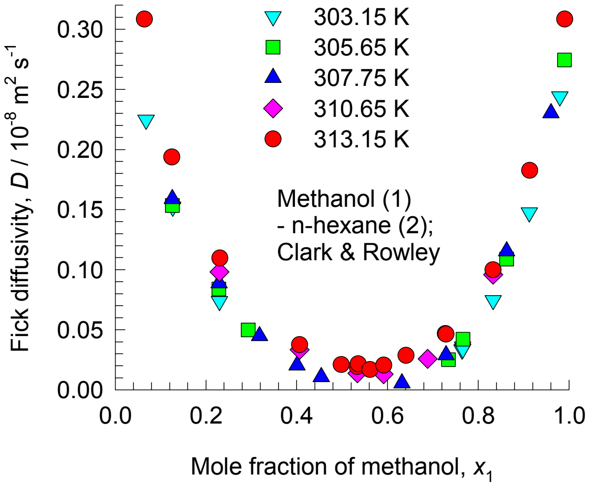

(b)

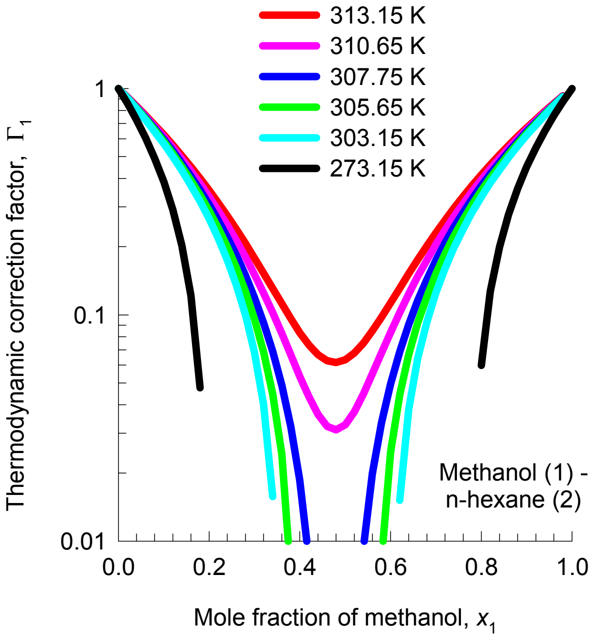

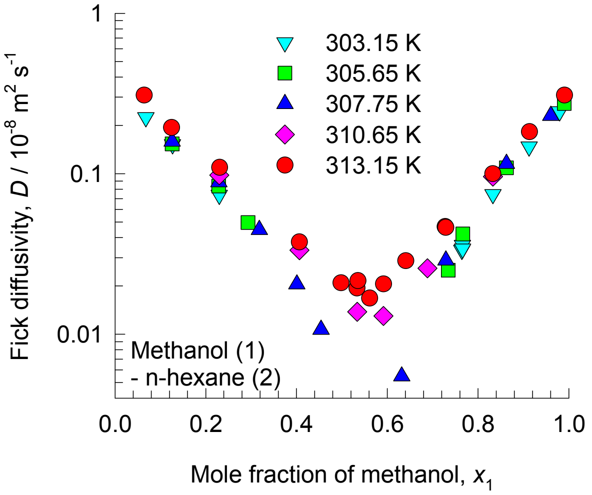

Methanol/n-hexane mixture diffusion

ESI Fig. 24

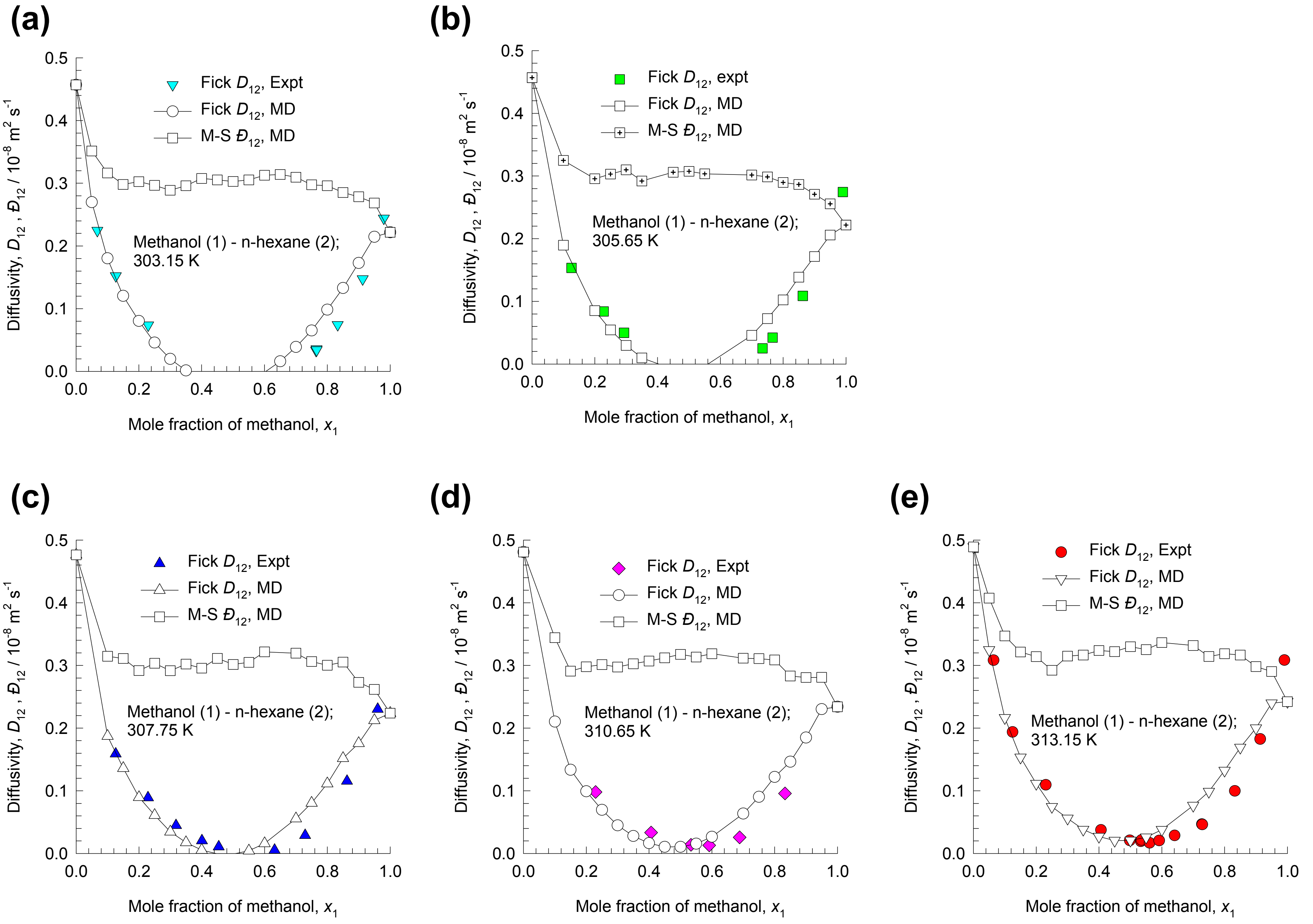

Methanol/n-hexane mixture diffusion

ESI Fig. 25

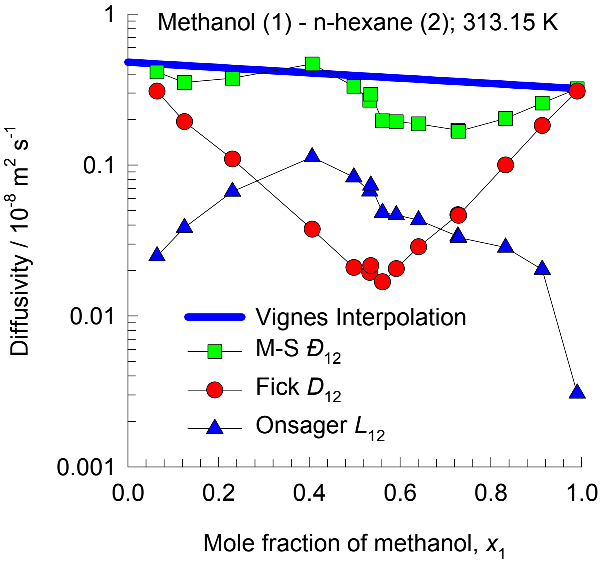

Triethylamine/water mixture diffusion

ESI Fig. 26

(a)

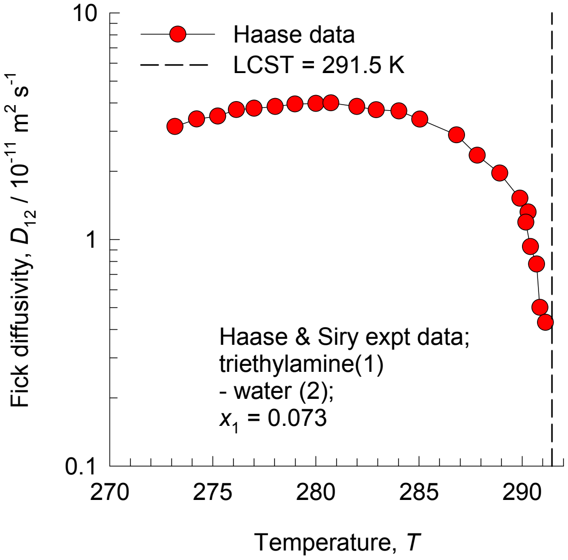

(b)

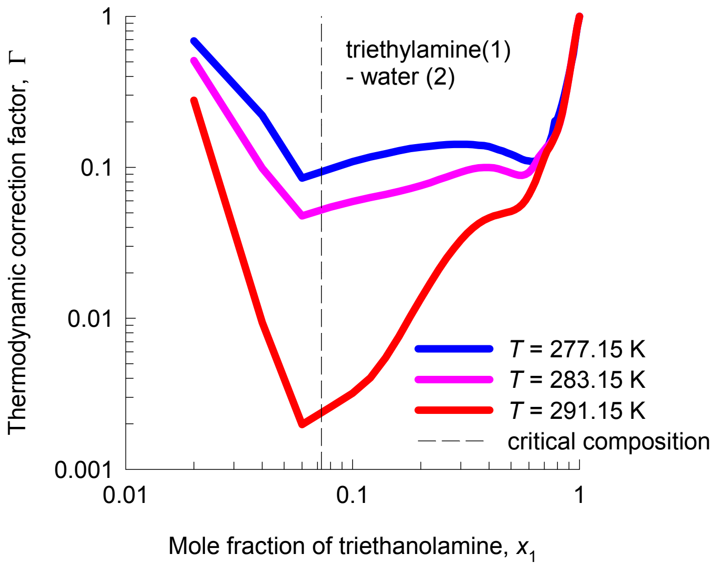

Tri-ethylamine/water mixture diffusion

ESI Fig. 27

(a)

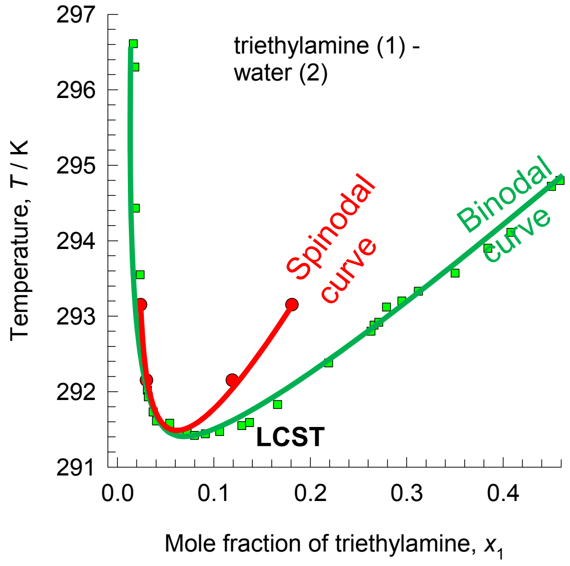

(b)

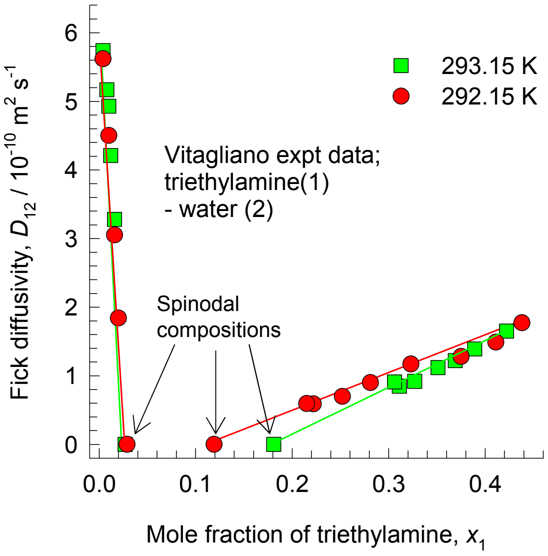

urea/water, glycine/water mixture diffusion

ESI Fig. 28

(a)

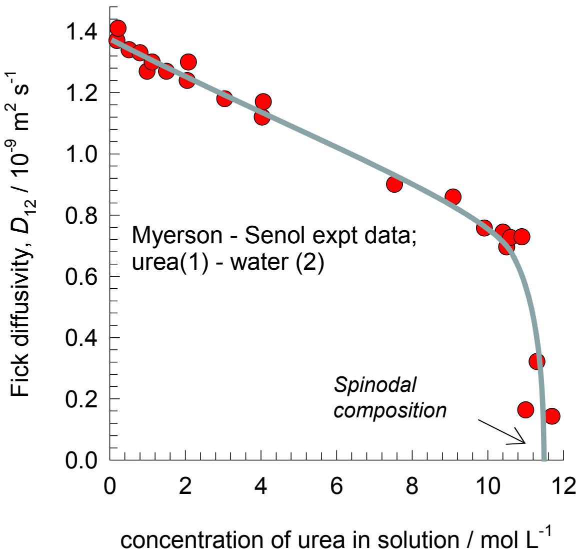

(b)

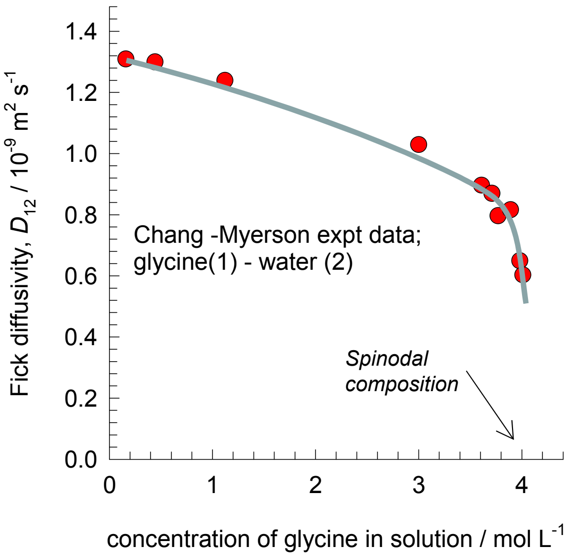

n-hexane(1)-nitrobenzene(2) diffusion

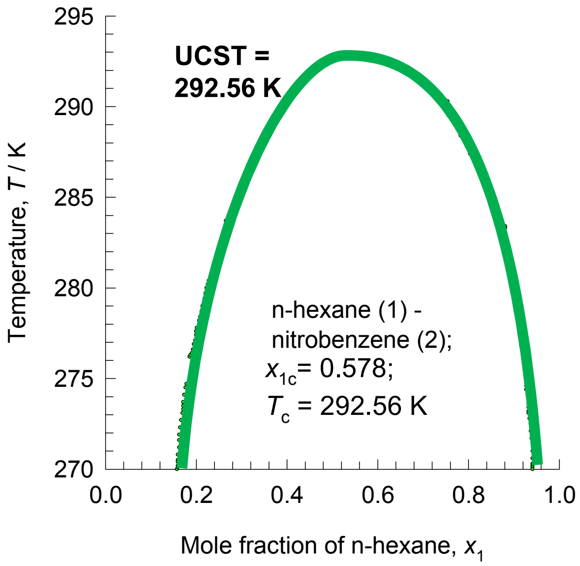

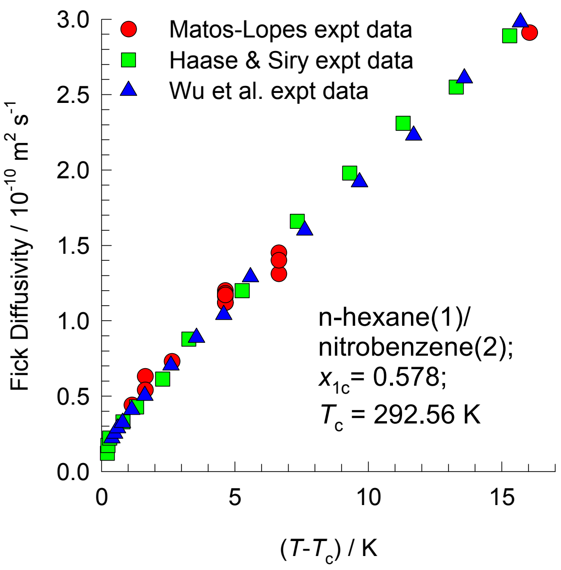

ESI Fig. 30

Nucleation and Growth

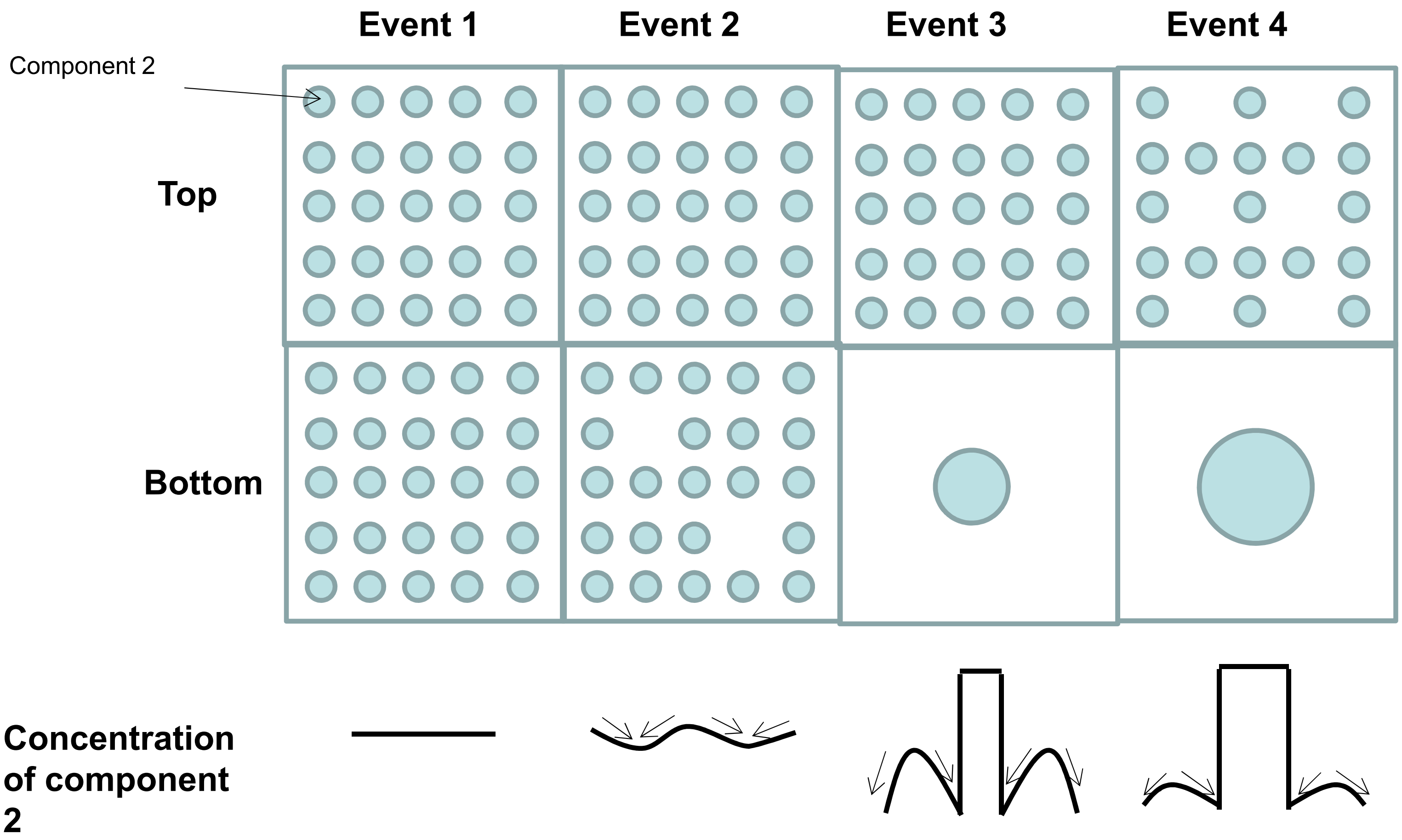

Event 1

Event 2

Event 3

Event 4

Component 2

Top

Bottom

Concentration of component 2

ESI Fig. 31

Spinodal Decomposition

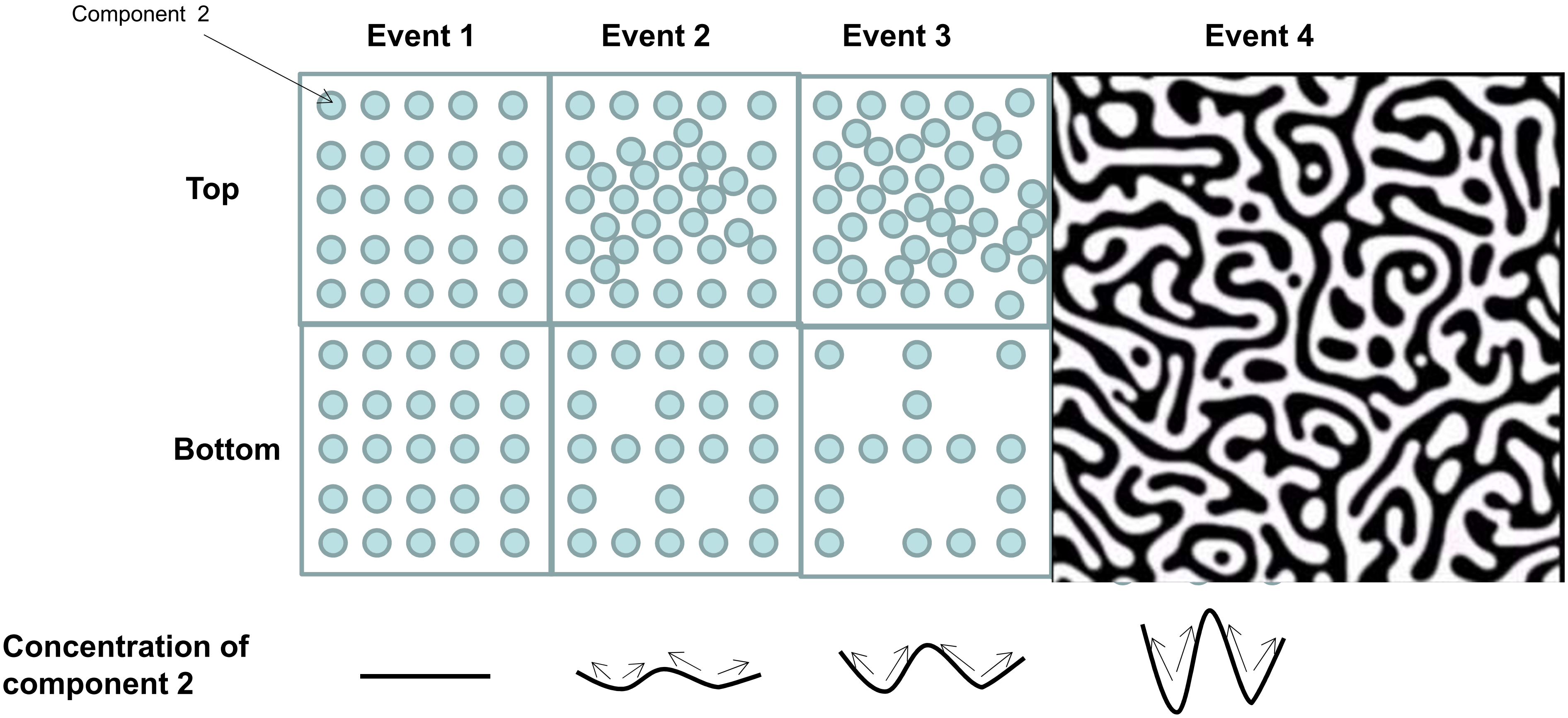

Component 2

Event 1 **Event 2** **Event 3** **Event 4**

Top

Bottom

Concentration of component 2

Ternary Liquid/Liquid System

ESI Fig. 32

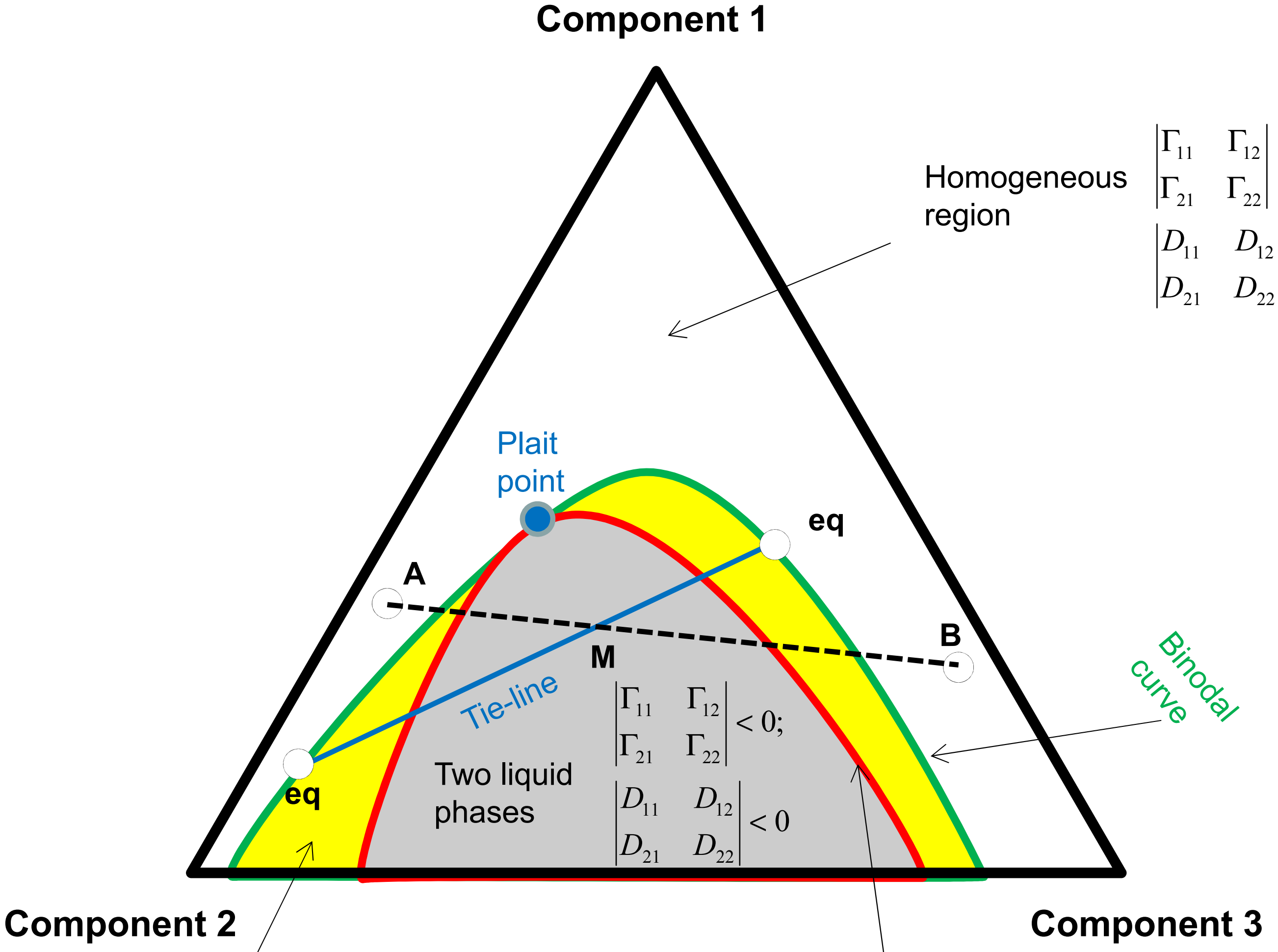

Homogeneous region
$$\begin{vmatrix} \Gamma_{11} & \Gamma_{12} \\ \Gamma_{21} & \Gamma_{22} \end{vmatrix} > 0;$$
$$\begin{vmatrix} D_{11} & D_{12} \\ D_{21} & D_{22} \end{vmatrix} > 0$$

Two liquid phases
$$\begin{vmatrix} \Gamma_{11} & \Gamma_{12} \\ \Gamma_{21} & \Gamma_{22} \end{vmatrix} < 0;$$
$$\begin{vmatrix} D_{11} & D_{12} \\ D_{21} & D_{22} \end{vmatrix} < 0$$

Meta-stable region

Spinodal curve
$$\begin{vmatrix} \Gamma_{11} & \Gamma_{12} \\ \Gamma_{21} & \Gamma_{22} \end{vmatrix} = 0;$$
$$\begin{vmatrix} D_{11} & D_{12} \\ D_{21} & D_{22} \end{vmatrix} = 0$$

ESI Fig. 33

Fick diffusivities in Glycerol/Acetone/Water

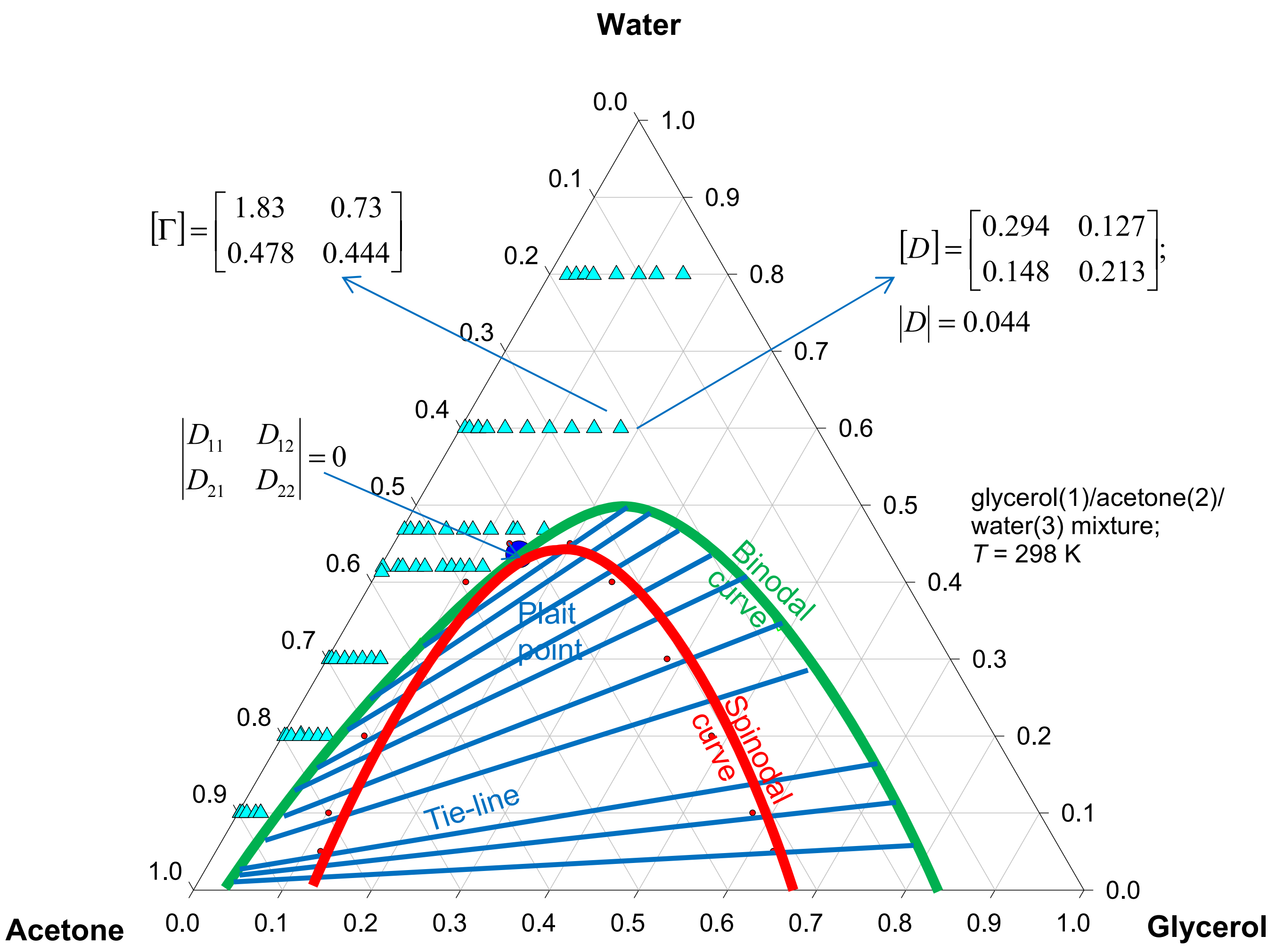

$$[\Gamma]=\begin{bmatrix}1.83 & 0.73\\ 0.478 & 0.444\end{bmatrix}$$

$$[D]=\begin{bmatrix}0.294 & 0.127\\ 0.148 & 0.213\end{bmatrix};$$

$$|D|=0.044$$

$$\begin{vmatrix}D_{11} & D_{12}\\ D_{21} & D_{22}\end{vmatrix}=0$$

glycerol(1)/acetone(2)/
water(3) mixture;
T = 298 K

ESI Fig. 34

Gamma matrix: Glycerol/Acetone/Water

(a)

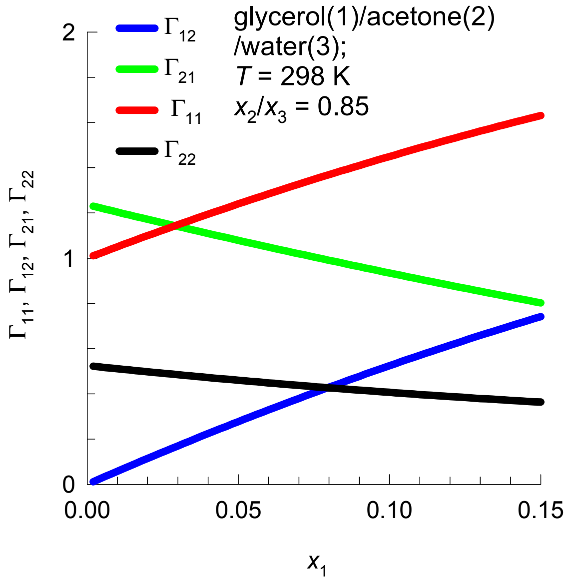

(b)

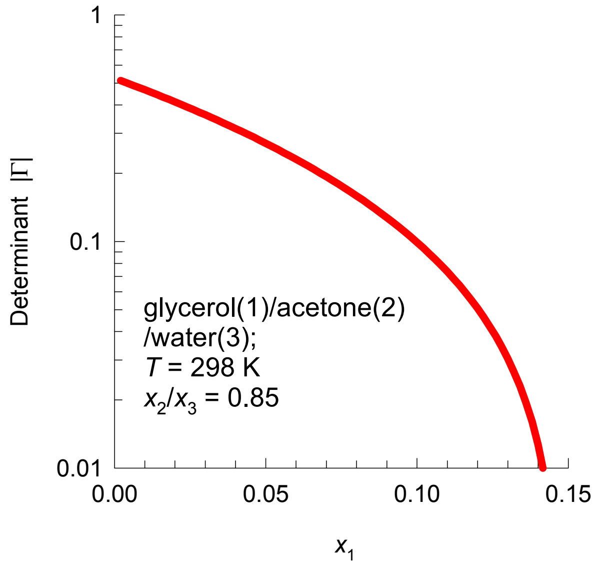

(c)

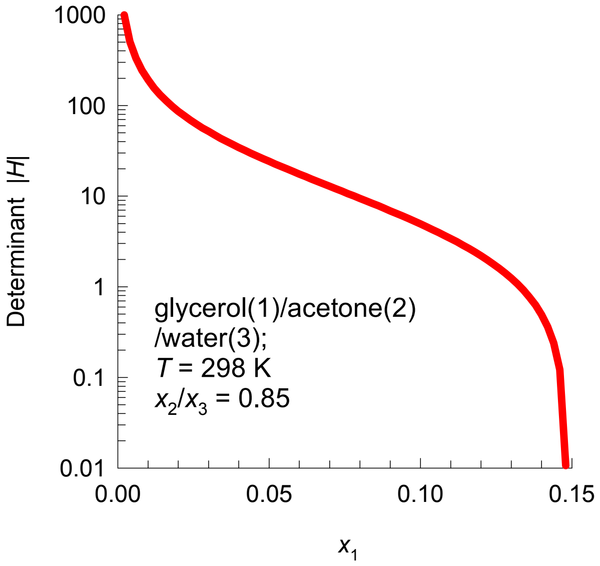

Fick matrix: Glycerol/Acetone/Water

ESI Fig. 35

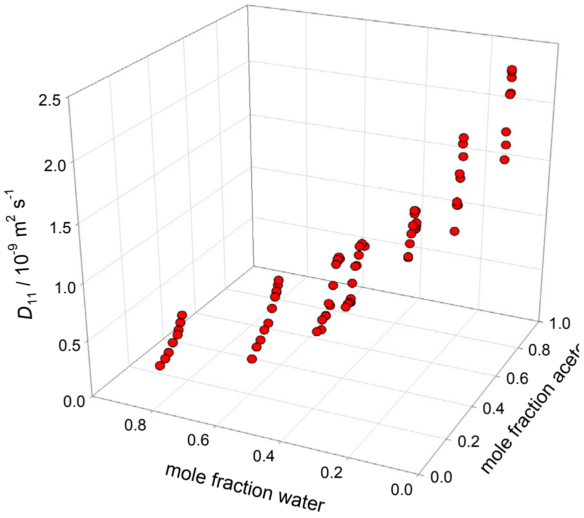

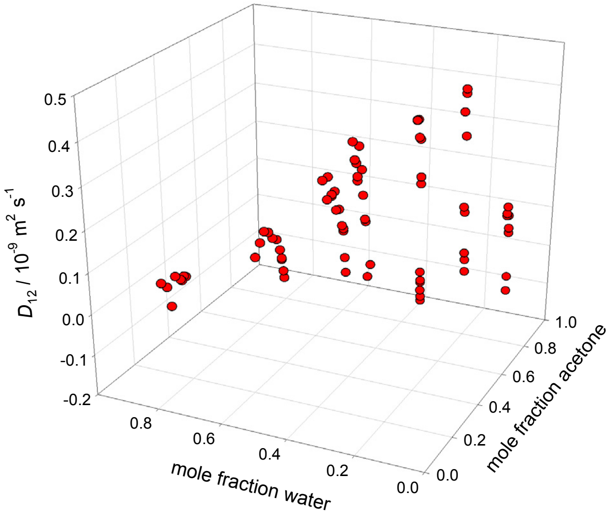

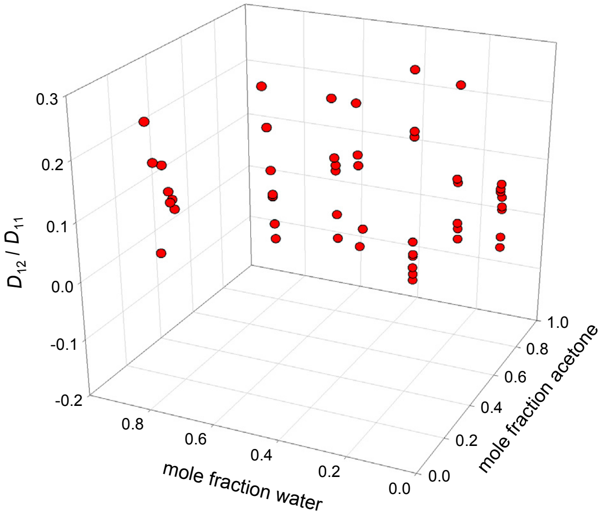

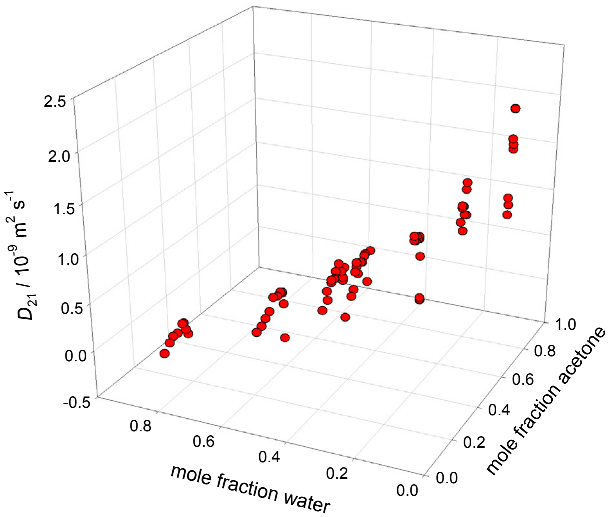

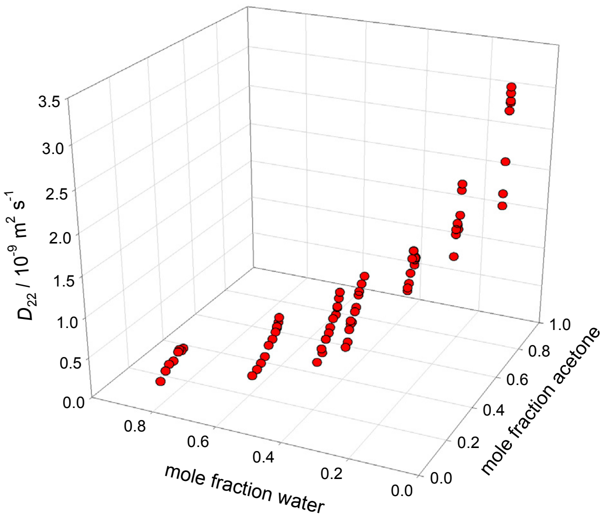

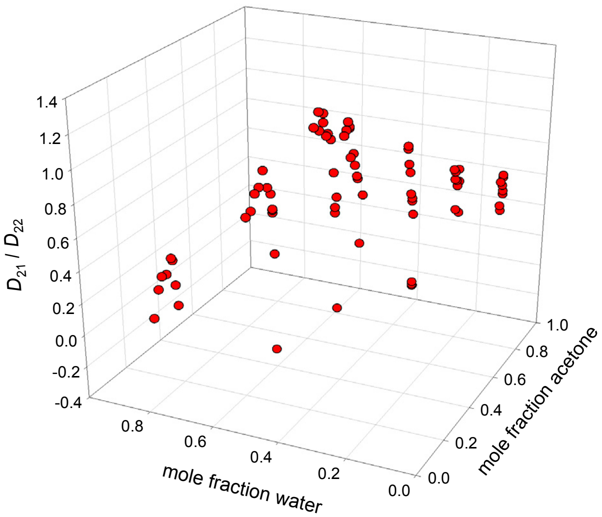

Glycerol/Acetone/Water Mixture Diffusion

ESI Fig. 36

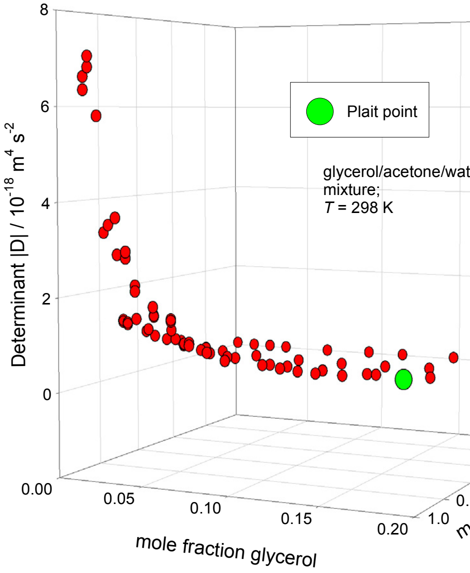

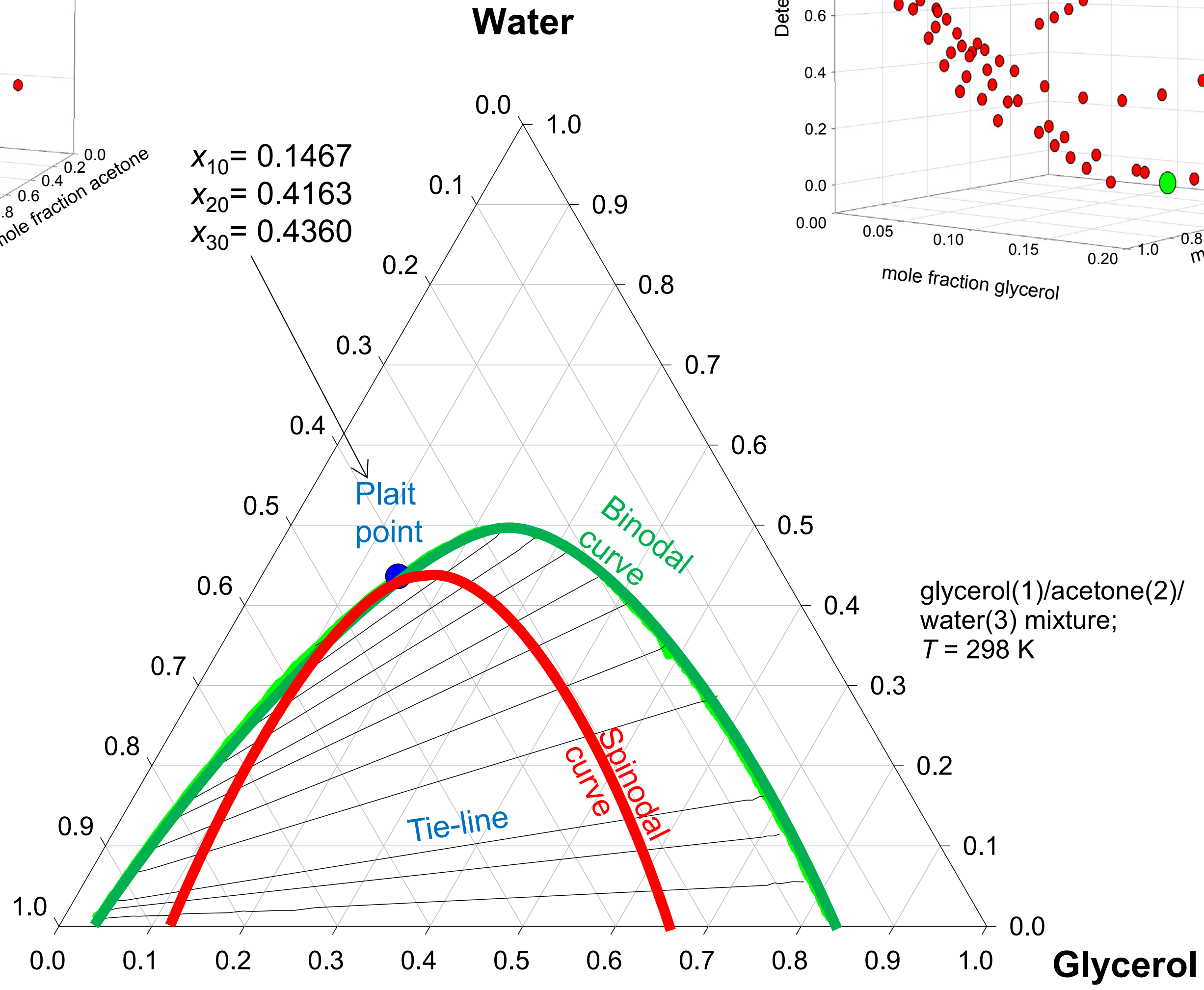

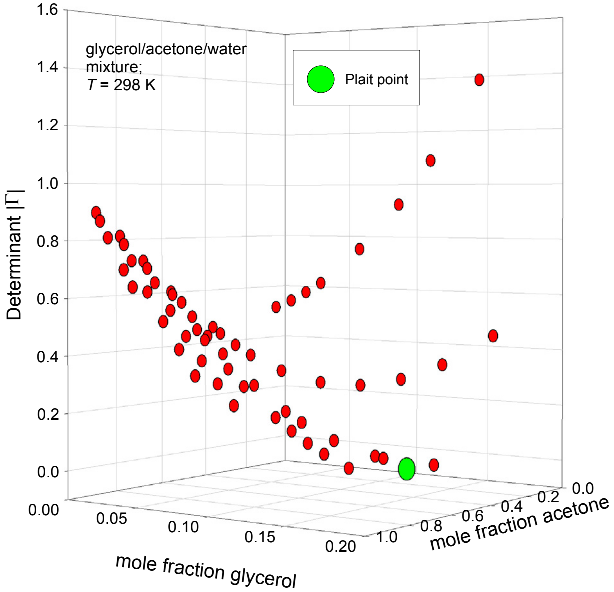

Glycerol/Acetone/Water Mixture Diffusion

ESI Fig. 37

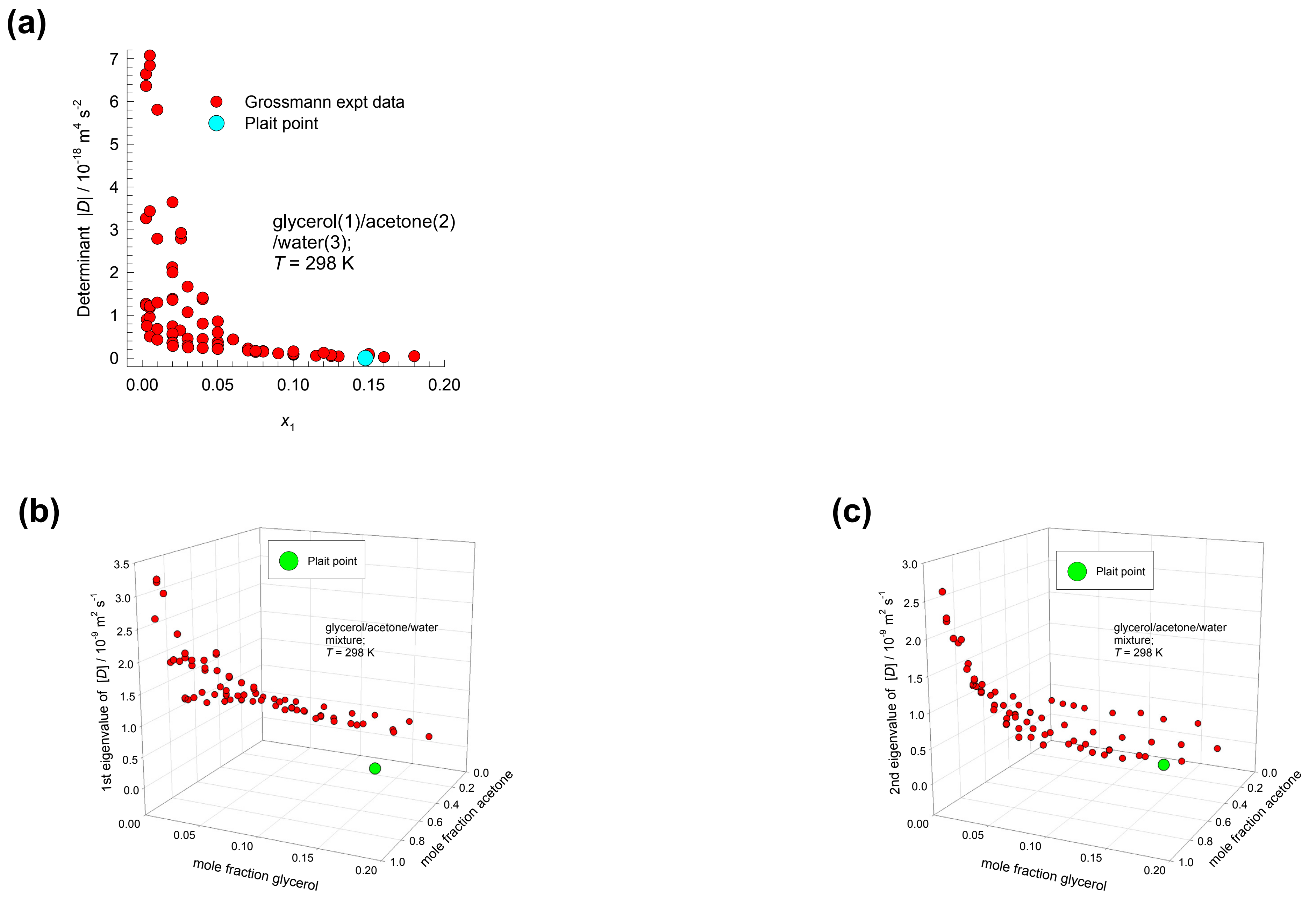

ESI Fig. 38

Strength of Coupling vs Determinant |*D*|

(a)

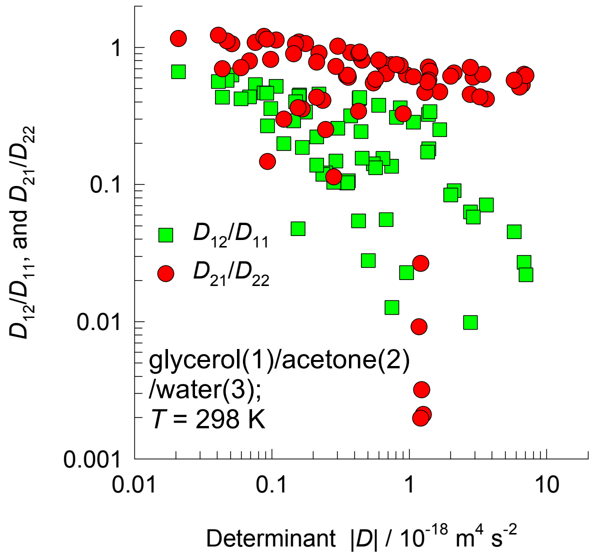

(b)

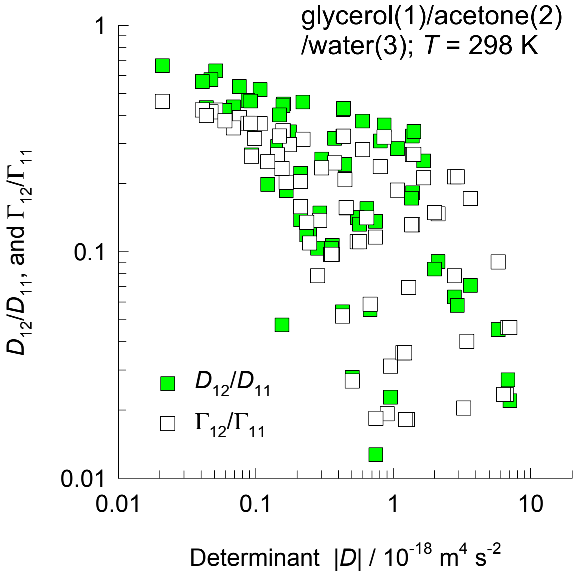

ESI Fig. 39

Factoring out thermodynamic influences

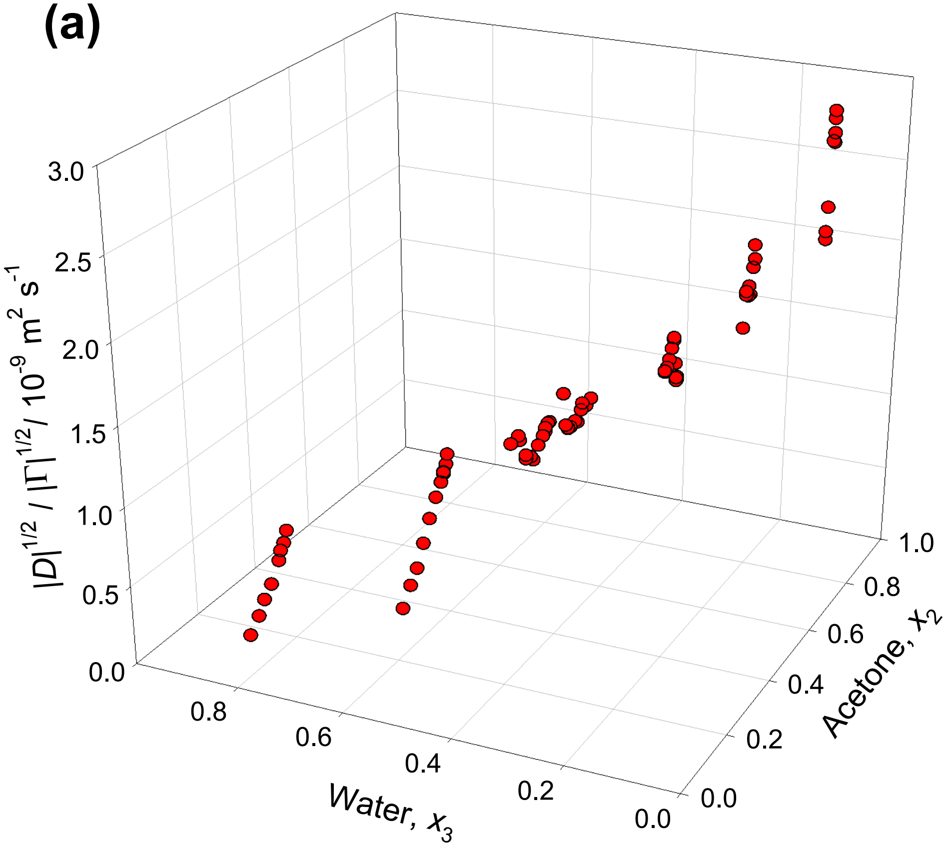

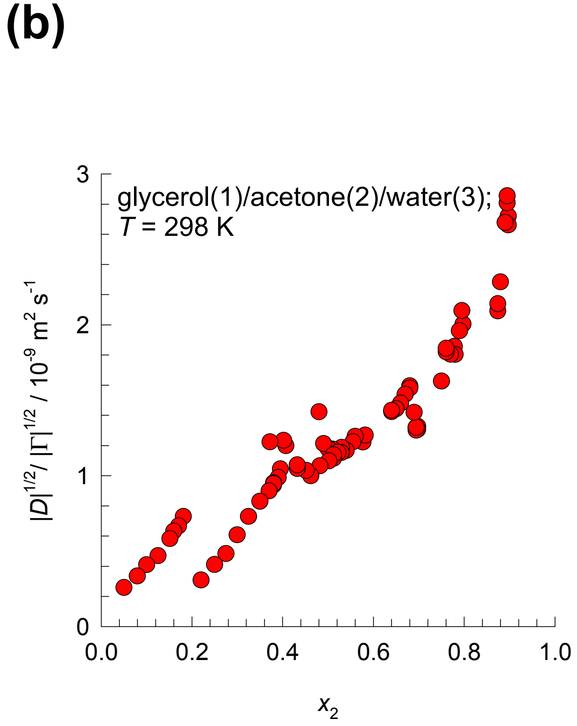

The ratio

$$\frac{|D|^{1/2}}{|\Gamma|^{1/2}}$$

can be viewed as the “magnitude” of the Maxwell-Stefan diffusivity in the *ternary* mixture.

Water/Chloroform/Acetic Acid Diffusion

ESI Fig. 40

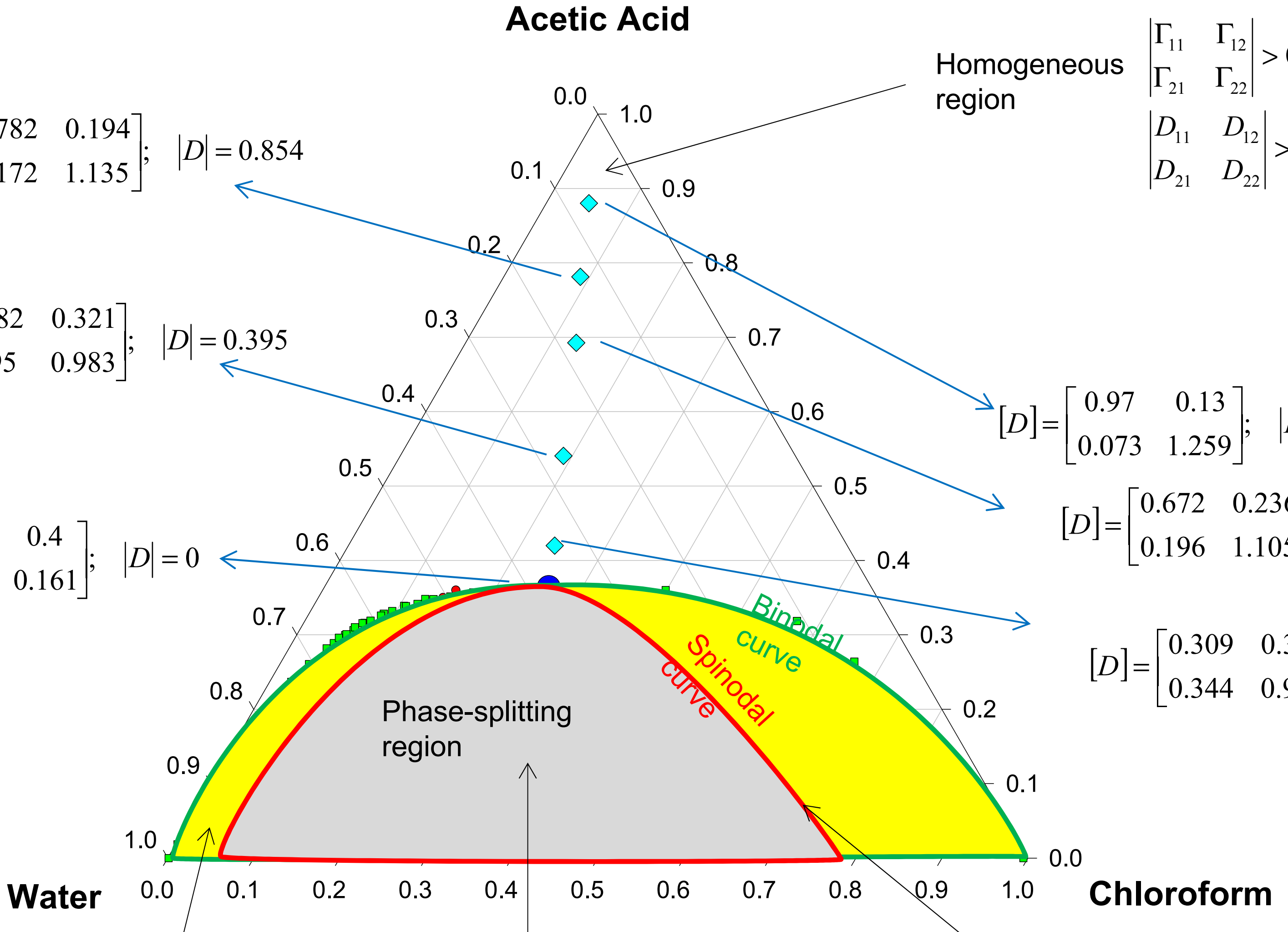

Homogeneous region

$$\begin{vmatrix} \Gamma_{11} & \Gamma_{12} \\ \Gamma_{21} & \Gamma_{22} \end{vmatrix} > 0;$$

$$\begin{vmatrix} D_{11} & D_{12} \\ D_{21} & D_{22} \end{vmatrix} > 0$$

$$[D] = \begin{bmatrix} 0.782 & 0.194 \\ 0.172 & 1.135 \end{bmatrix}; \quad |D| = 0.854$$

$$[D] = \begin{bmatrix} 0.4982 & 0.321 \\ 0.295 & 0.983 \end{bmatrix}; \quad |D| = 0.395$$

$$[D] = \begin{bmatrix} 0.92 & 0.4 \\ 0.37 & 0.161 \end{bmatrix}; \quad |D| = 0$$

$$[D] = \begin{bmatrix} 0.97 & 0.13 \\ 0.073 & 1.259 \end{bmatrix}; \quad |D| = 1.21$$

$$[D] = \begin{bmatrix} 0.672 & 0.236 \\ 0.196 & 1.105 \end{bmatrix}; \quad |D| = 0.696$$

$$[D] = \begin{bmatrix} 0.309 & 0.368 \\ 0.344 & 0.939 \end{bmatrix}; \quad |D| = 0.164$$

Meta-stable region

$$\begin{vmatrix} \Gamma_{11} & \Gamma_{12} \\ \Gamma_{21} & \Gamma_{22} \end{vmatrix} < 0;$$

$$\begin{vmatrix} D_{11} & D_{12} \\ D_{21} & D_{22} \end{vmatrix} < 0$$

$$\begin{vmatrix} \Gamma_{11} & \Gamma_{12} \\ \Gamma_{21} & \Gamma_{22} \end{vmatrix} = 0;$$

$$\begin{vmatrix} D_{11} & D_{12} \\ D_{21} & D_{22} \end{vmatrix} = 0$$

Water/Chloroform/Acetic Acid Diffusion

ESI Fig. 41

$$[D]=\begin{bmatrix}0.564 & 0.403\\ 0.185 & 0.728\end{bmatrix};\quad |D|=0.336$$

$$[D]=\begin{bmatrix}0.685 & 0.394\\ 0.107 & 0.753\end{bmatrix};\quad |D|=0.474$$

$$[D]=\begin{bmatrix}0.386 & 0.540\\ 0.117 & 0.699\end{bmatrix};\quad |D|=0.207$$

$$[D]=\begin{bmatrix}0.632 & 0.451\\ 0.138 & 0.811\end{bmatrix};\quad |D|=0.450$$

$$[D]=\begin{bmatrix}0.406 & 0.461\\ 0.181 & 0.544\end{bmatrix};\quad |D|=0.137$$

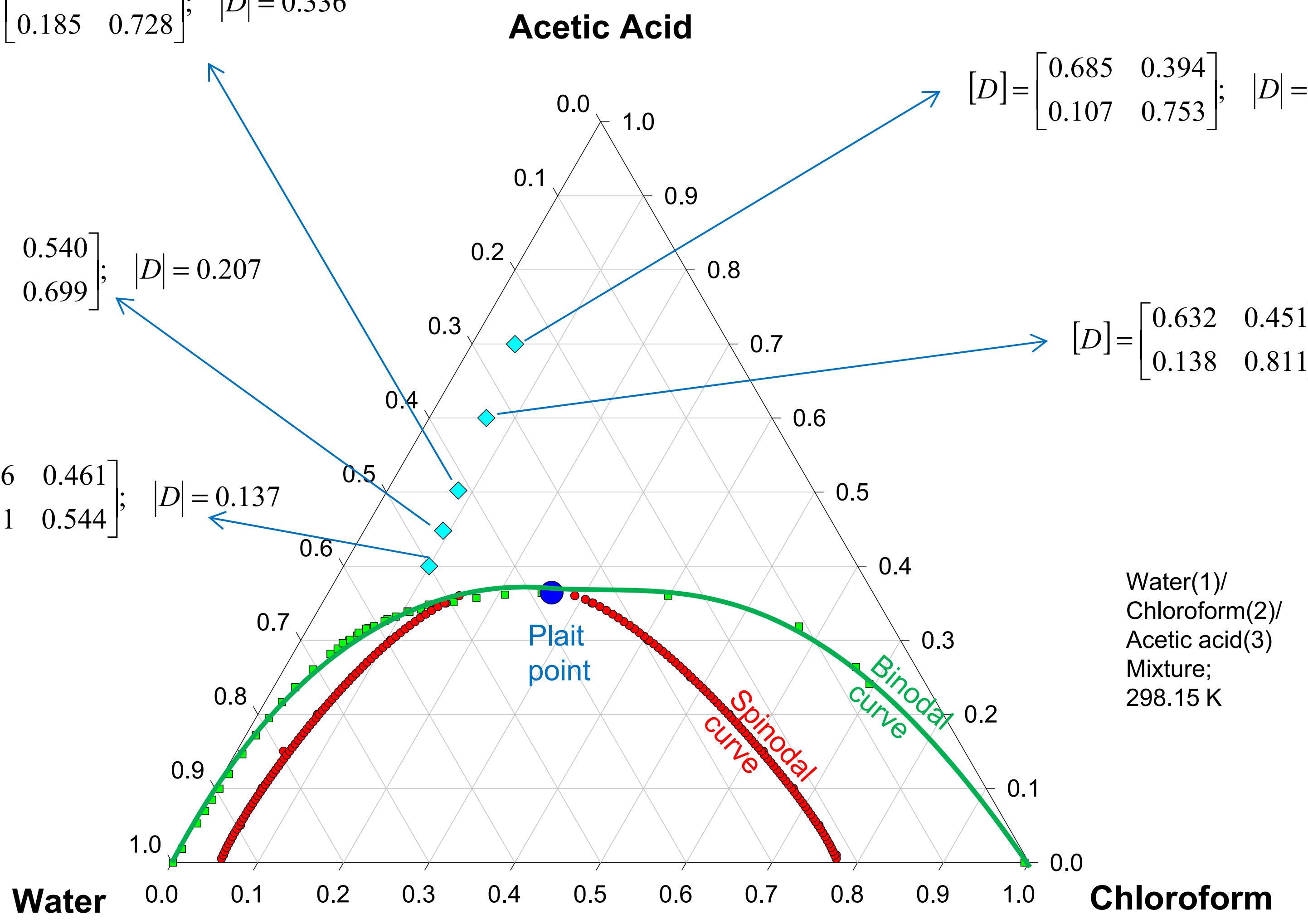

Water(1)/
Chloroform(2)/
Acetic acid(3)
Mixture;
298.15 K

ESI Fig. 42

Strength of Coupling vs Determinant of [*D*]

(a)

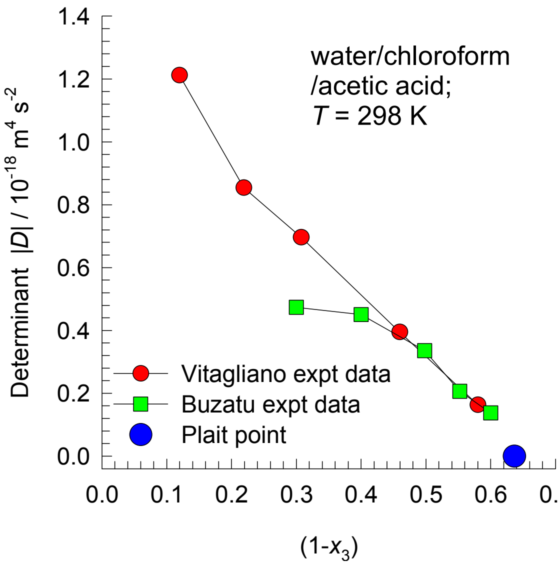

(b)

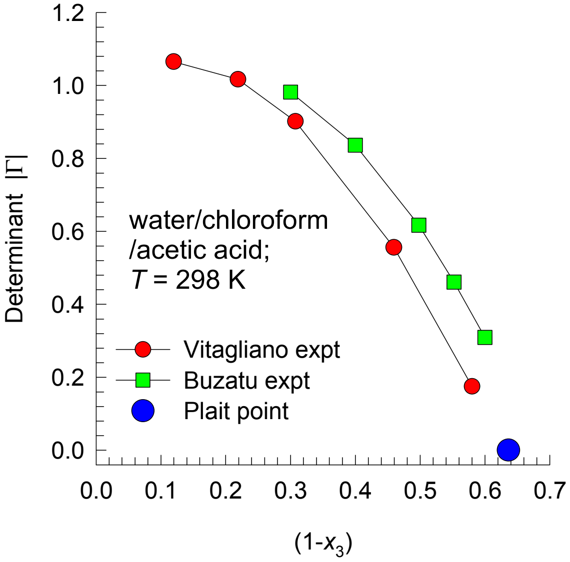

(c)

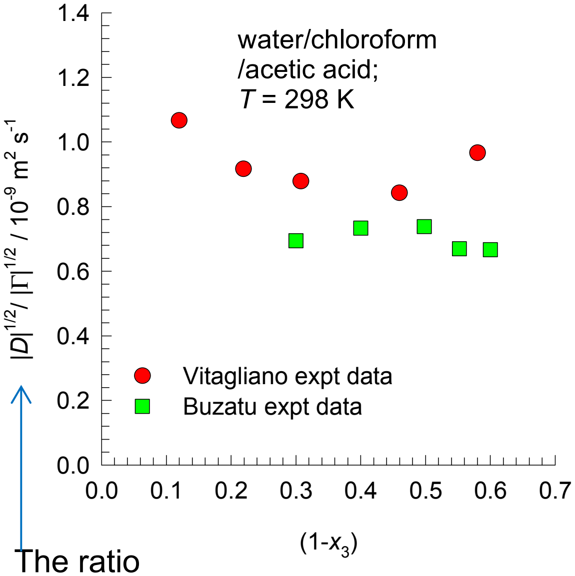

The ratio

$$\frac{|D|^{1/2}}{|\Gamma|^{1/2}}$$

can be viewed as the “magnitude” of the Maxwell-Stefan diffusivity in the *ternary* mixture.

(d)

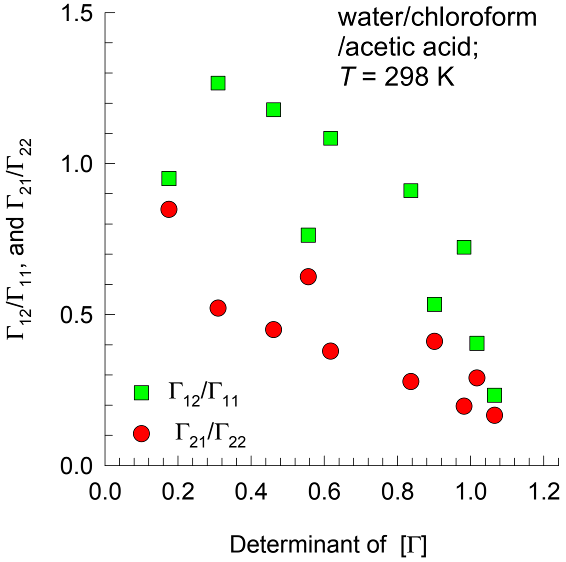

(e)

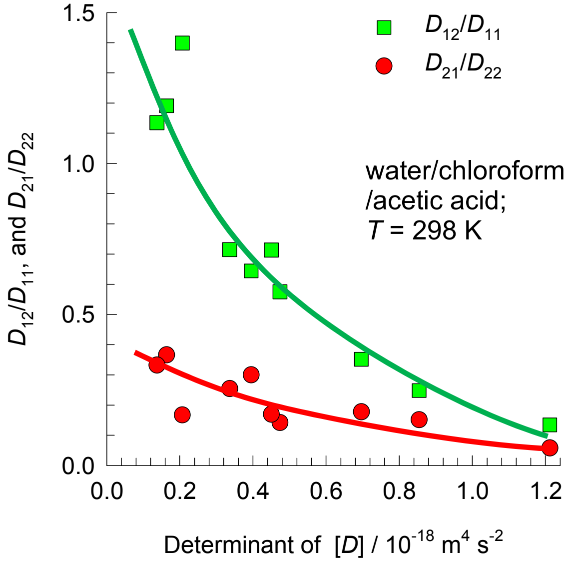

Water/2-propanol/cyclohexane mixture diffusion

ESI Fig. 43

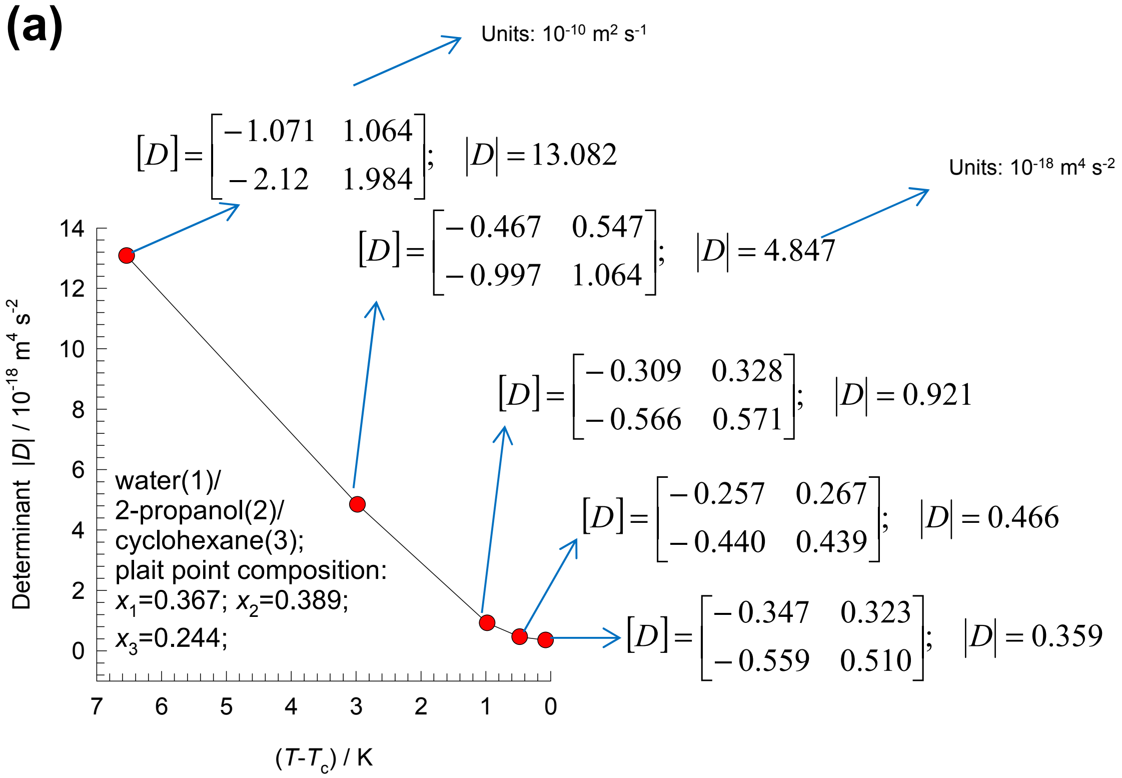

Units: 10^{-10} m^2 s^{-1}

Units: 10^{-18} m^4 s^{-2}

$$[D]=\begin{bmatrix}-1.071 & 1.064\\ -2.12 & 1.984\end{bmatrix};\quad |D|=13.082$$

$$[D]=\begin{bmatrix}-0.467 & 0.547\\ -0.997 & 1.064\end{bmatrix};\quad |D|=4.847$$

$$[D]=\begin{bmatrix}-0.309 & 0.328\\ -0.566 & 0.571\end{bmatrix};\quad |D|=0.921$$

$$[D]=\begin{bmatrix}-0.257 & 0.267\\ -0.440 & 0.439\end{bmatrix};\quad |D|=0.466$$

$$[D]=\begin{bmatrix}-0.347 & 0.323\\ -0.559 & 0.510\end{bmatrix};\quad |D|=0.359$$

water(1)/
2-propanol(2)/
cyclohexane(3);
plait point composition:
x_1=0.367; x_2=0.389;
x_3=0.244;

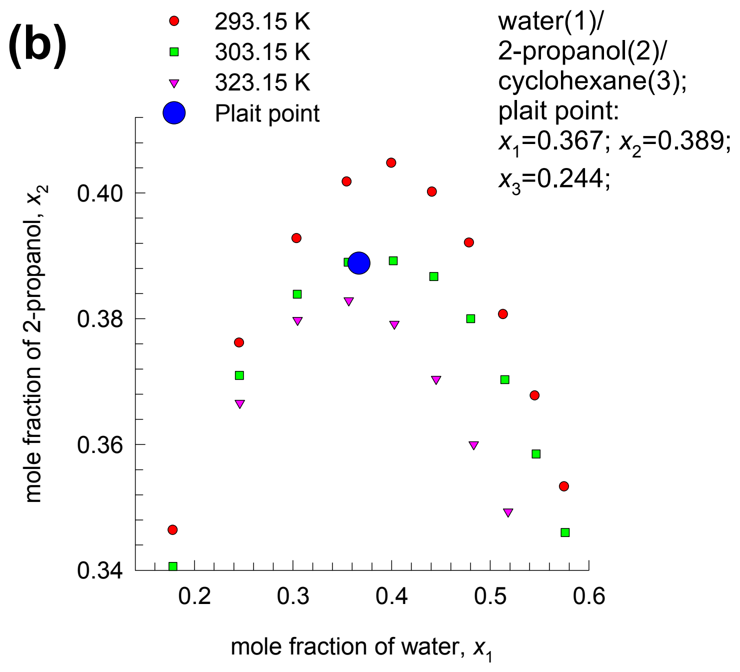

water(1)/
2-propanol(2)/
cyclohexane(3);
plait point:
x_1=0.367; x_2=0.389;
x_3=0.244;

Acetone/Water/Ethylacetate: Diffusivities in EA rich region

ESI Fig. 44

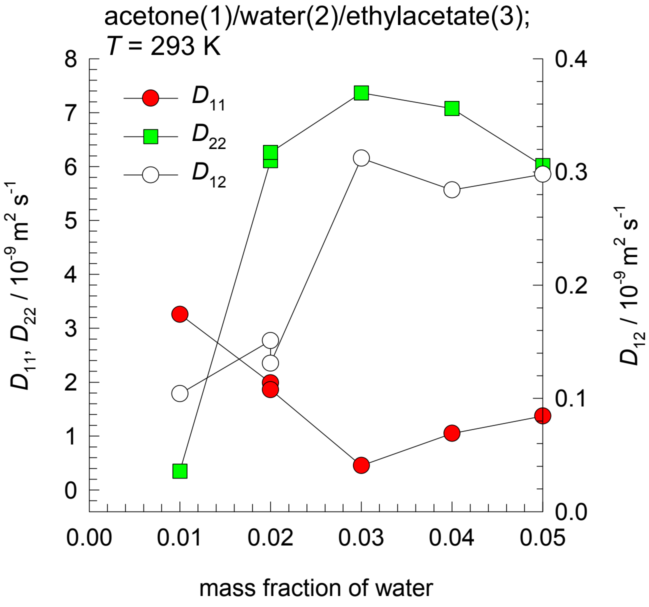

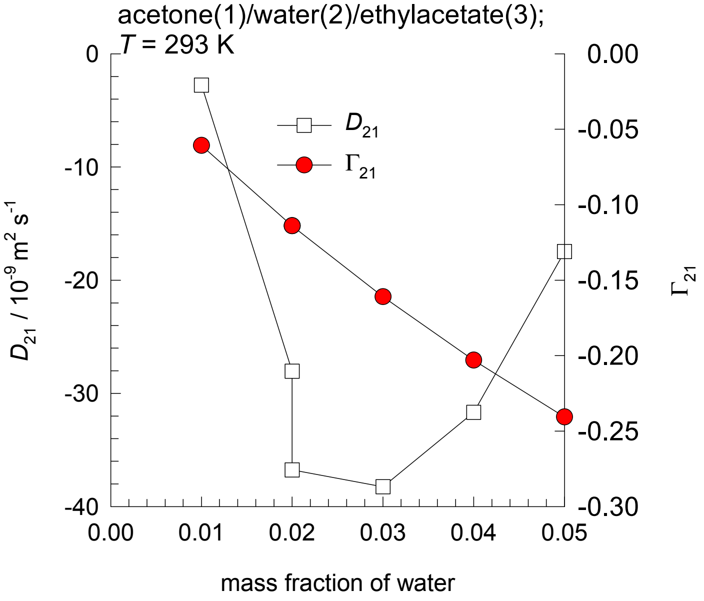

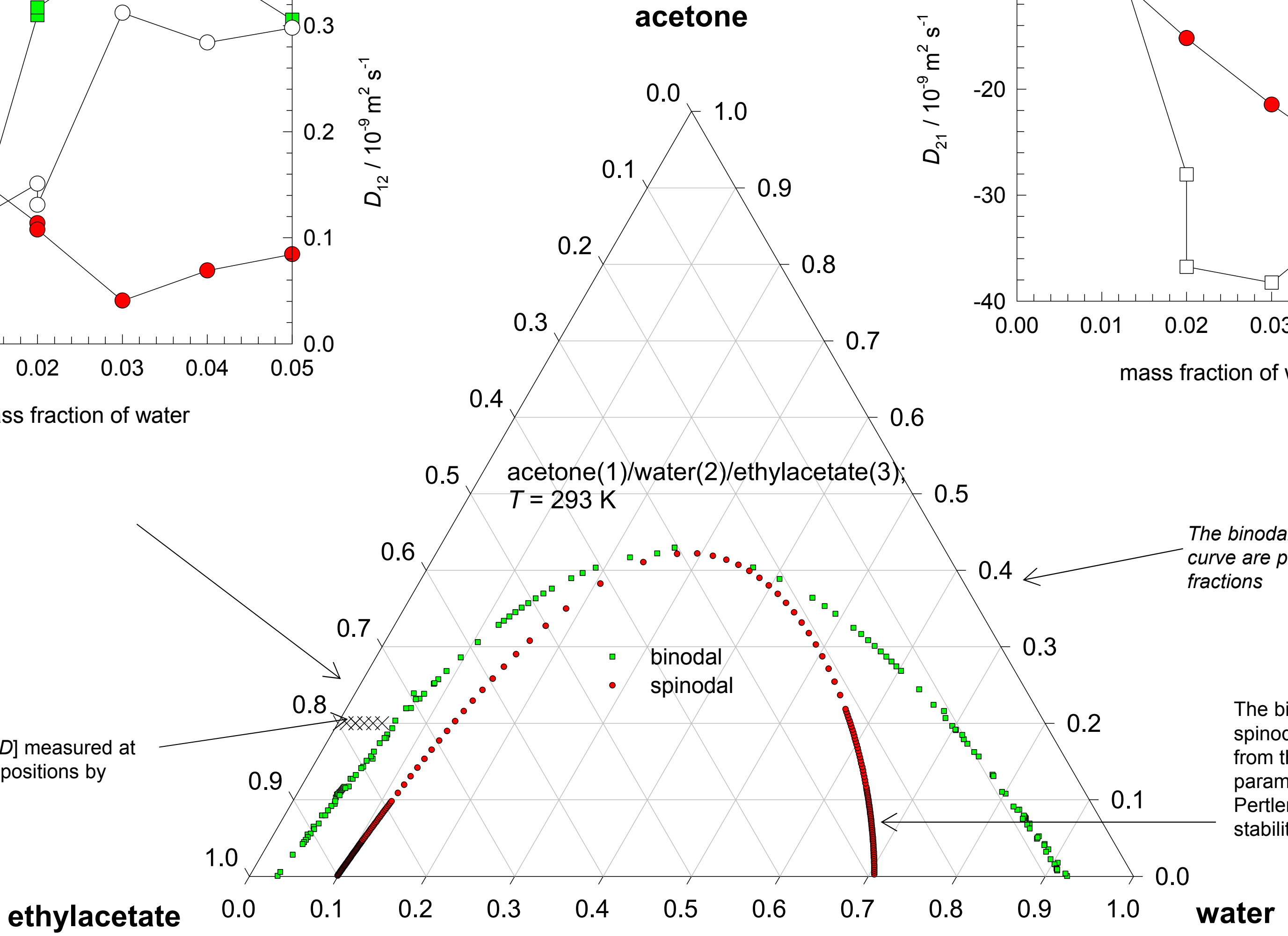

The binodal and spinodal curve are plotted in mass fractions

Fick matrix [*D*] measured at these 6 compositions by Pertler

The binodal and spinodal curves calculated from the UNIQUAC parameters supplied by Pertler, by applying the stability constraints

Acetone/Ethylacetate/Water: Diffusivities in water rich region

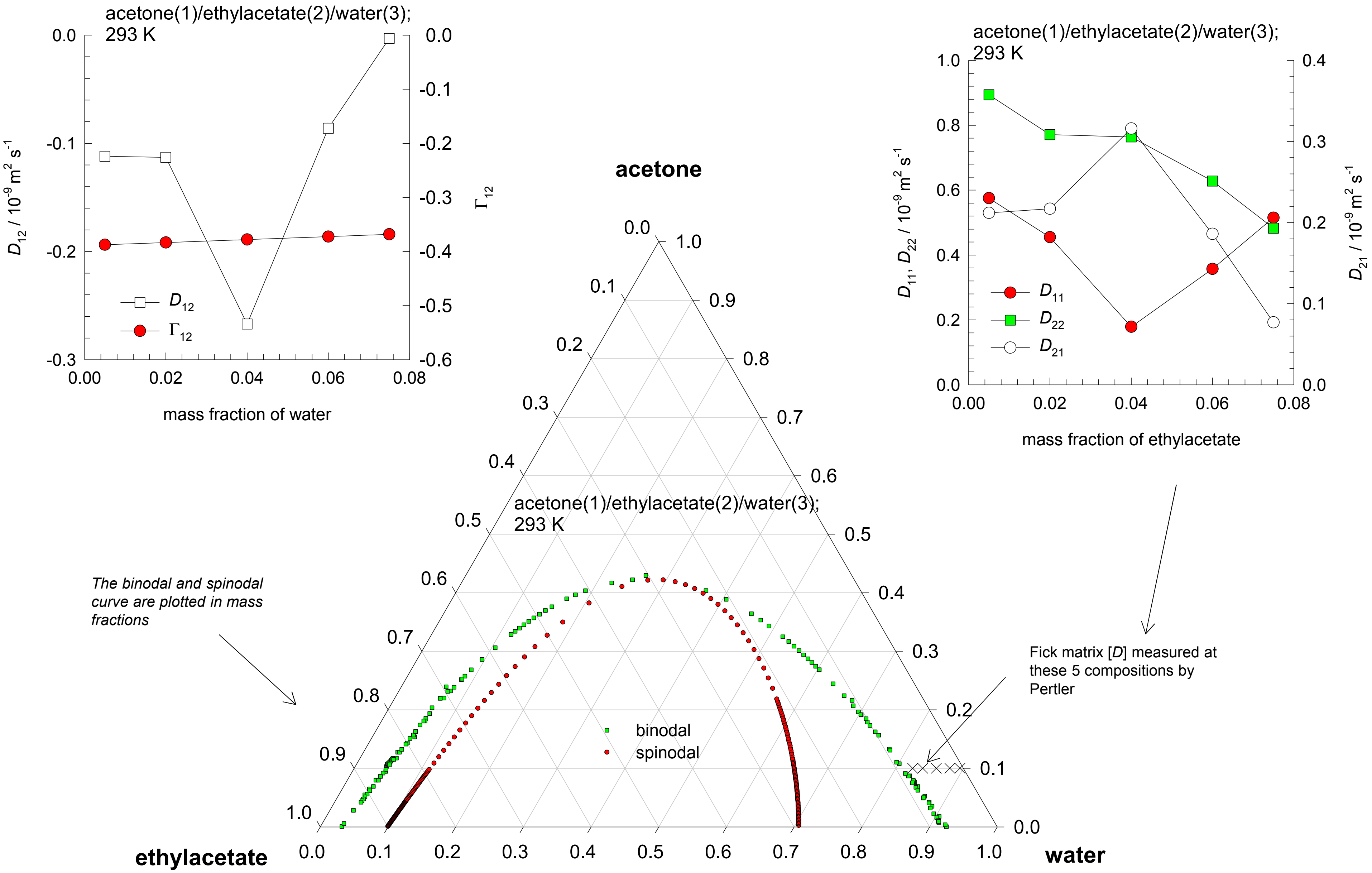

The binodal and spinodal curve are plotted in mass fractions

Fick matrix [*D*] measured at these 5 compositions by Pertler

Water/Chloroform/Acetic Acid Diffusion

ESI Fig. 46

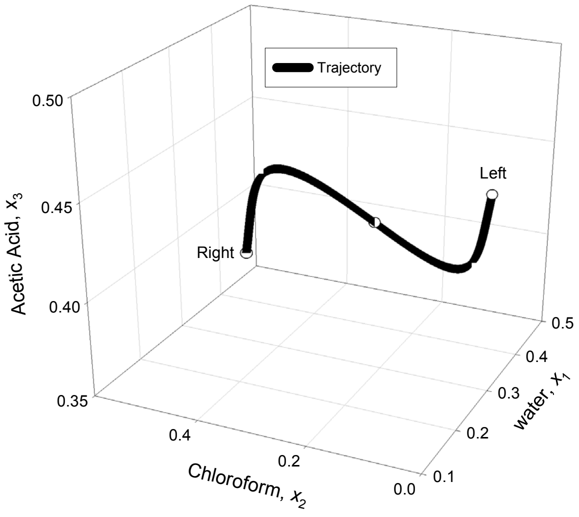

Trajectory calculated using

$$[D] = \begin{bmatrix} 0.309 & 0.368 \\ 0.344 & 0.939 \end{bmatrix}; \quad |D| = 0.164$$

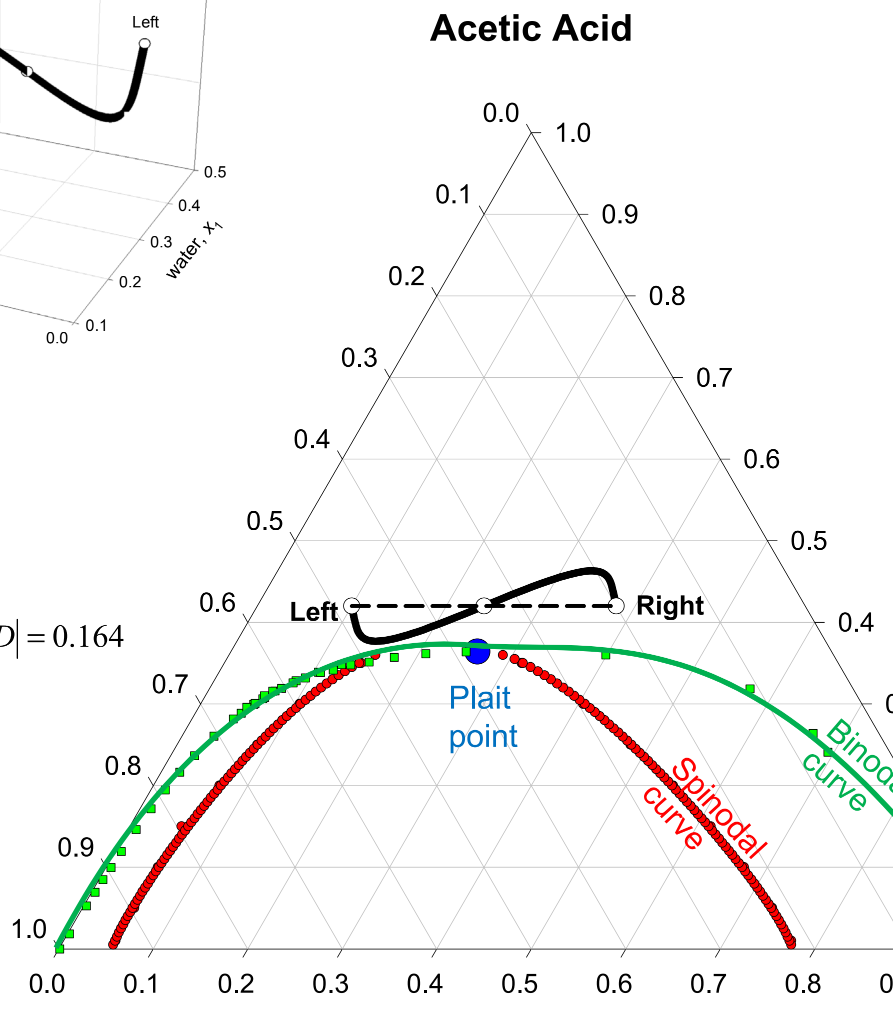

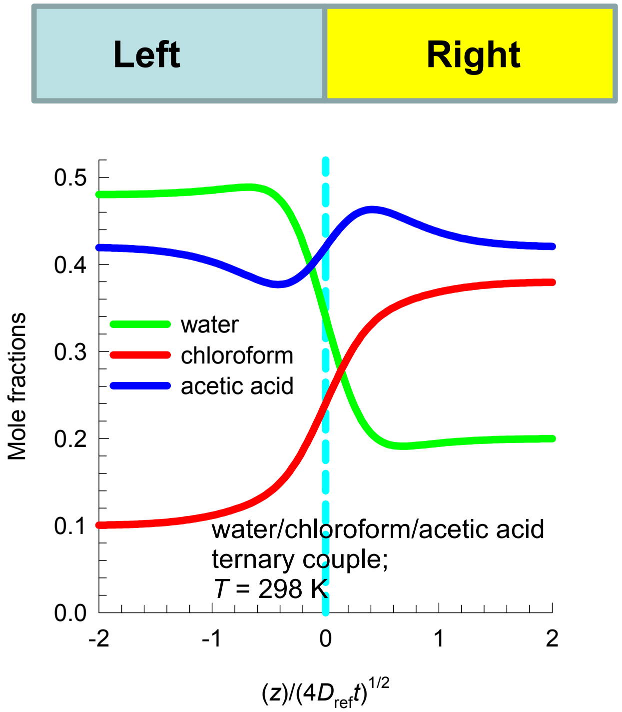

Glycerol/Acetone/Water Equilibration

ESI Fig. 47

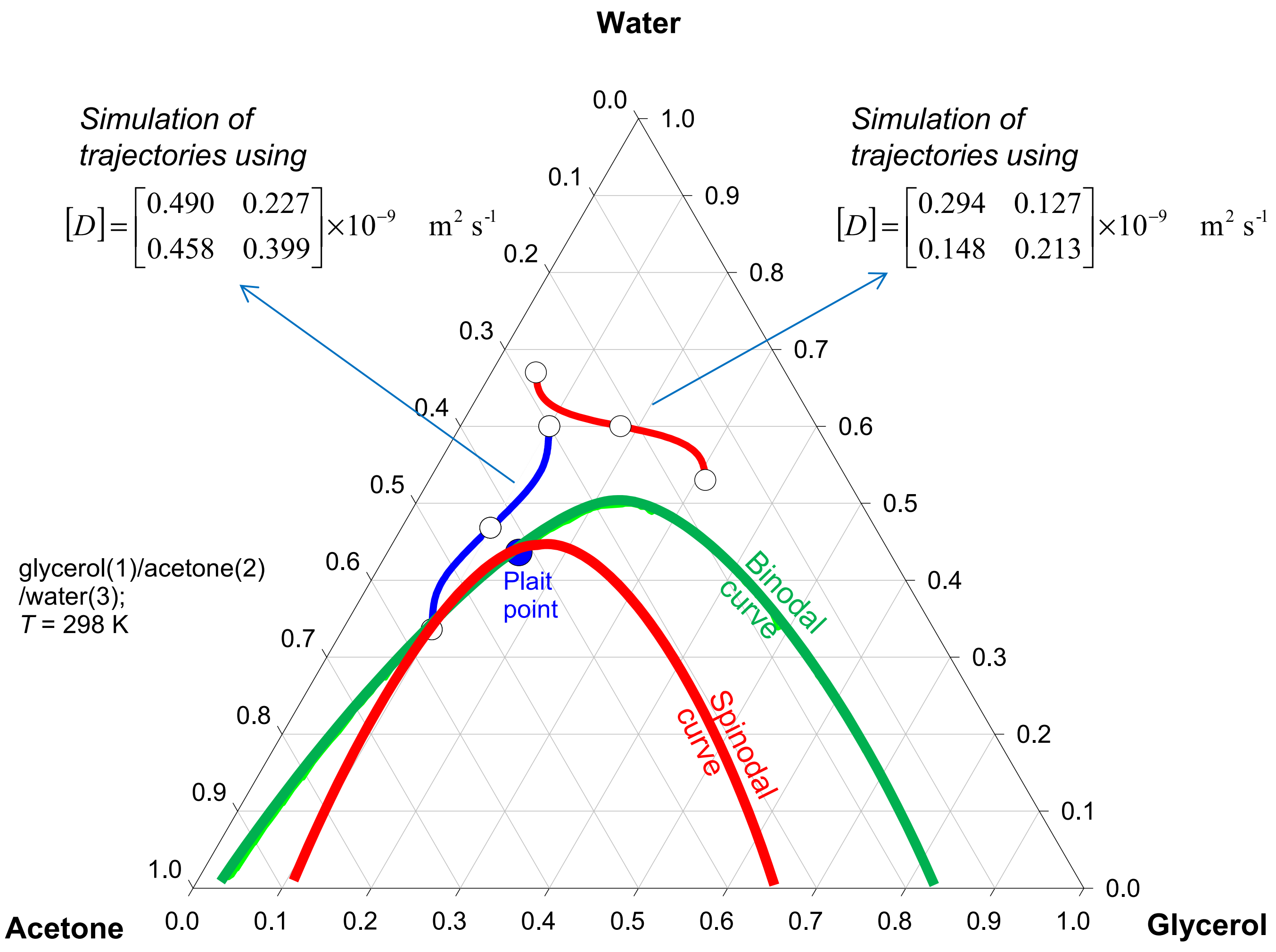

Simulation of trajectories using

$$[D]=\begin{bmatrix}0.490 & 0.227\\0.458 & 0.399\end{bmatrix}\times10^{-9}\quad \mathrm{m^2\ s^{-1}}$$

Simulation of trajectories using

$$[D]=\begin{bmatrix}0.294 & 0.127\\0.148 & 0.213\end{bmatrix}\times10^{-9}\quad \mathrm{m^2\ s^{-1}}$$

glycerol(1)/acetone(2)
/water(3);
T = 298 K

Glycerol/Acetone/Water Equilibration

ESI Fig. 48

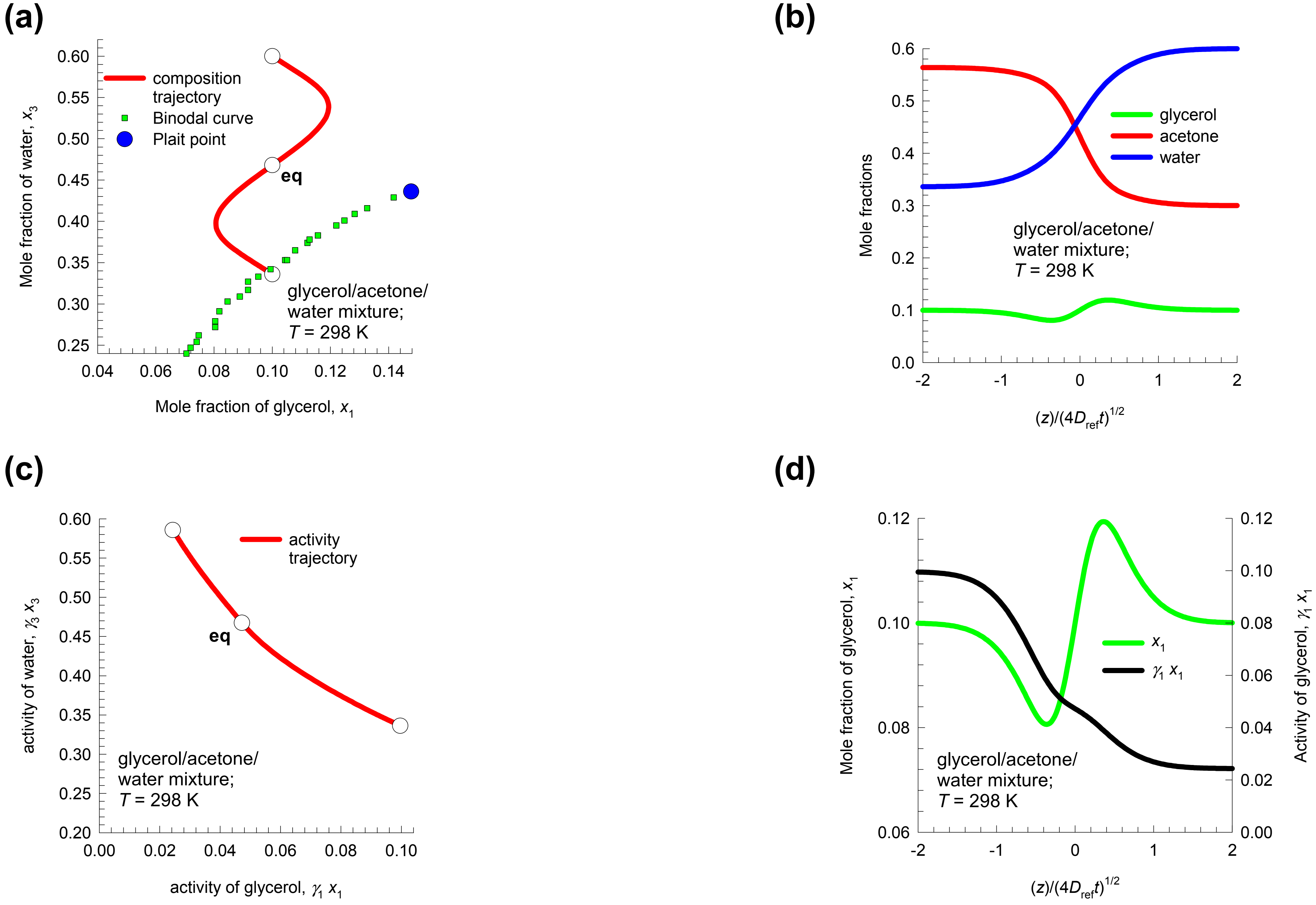

Glycerol/Acetone/Water Equilibration

ESI Fig. 49

(a)

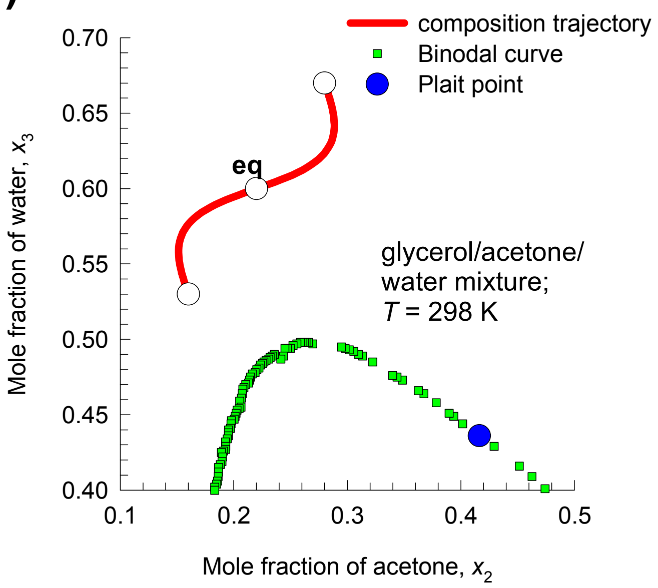

(b)

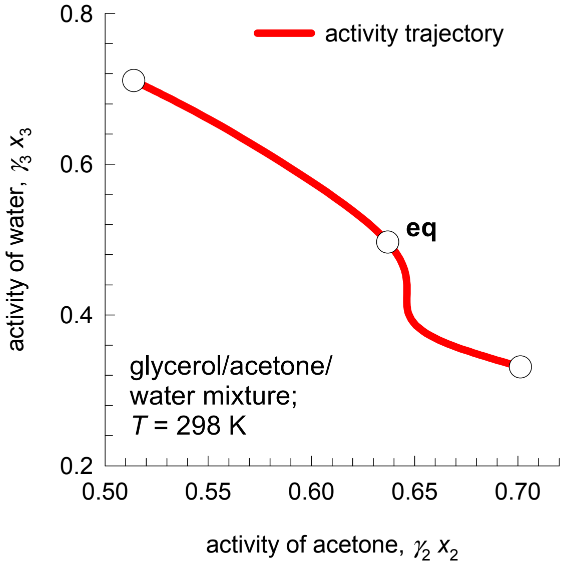

(c)

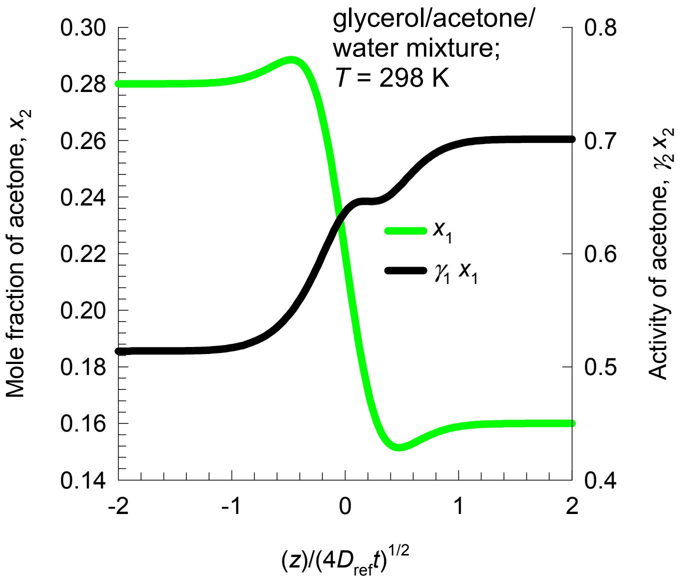

Water/Chloroform/Acetic Acid Diffusion

ESI Fig. 50

Trajectory calculated using

$$[D] = \begin{bmatrix} 0.92 & 0.4 \\ 0.37 & 0.161 \end{bmatrix}; \quad |D| = 0$$

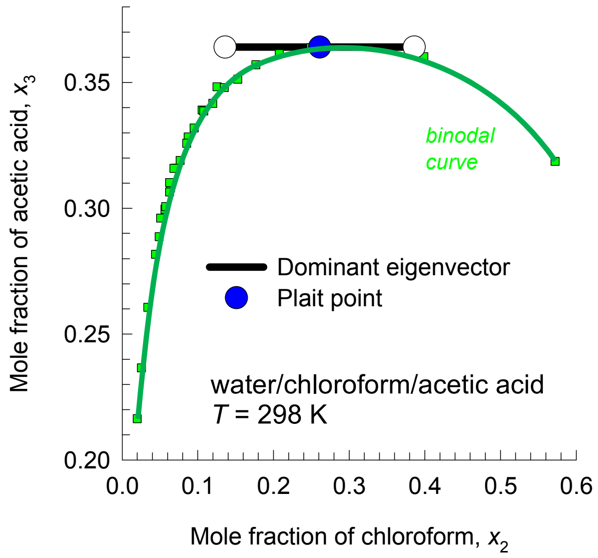

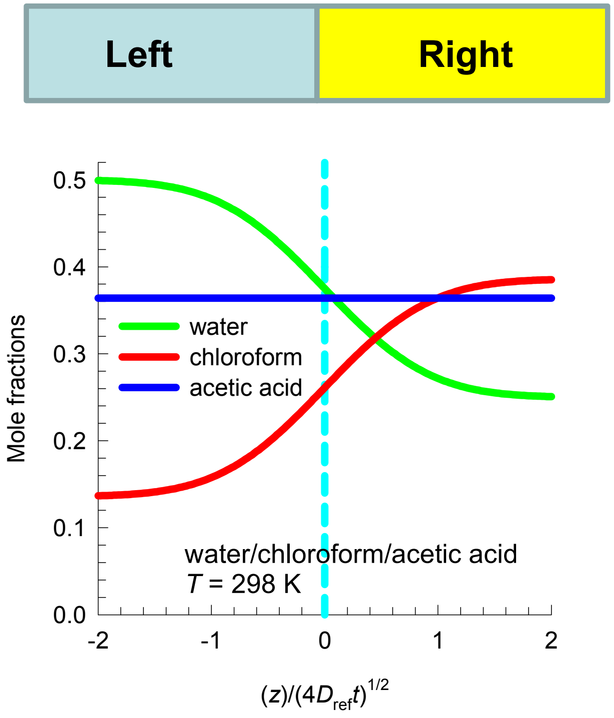

Glycerol/Acetone/Water Diffusion

ESI Fig. 51

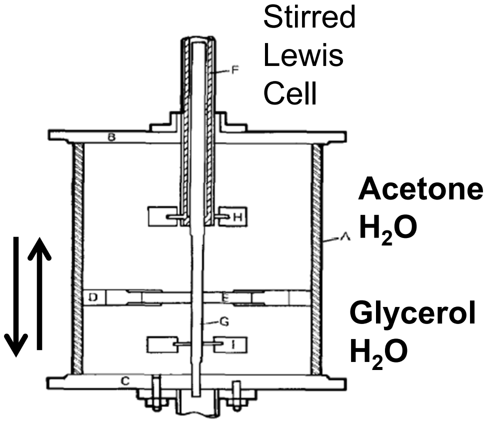

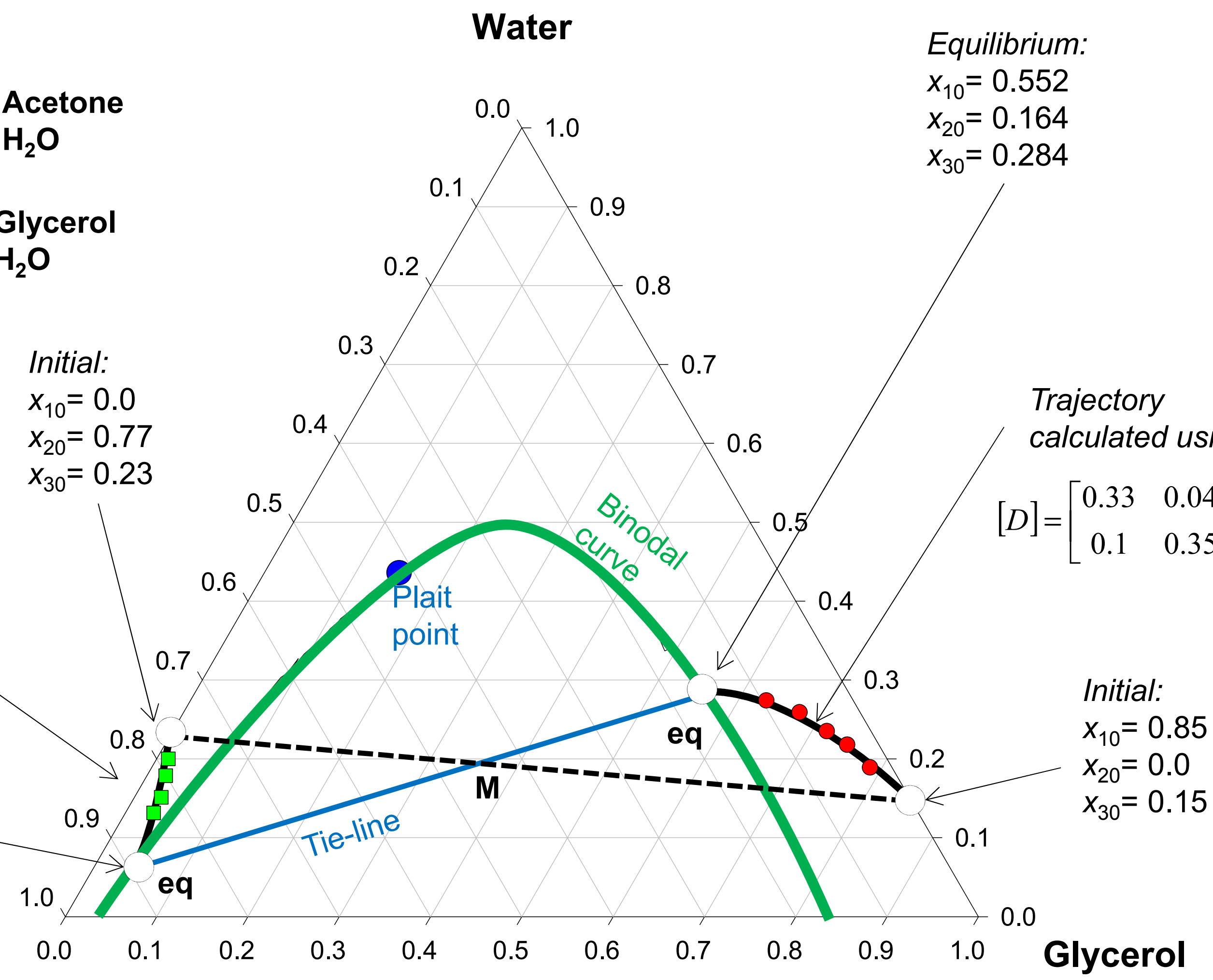

Initial:
x_{10}= 0.0
x_{20}= 0.77
x_{30}= 0.23

Trajectory calculated using

$$[D]=\begin{bmatrix}2.4 & 0.1\\ 1 & 1.1\end{bmatrix}\times10^{-9}\quad \mathrm{m^2\ s^{-1}}$$

Equilibrium:
x_{10}= 0.042
x_{20}= 0.894
x_{30}= 0.064

Equilibrium:
x_{10}= 0.552
x_{20}= 0.164
x_{30}= 0.284

Trajectory calculated using

$$[D]=\begin{bmatrix}0.33 & 0.04\\ 0.1 & 0.35\end{bmatrix}\times10^{-9}\quad \mathrm{m^2\ s^{-1}}$$

Initial:
x_{10}= 0.85
x_{20}= 0.0
x_{30}= 0.15

ESI Fig. 52

Transient trajectory to equilibrium

Transient equilibration is captured by coupled Fick matrix

$$[D]=\begin{bmatrix}0.33 & 0.04\\ 0.1 & 0.35\end{bmatrix}\times10^{-9}\quad \mathrm{m^2\ s^{-1}}$$

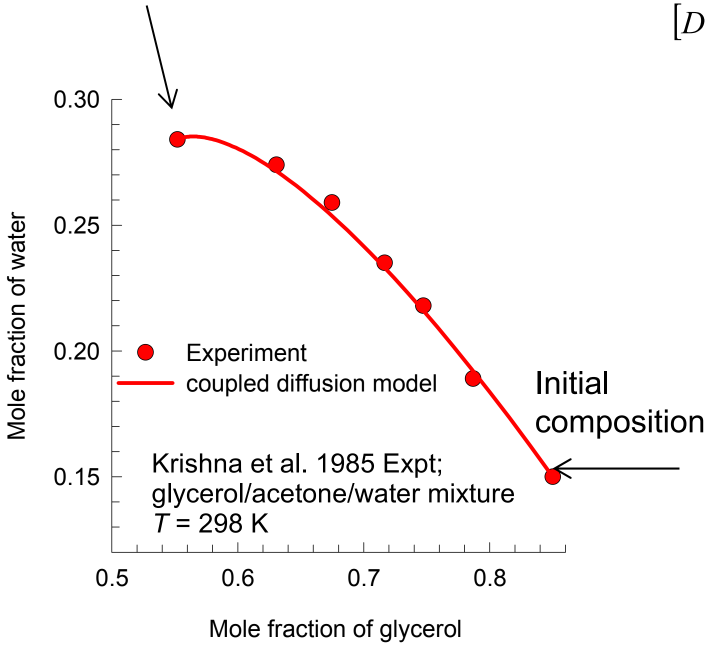

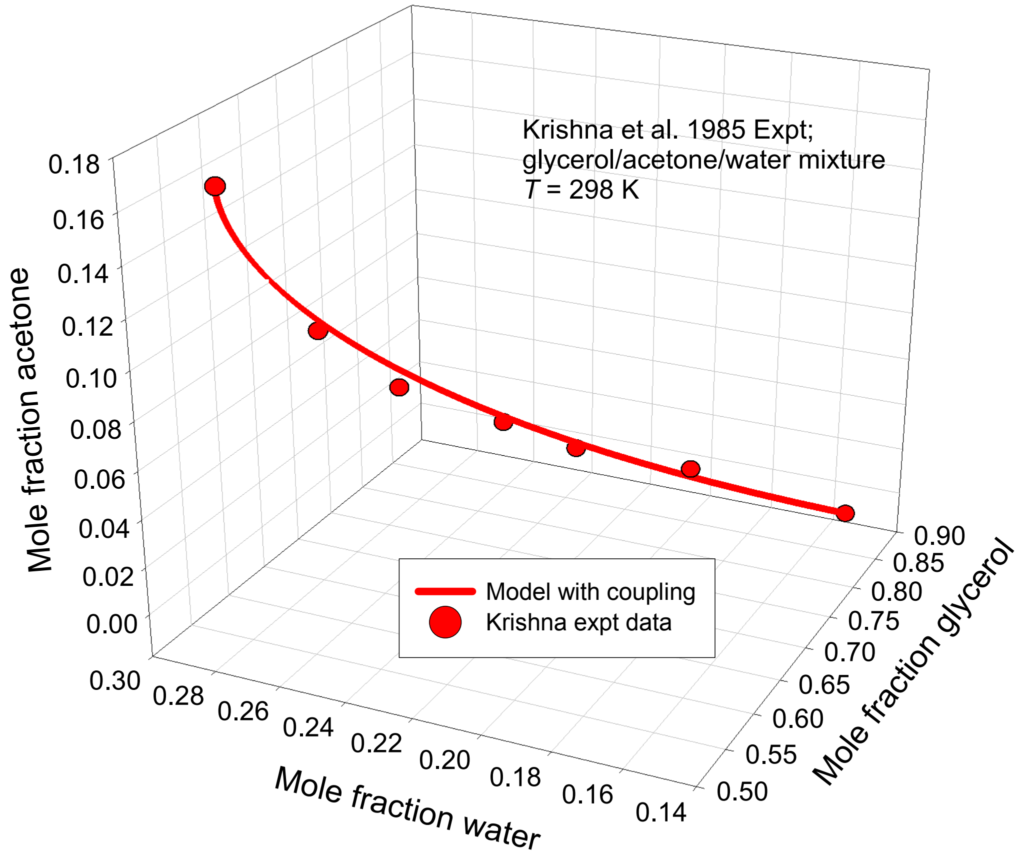

Please note that the component numbering is
1 = glycerol
2 = acetone
3 = water

ESI Fig. 53

Transient trajectory to equilibrium

Initial composition

Transient equilibration is captured by coupled Fick matrix

$$[D] = \begin{bmatrix} 2.4 & 0.1 \\ 1 & 1.1 \end{bmatrix} \times 10^{-9} \quad \mathrm{m^2\ s^{-1}}$$

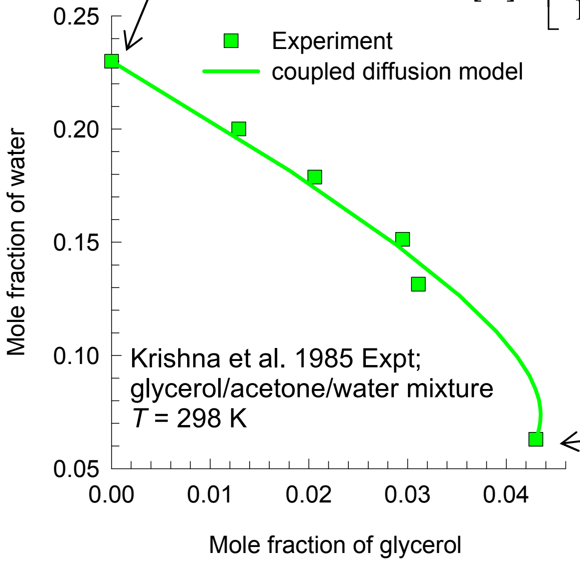

Equilibrium

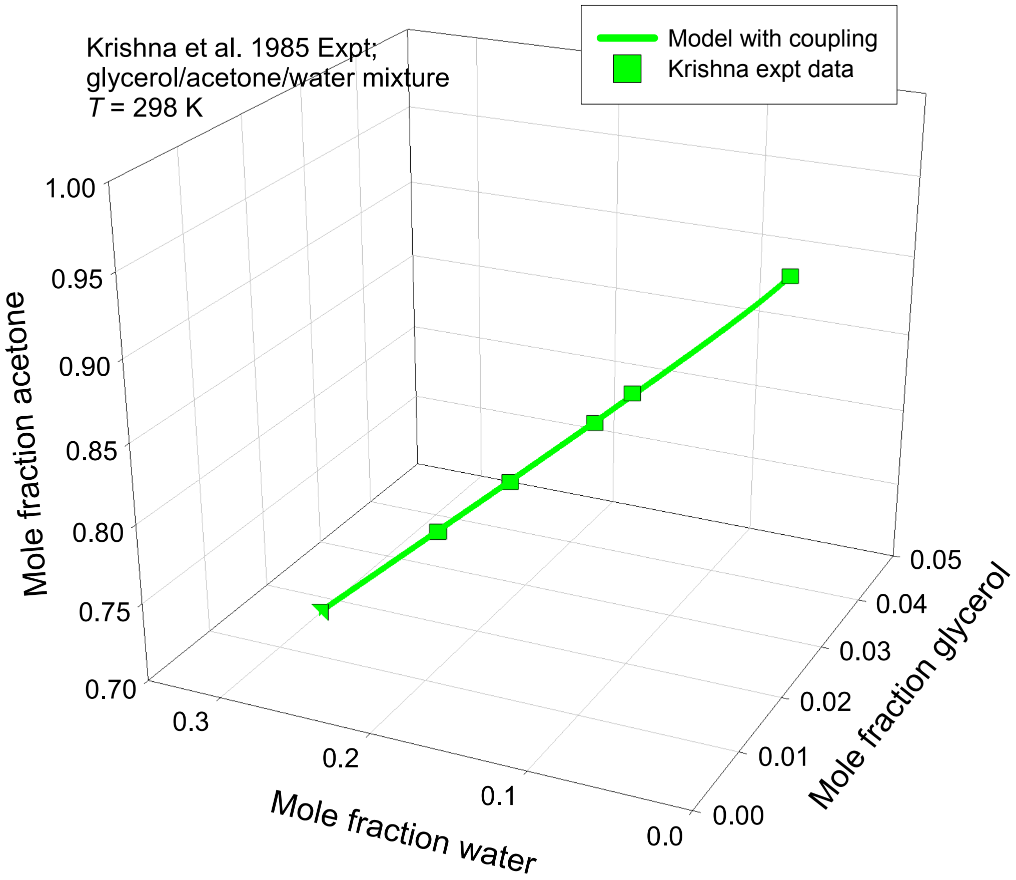

Please note that the component numbering is
1 = glycerol
2 = acetone
3 = water

Acetone/Ethylacetate/Water: equilibration trajectory

ESI Fig. 54

The phase diagram is drawn in mass fractions

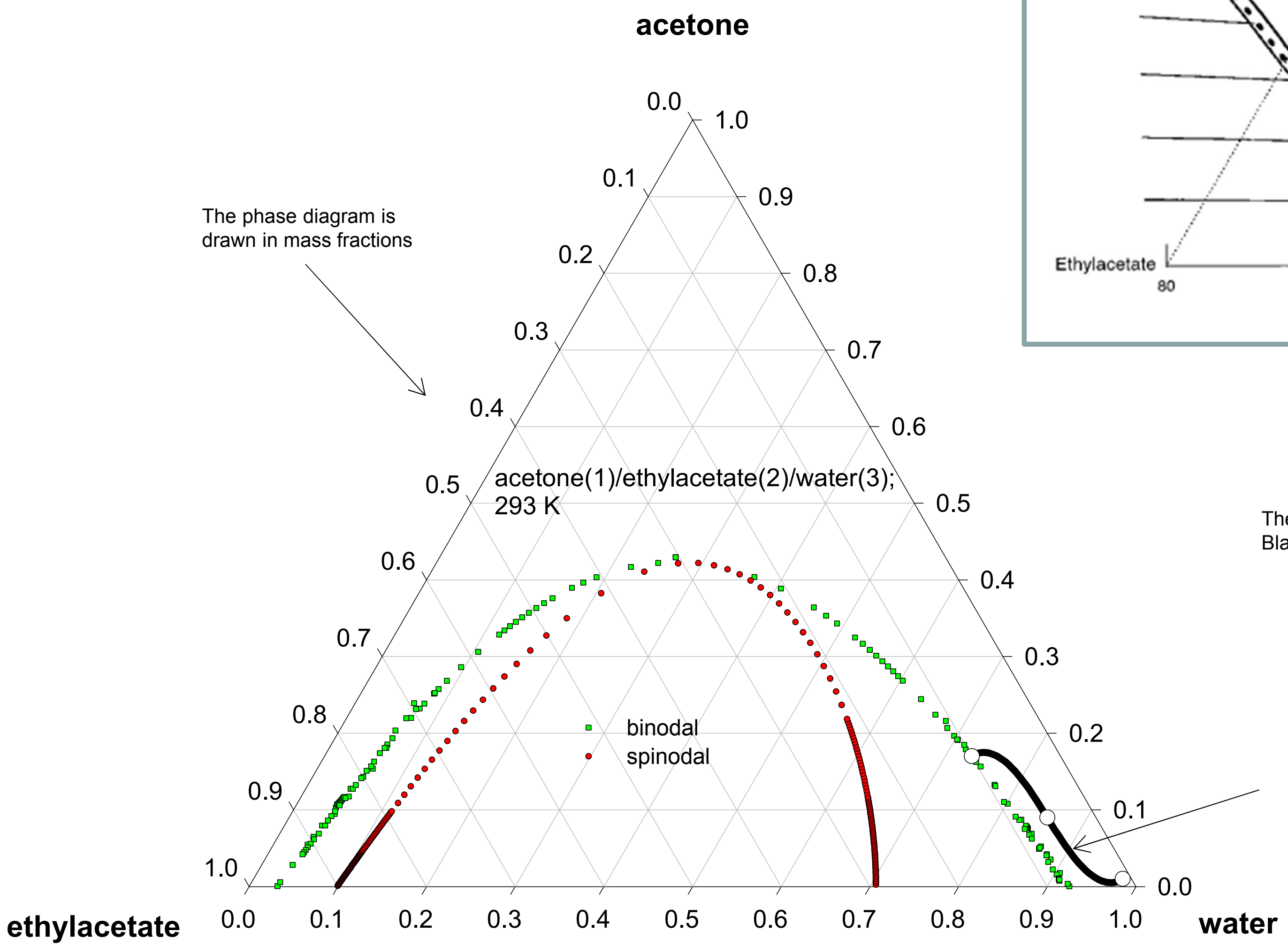

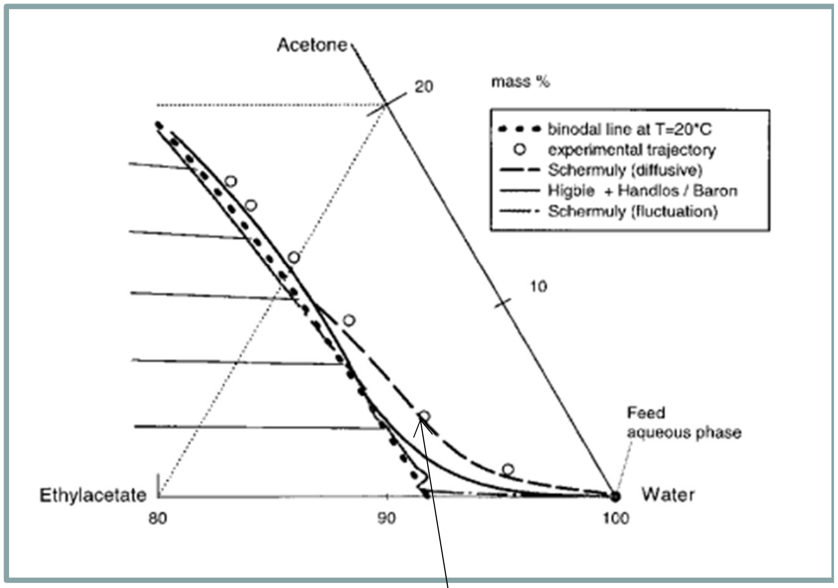

These are experimental data points of Haeberl and Blass.

Serpentine trajectory
The simulations are performed with the values of the Fick diffusivity matrix corresponding to the thrid data point of Pertler

$$[D]=\begin{bmatrix}0.179 & -0.287\\ 0.316 & 0.764\end{bmatrix}\times10^{-9} \quad \mathrm{m^2\ s^{-1}}$$

Glycerol/Acetone/Water Mixture Diffusion

ESI Fig. 55

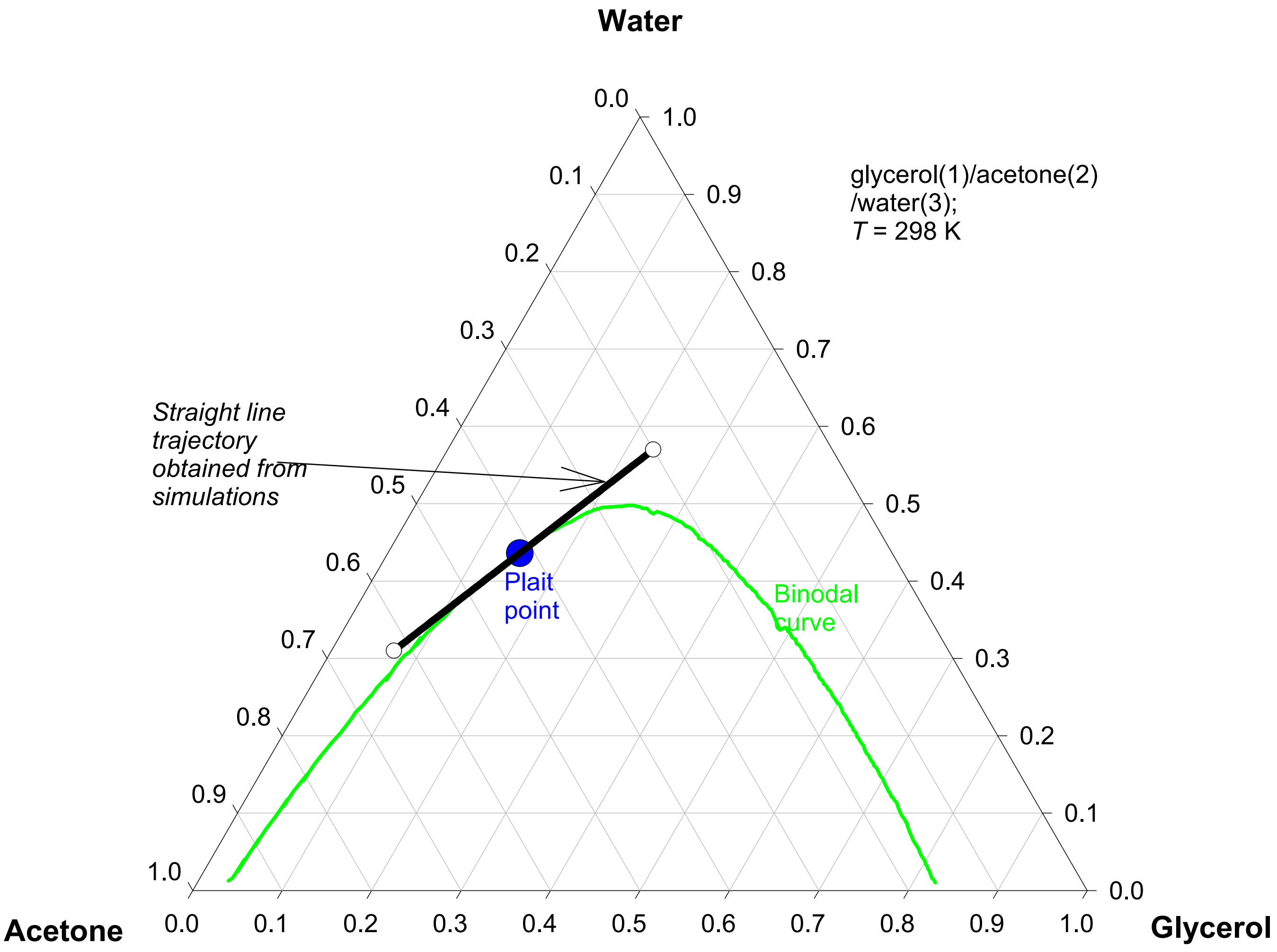

The Ouzo Effect

ESI Fig. 56

45% vol ethanol
55% vol water
≈ 0.1% vol trans-anethol

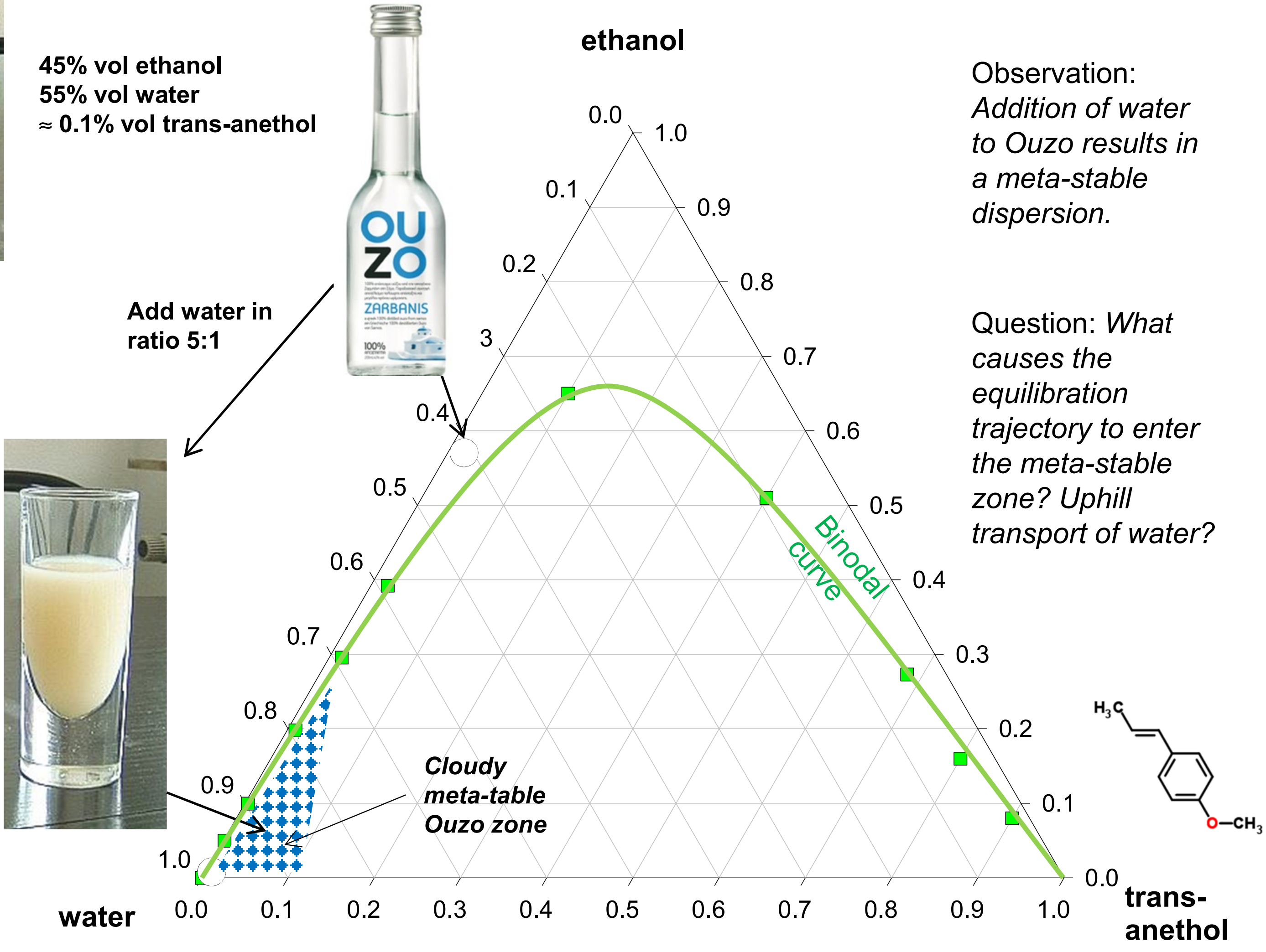

Observation: *Addition of water to Ouzo results in a meta-stable dispersion.*

Question: *What causes the equilibration trajectory to enter the meta-stable zone? Uphill transport of water?*

Equilibration trajectory – Ouzo effect

ESI Fig. 57

Ruschak-Miller straight line equilibration for addition of water to neat Ouzo

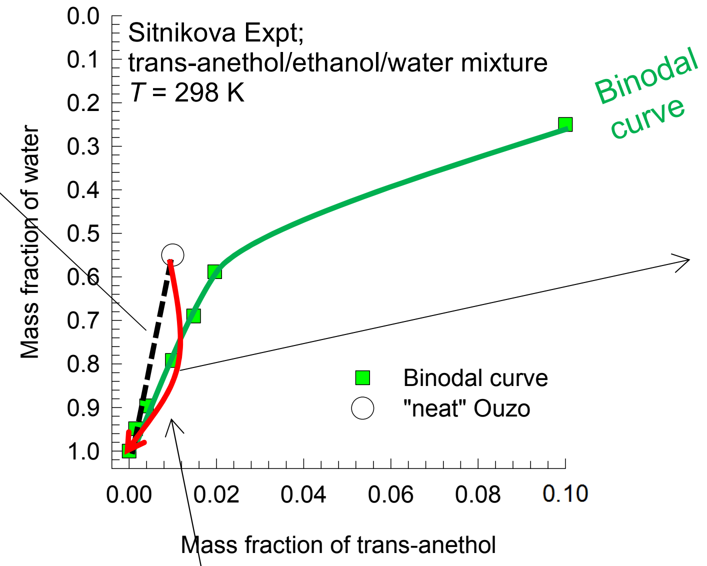

Does the equilibration follow a curvilinear trajectory?

45% vol ethanol
55% vol water
≈ 0.1% vol trans-anethol

Add water in ratio 5:1

This must lie in the meta-stable region between the binodal and spinodal envelopes

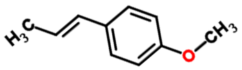

Linear and Serpentine Trajectories

ESI Fig. 58

These are not simulated trajectories, just scenarios that are possible.

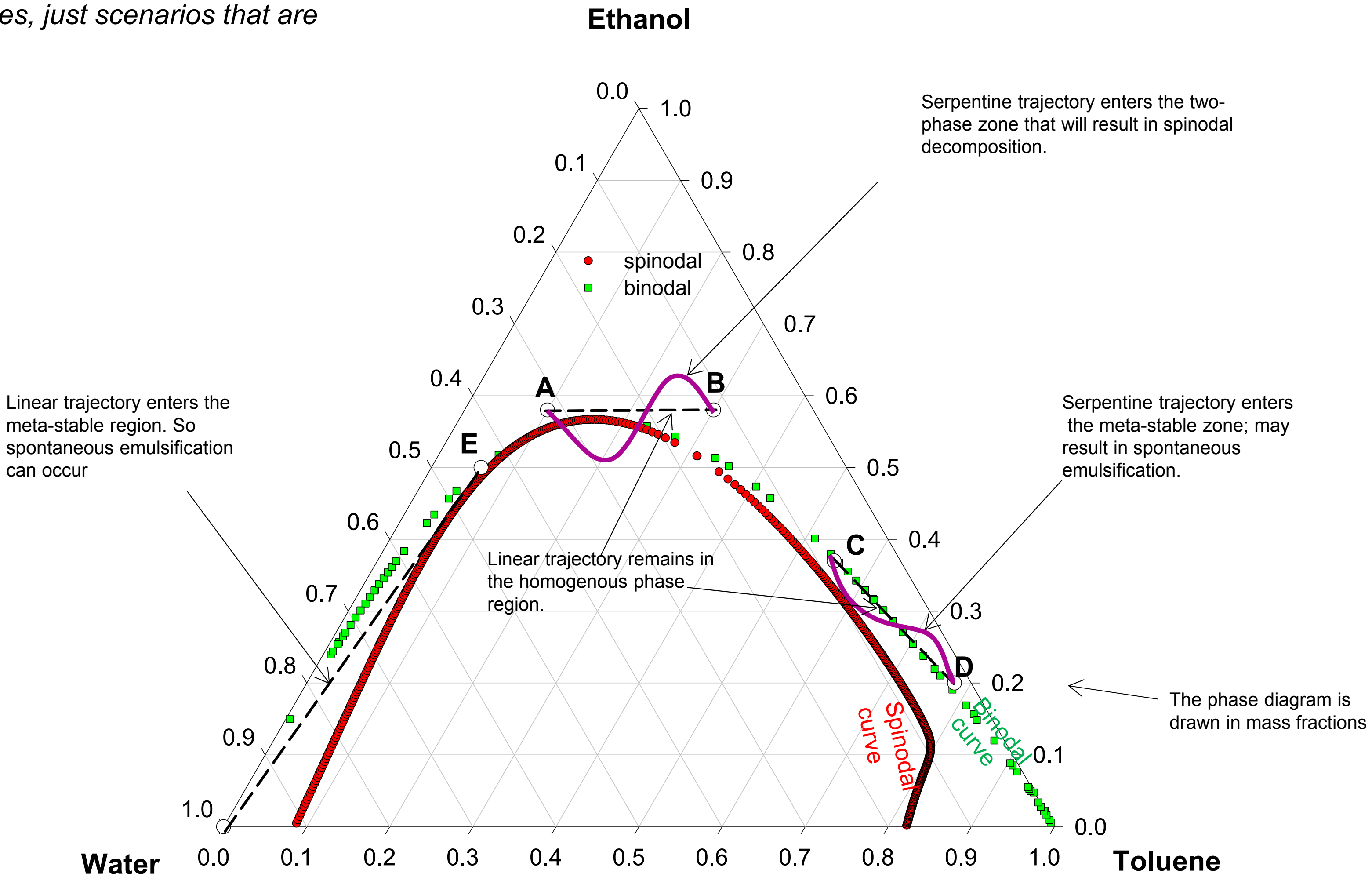

Serpentine trajectory enters the two-phase zone that will result in spinodal decomposition.

Linear trajectory enters the meta-stable region. So spontaneous emulsification can occur

Serpentine trajectory enters the meta-stable zone; may result in spontaneous emulsification.

Linear trajectory remains in the homogenous phase region.

The phase diagram is drawn in mass fractions

Water/Chloroform/Acetic Acid Diffusion

ESI Fig. 59

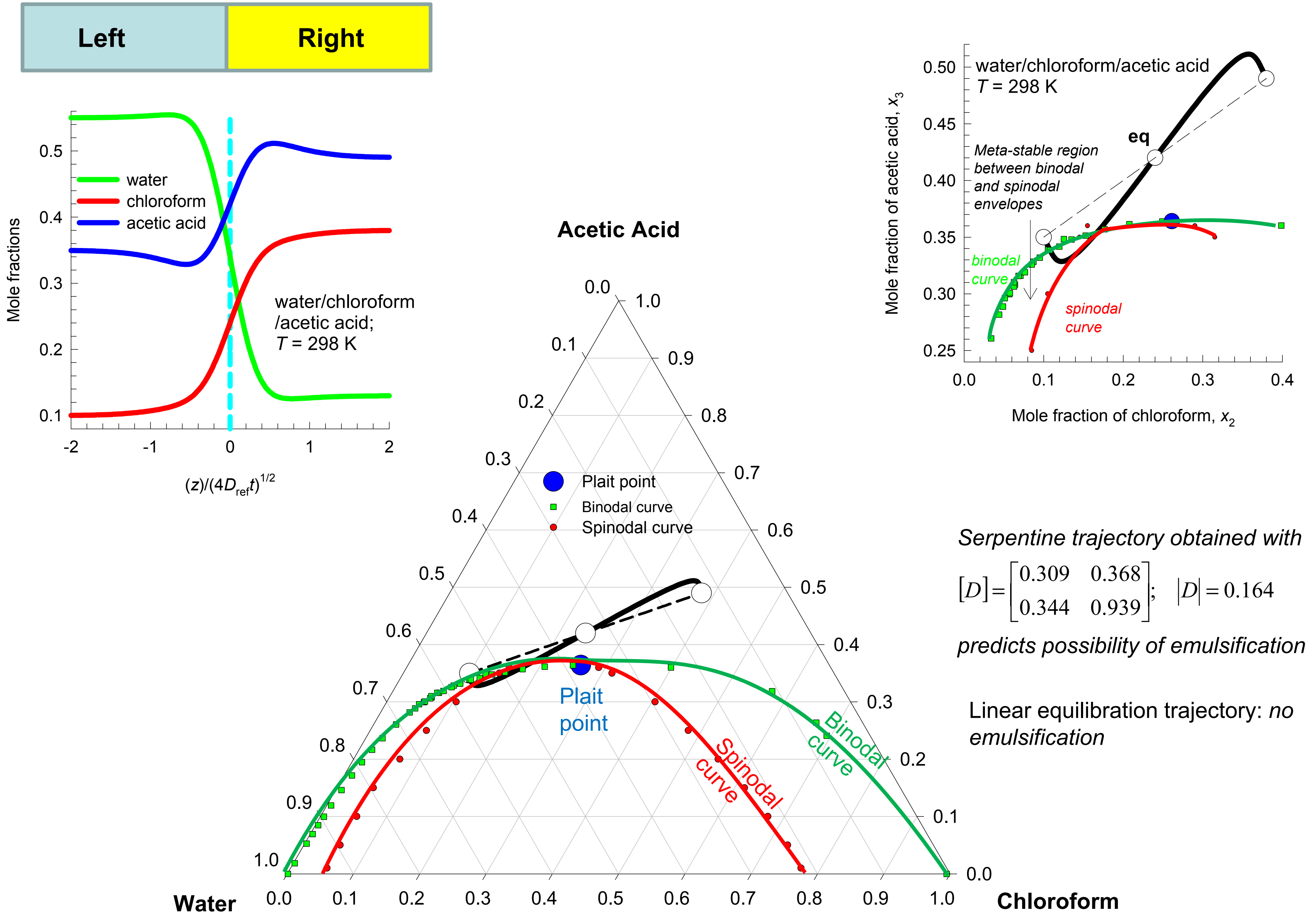

Serpentine trajectory obtained with

$$[D]=\begin{bmatrix}0.309 & 0.368\\ 0.344 & 0.939\end{bmatrix};\quad |D|=0.164$$

predicts possibility of emulsification

Linear equilibration trajectory: *no emulsification*

Water/Chloroform/Acetic Acid Diffusion

ESI Fig. 60

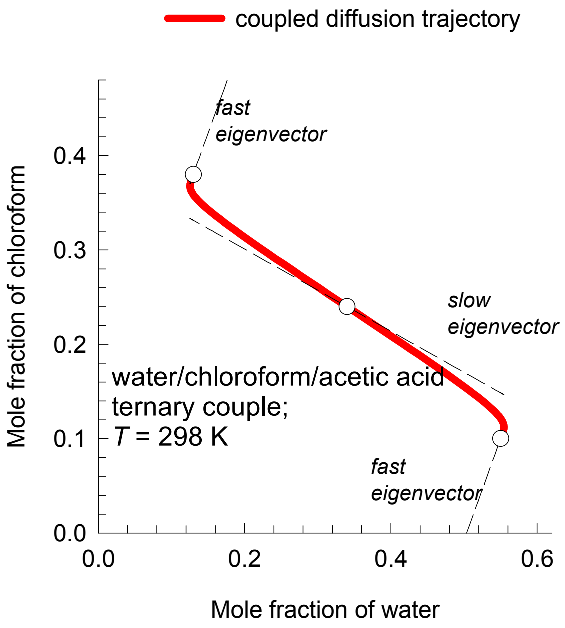

Acetone/Water/Ethylacetate: equilibration trajectory

ESI Fig. 61

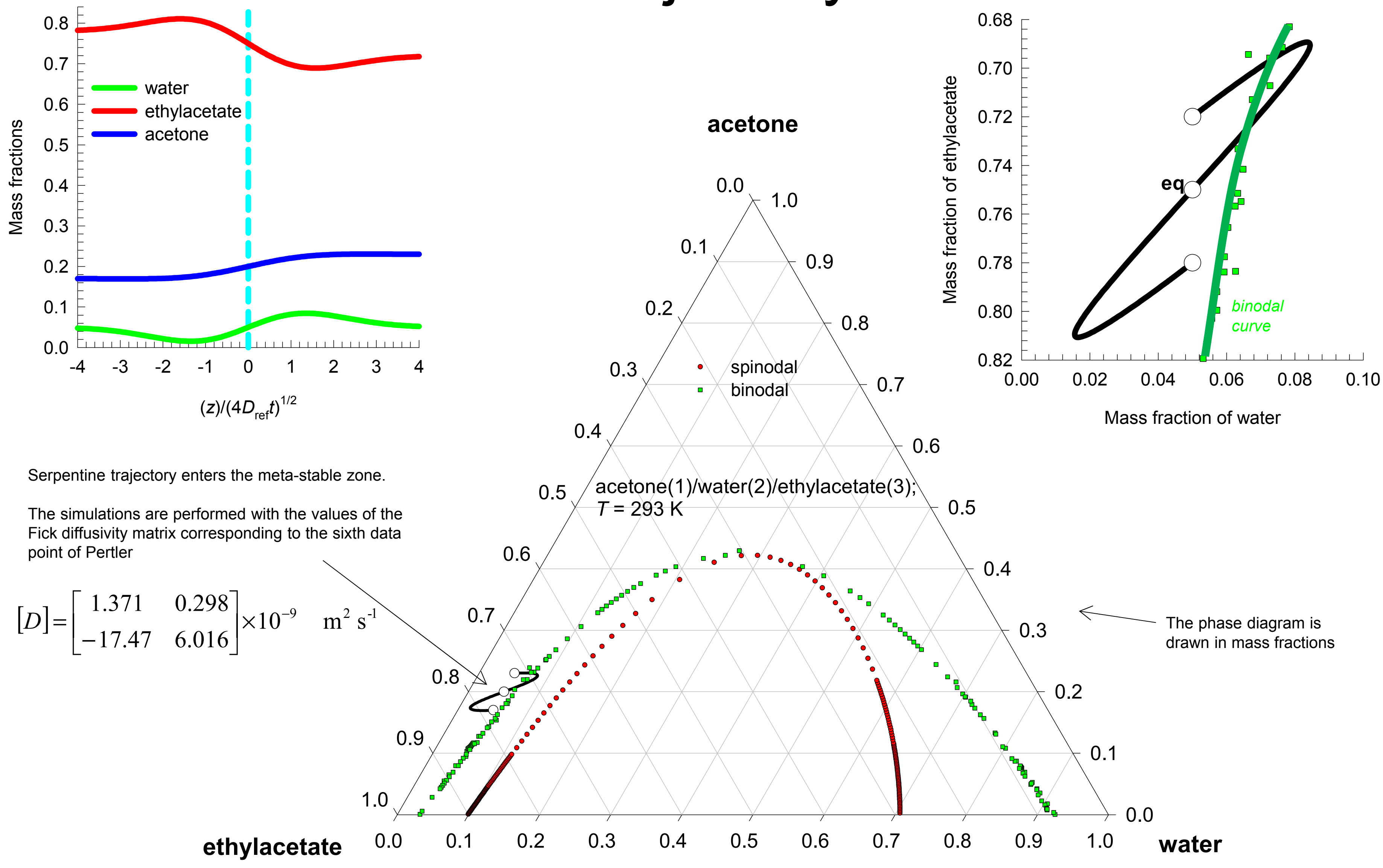

Serpentine trajectory enters the meta-stable zone.

The simulations are performed with the values of the Fick diffusivity matrix corresponding to the sixth data point of Pertler

$$[D]=\begin{bmatrix} 1.371 & 0.298 \\ -17.47 & 6.016 \end{bmatrix}\times 10^{-9} \quad \mathrm{m^2\ s^{-1}}$$

The phase diagram is drawn in mass fractions

Water/2-propanol/cyclohexane mixture diffusion

ESI Fig. 62

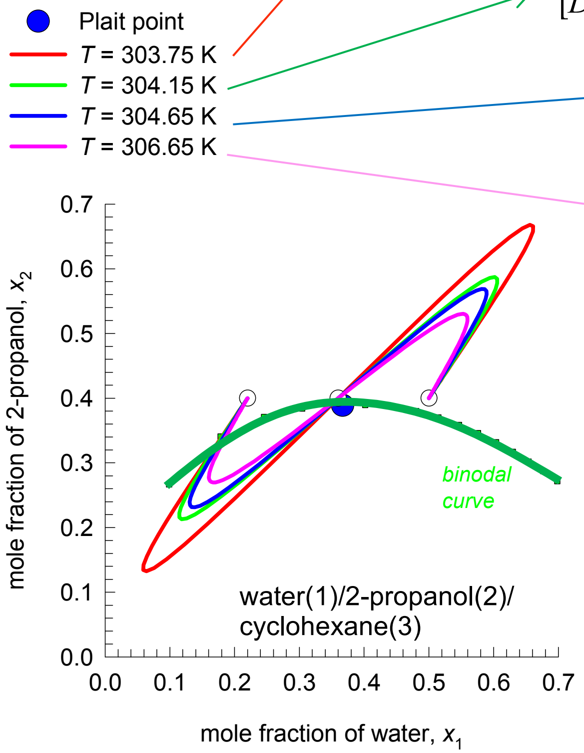

Units: 10^{-10} m^2 s^{-1}

$$[D]=\begin{bmatrix}-0.347 & 0.323\\ -0.559 & 0.510\end{bmatrix};\quad |D|=0.359$$

Units: 10^{-18} m^4 s^{-2}

$$[D]=\begin{bmatrix}-0.257 & 0.267\\ -0.440 & 0.439\end{bmatrix};\quad |D|=0.466$$

$$[D]=\begin{bmatrix}-0.309 & 0.328\\ -0.566 & 0.571\end{bmatrix};\quad |D|=0.921$$

$$[D]=\begin{bmatrix}-0.467 & 0.547\\ -0.997 & 1.064\end{bmatrix};\quad |D|=4.847$$

ESI Fig. 63

Water/Acetone/Toluene diffusion

The simulations are performed with the values of the Fick diffusivity matrix that are estimated to be

$$[D]=\begin{bmatrix}-0.19 & -1.29\\ 0.574 & 2.38\end{bmatrix}\times10^{-9}\quad \mathrm{m^2\ s^{-1}}$$

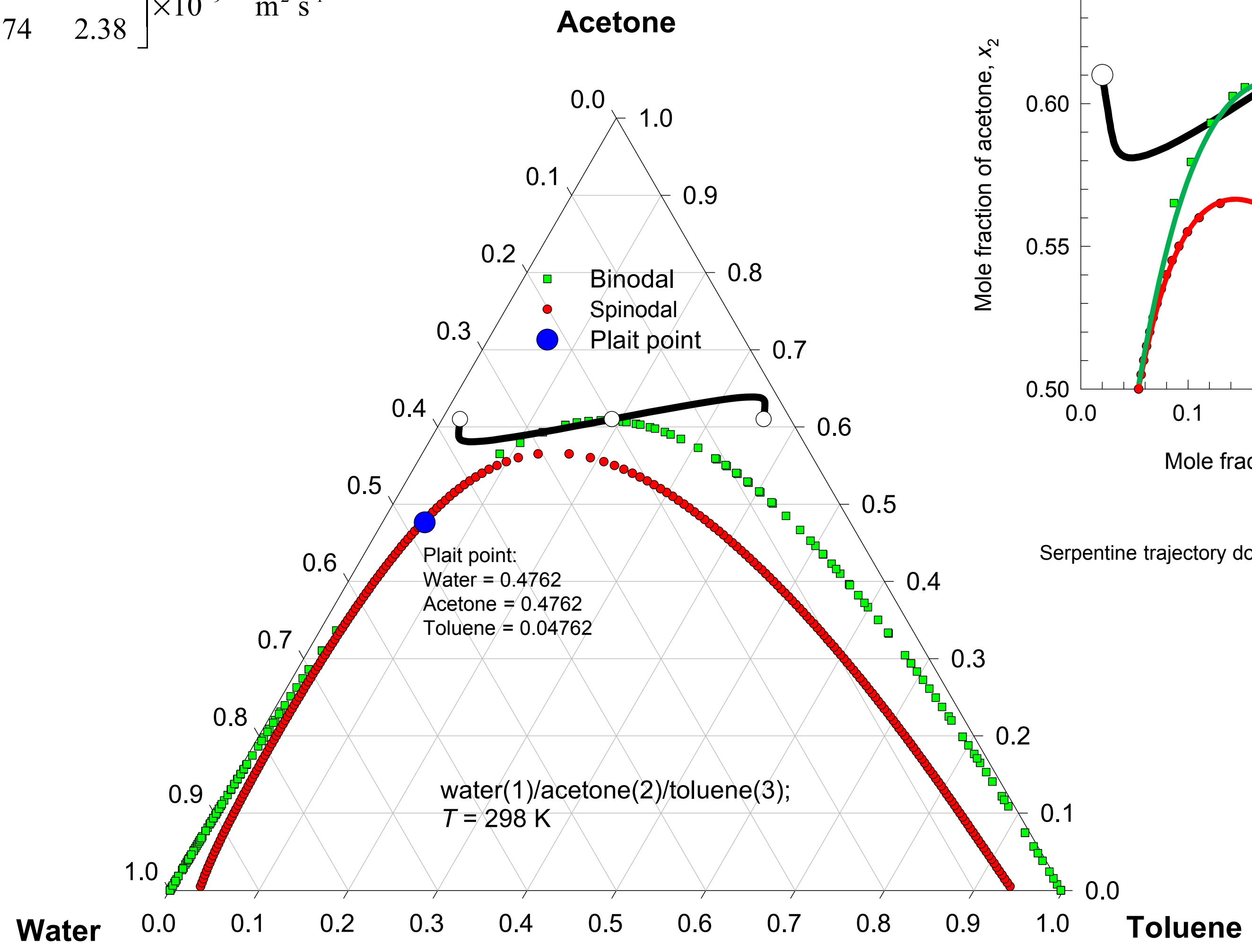

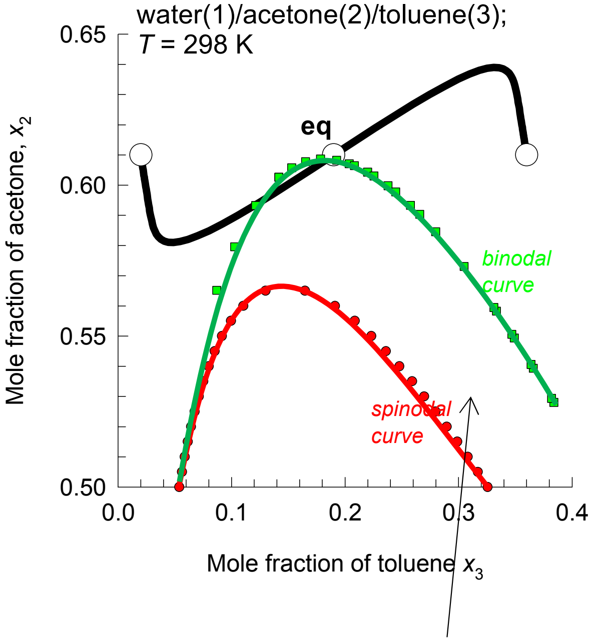

Serpentine trajectory does not enter the meta-stable zone.

Toluene/ethanol/water equilibration

ESI Fig. 64

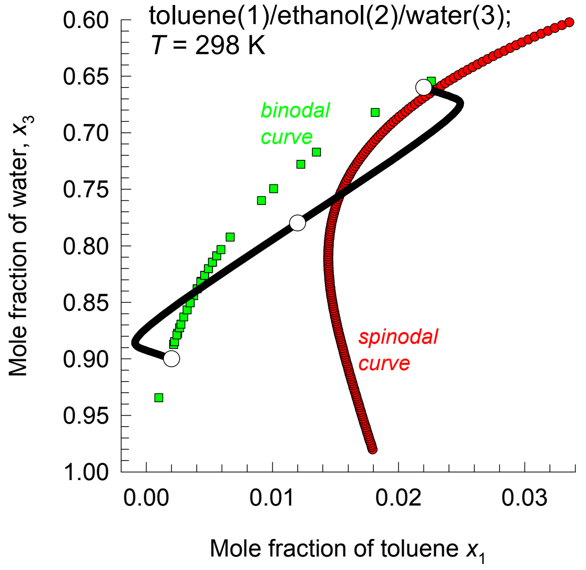

The simulations are performed with the values of the Fick diffusivity matrix that are estimated to be

$$[D]=\begin{bmatrix}0.6 & -0.1\\ -2.6 & 0.53\end{bmatrix}\times10^{-9}\quad \mathrm{m}^2\ \mathrm{s}^{-1}$$

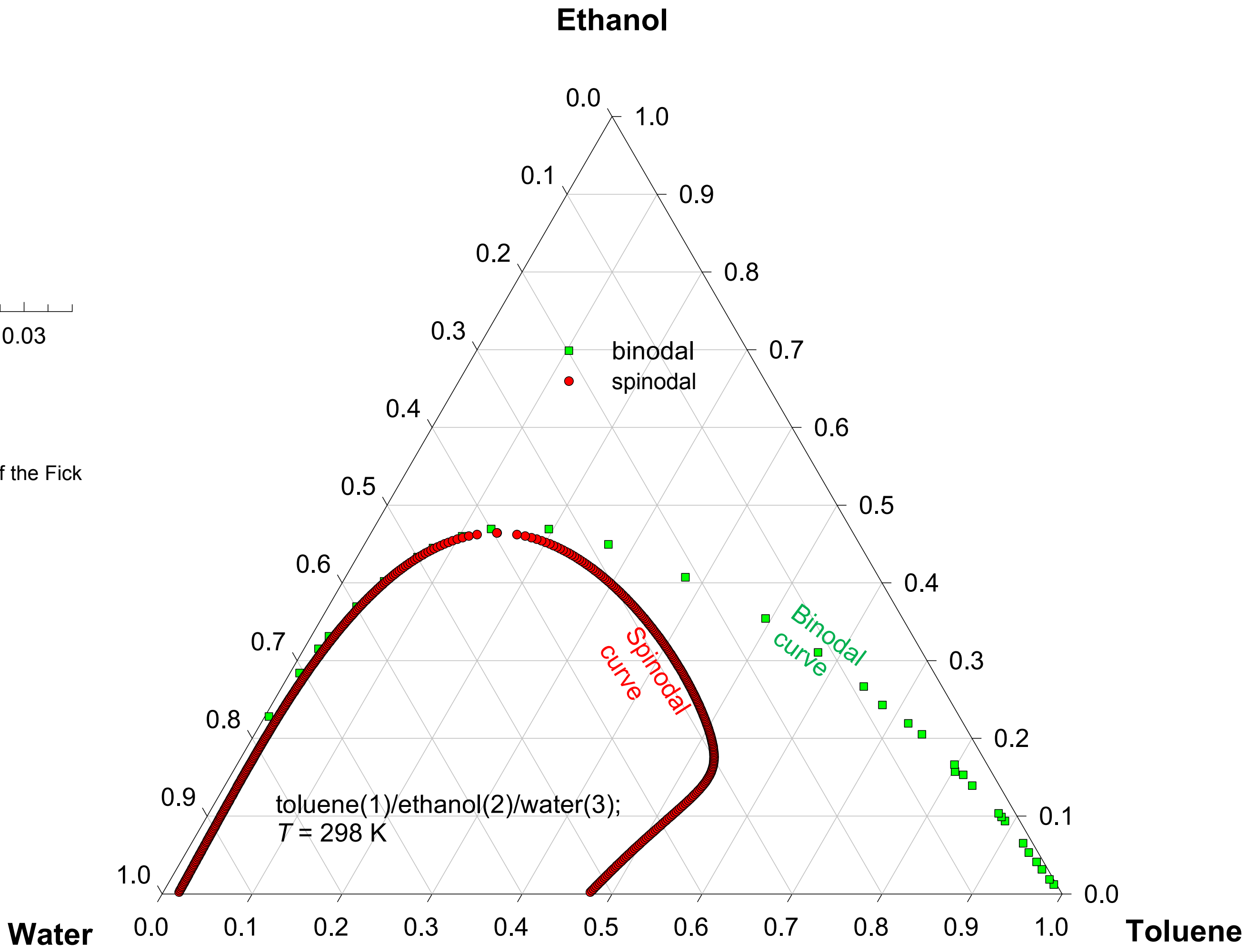

ESI Fig. 65

Water/Caprolactam/Toluene Emulsification

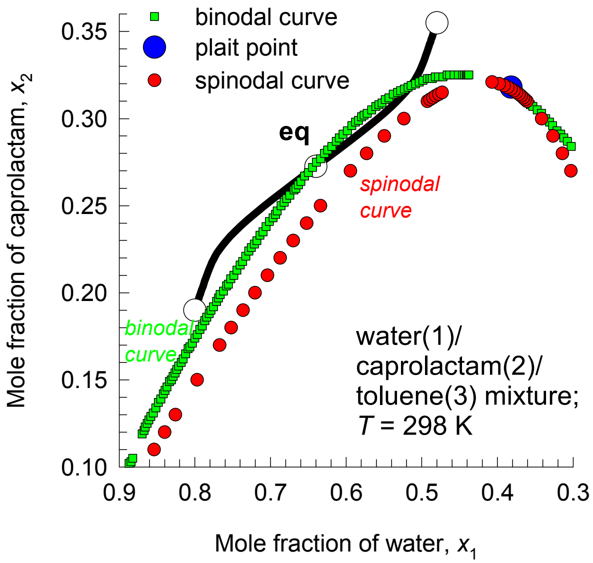

Serpentine trajectory obtained with

$$[D]=\begin{bmatrix}-0.176 & -1.52\\ 0.42 & 2.10\end{bmatrix}\times10^{-9}\quad \mathrm{m^2\ s^{-1}}$$

predicts possibility of emulsification

Linear equilibration trajectory: *no emulsification*

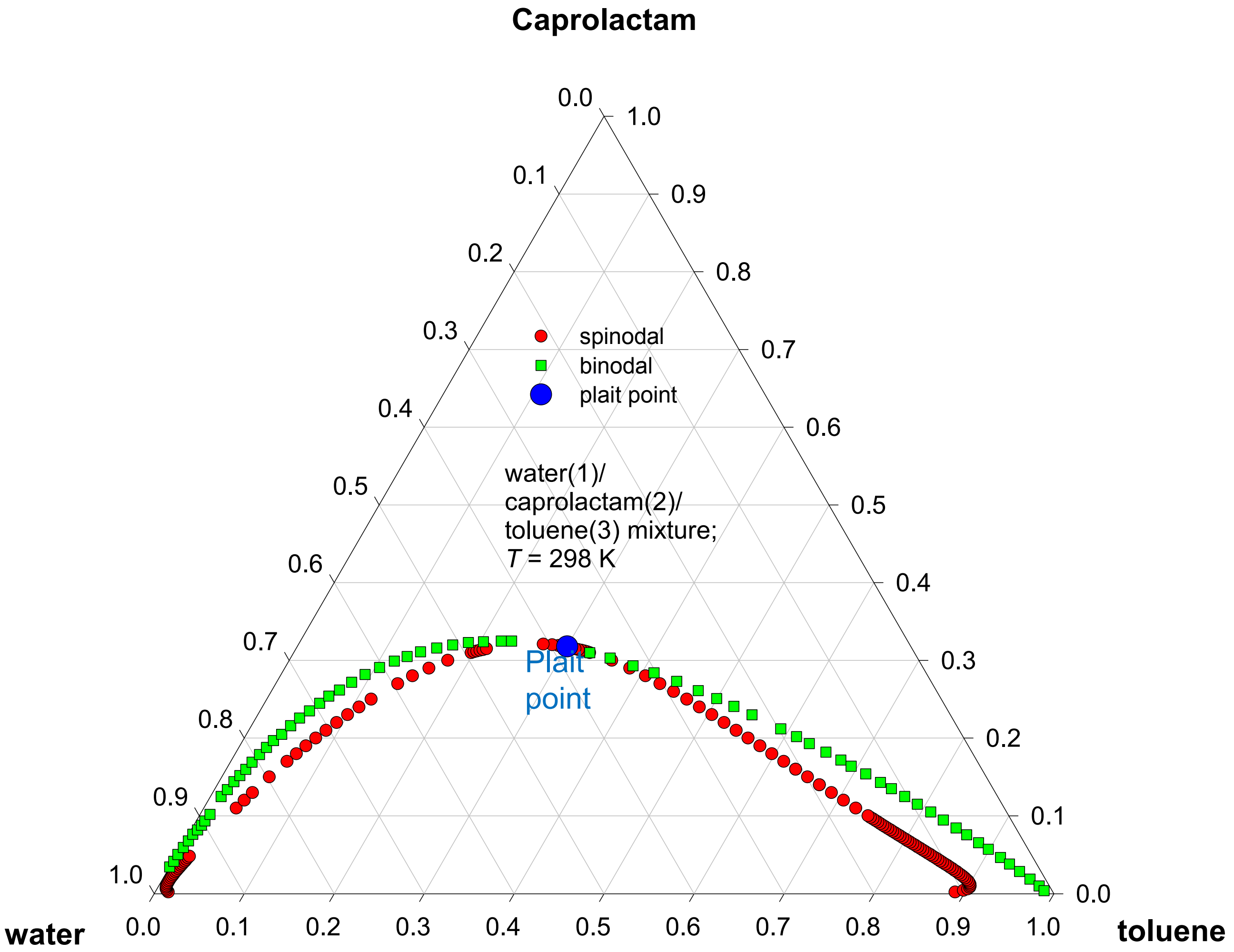

Water/Caprolactam/Benzene Emulsification

ESI Fig. 66

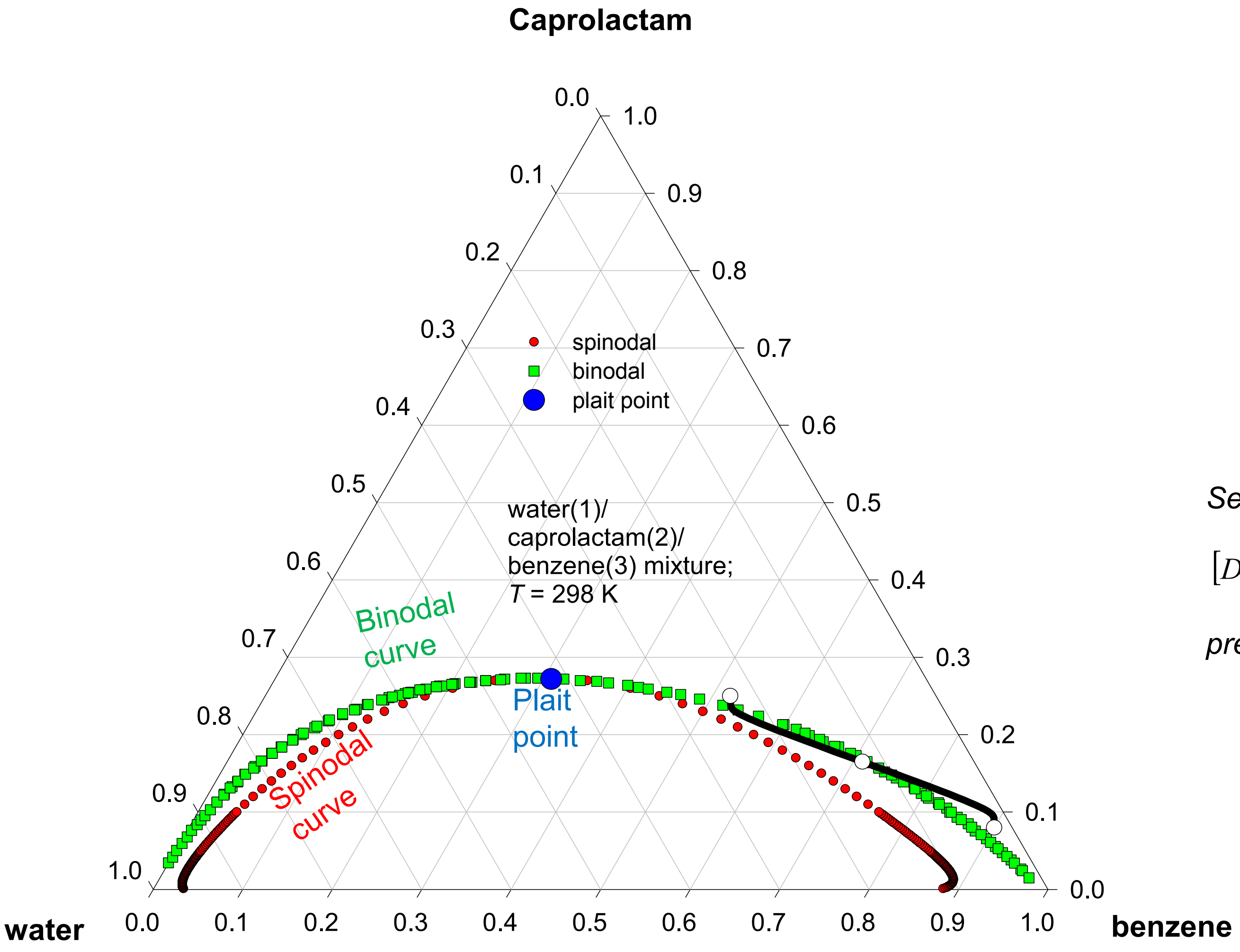

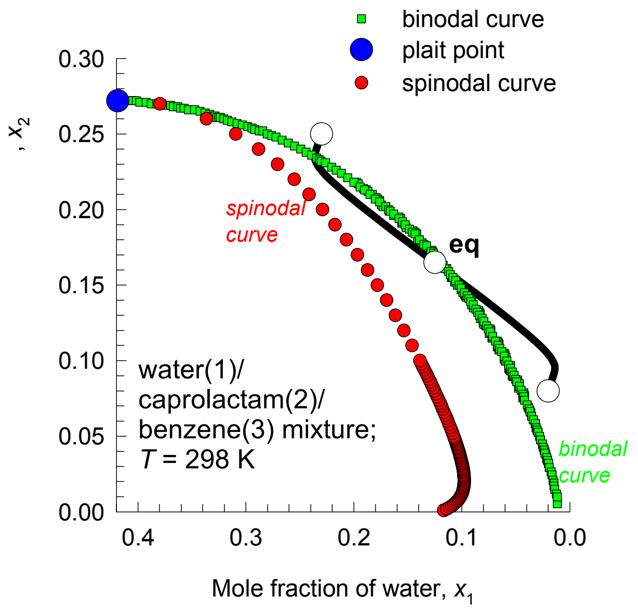

Serpentine trajectory obtained with

$$[D]=\begin{bmatrix}0.591 & -0.925\\ -0.878 & 2.11\end{bmatrix}\times10^{-9}\quad \mathrm{m^2\ s^{-1}}$$

predicts possibility of emulsification

Linear equilibration trajectory: *no emulsification*

ESI Fig. 67

Toluene//Propionic acid/Water Emulsification

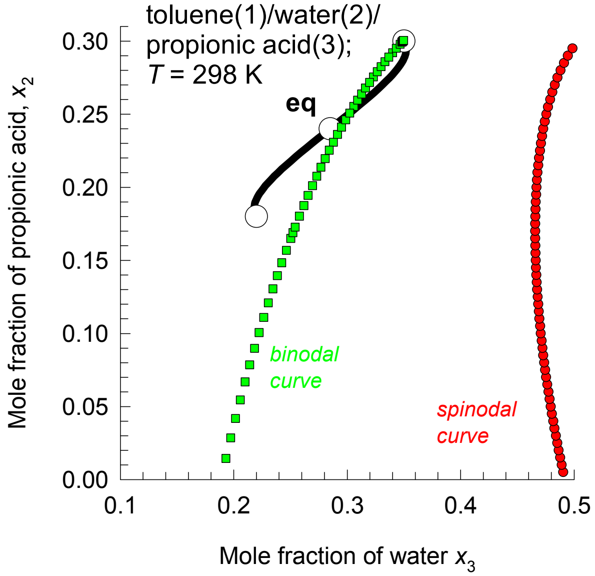

Serpentine trajectory obtained with

$$[D]=\begin{bmatrix}0.3267 & -0.2963\\ 0.1806 & 1.1958\end{bmatrix}\times10^{-9}\quad \mathrm{m^2\ s^{-1}}$$

predicts possibility of emulsification

Linear equilibration trajectory: *no emulsification*

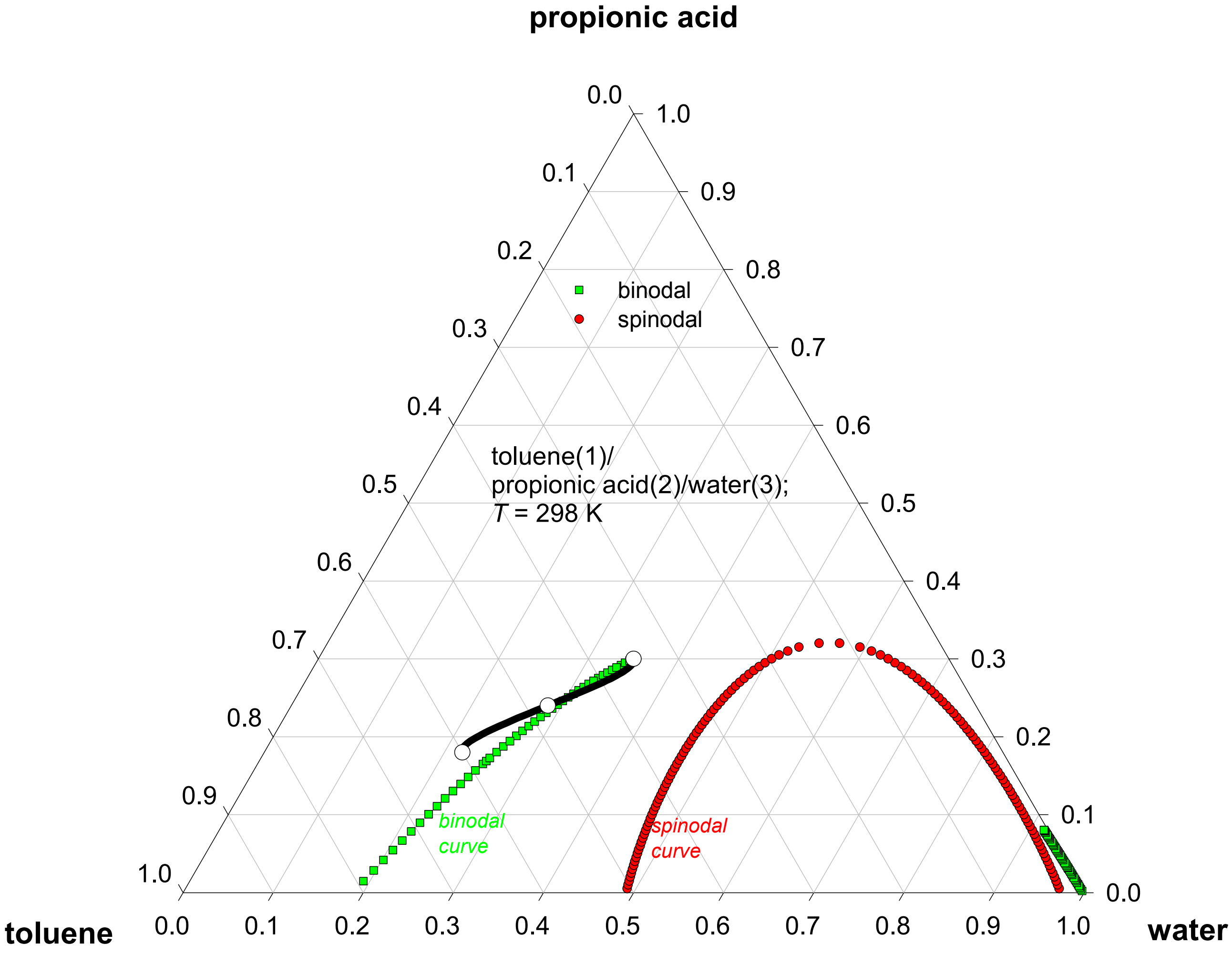

ESI Fig. 68

Ethylacetate/Propionic acid/Water Emulsification

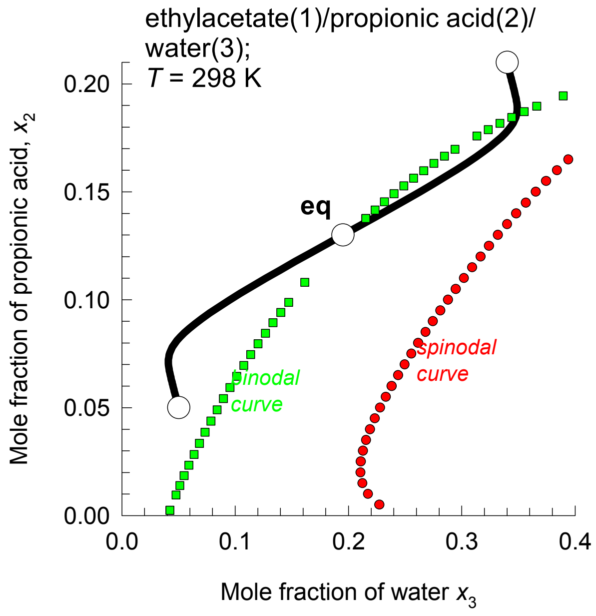

Serpentine trajectory obtained with

$$[D]=\begin{bmatrix}-0.0358 & -1.7447\\ 0.5700 & 3.6379\end{bmatrix}\times10^{-9}\quad \mathrm{m^2\ s^{-1}}$$

predicts possibility of emulsification

Linear equilibration trajectory: *no emulsification*

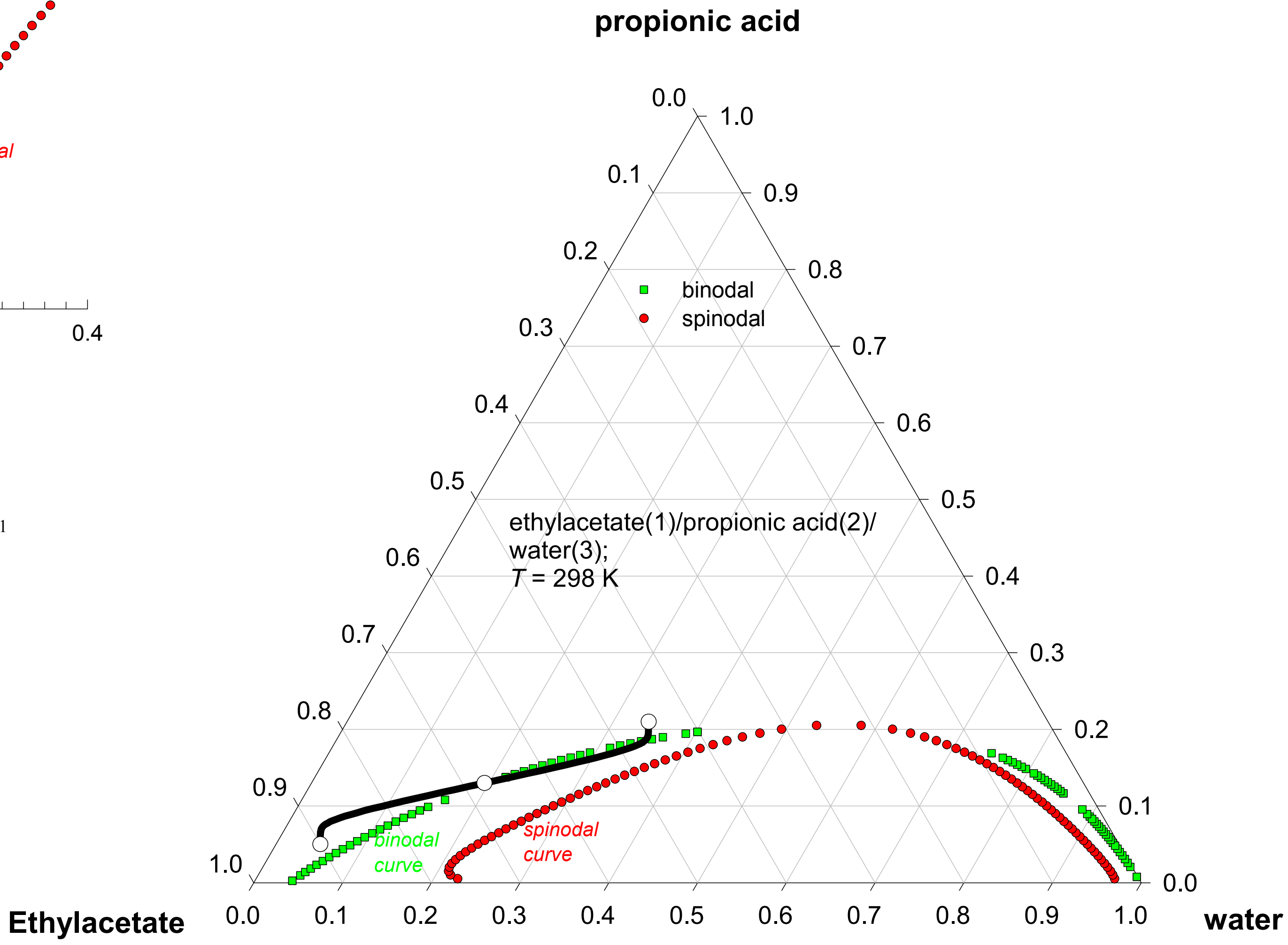

Membrane formation

ESI Fig. 69

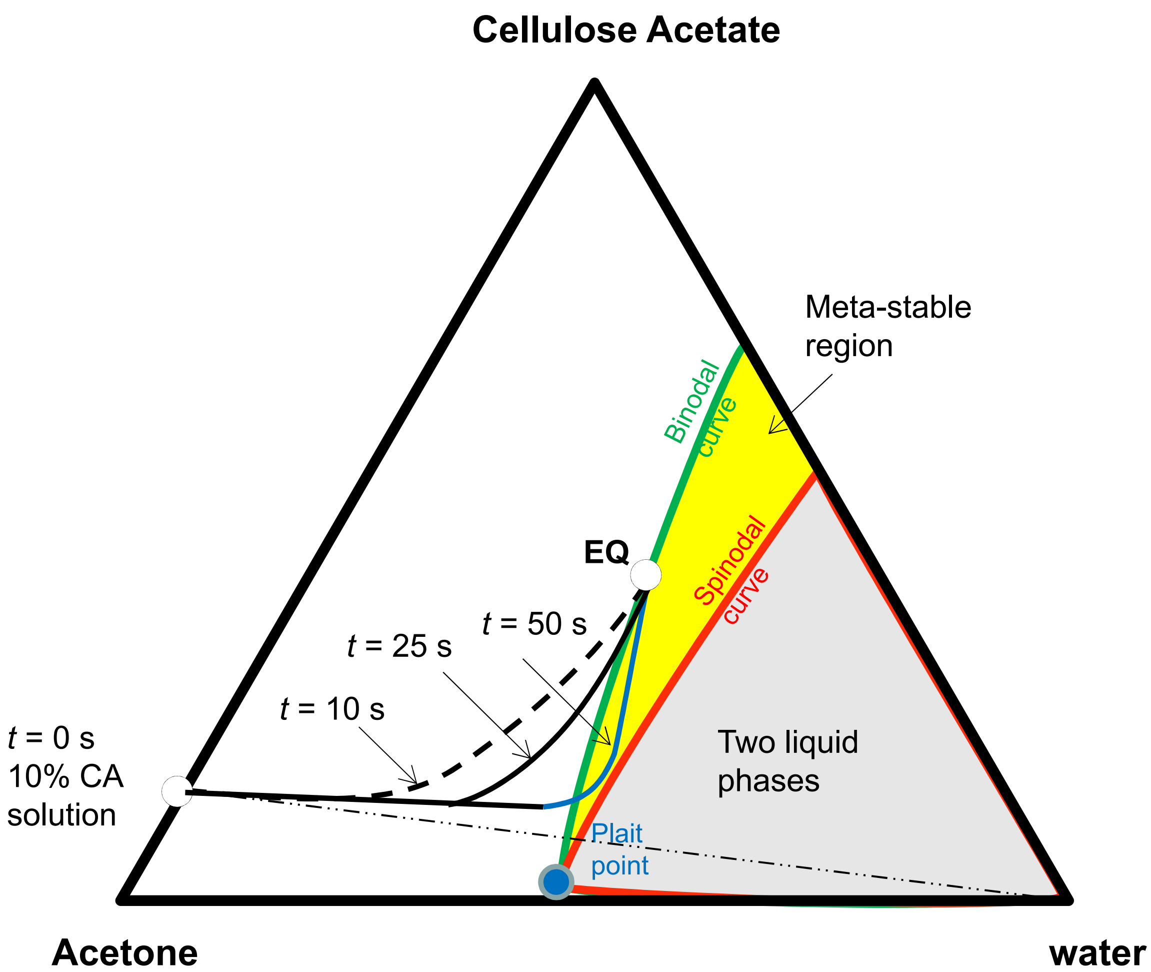

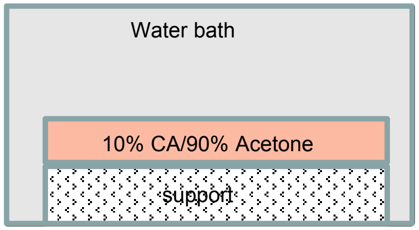

ESI Fig. 70

Drying of food liquids

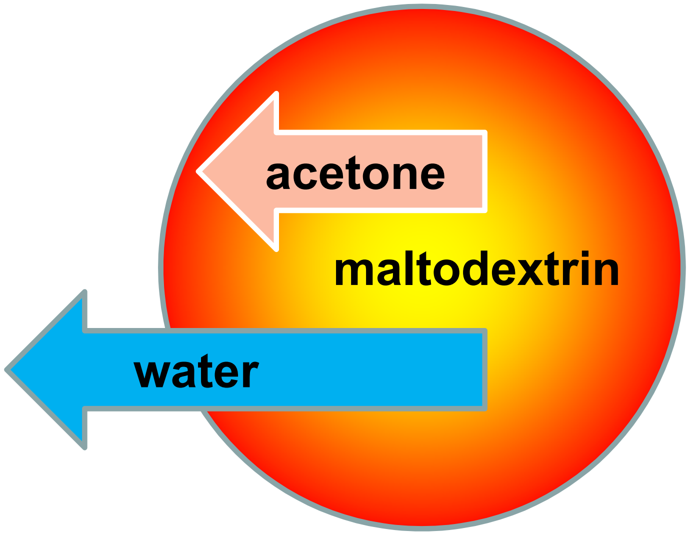

(a)

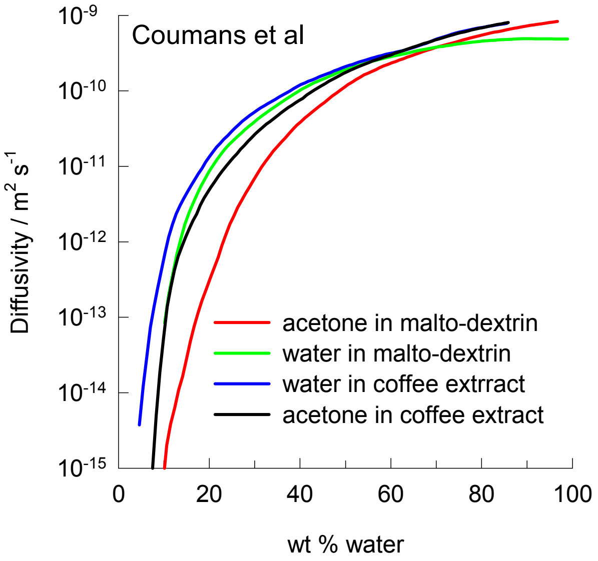

(b)

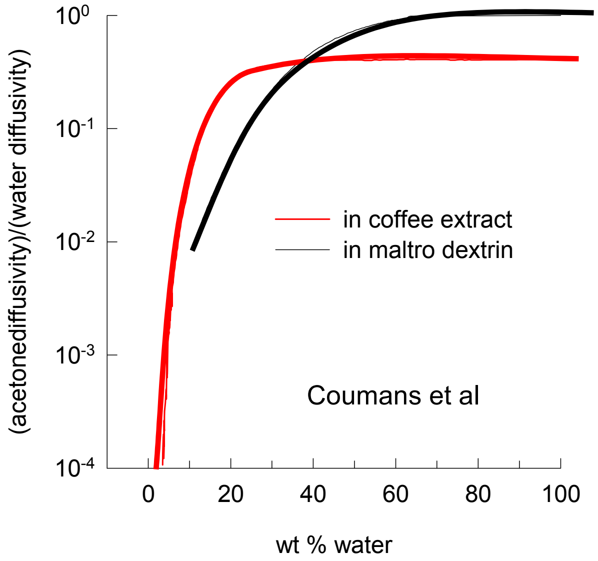

ESI Fig. 71

Classic Darken Experiments

Higher activity of C *Lower activity of C*

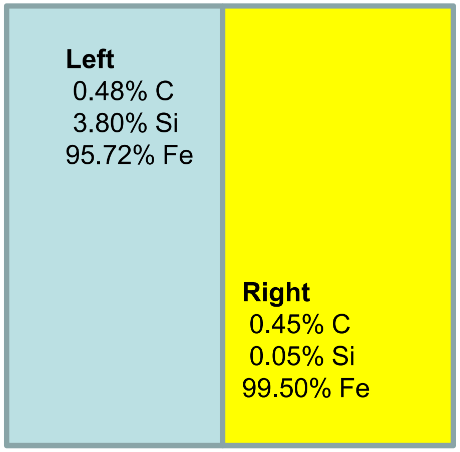

Left
0.48% C
3.80% Si
95.72% Fe

Right
0.45% C
0.05% Si
99.50% Fe

High C = Hard **Bulk = Tough**

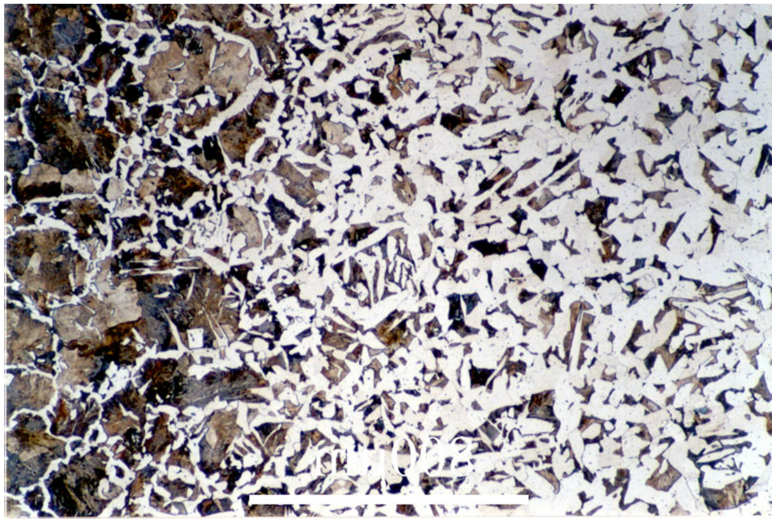

(a)

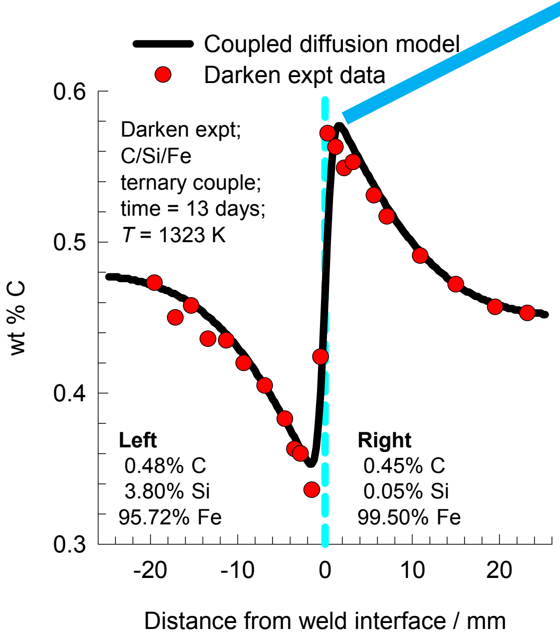

Higher C content near the surface results in surface hardening

Fick diffusivity matrix used in the simulations

$$[D]=\begin{bmatrix}480 & 34\\ 0 & 2.3\end{bmatrix}\times10^{-13}\quad \mathrm{m^2\ s^{-1}}$$

(b)

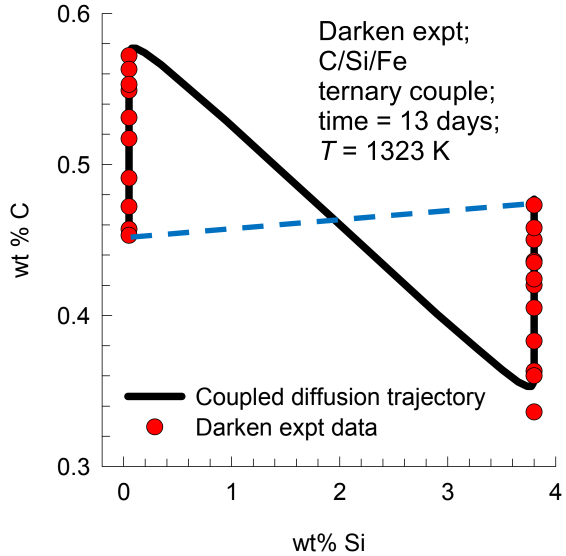

ESI Fig. 72

Cu(1)/Ag(2)/Au(3) equilibration: Ziebold

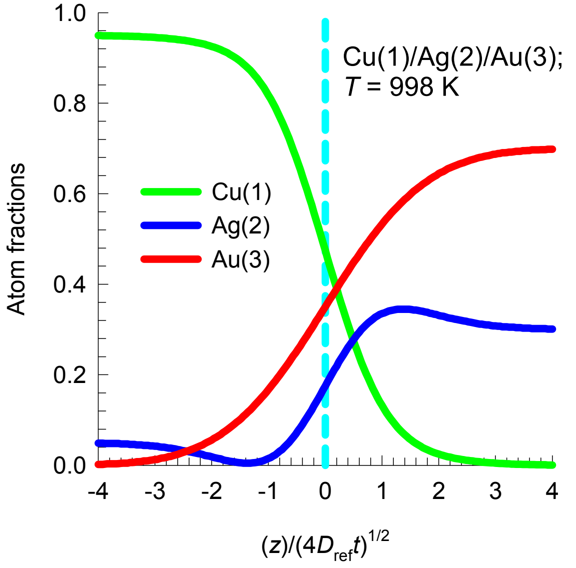

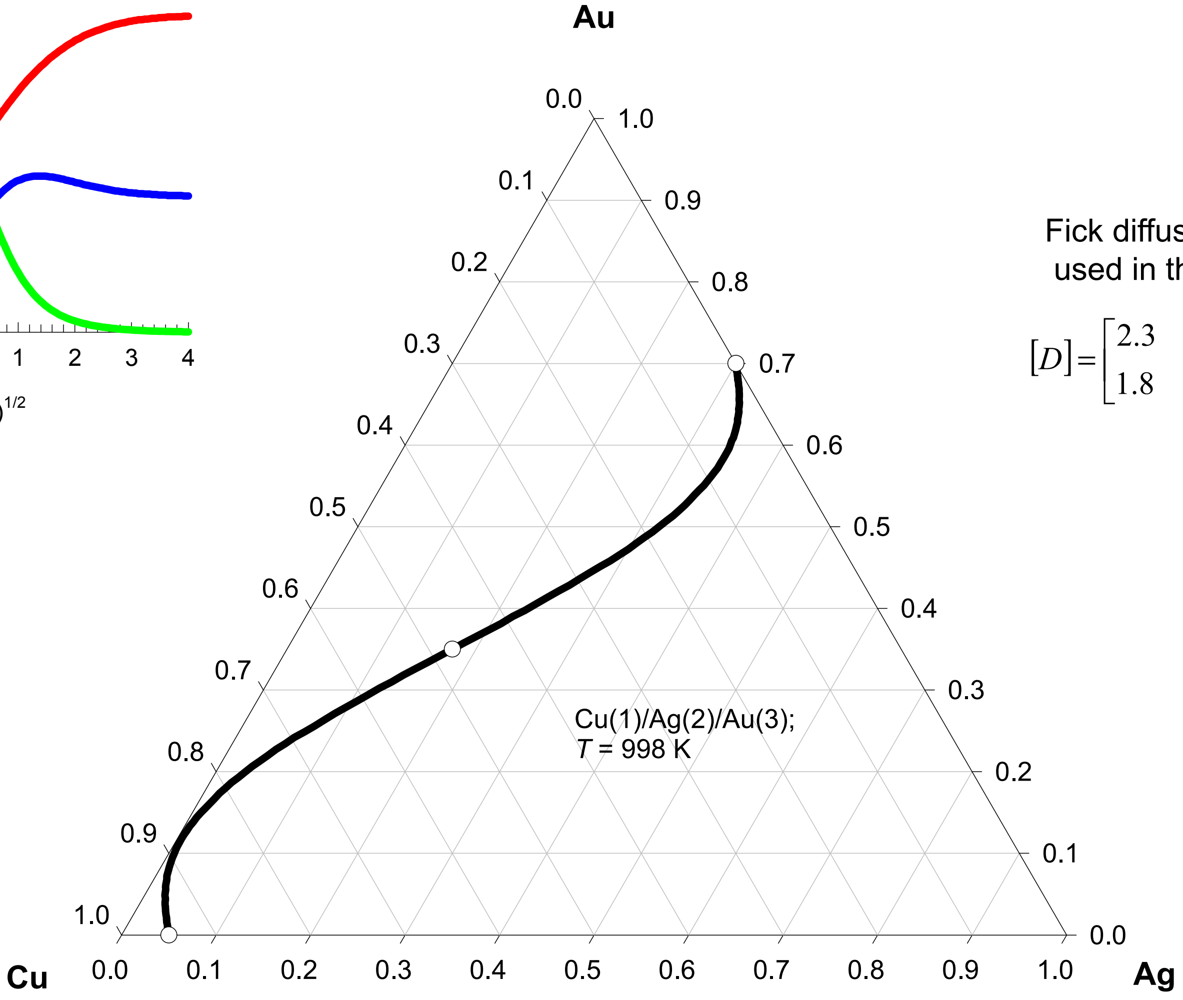

Fick diffusivity matrix
used in the simulations

$$[D]=\begin{bmatrix}2.3 & 1.11\\ 1.8 & 3.1\end{bmatrix}\times10^{-14}\quad \mathrm{m}^2\ \mathrm{s}^{-1}$$

ESI Fig. 73

Uphill diffusion in glasses

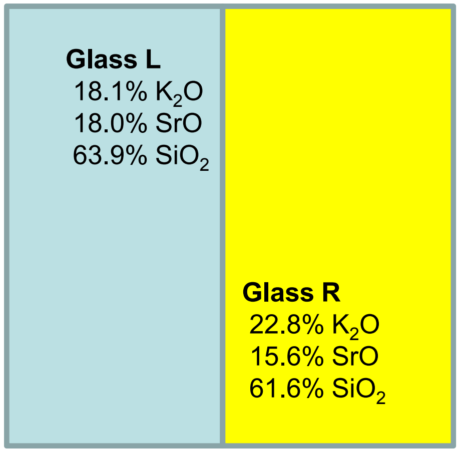

Glass L
18.1% K_2O
18.0% SrO
63.9% SiO_2

Glass R
22.8% K_2O
15.6% SrO
61.6% SiO_2

Fick diffusivity matrix

$$[D]=\begin{bmatrix} 1 & -0.267 \\ -1.22 & 0.33 \end{bmatrix}\times 10^{-13} \quad \mathrm{m^2\ s^{-1}}$$

(a)

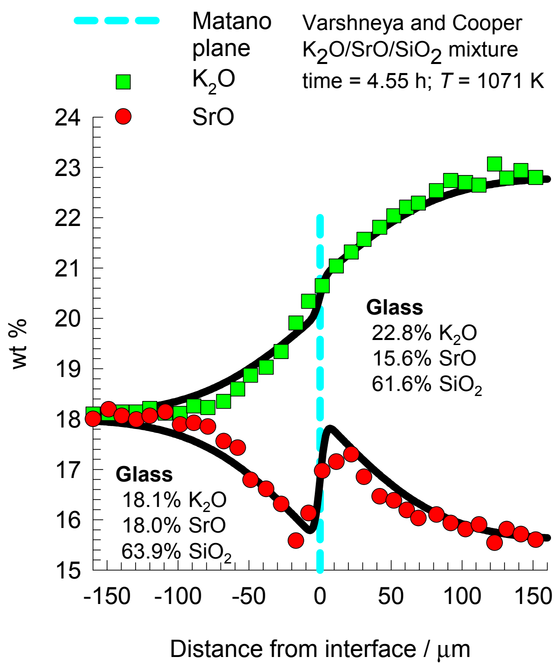

(b)

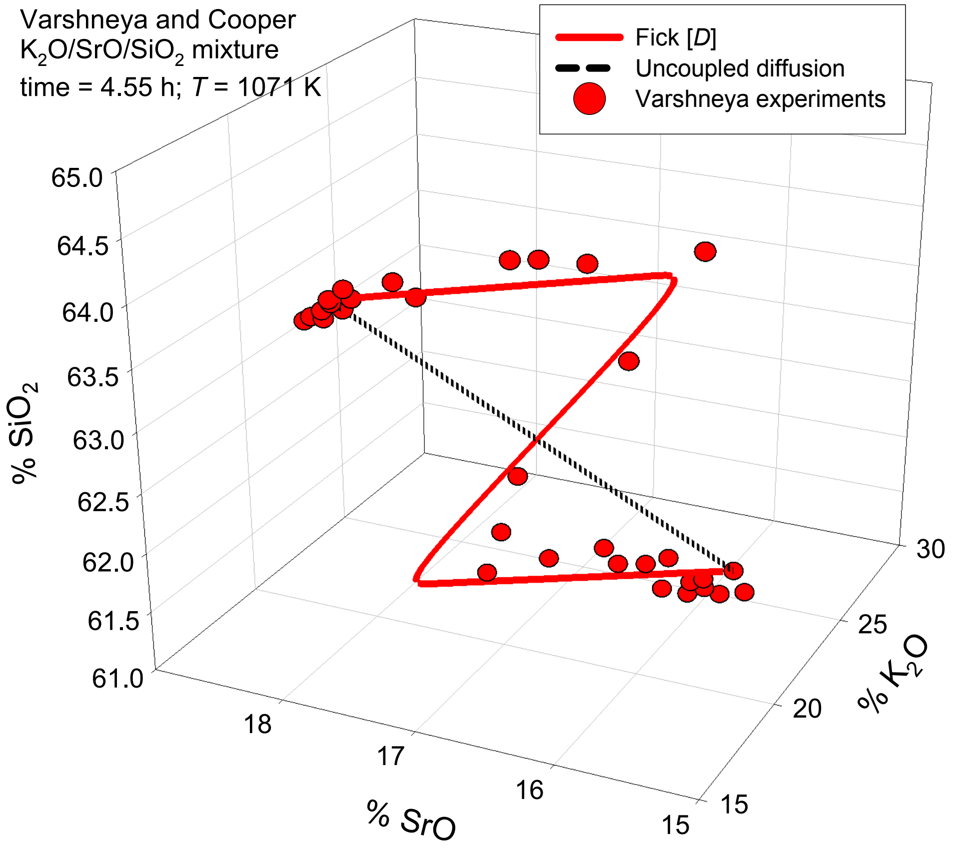

ESI Fig. 74

Fe/Mg/Ca diffusion couple

(a)

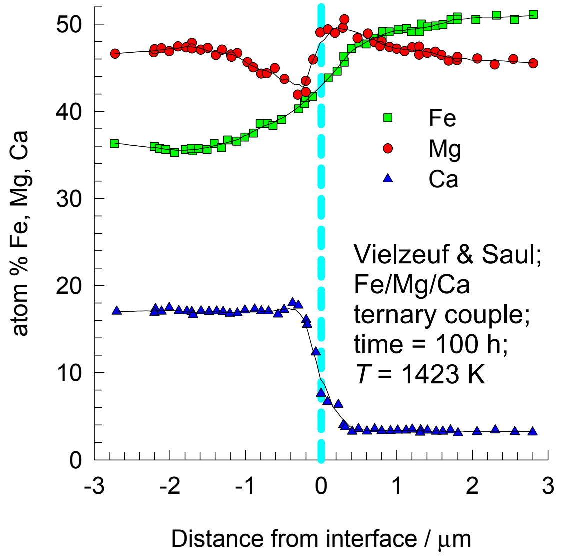

Left	**Right**
35.85 % Fe	50.85 % Fe
47.00 % Mg	46.00 % Mg
17.15 % Ca	3.15 % Ca

(b)

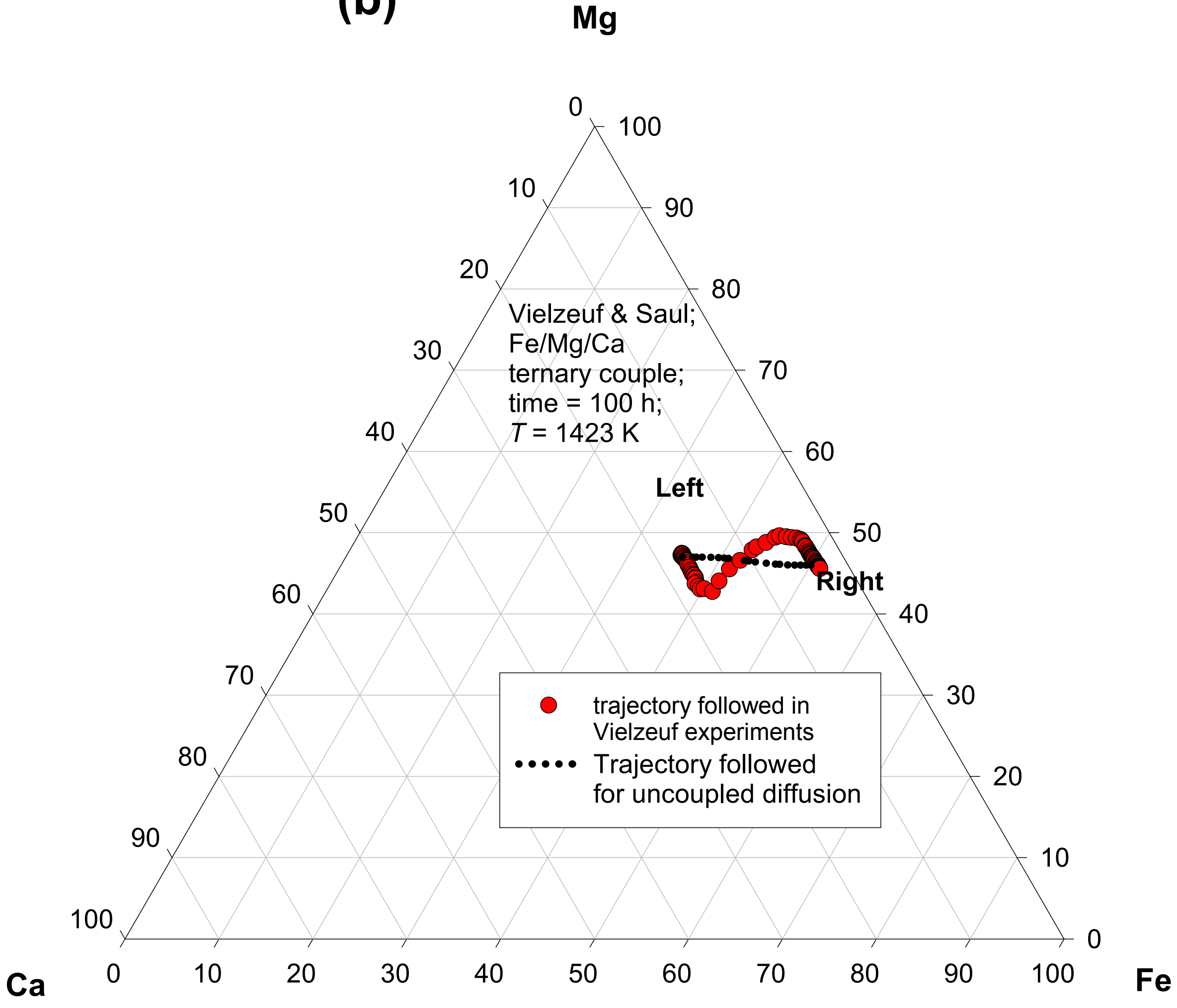

Ternary Diffusion Couple

ESI Fig. 75

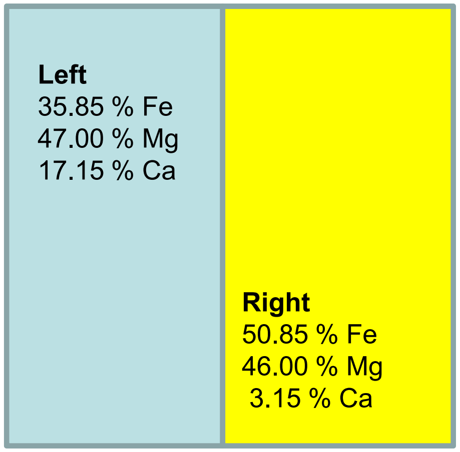

Left
35.85 % Fe
47.00 % Mg
17.15 % Ca

Right
50.85 % Fe
46.00 % Mg
3.15 % Ca

Fick diffusivity matrix used in the simulations

$$[D]=\begin{bmatrix} 5.86 & -1.02 \\ -5.5 & 1.18 \end{bmatrix}\times 10^{-19} \quad \mathrm{m^2\ s^{-1}}$$

(a)

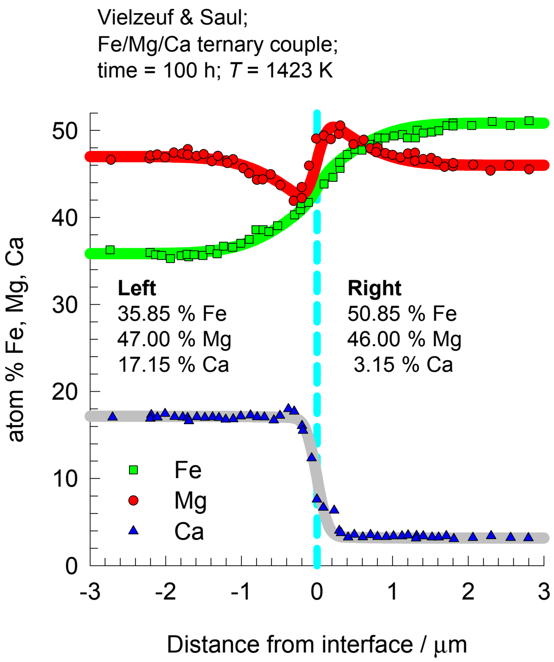

(b)

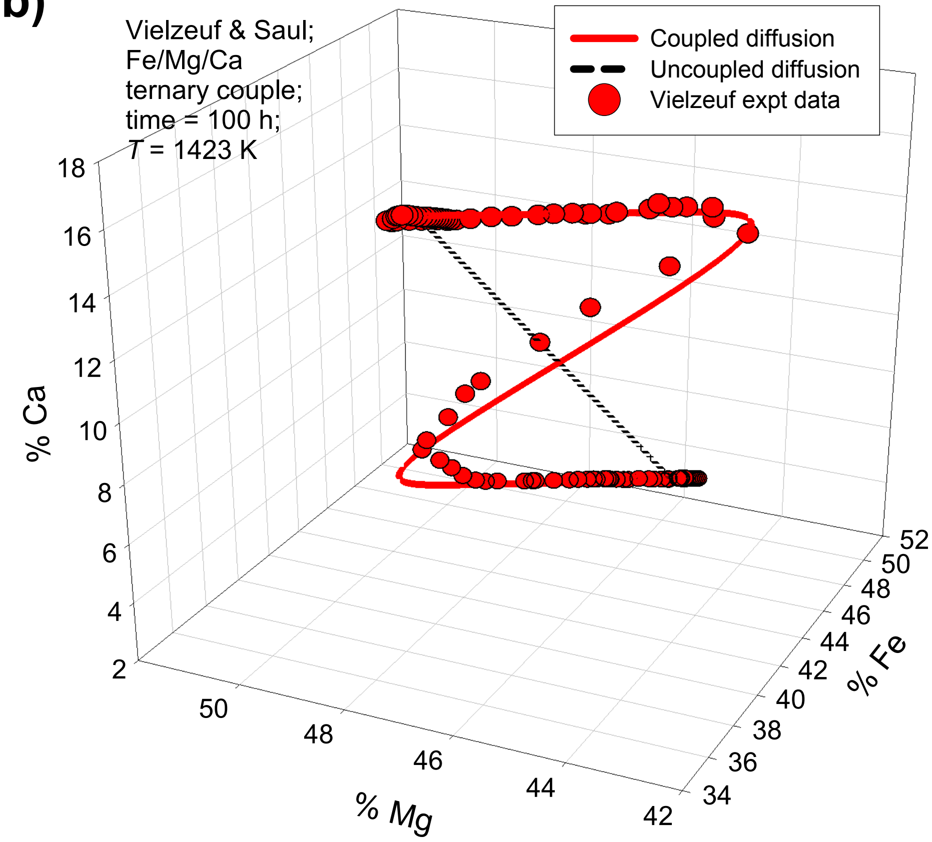

ESI Fig. 76

Mass transfer in distillation

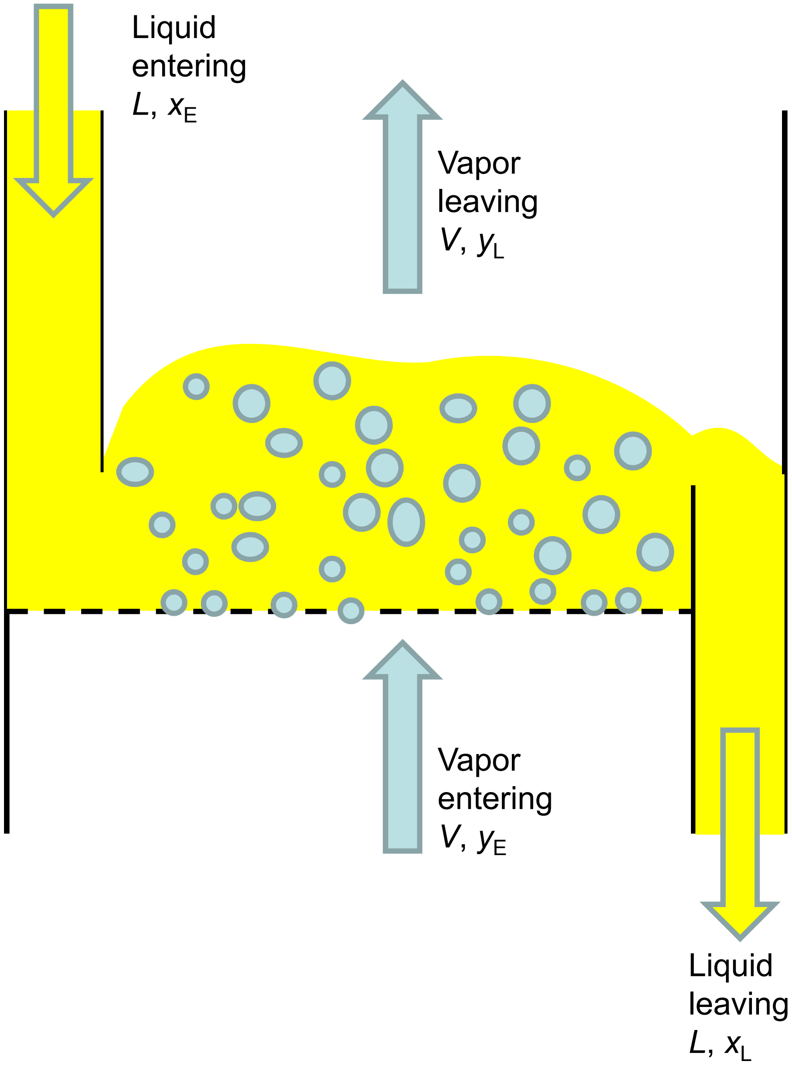

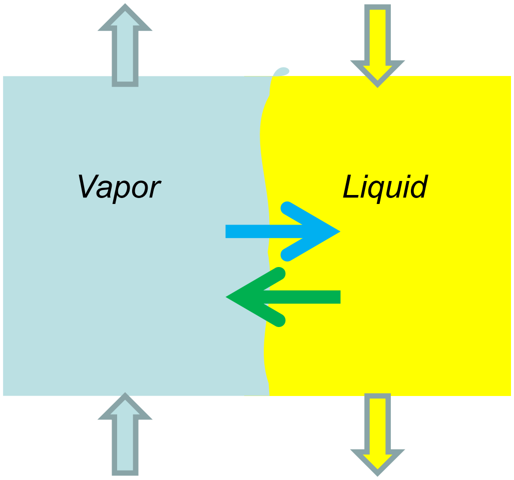

Diffusional coupling effects need to be accounted for in either phase

Murphree component efficiencies

ESI Fig. 77

(c)

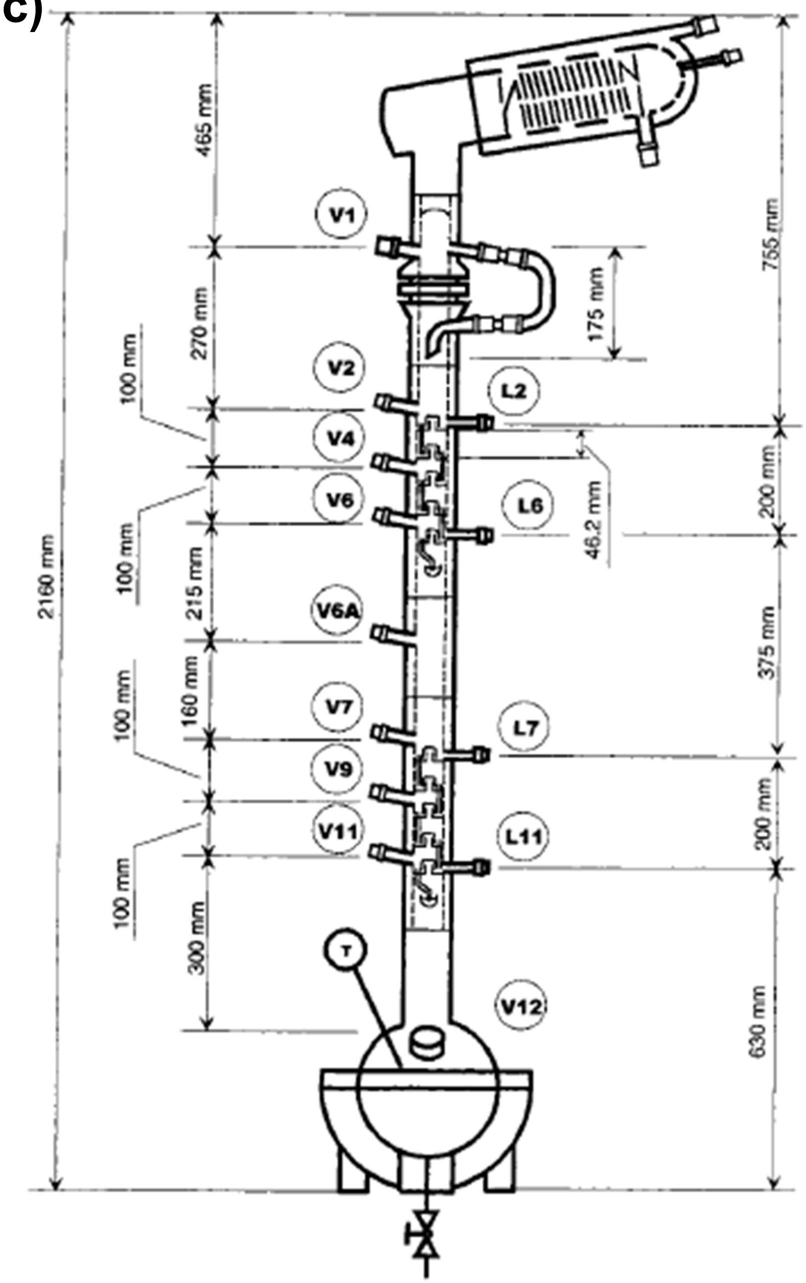

(b)

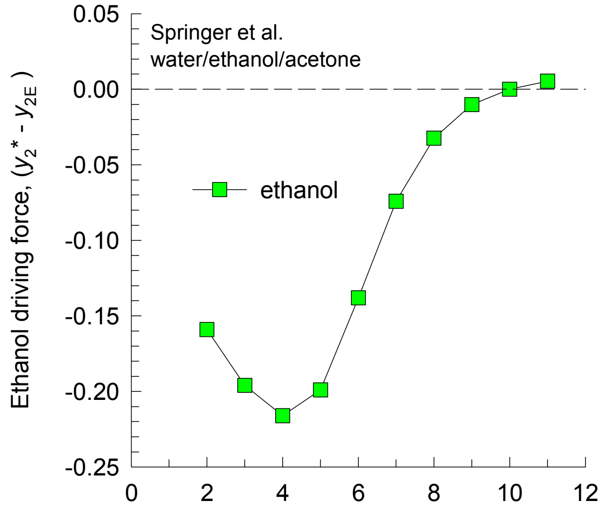

(c)

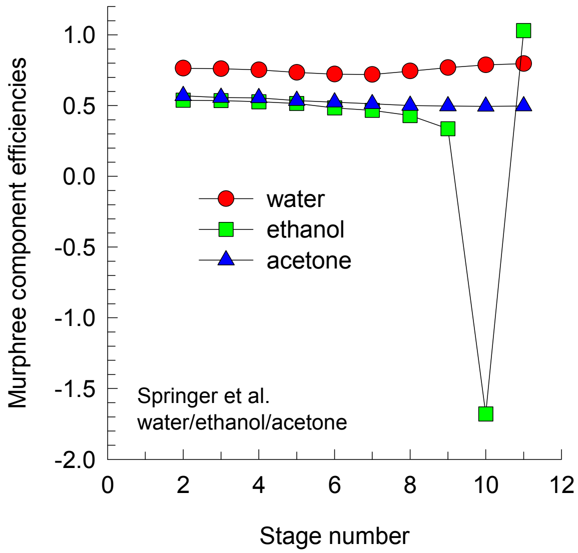

Crossing distillation boundaries

ESI Fig. 78

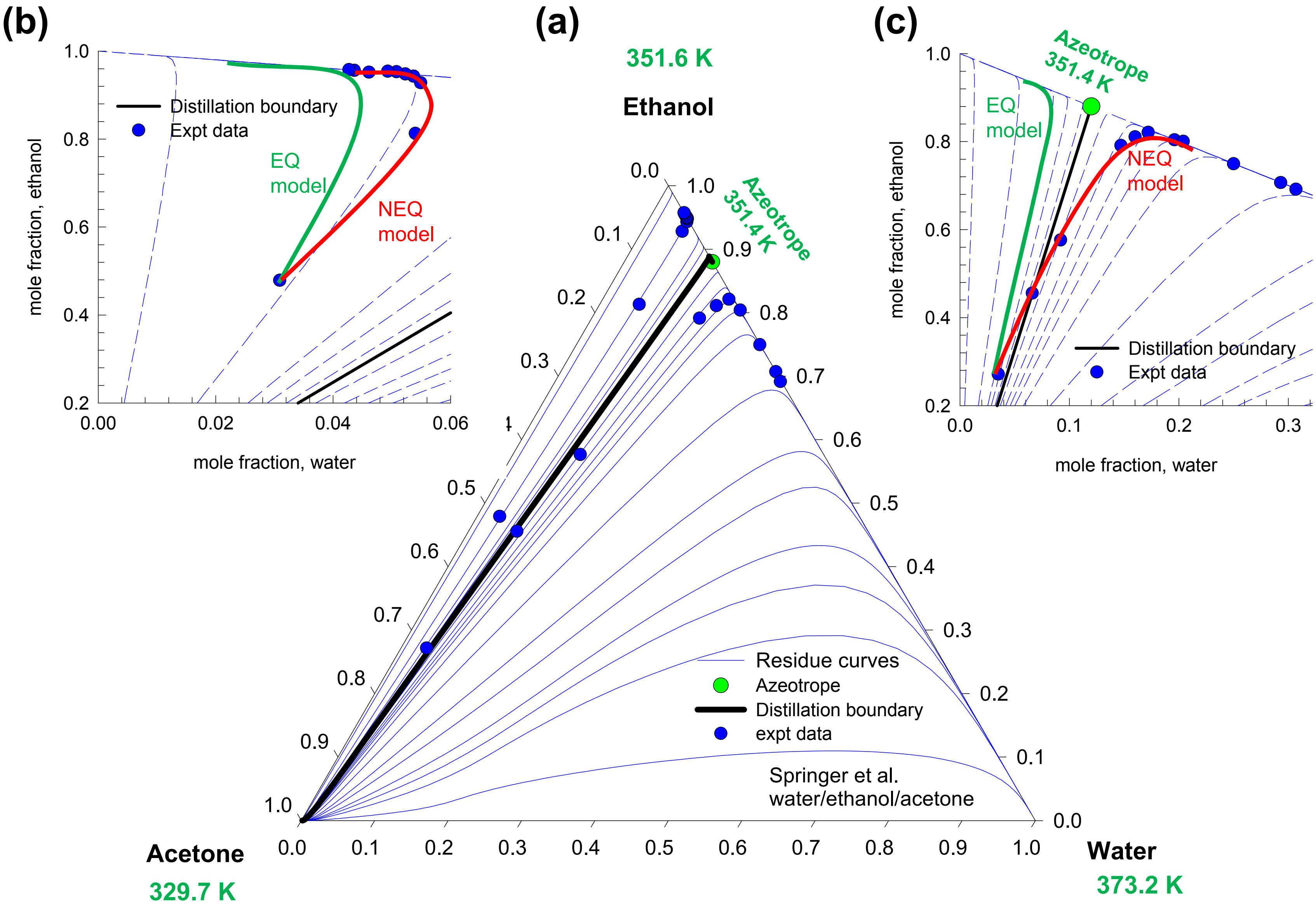

Crossing distillation boundaries

ESI Fig. 79

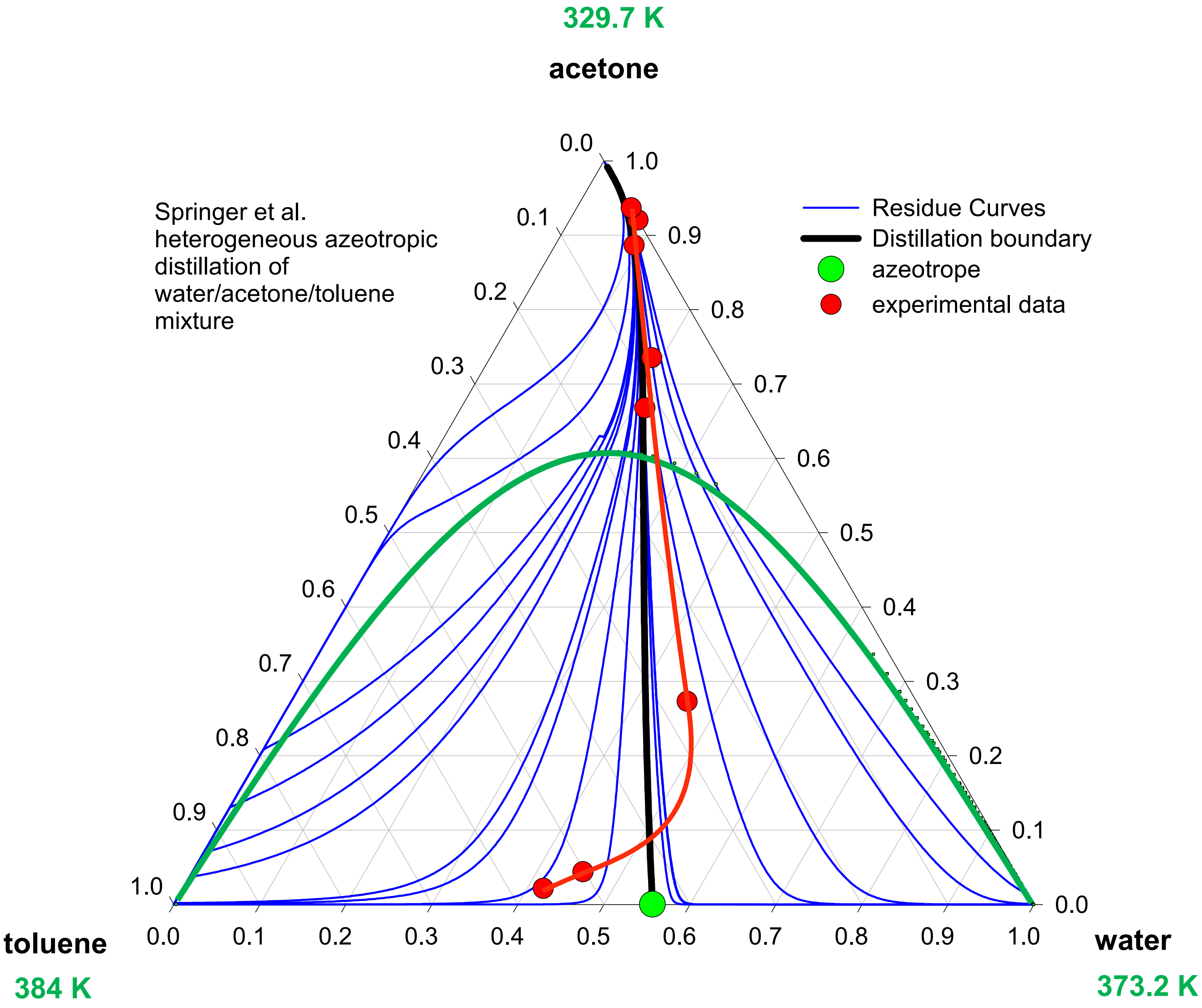

Springer et al.
heterogeneous azeotropic
distillation of
water/acetone/toluene
mixture

ESI Fig. 80

Diffusion of Mixed Ions

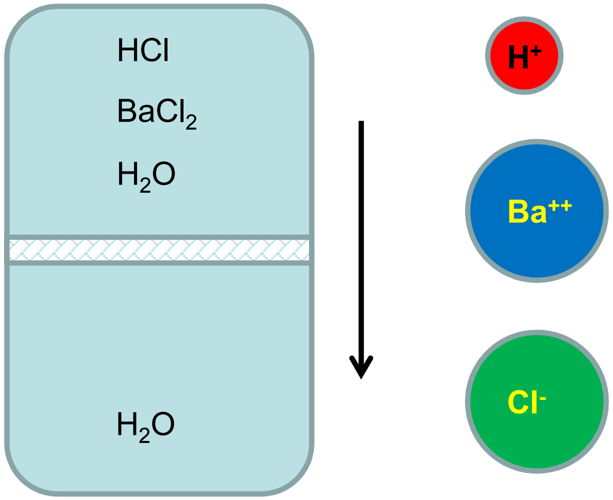

Electroneutrality acts as a leash retarding the motion of tardy Ba^{++}

Electroneutrality acts to accelerate the motion of Cl^-

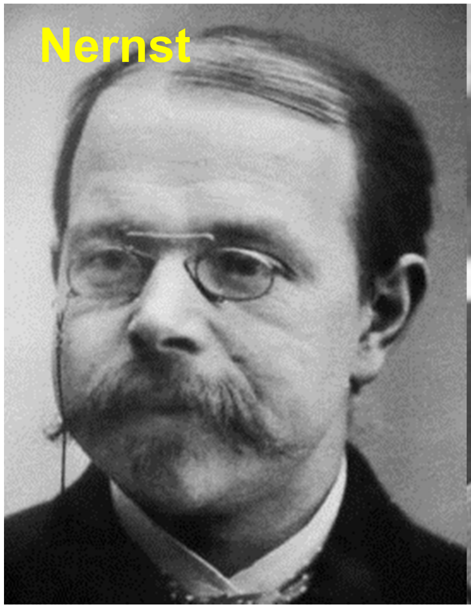

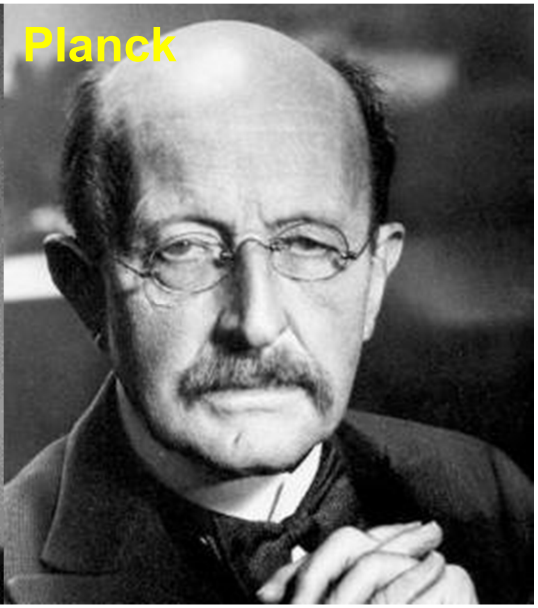

The continuous solid lines are the calculations following the Nernst-Planck equation

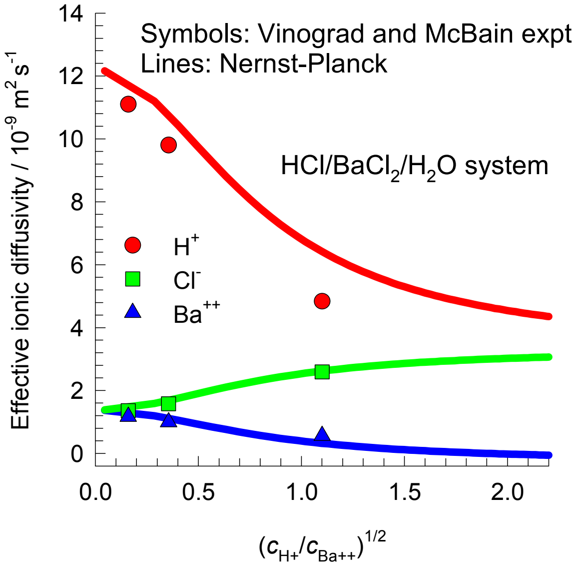

ESI Fig. 81

Asymmetry in Ion-Exchange Kinetics

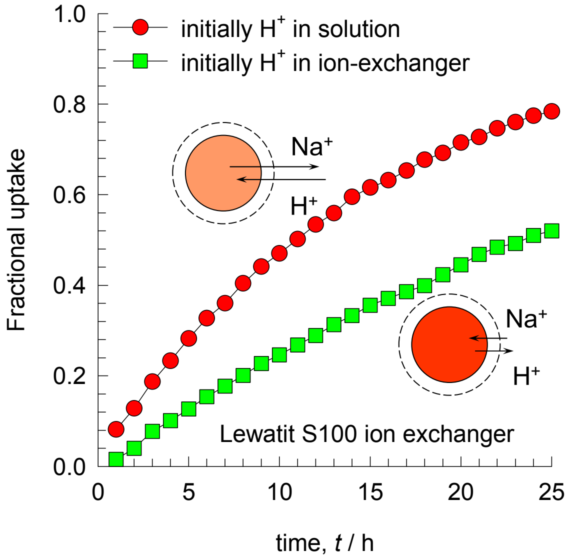

ESI Fig. 82

Transport across cation-exchange membrane

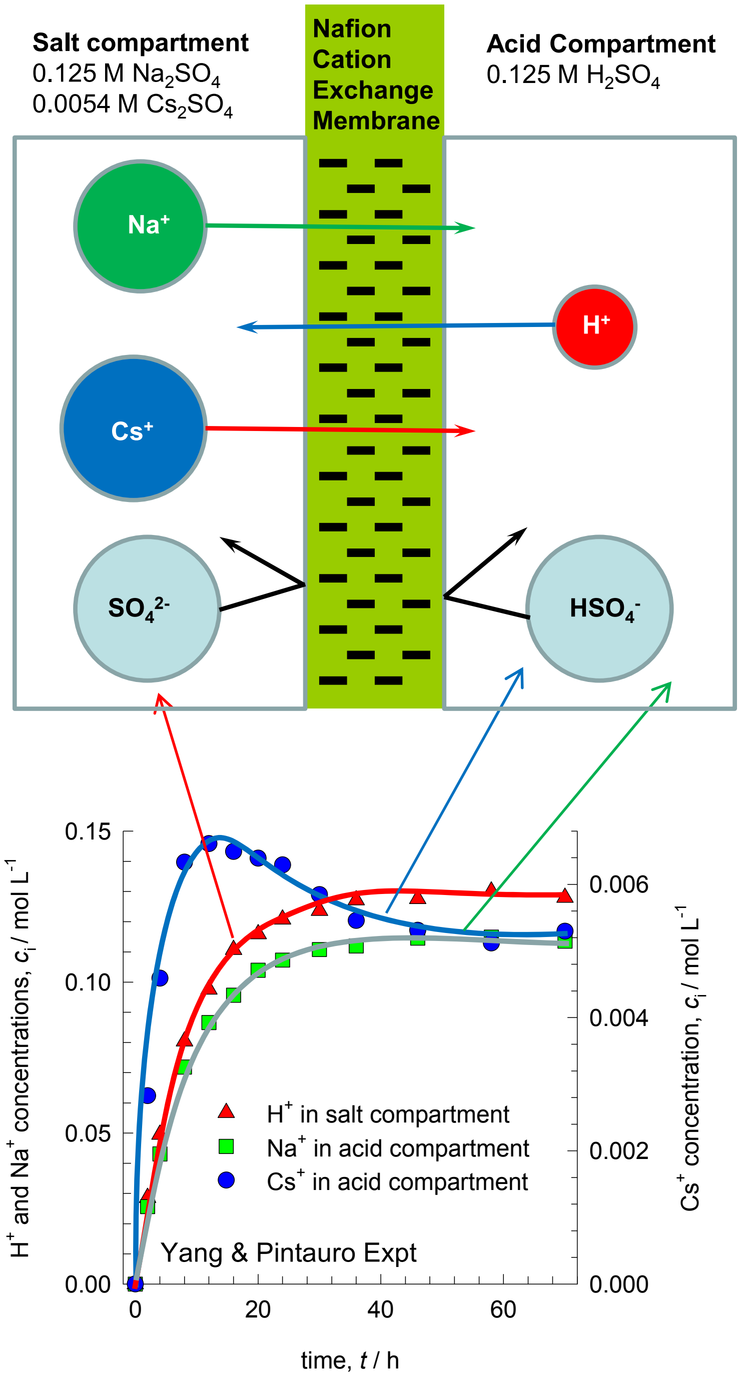

ESI Fig. 83

Reverse osmosis

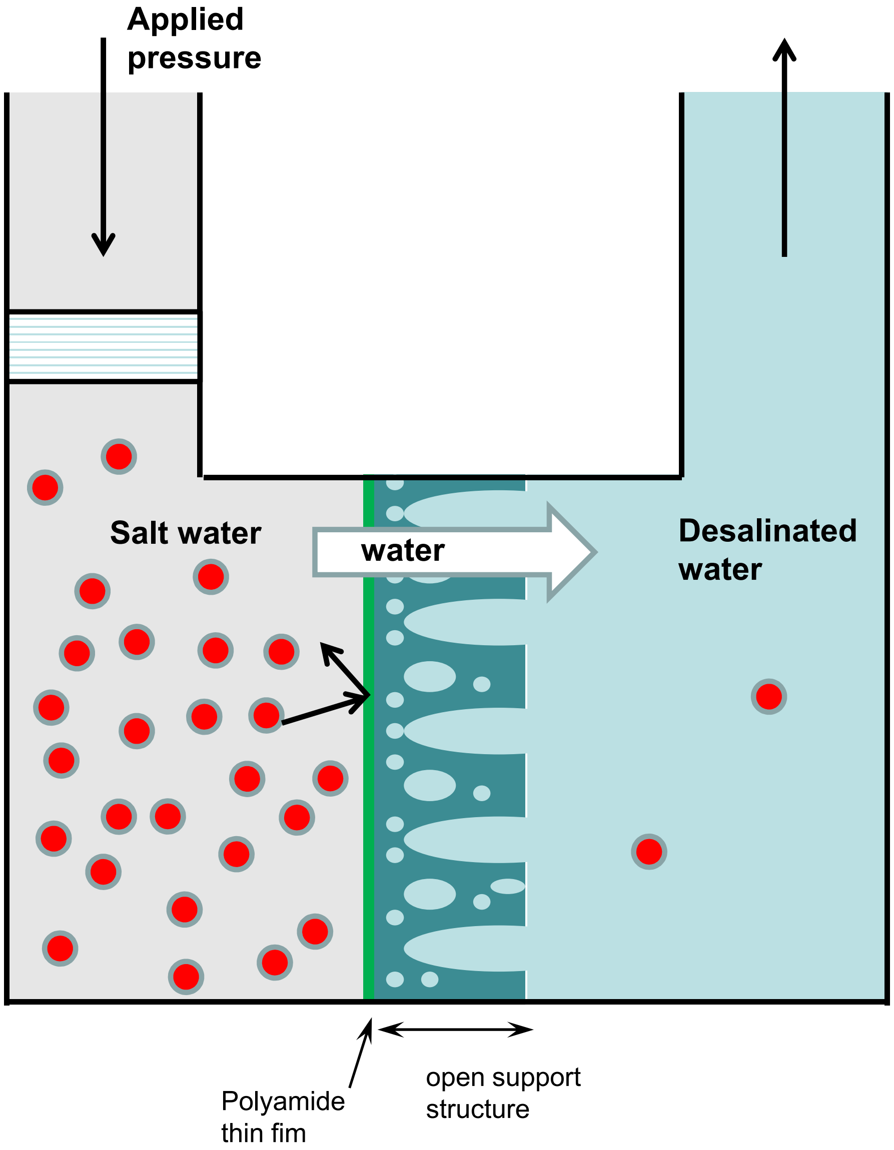

$$-\frac{x_w}{RT}\frac{d\mu_w}{dz}-\frac{1}{RT}\overline{V}_w\frac{dp}{dz}=\frac{N_w}{c_t Đ_{wM}}$$

ESI Fig. 84

Microporous materials: 1D channels

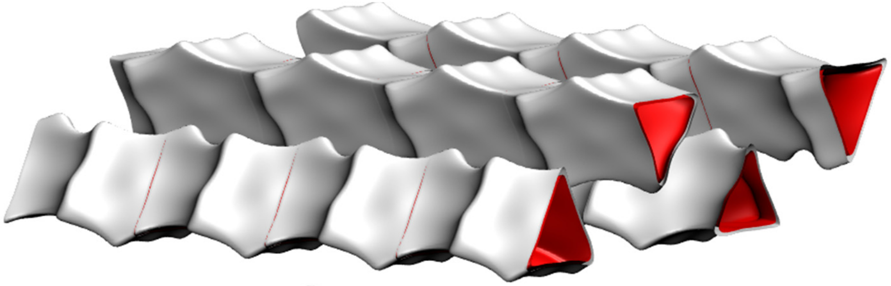

$Fe_2(BDP)_3$

AFI

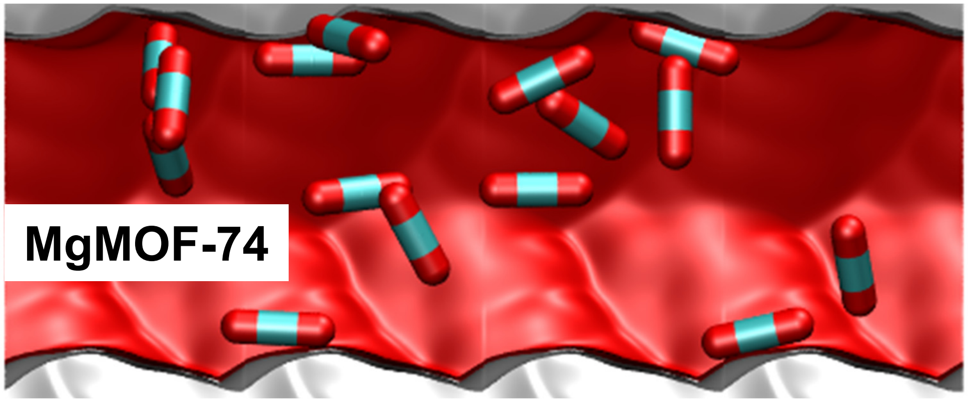

MgMOF-74

MIL-53(Cr)-lp

BTP-COF

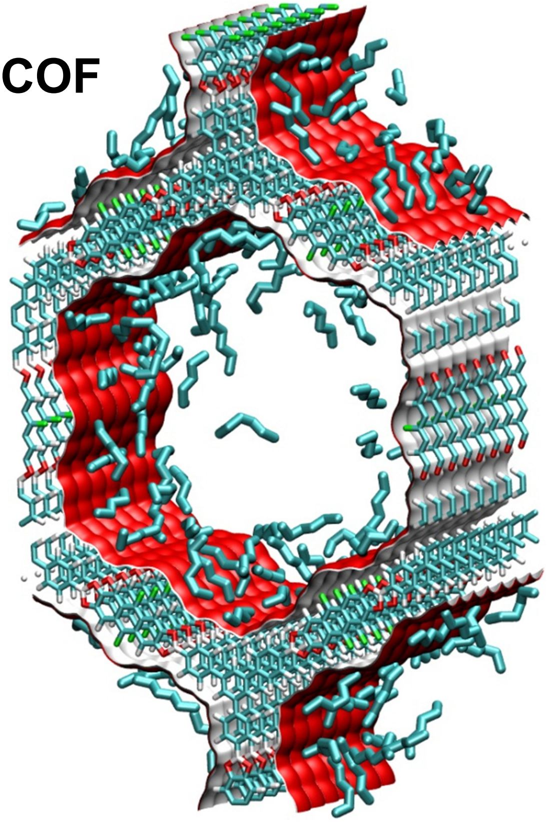

ESI Fig. 85

1D channels with side pockets

MOR

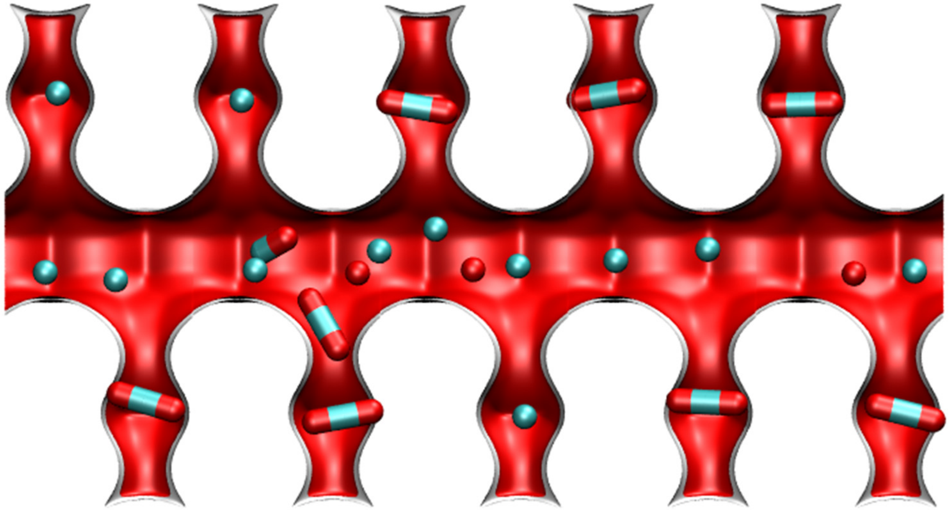

FER

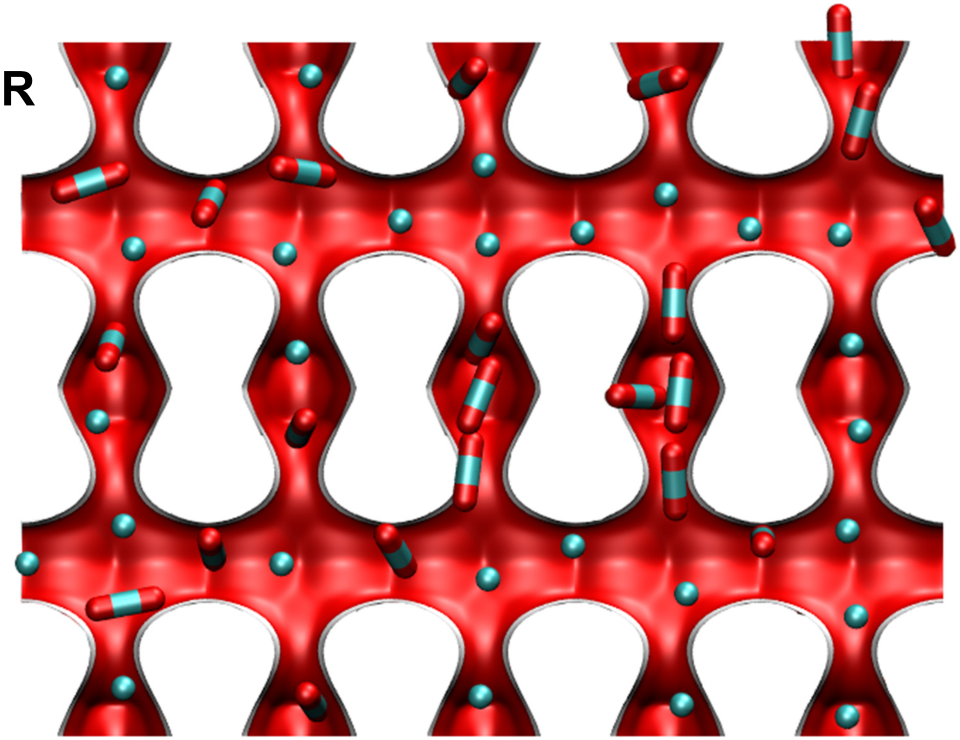

Intersecting channels

MFI

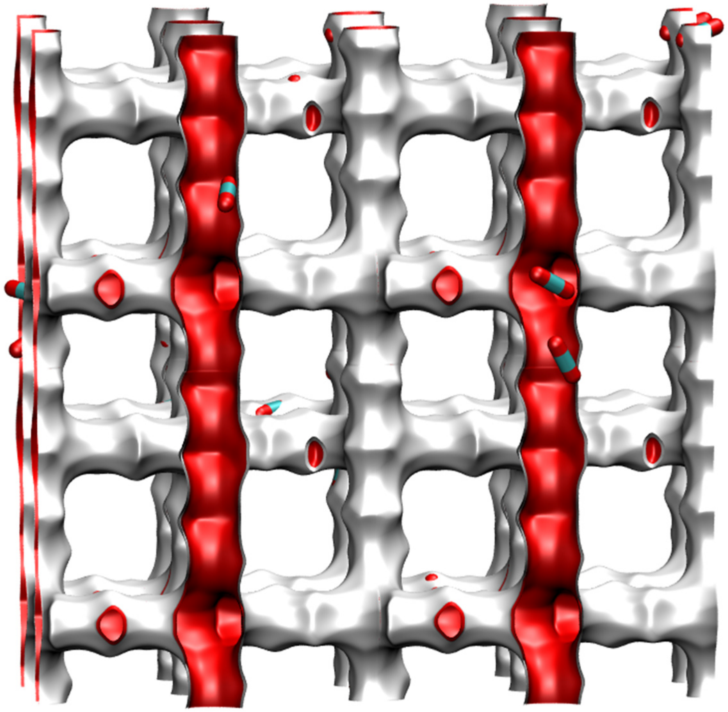

Zn(bdc)dabco

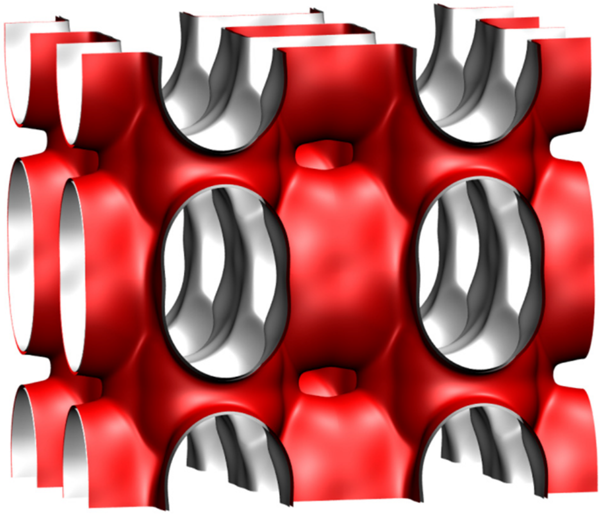

ESI Fig. 87

Cages with narrow windows

LTA

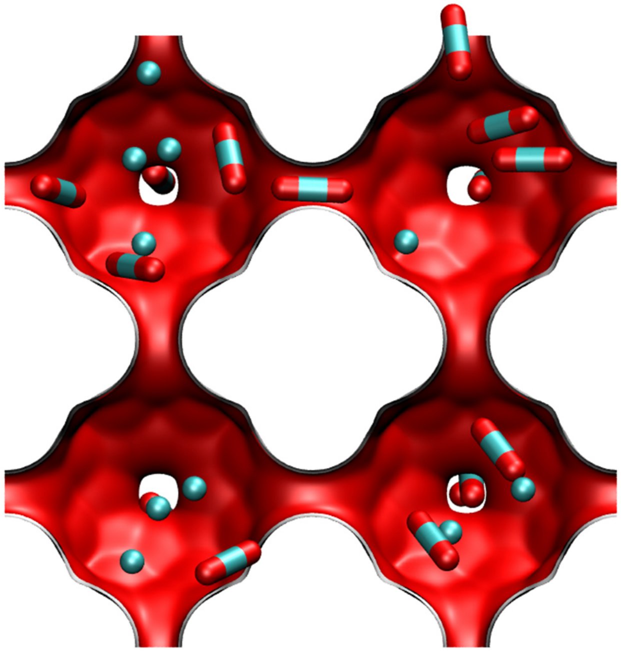

ZIF-8

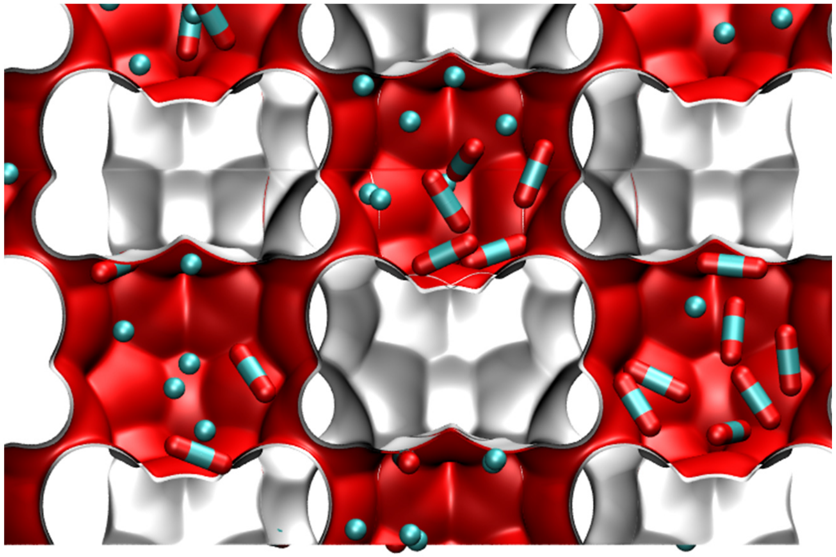

CHA

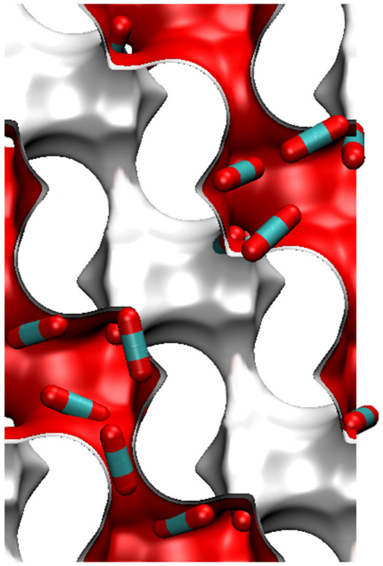

DDR

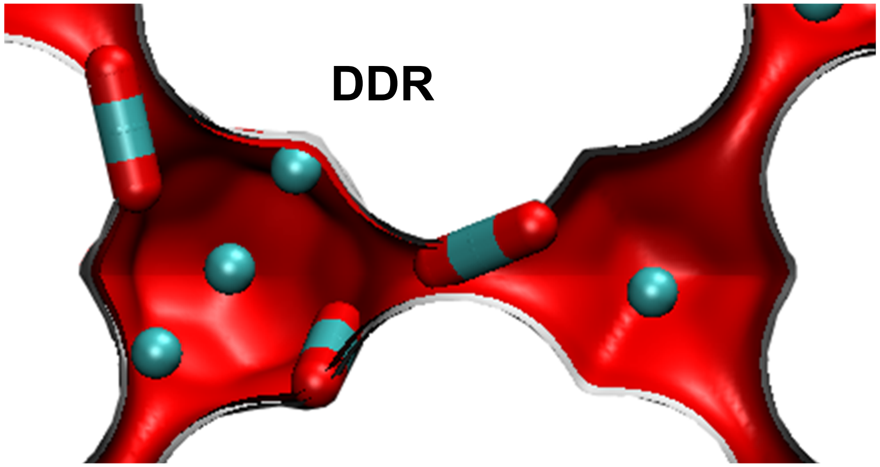

ESI Fig. 88

Cages with large windows

IRMOF-1

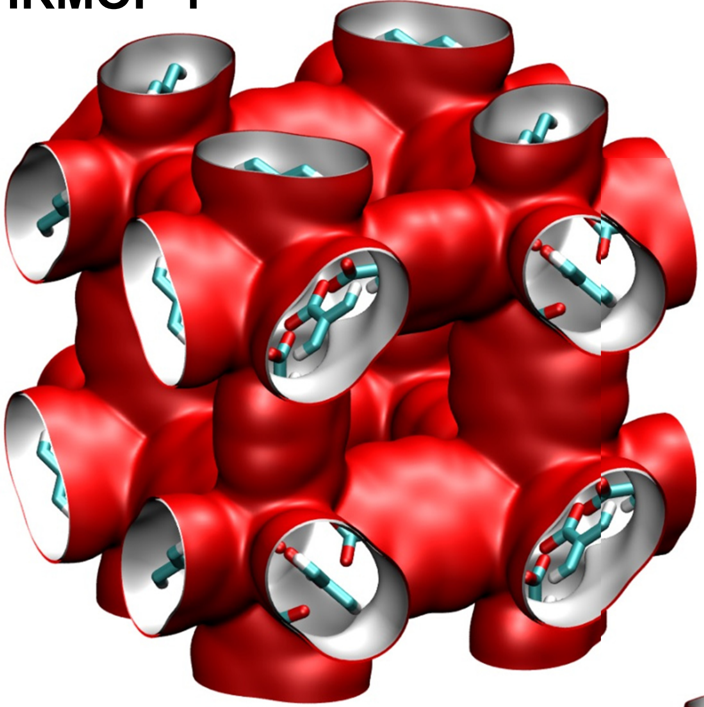

FAU

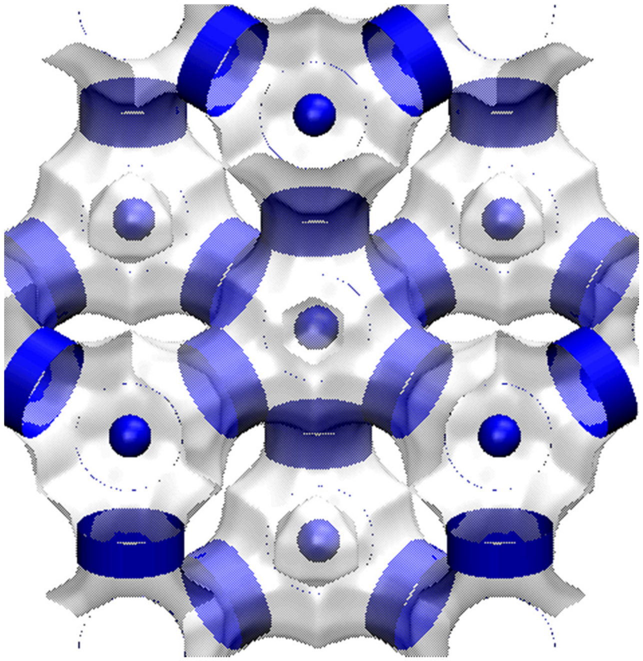

CuBTC

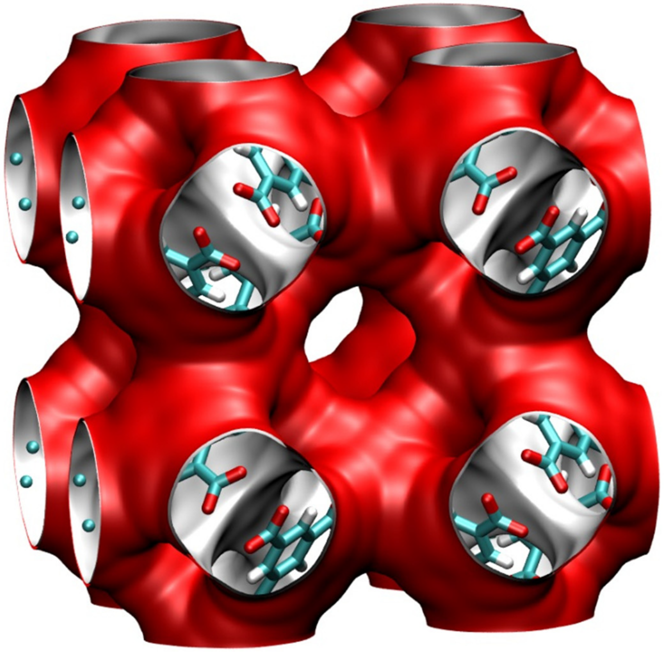

PSA separations for O_2/N_2

ESI Fig. 89

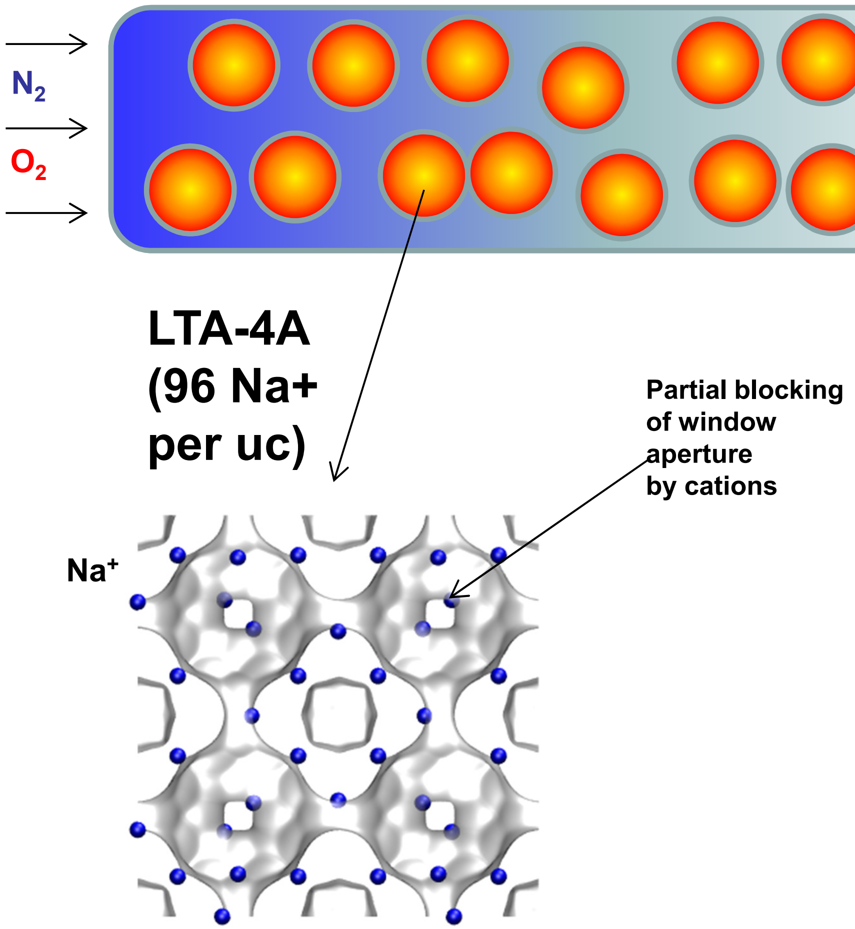

LTA-4A (96 Na+ per uc)

Partial blocking of window aperture by cations

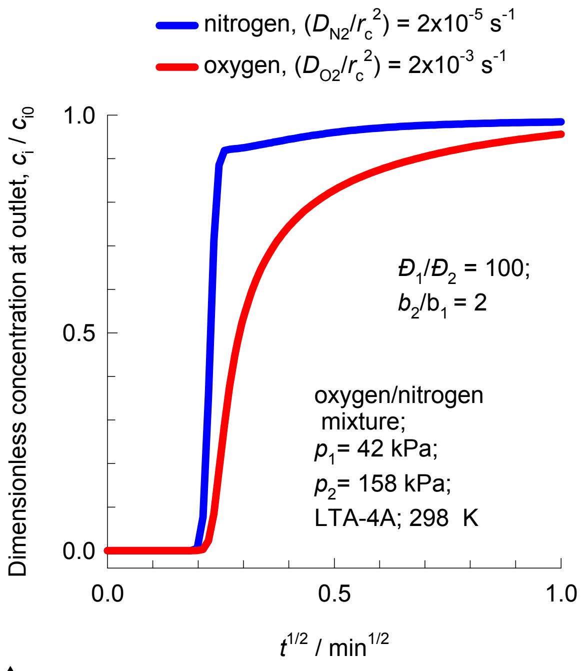

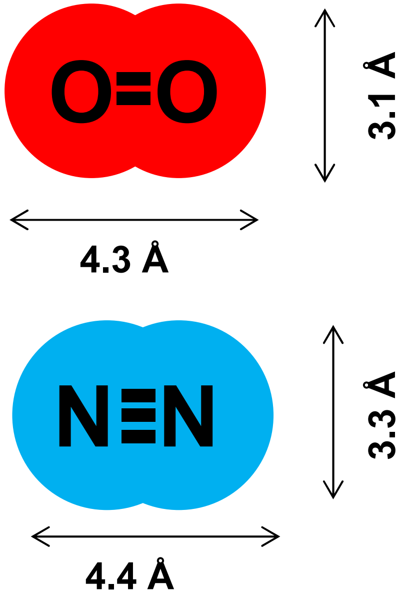

ESI Fig. 90

Membrane separation

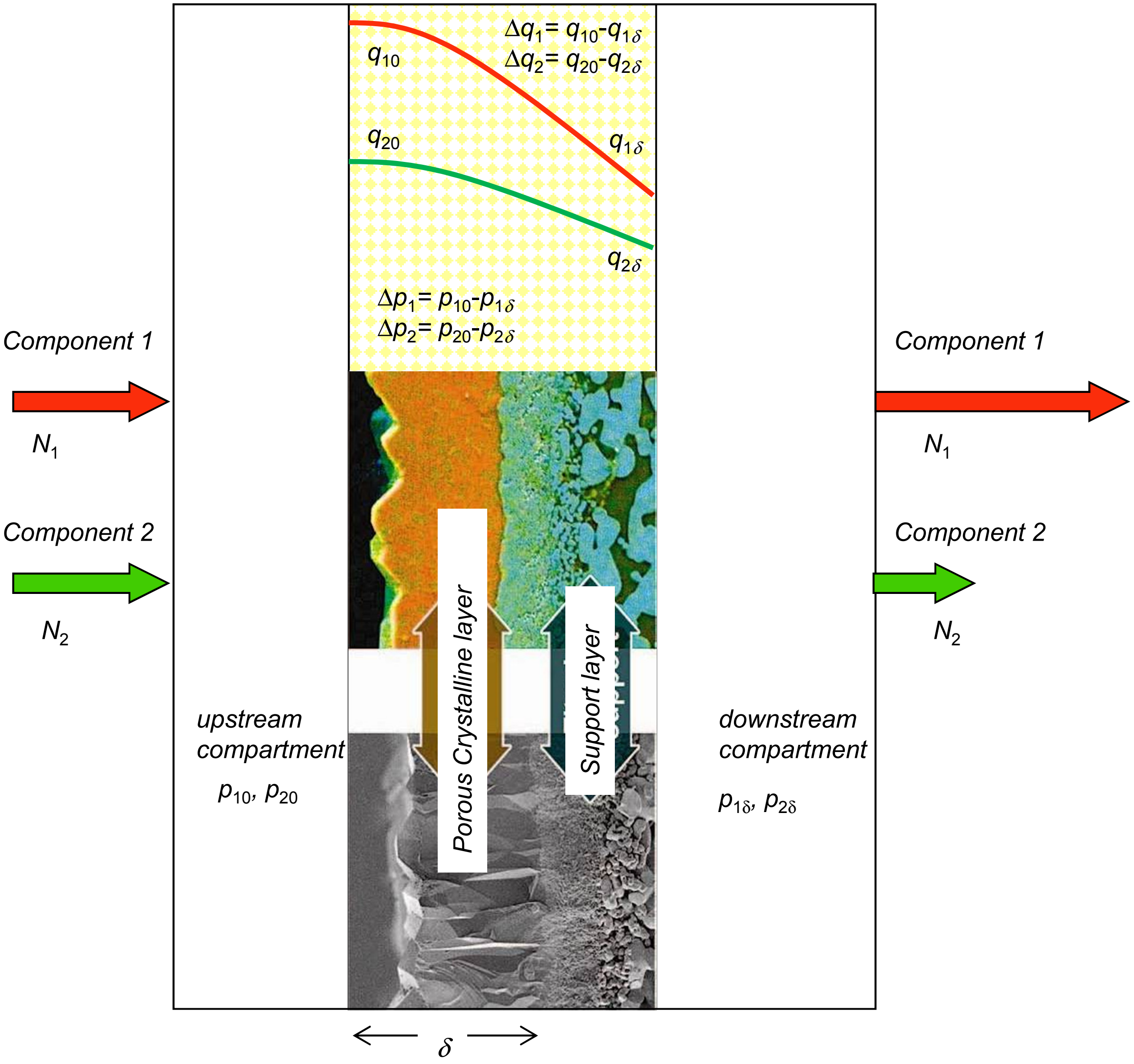

Thermodynamic Factor: unary adsorption

ESI Fig. 91

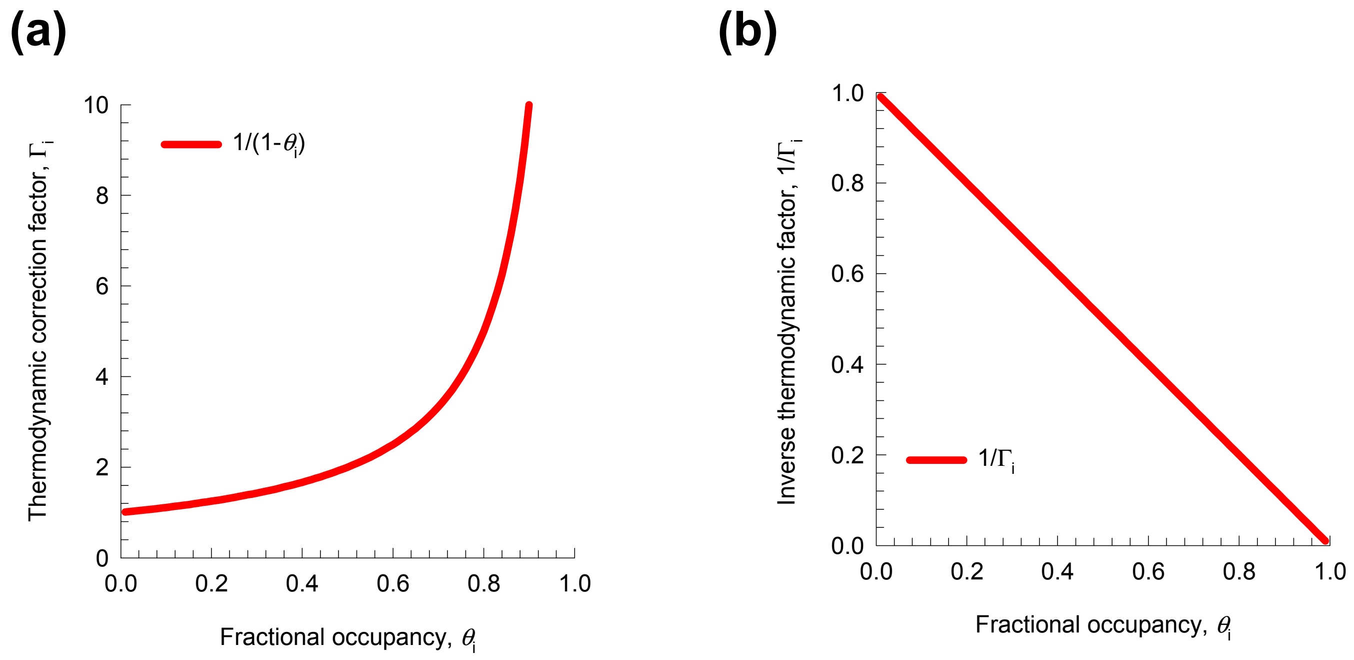

Adsorption/Desorption asymmetry

ESI Fig. 92

LTA-4A
(96 Na+)

Partial blocking of window aperture by cations

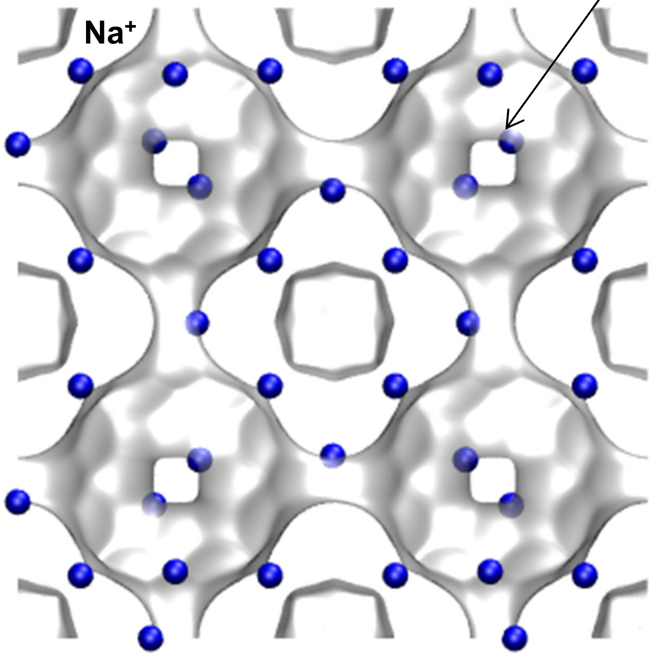

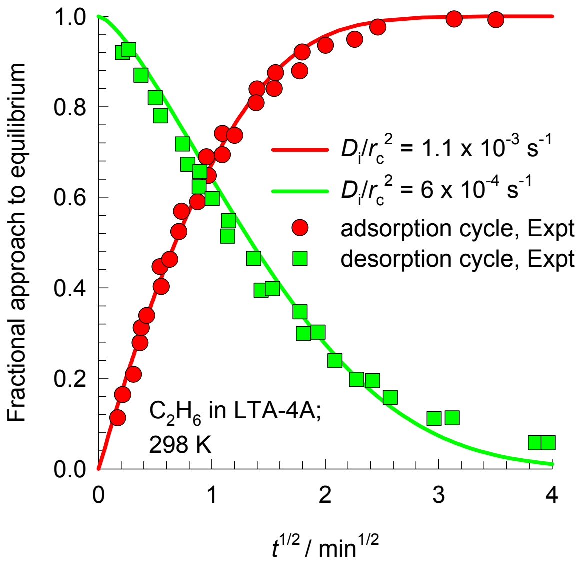

Adsorption/Desorption asymmetry

ESI Fig. 93

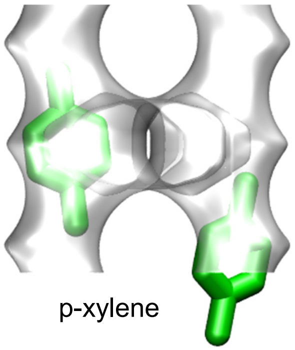

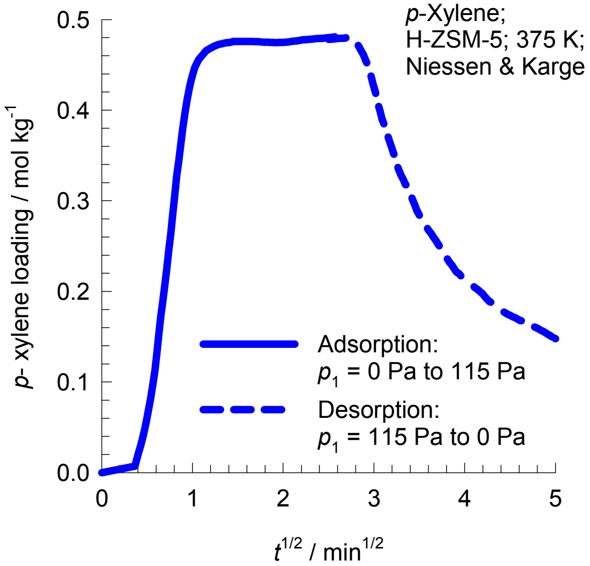

Influence of thermodynamic factor

ESI Fig. 94

(a)

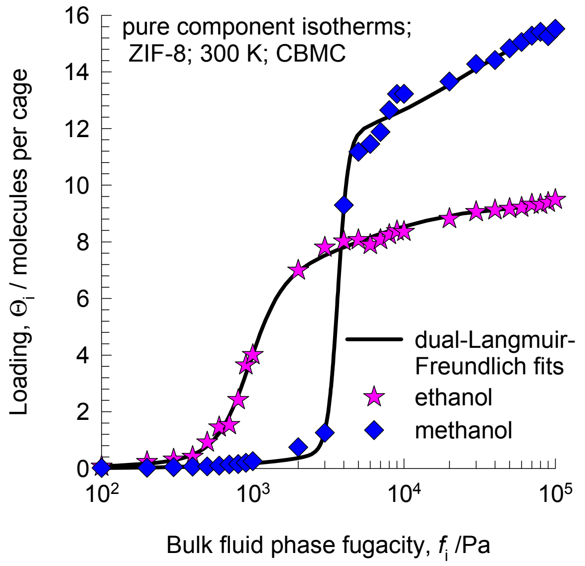

Snapshots of methanol in ZIF-8

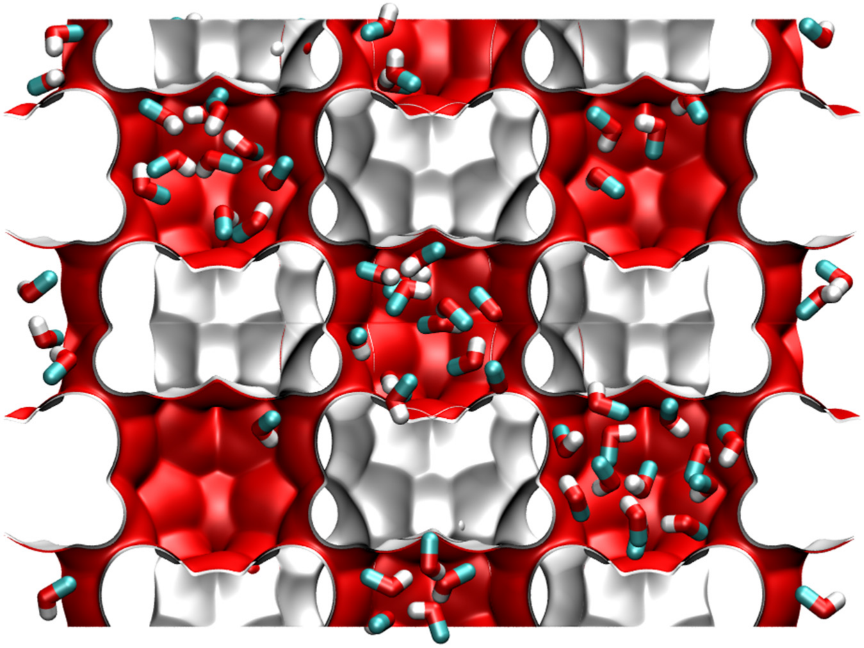

(b)

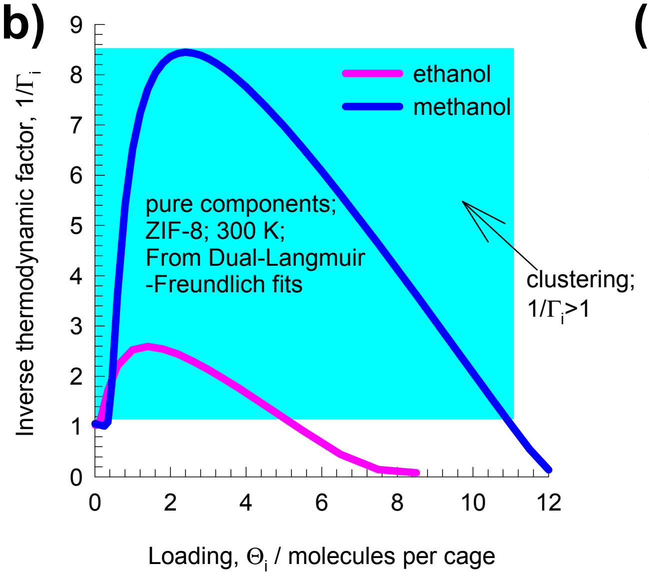

(c)

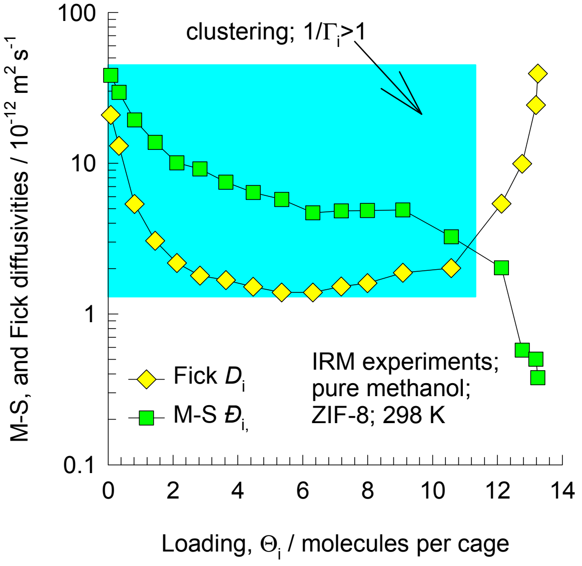

(d)

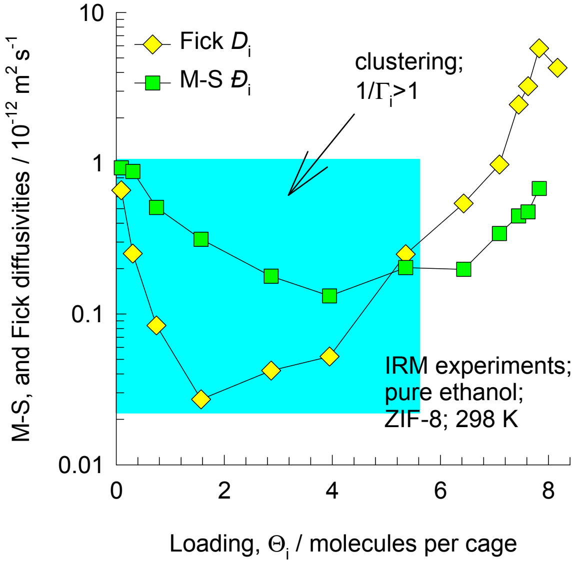

N_2/CH_4 mixture uptake in LTA-4A

ESI Fig. 95

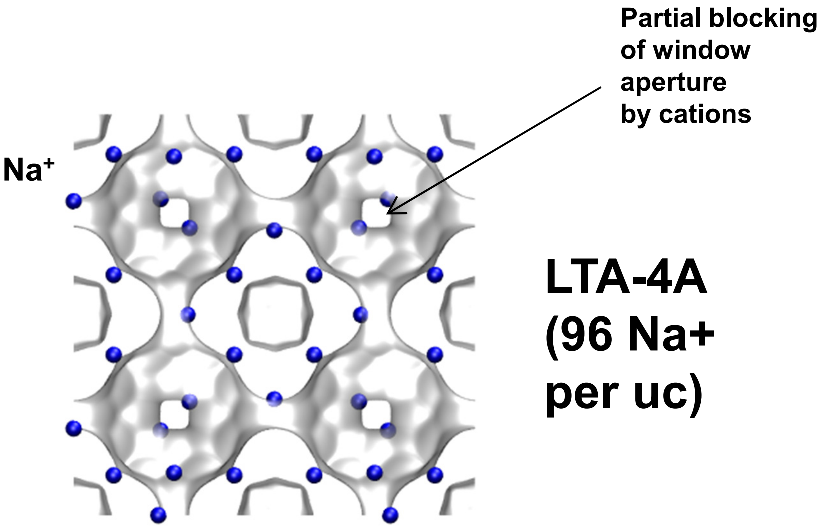

LTA-4A (96 Na+ per uc)

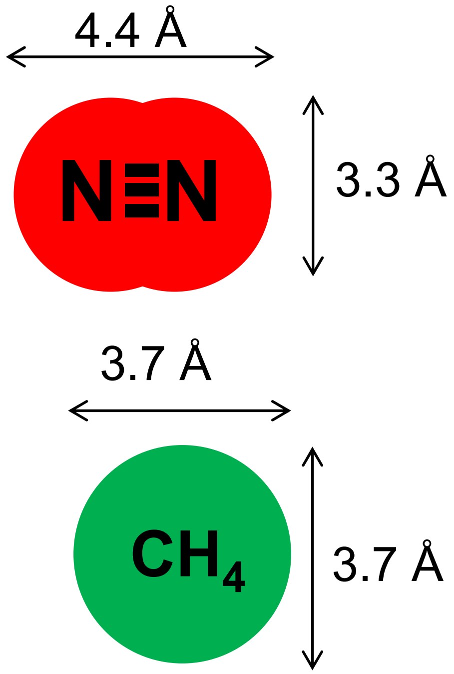

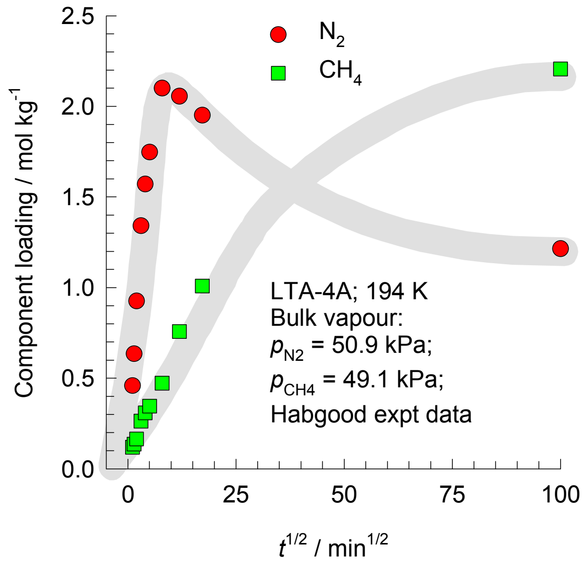

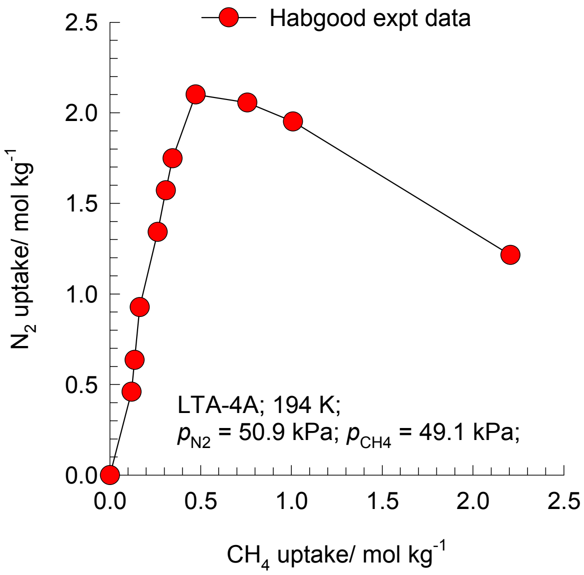

ESI Fig. 96

Thermodynamic factors N_2/CH_4 in LTA-4A

(a)

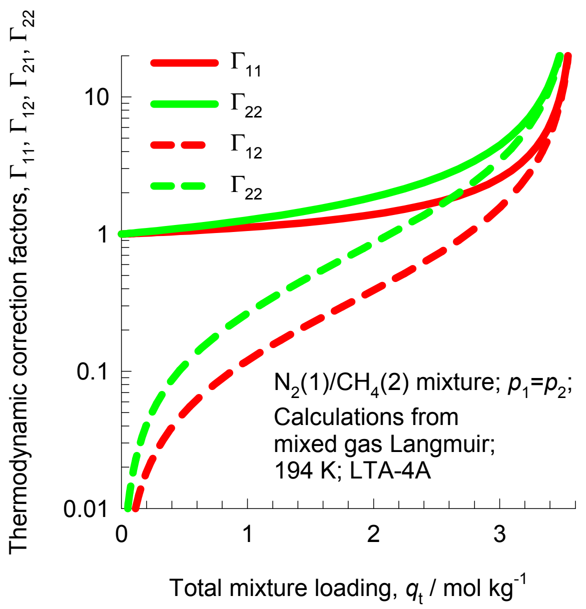

(b)

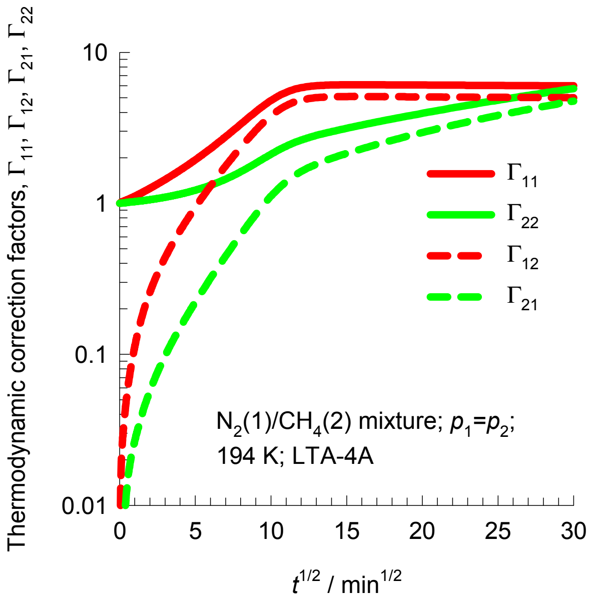

(c)

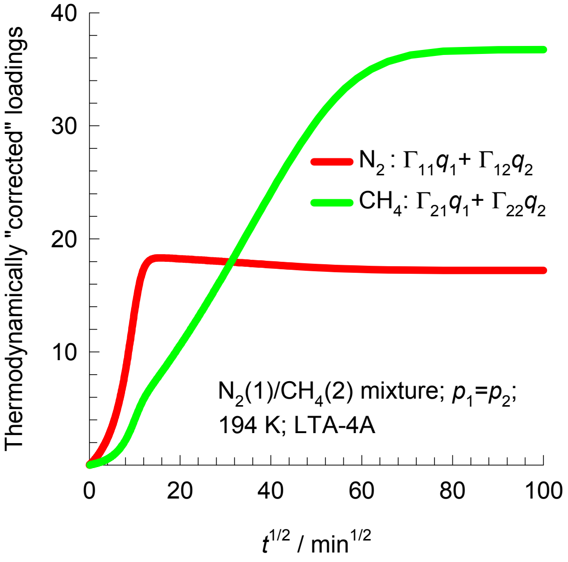

ESI Fig. 97

N_2/CH_4 mixture uptake LTA-4A

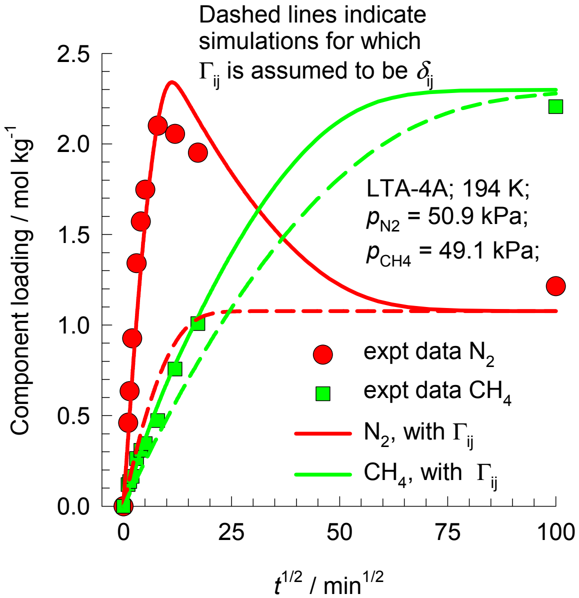
Dashed lines indicate simulations for which Γ_{ij} is assumed to be δ_{ij}

LTA-4A; 194 K; p_{N2} = 50.9 kPa; p_{CH4} = 49.1 kPa;

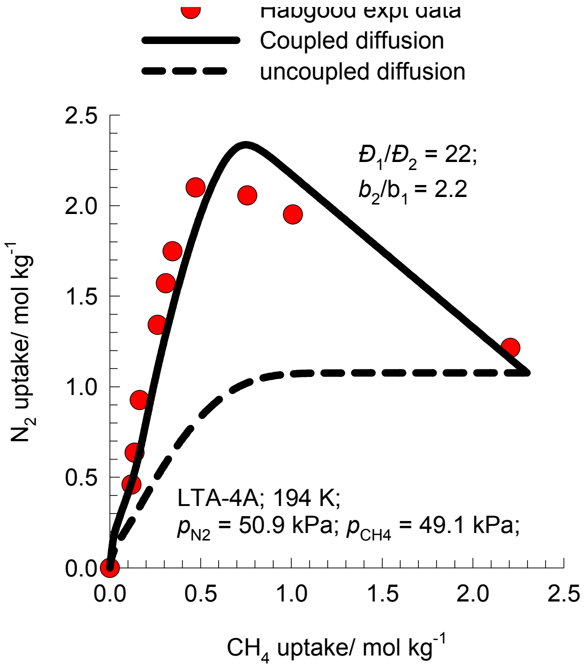
$Ð_1/Ð_2$ = 22; b_2/b_1 = 2.2

LTA-4A; 194 K; p_{N2} = 50.9 kPa; p_{CH4} = 49.1 kPa;

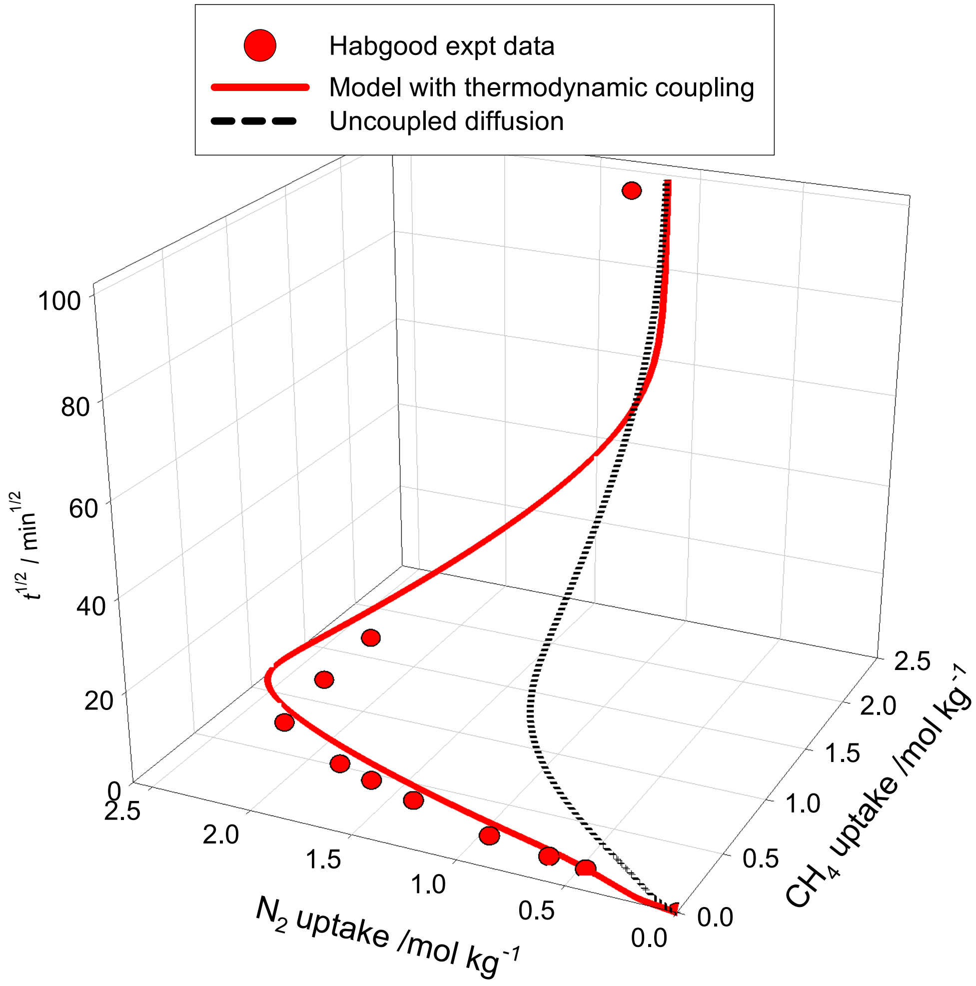

ESI Fig. 98

Adsorption-Desorption Asymmetry

(a)

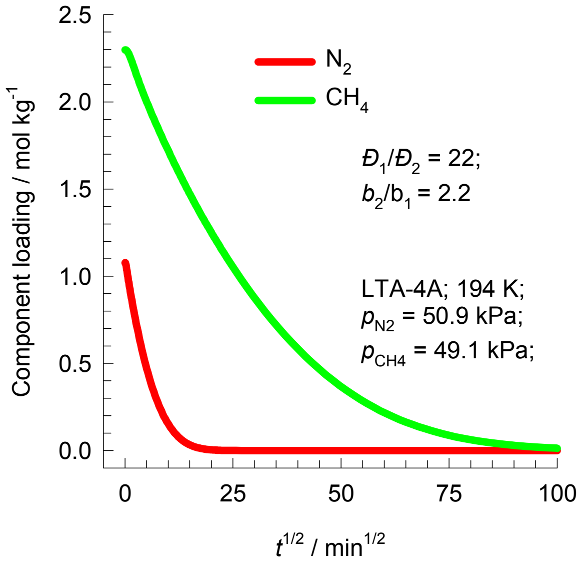

(b)

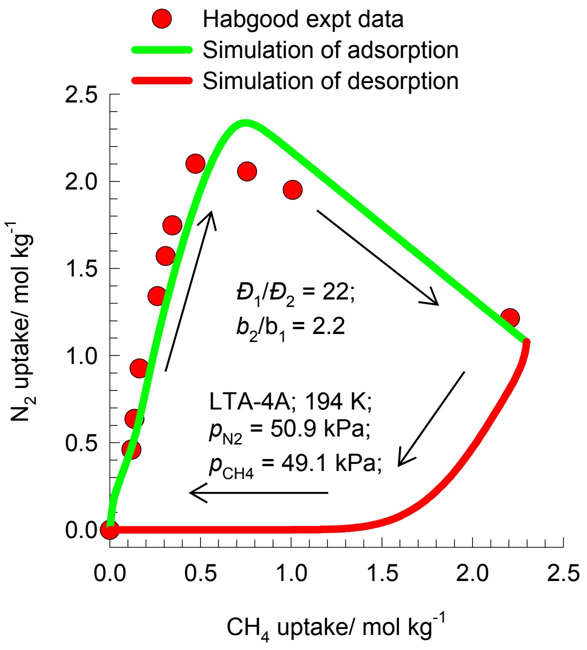

Separations of N_2/CH_4 mixtures in PSA unit

ESI Fig. 99

Inlet gas contains 10% N_2

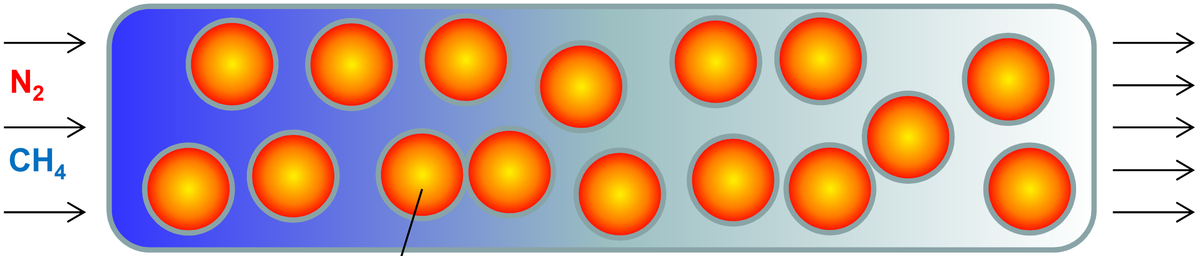

LTA-4A (96 Na+ per uc)

Partial blocking of window aperture by cations

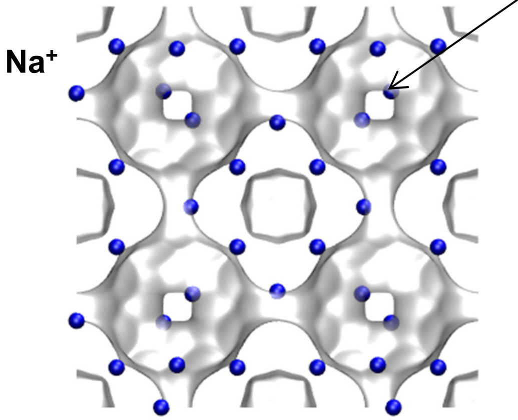

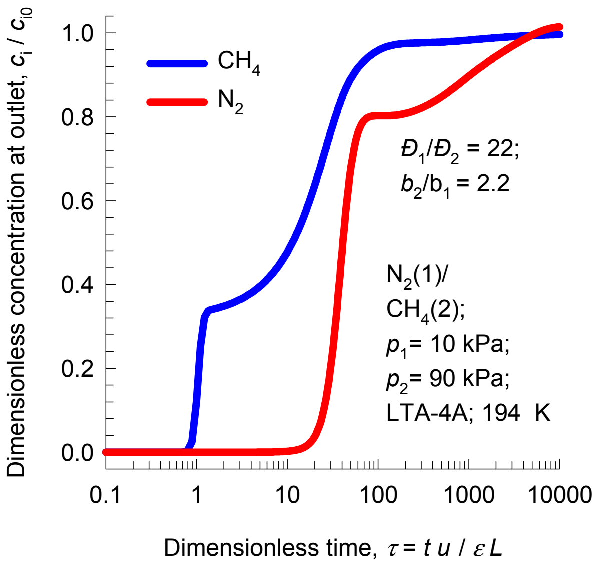

Nearly pure CH_4 can be recovered during this time interval

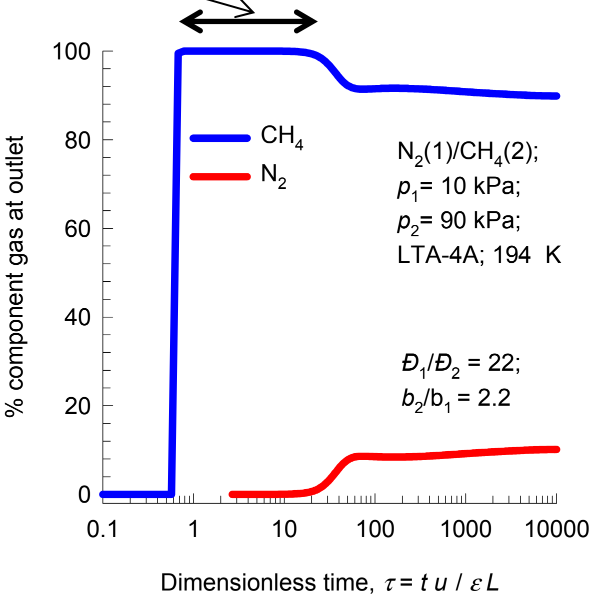

BaETS-4 transient N_2/CH_4 mixture uptake

ESI Fig. 100

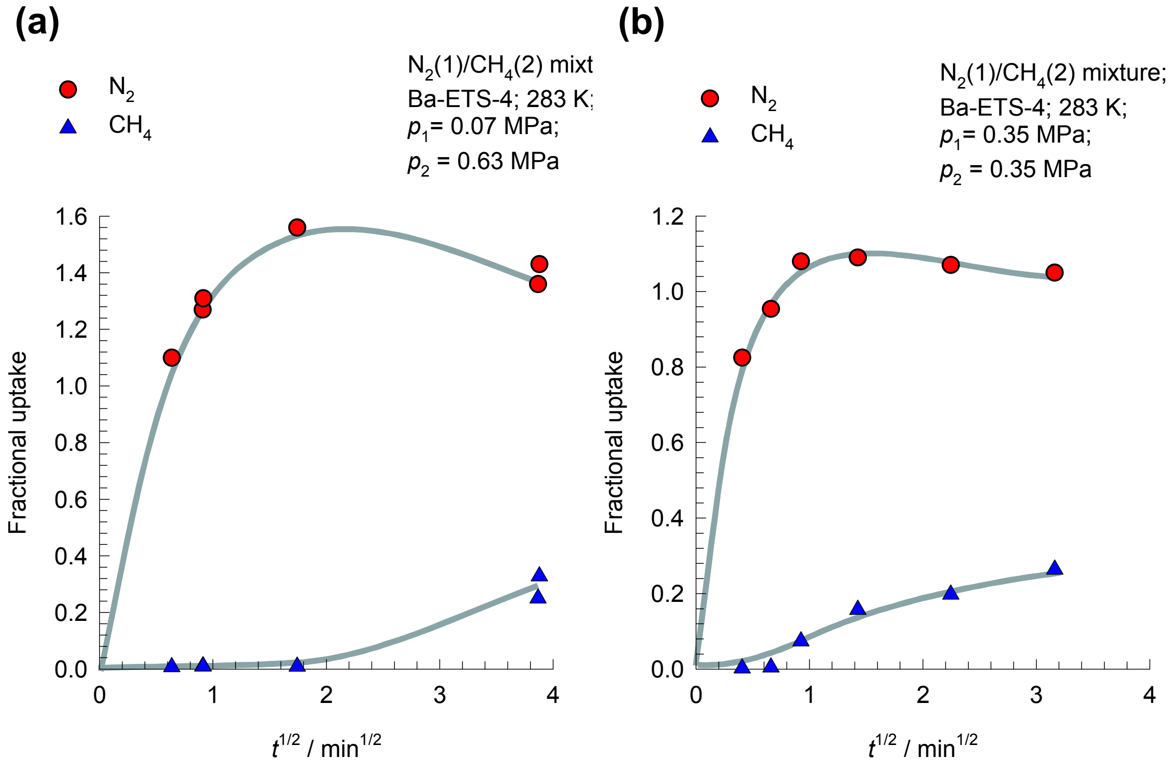

Transient uptake of O_2/N_2 in LTA-4A

ESI Fig. 101

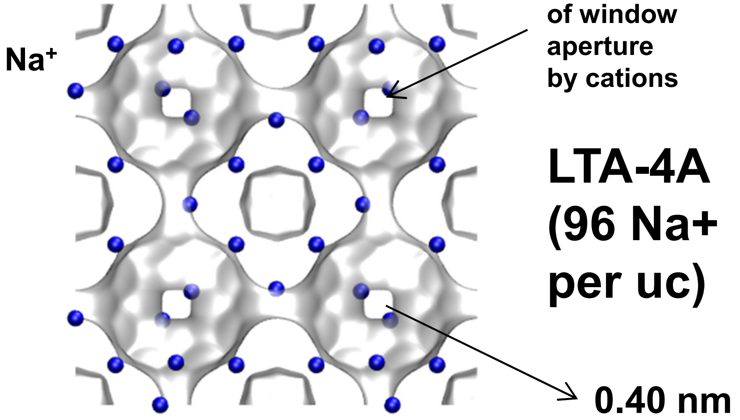

Partial blocking of window aperture by cations

LTA-4A (96 Na+ per uc)

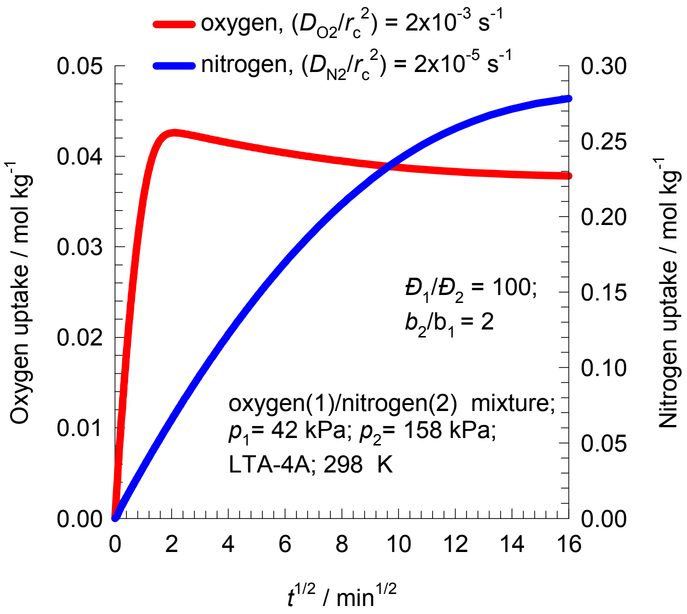

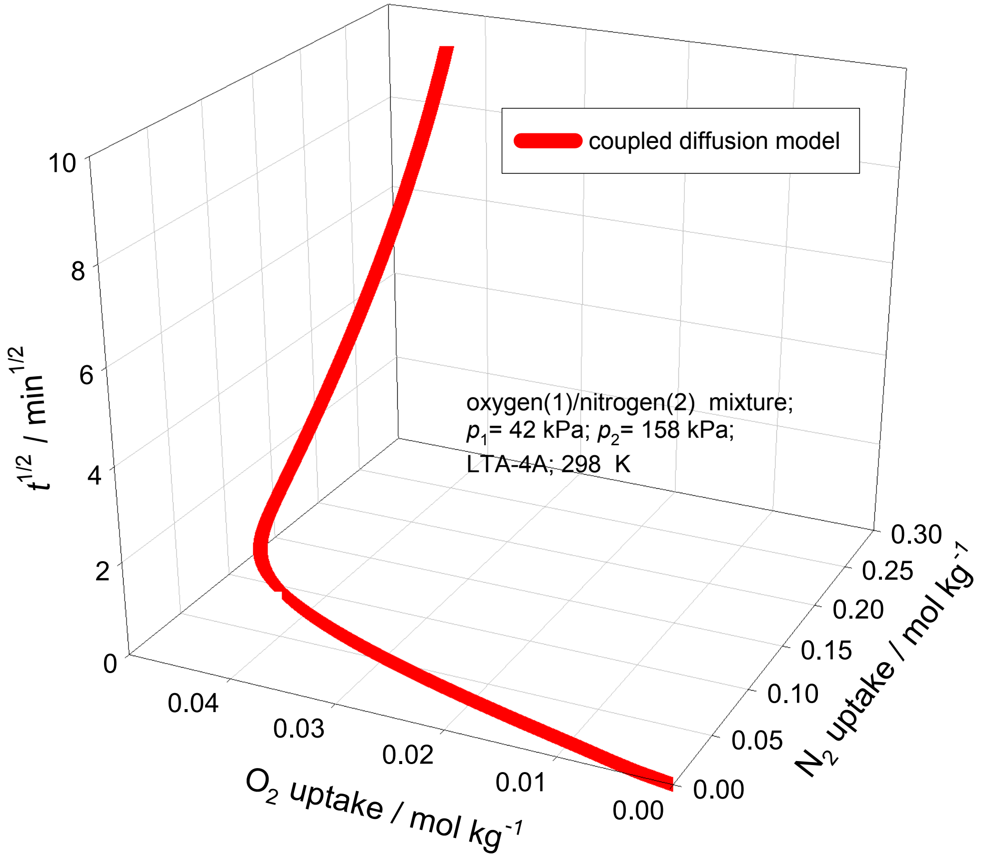

Transient uptake of O_2/N_2 in CMS

ESI Fig. 102

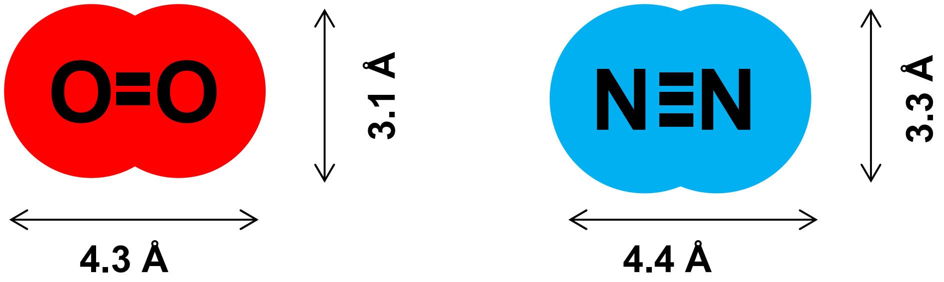

(a)

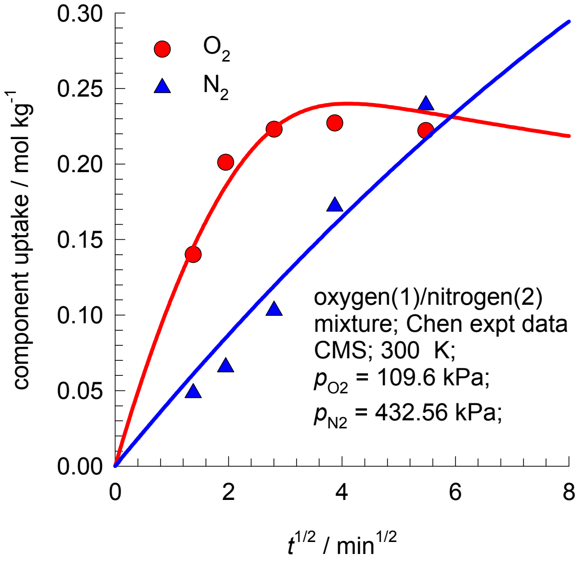

(b)

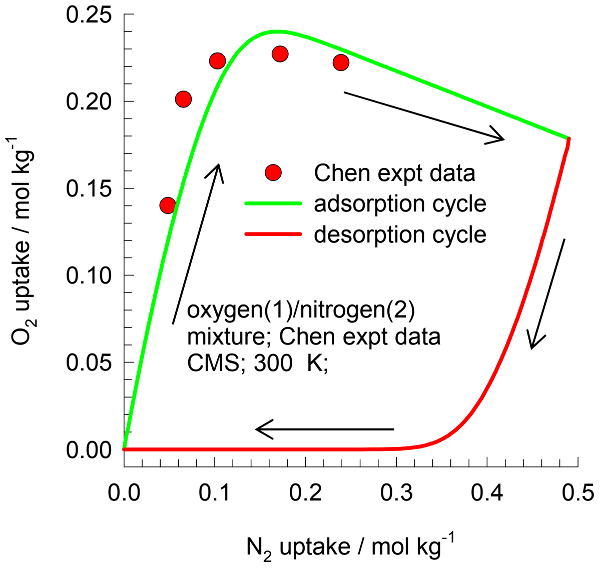

Transient uptake CH_4/C_2H_6 in LTA-4A

LTA-4A
(96 Na+)

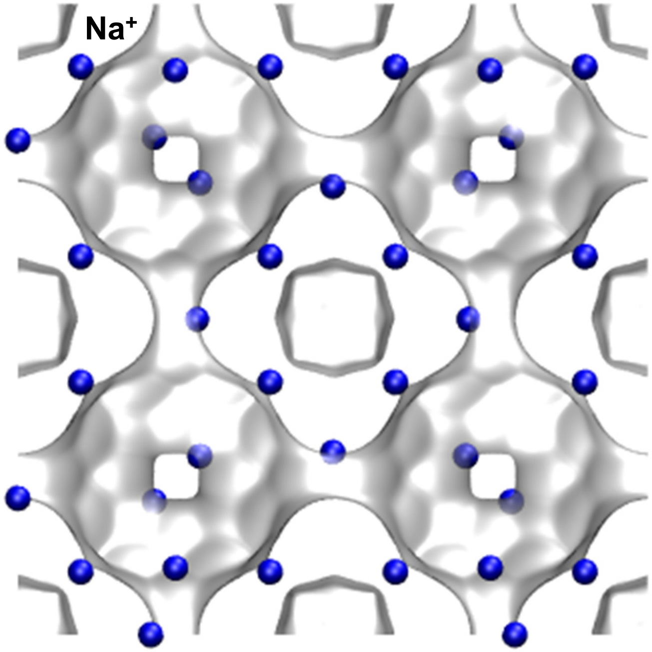

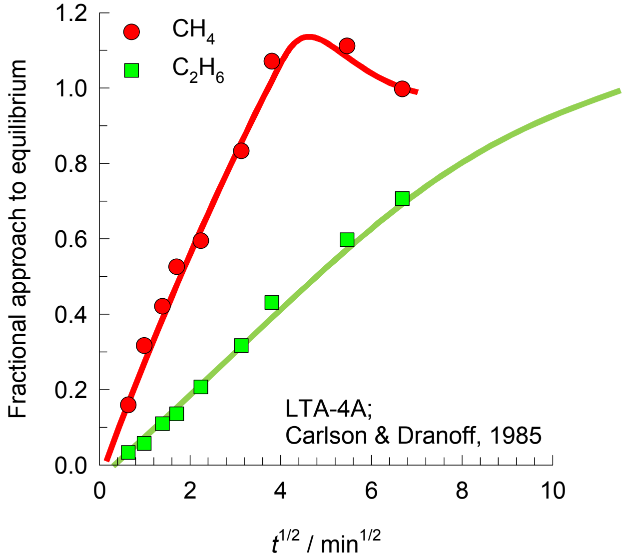

LTA-4A;
Carlson & Dranoff, 1985

ESI Fig. 104

Propene/propane uptake in ZIF-8

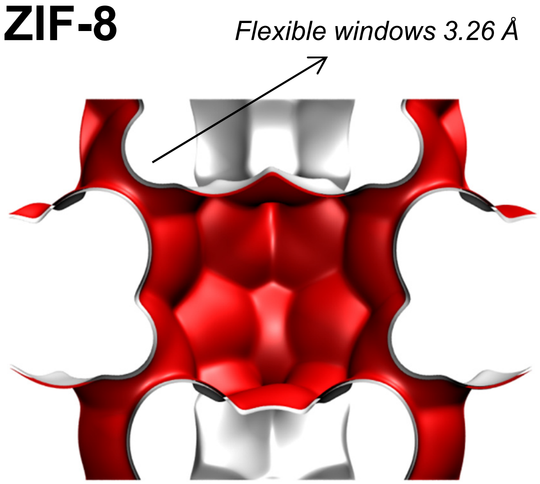

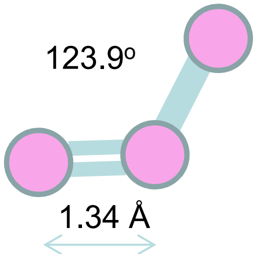

propene

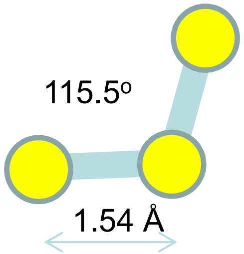

propane

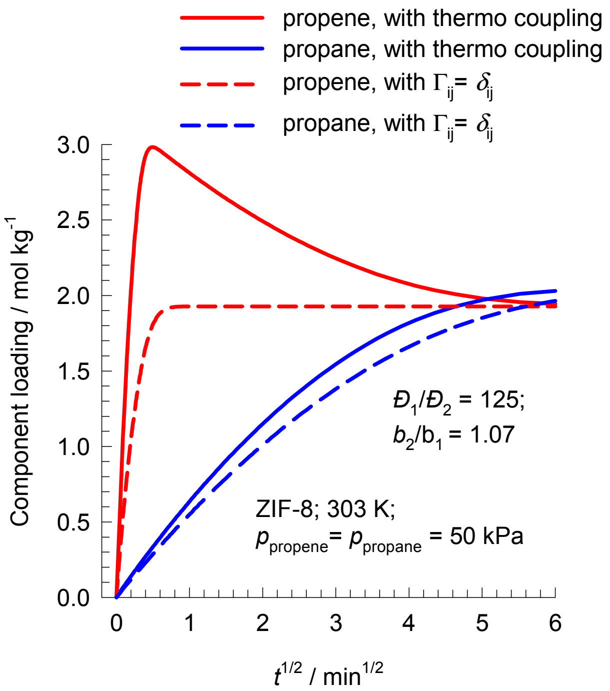

ESI Fig. 105

Propene/propane uptake in CHA

CHA

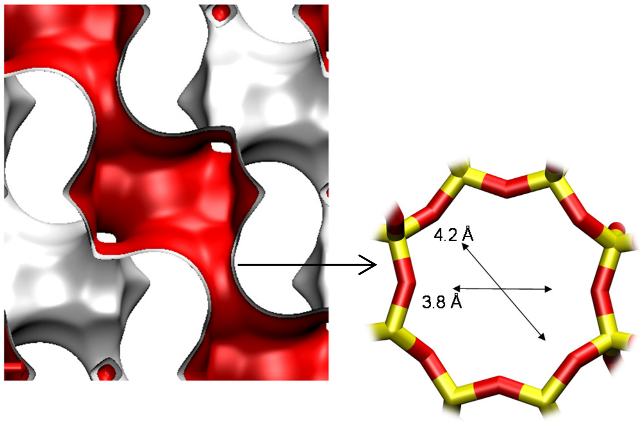

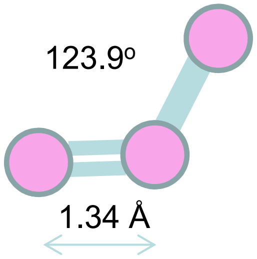

propene

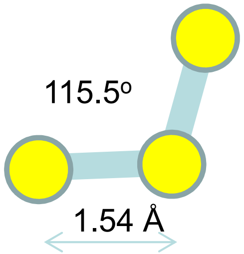

propane

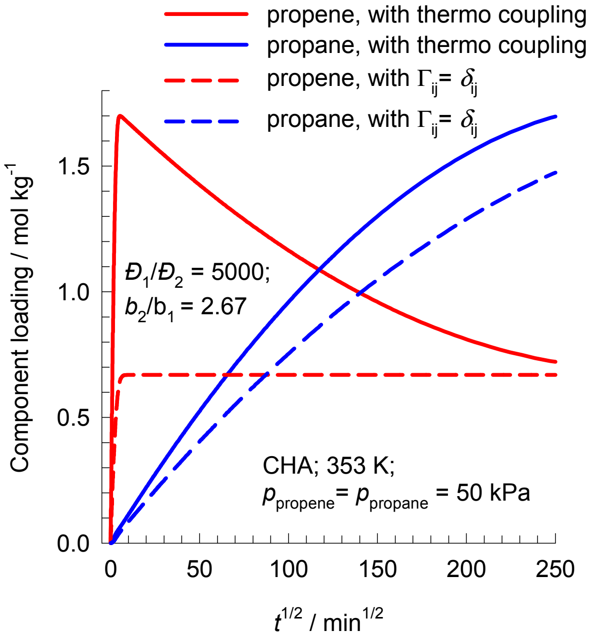

SAPO-34:
Transient uptake of 1-alcohols

ESI Fig. 106

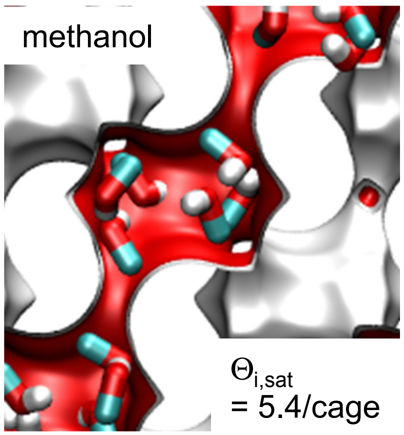

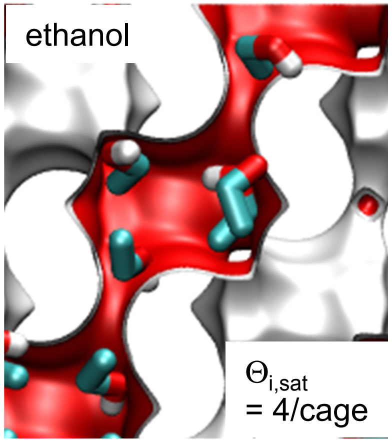

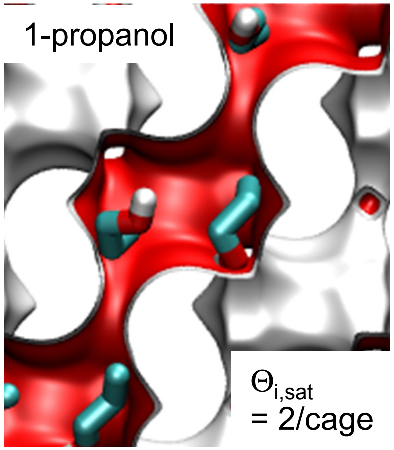

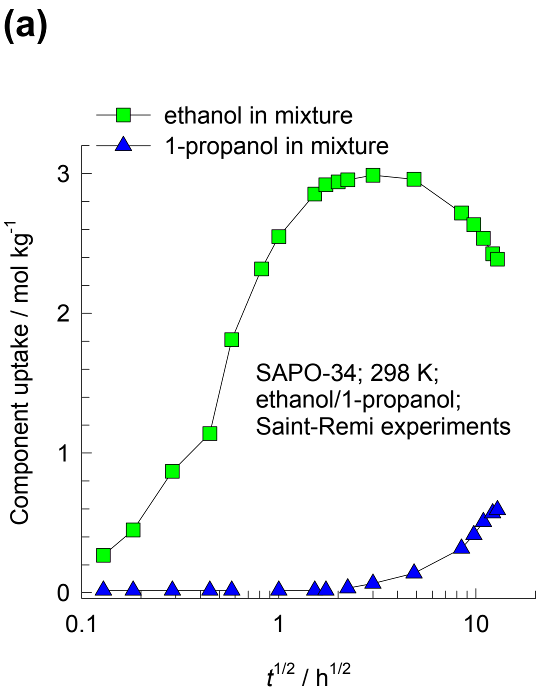

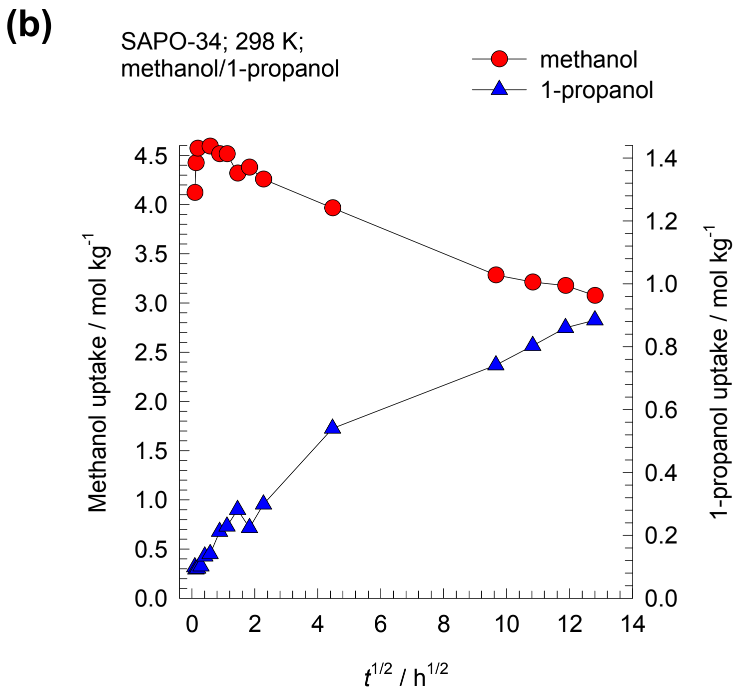

Radial profiles for ethanol/1-propanol transient uptake in CHA

ESI Fig. 107

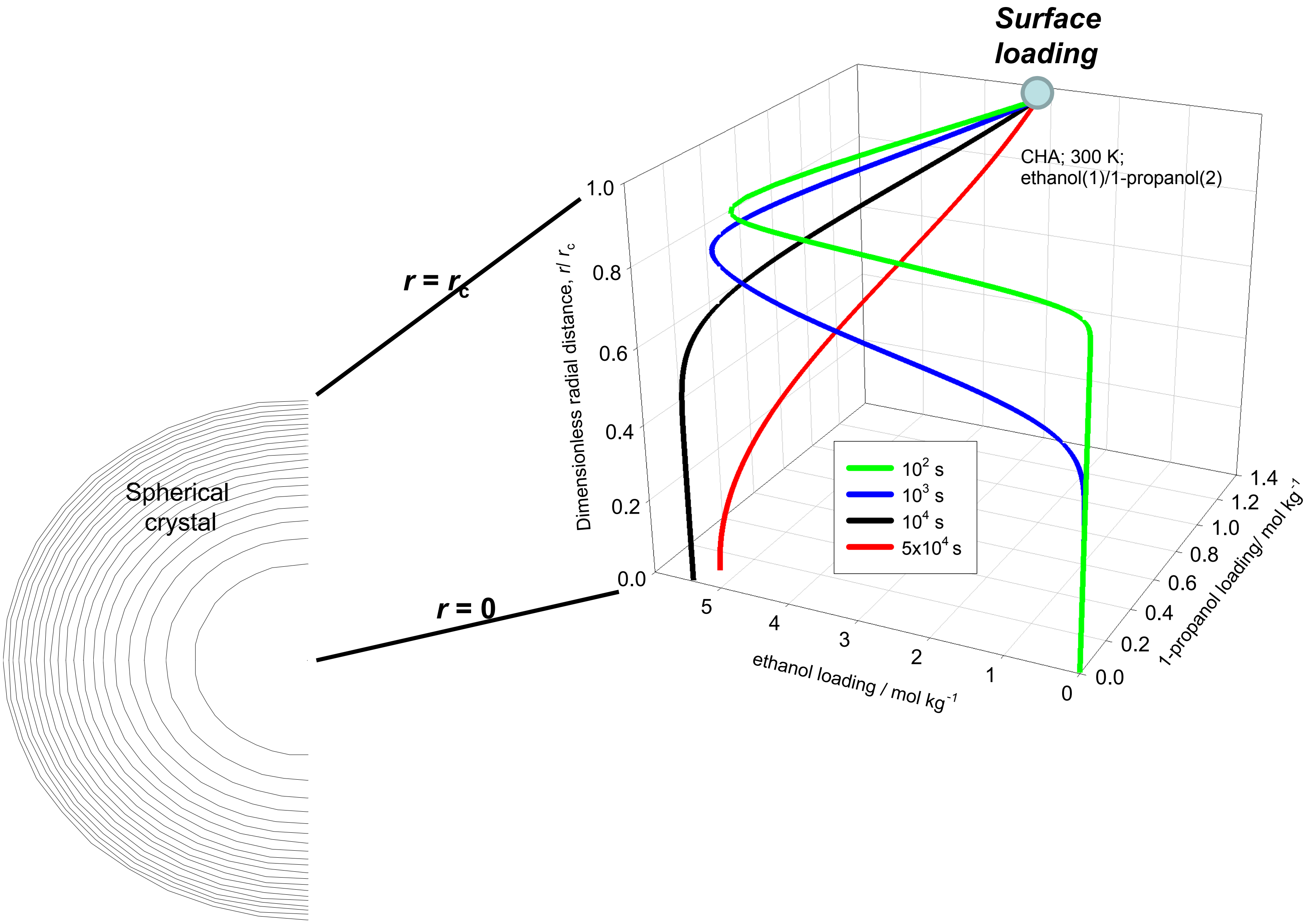

SAPO-34: Transient uptake, and breakthrough

ESI Fig. 108

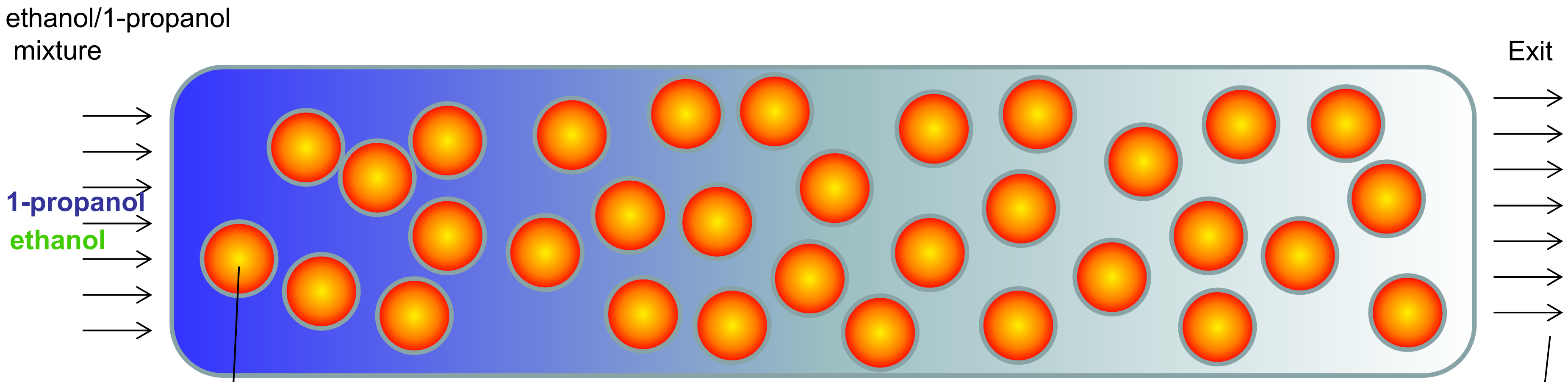

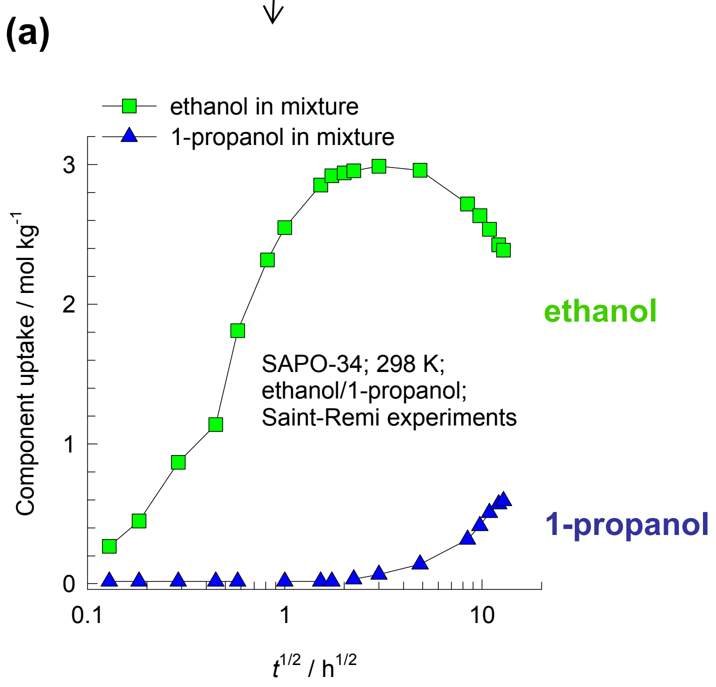

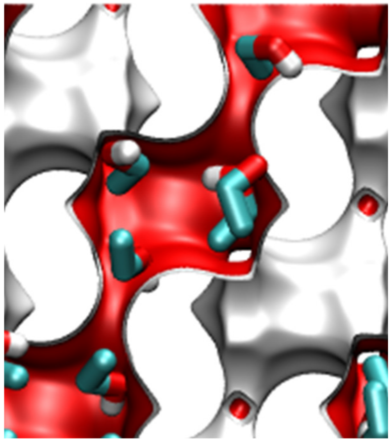

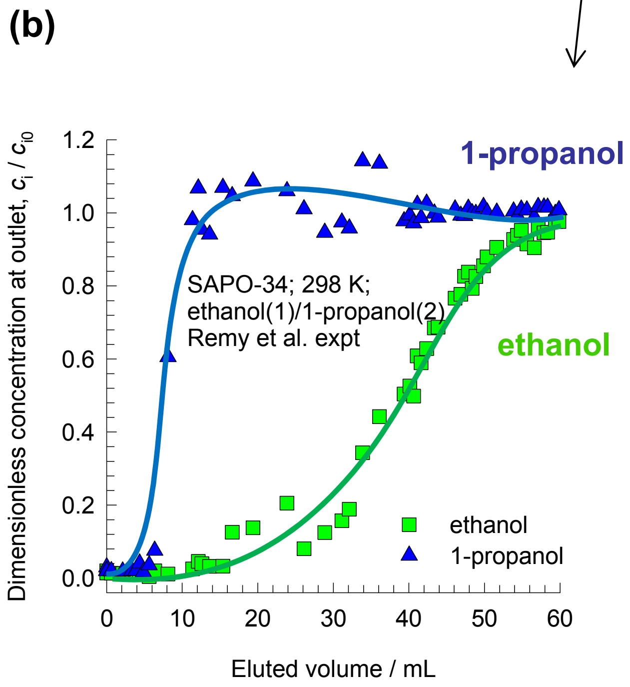

ESI Fig. 109

Adsorption/Desorption 1-alcohols in CHA

(a)

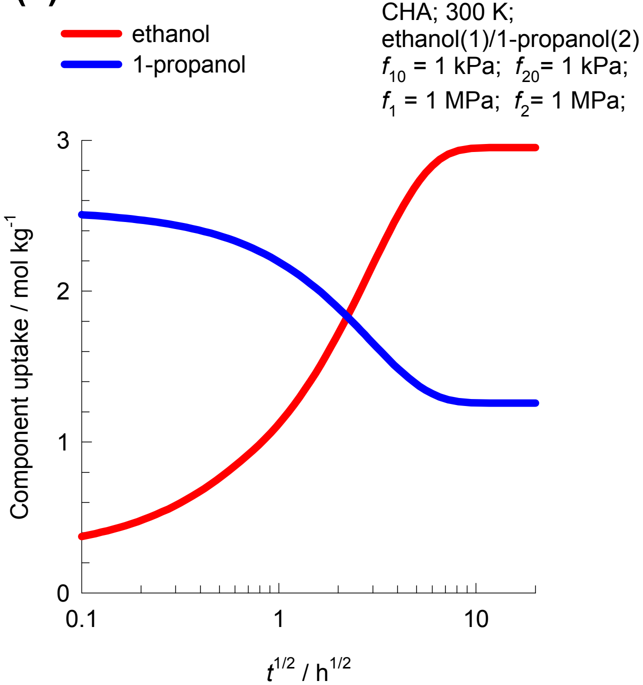

(b)

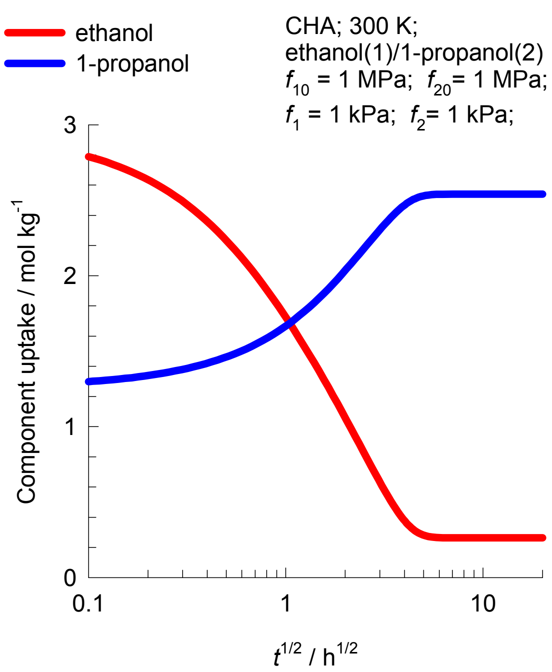

(c)

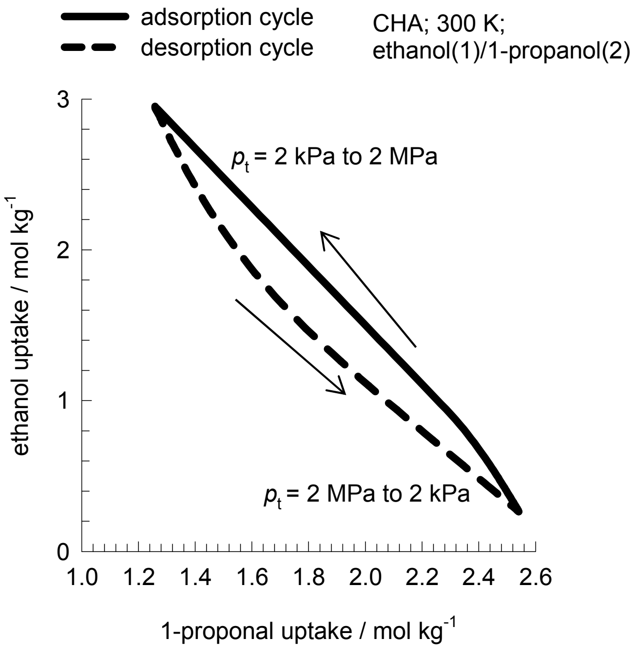

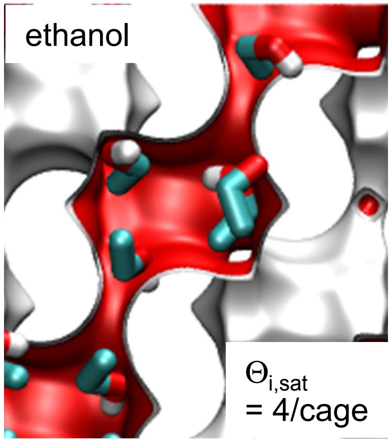

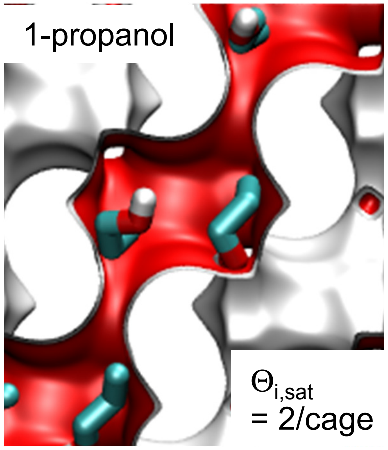

ESI Fig. 110

Transient n-heptane/benzene uptake in NaX

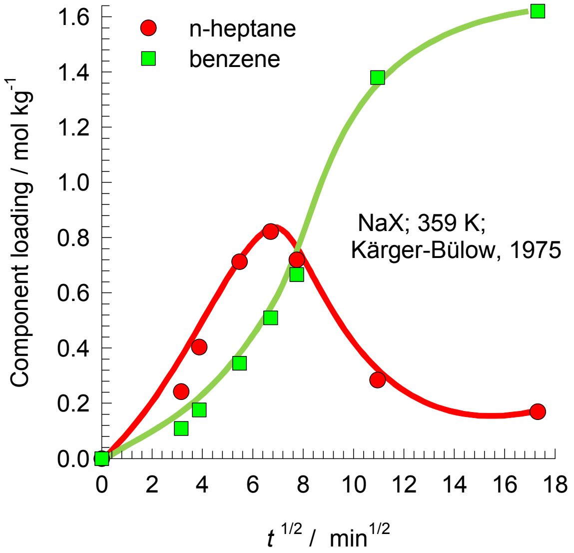

NaX zeolite

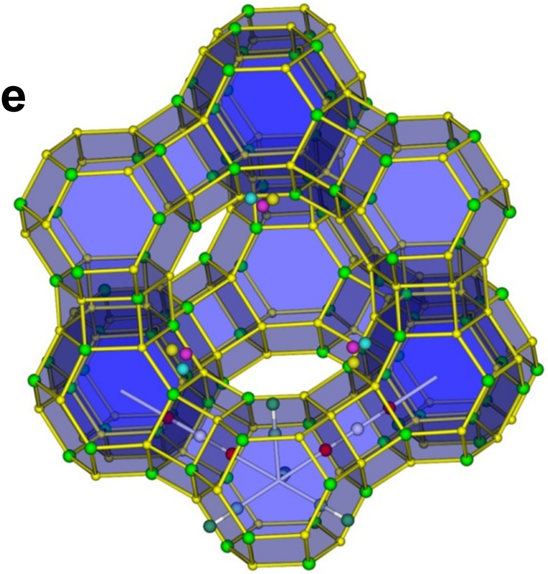

Kärger

MFI: Transient uptake of benzene/ethylbenzene mixture

ESI Fig. 111

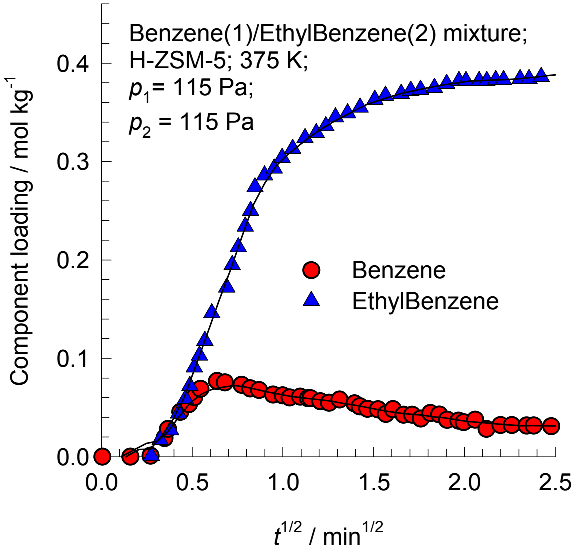

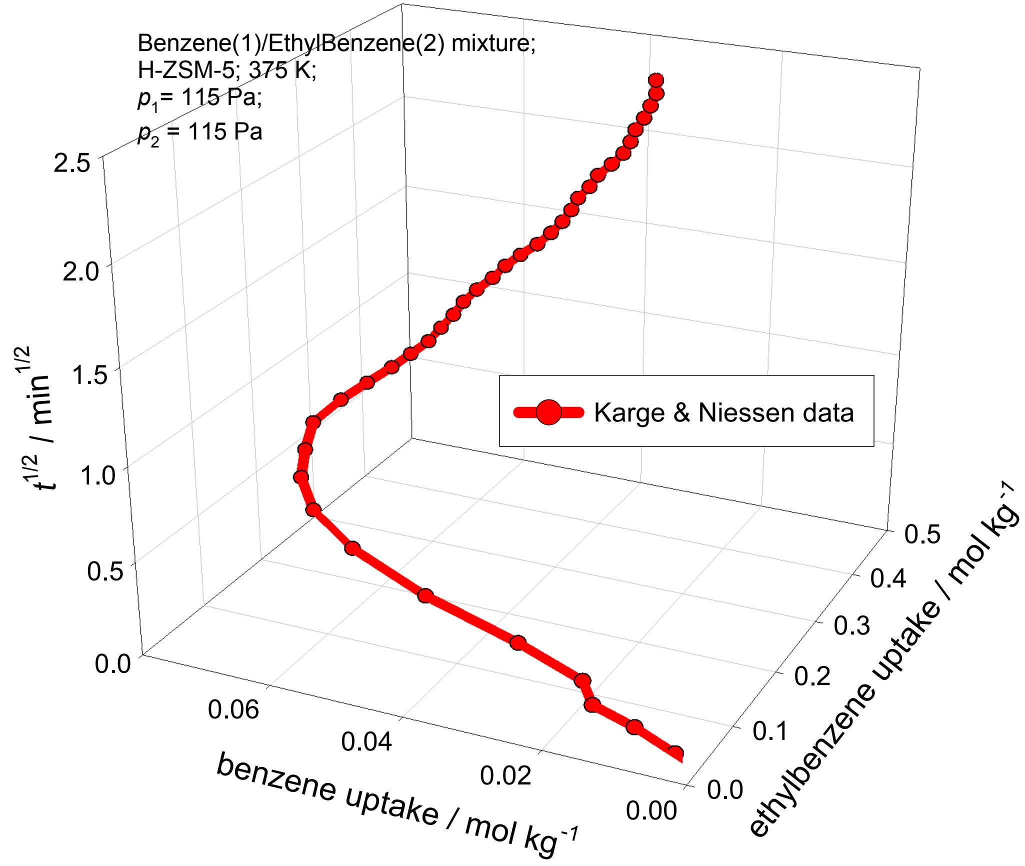

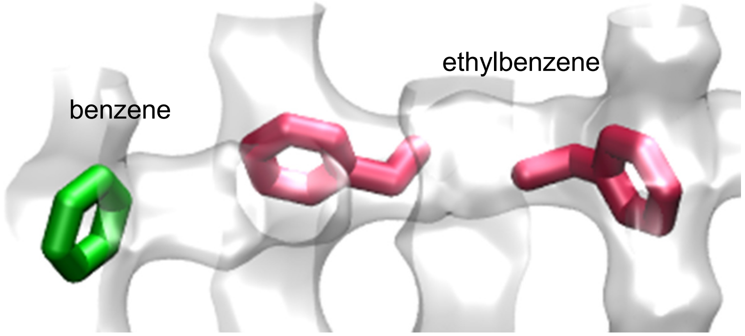

MFI: Transient uptake of benzene/p-xylene mixtures

ESI Fig. 112

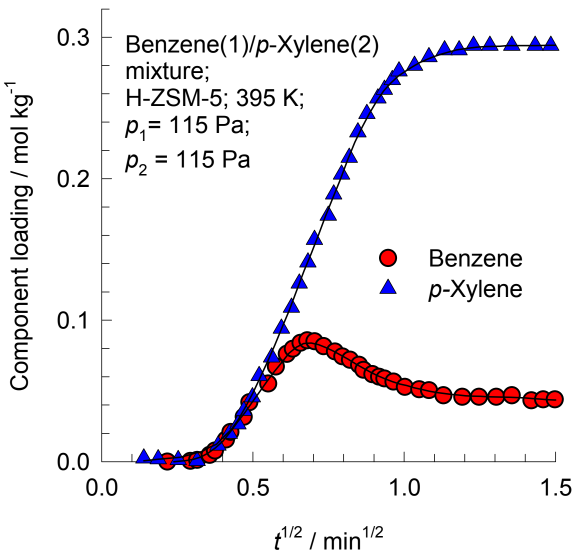

p-xylene

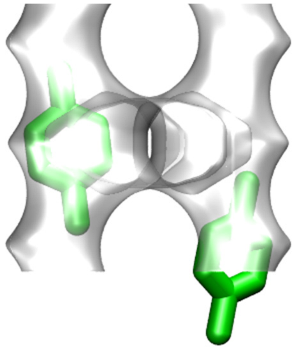

benzene

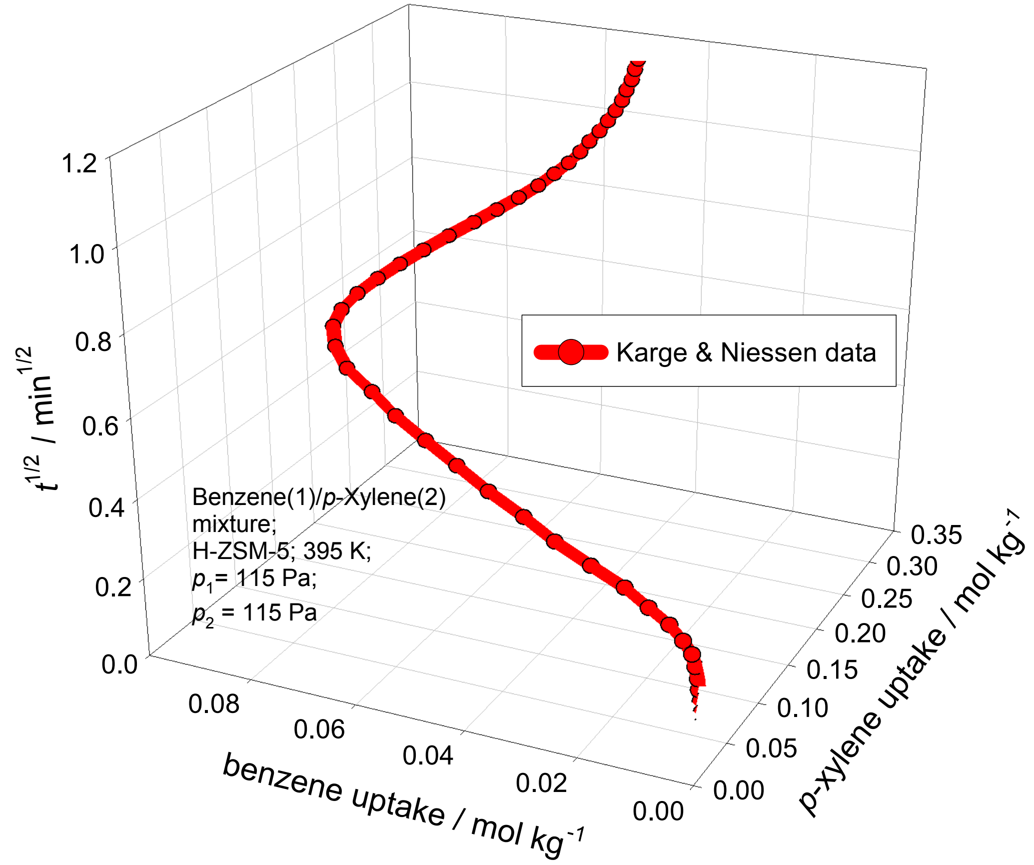

MFI transient nC6/2MP mixture uptake

ESI Fig. 113

(a)

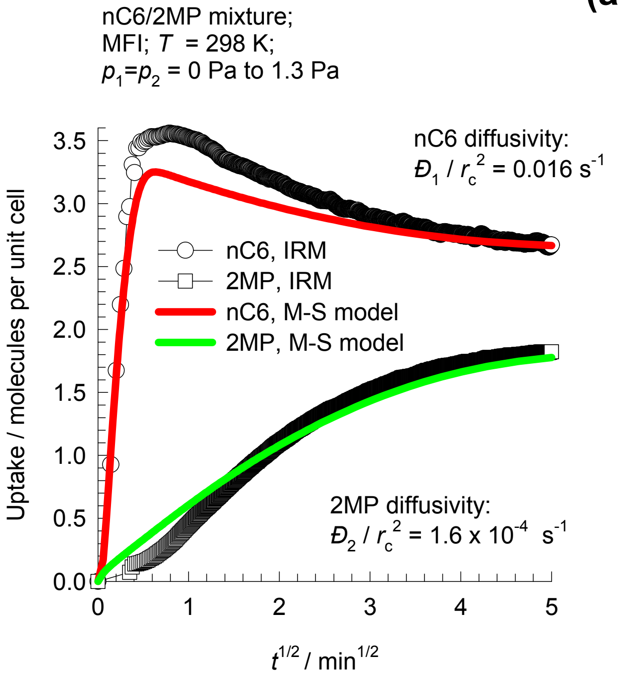

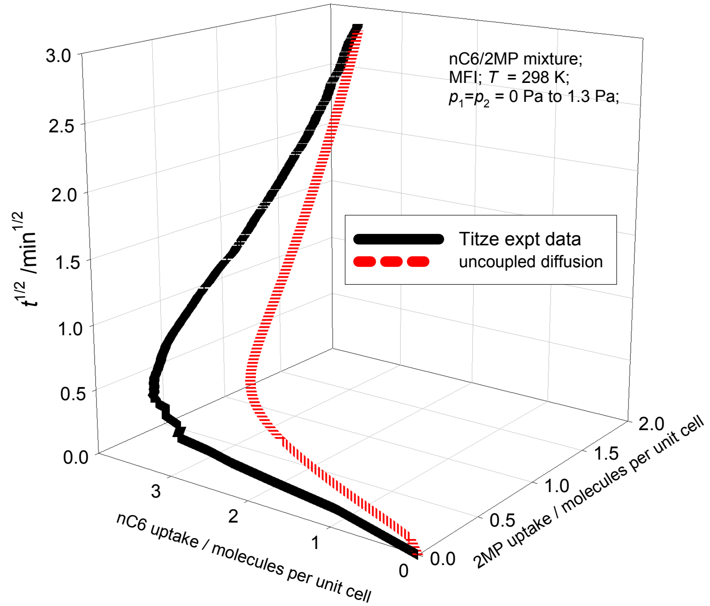

(c)

(b)

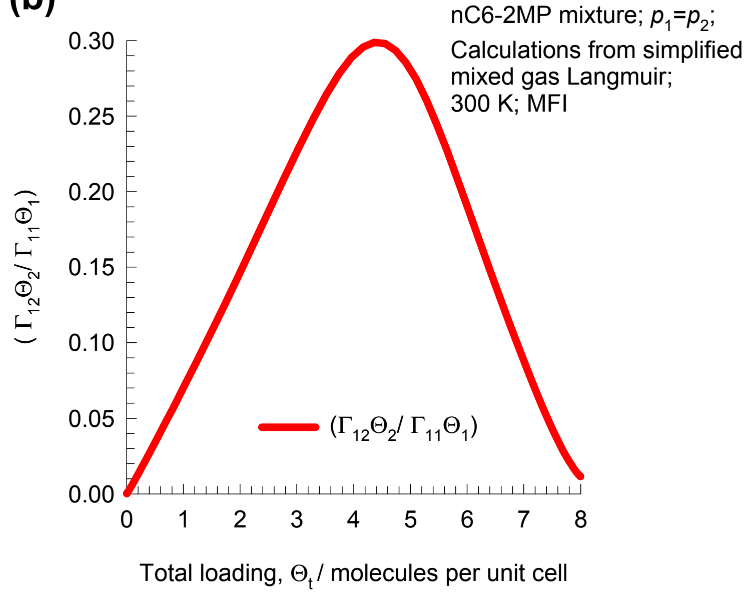

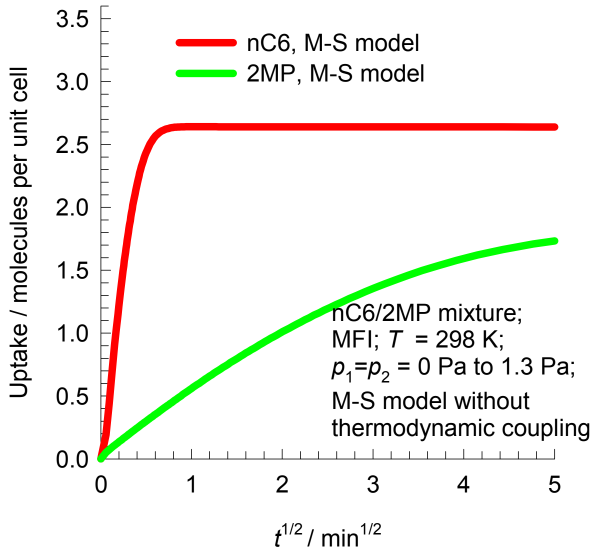

Radial profiles for transient nC6/2MP mixture uptake in MFI

ESI Fig. 114

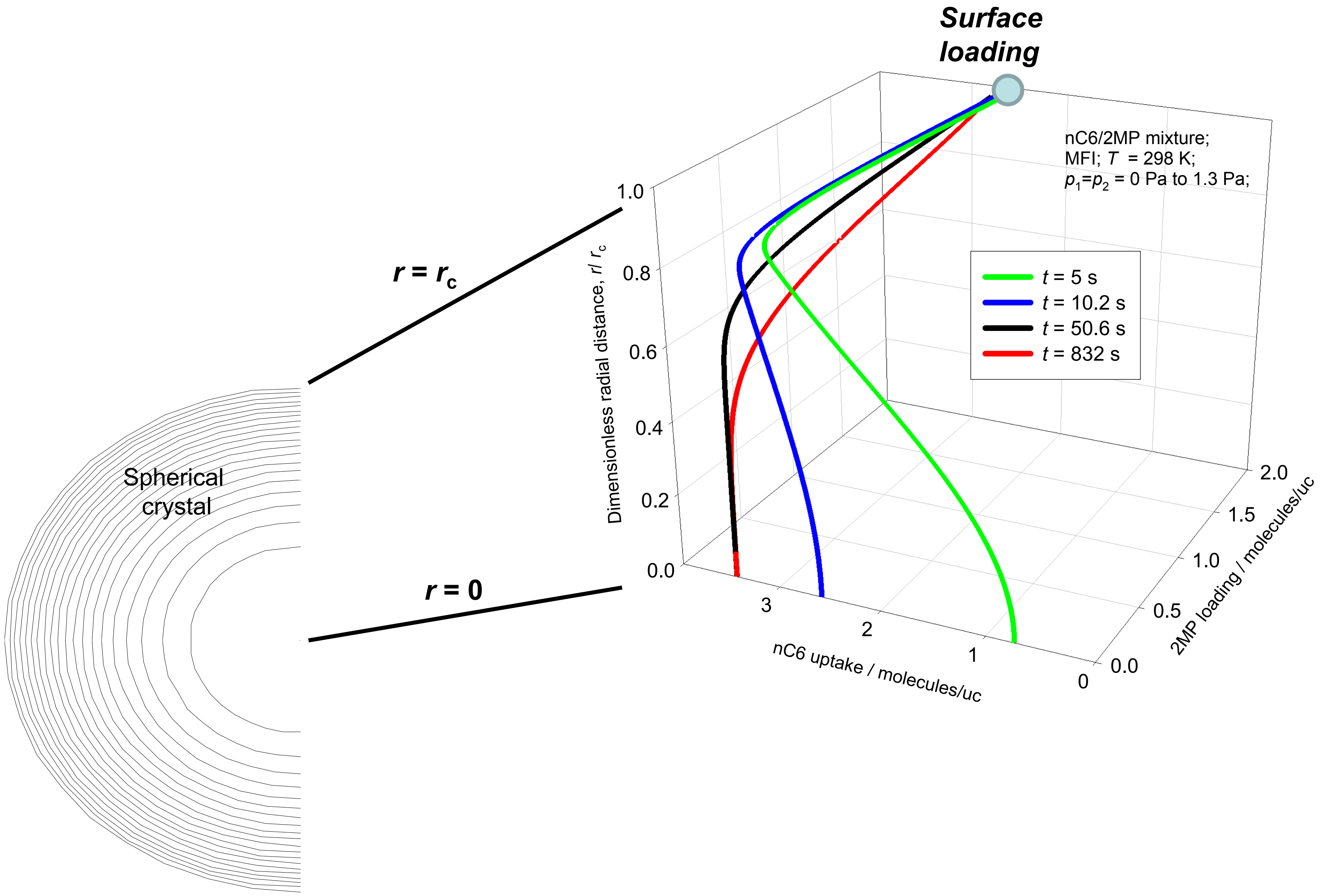

Adsorption-Desorption Asymmetry

ESI Fig. 115

(a)

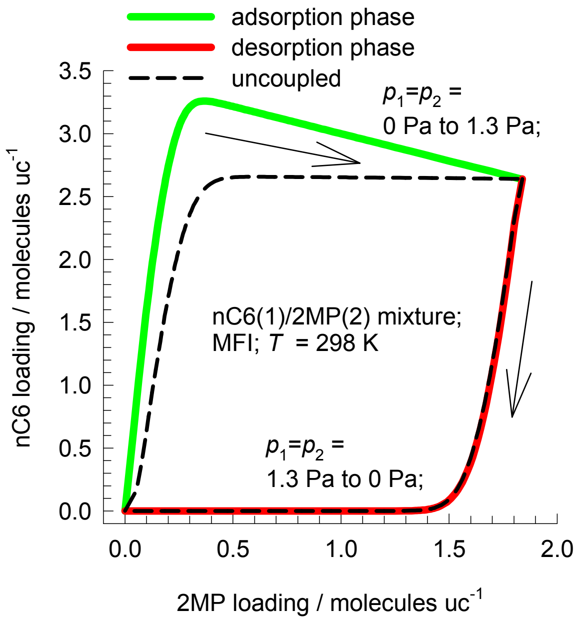

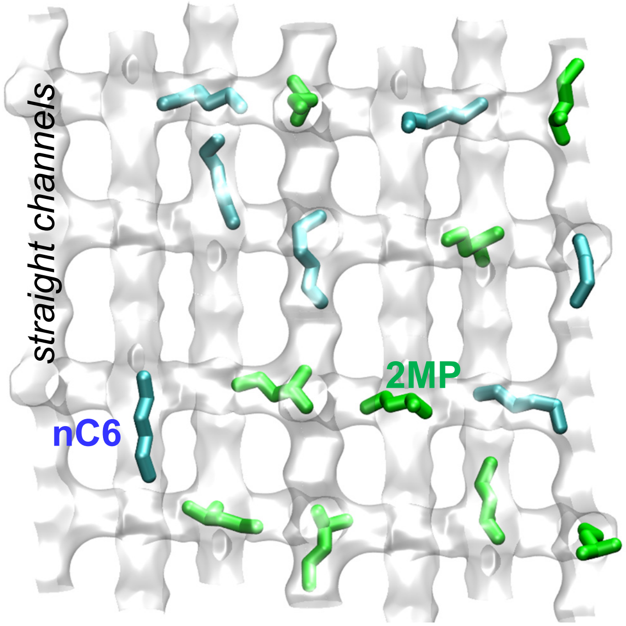

(b)

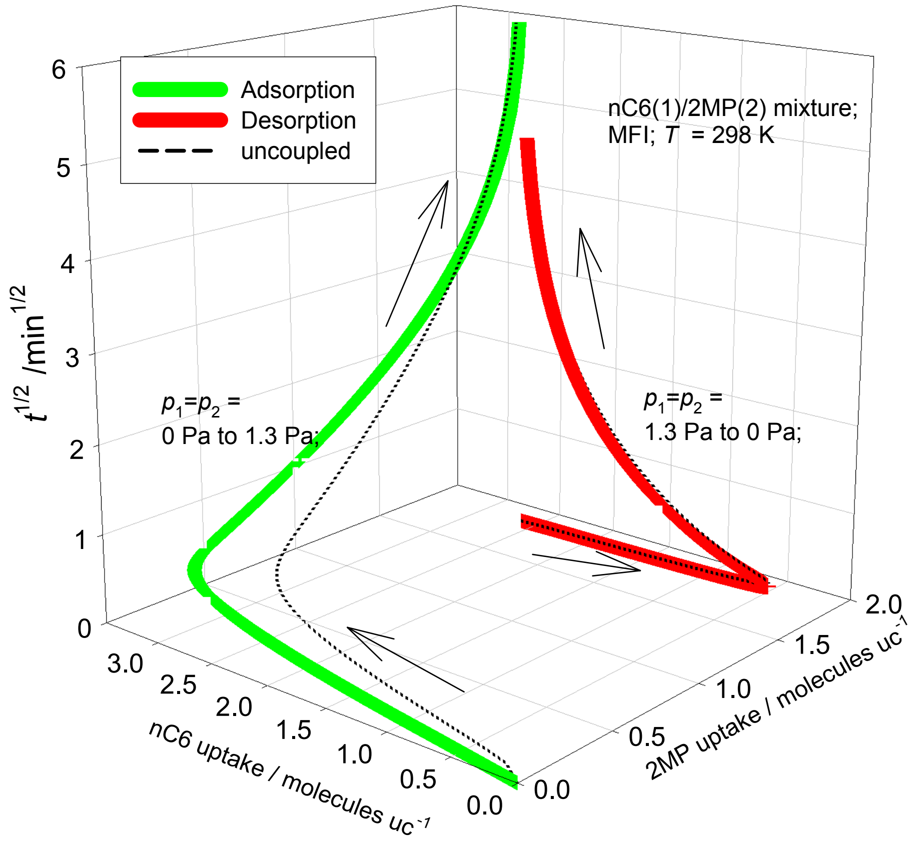

Undershoots and Overshoots

ESI Fig. 116

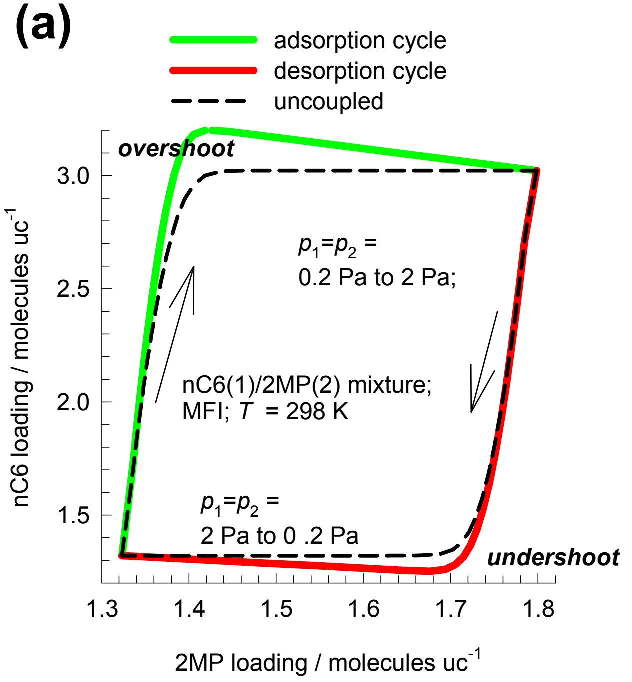

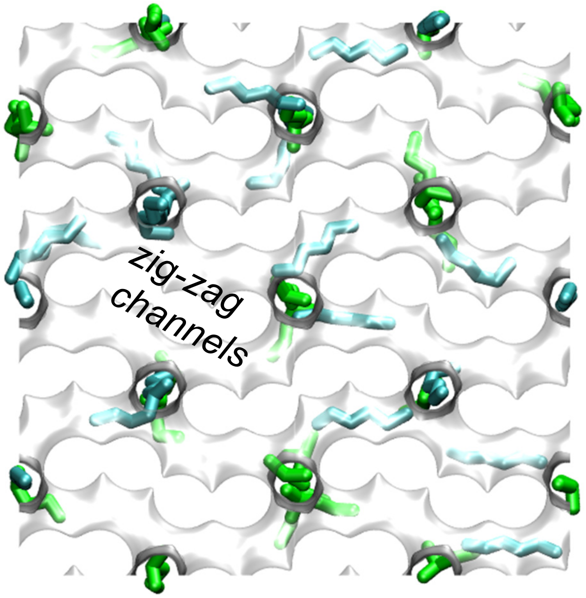

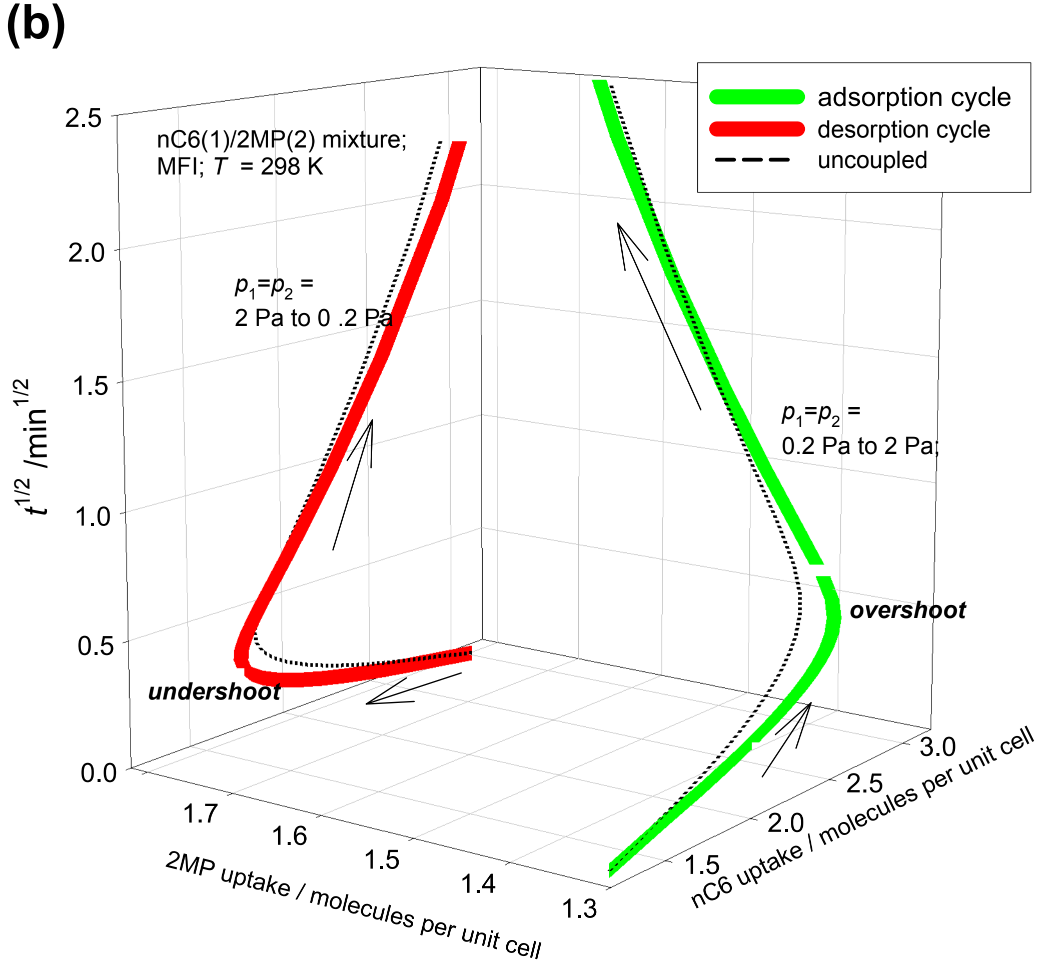

ESI Fig. 117

nC4/iC4 adsorption-desorption asymmetry

(a)

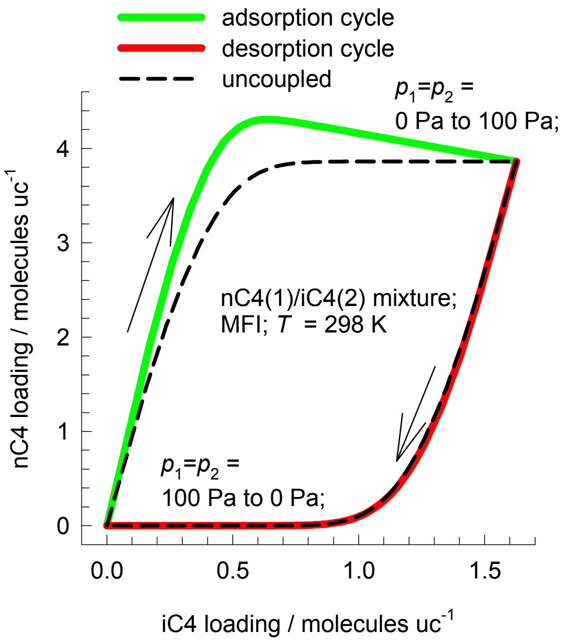

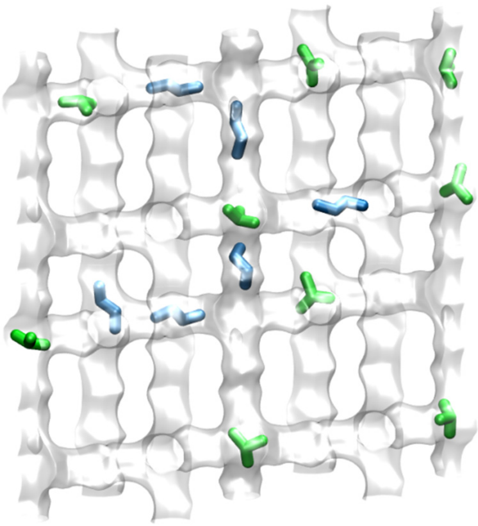

(b)

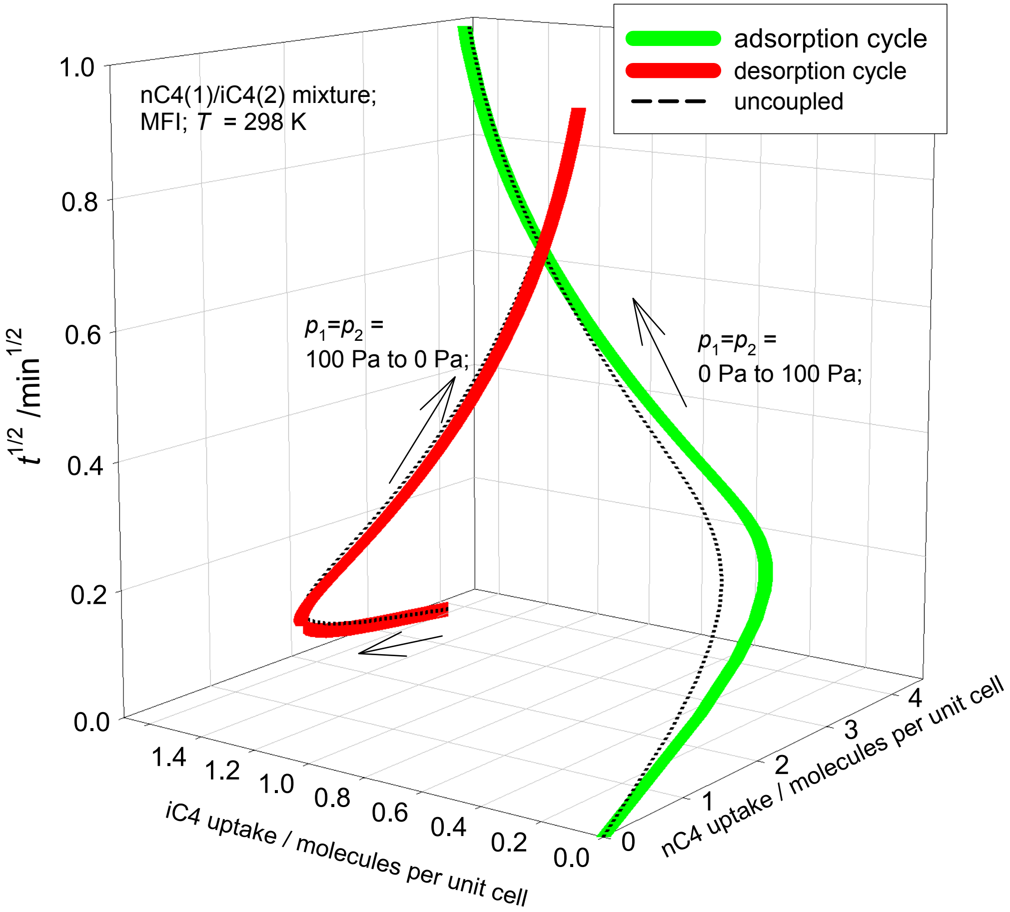

MFI: Transient adsorption/desorption benzene/p-xylene mixtures

ESI Fig. 118

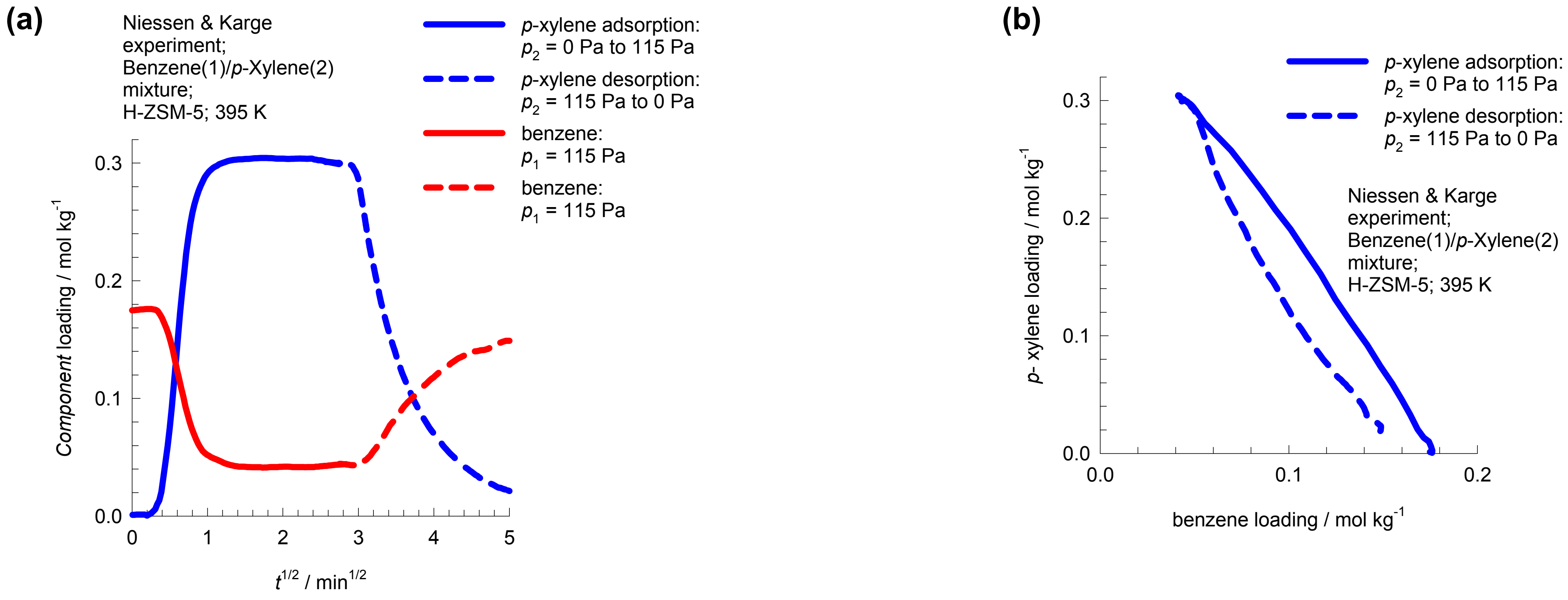

p-xylene

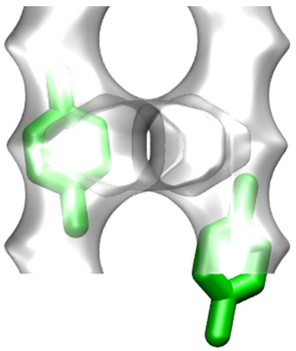

benzene

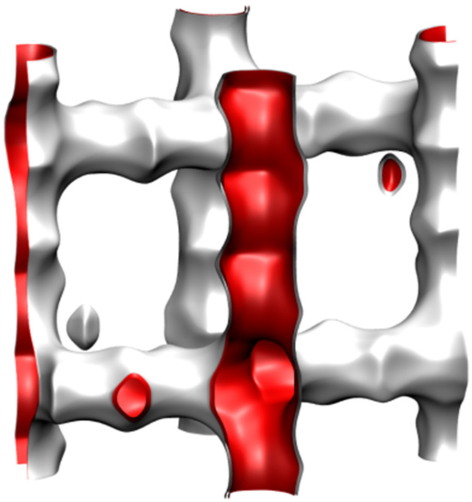

ESI Fig. 119

Counter-current uptake

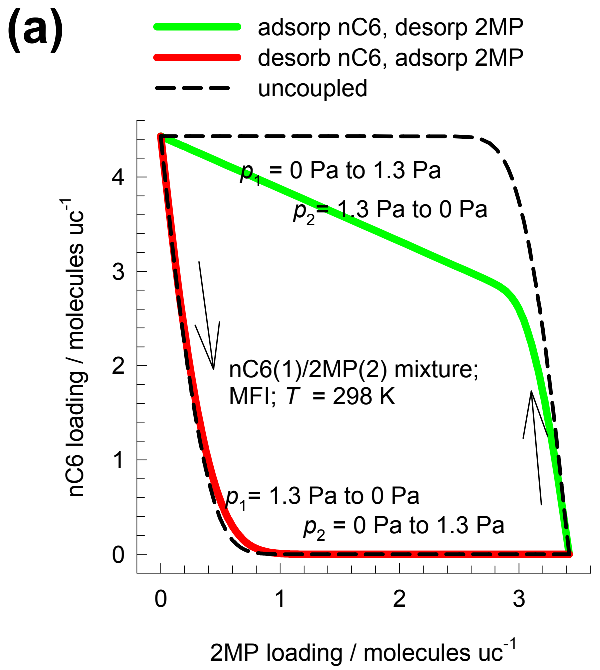

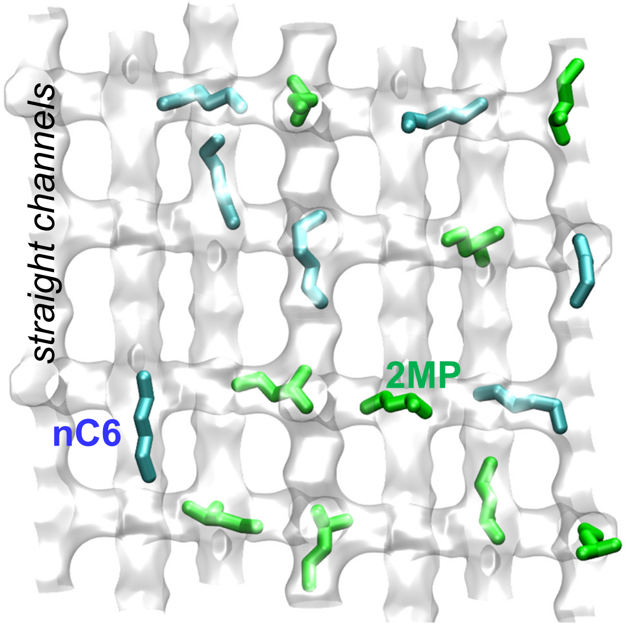

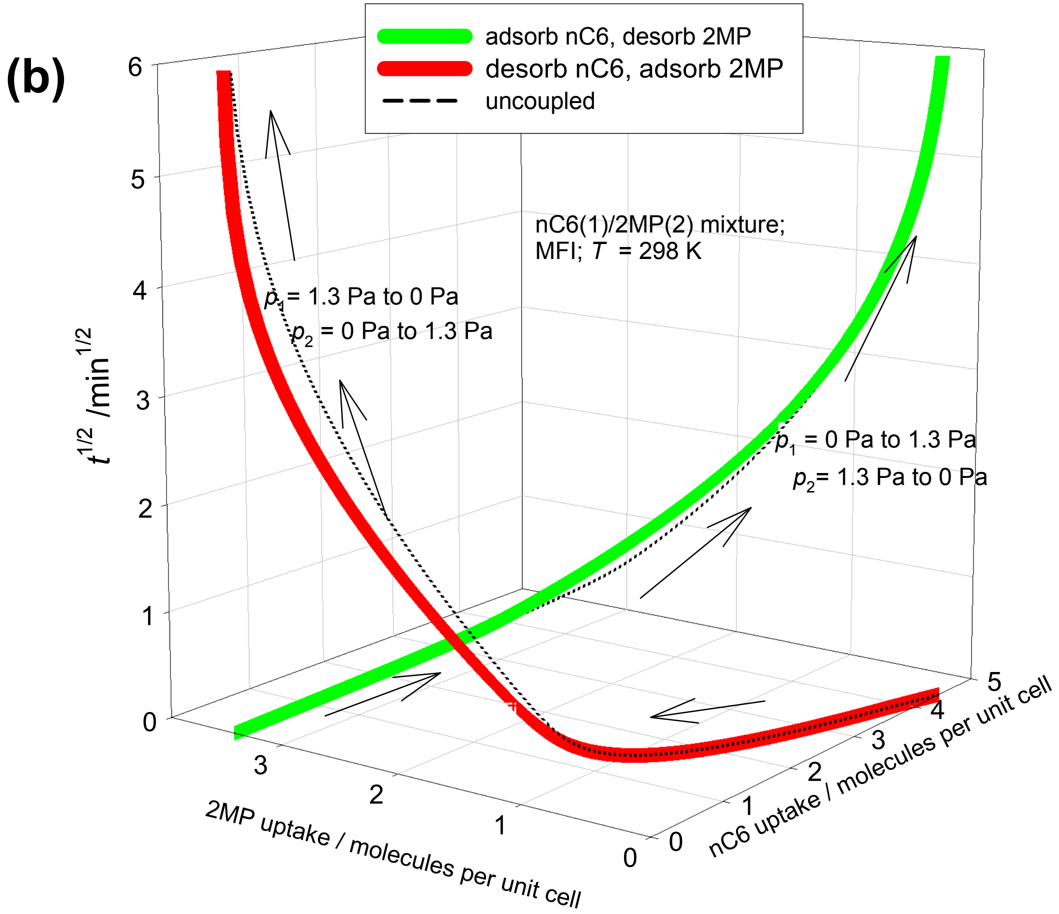

Transient uptake of hexane isomers in MFI crystal

(a)

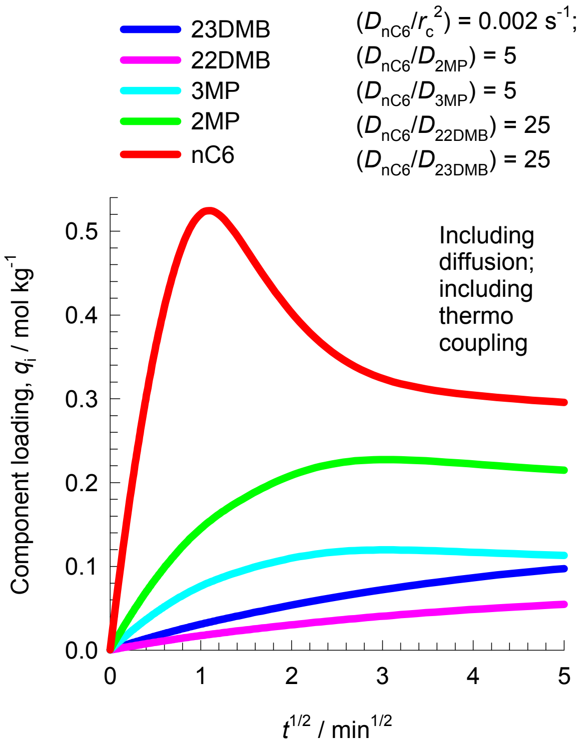

(b)

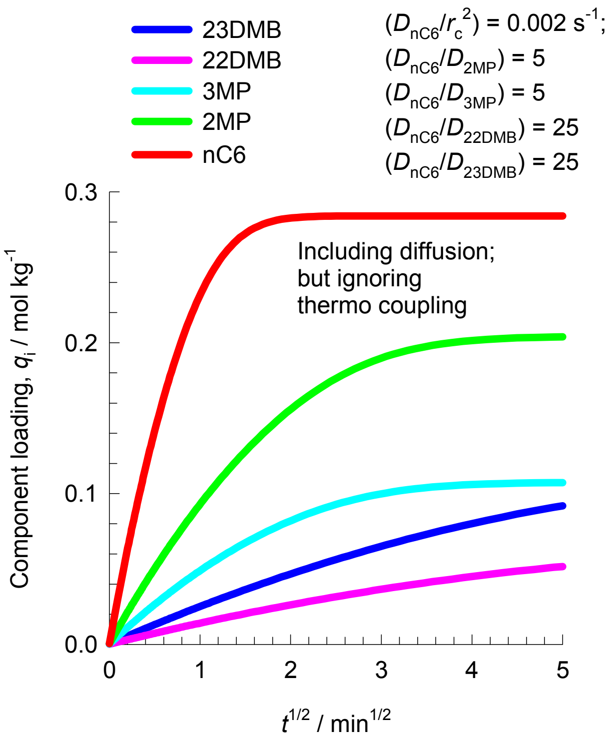

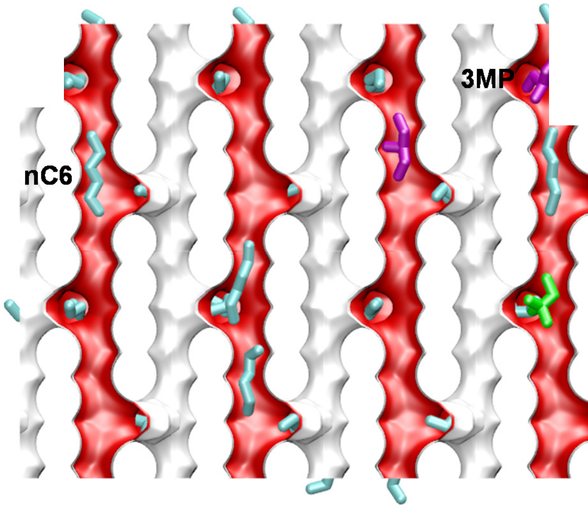

ESI Fig. 121

Transient uptake of linear alkanes in MFI crystal

(a)

MFI; 300 K;
$CH_4(1)/C_2H_6(2)/C_3H_8(3)/nC_4H_{10}(4)$;
p_{10} = 85 kPa; p_{20} = 11 kPa; p_{30} =3.5 kPa; p_{40} = 0.5 kPa

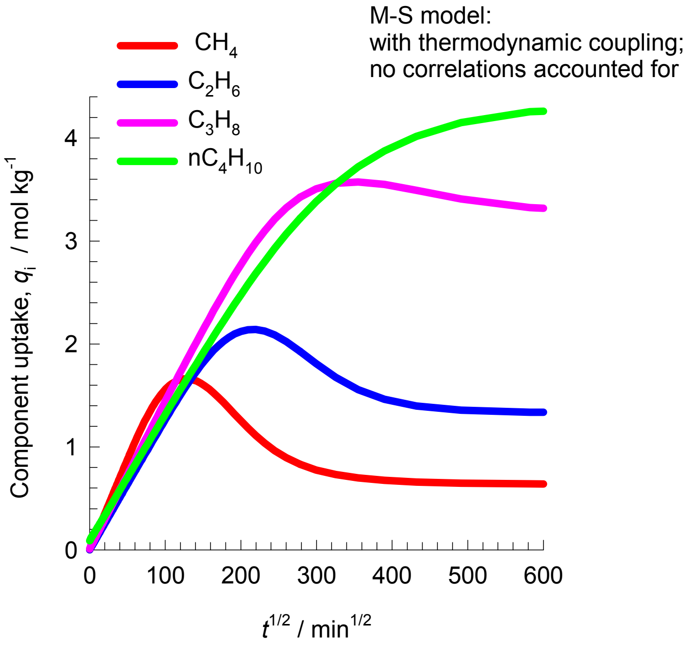

(b)

MFI; 300 K;
$CH_4(1)/C_2H_6(2)/C_3H_8(3)/nC_4H_{10}(4)$;
p_{10} = 85 kPa; p_{20} = 11 kPa; p_{30} =3.5 kPa; p_{40} = 0.5 kPa

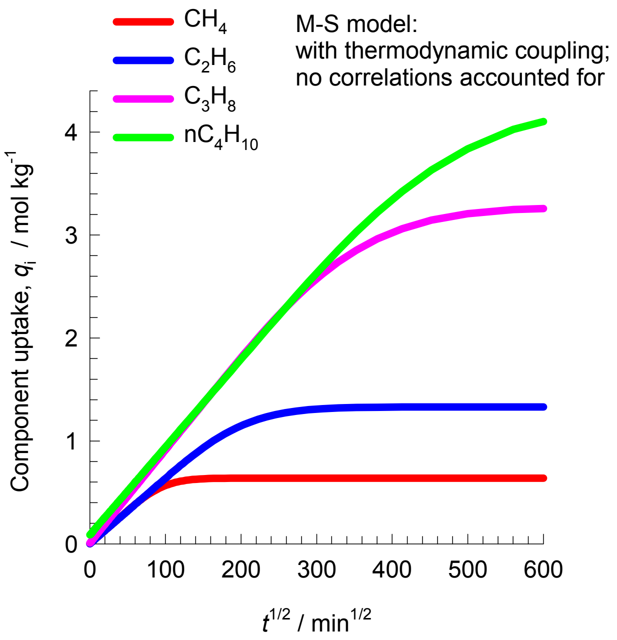

Propene/propane permeation

ESI Fig. 122

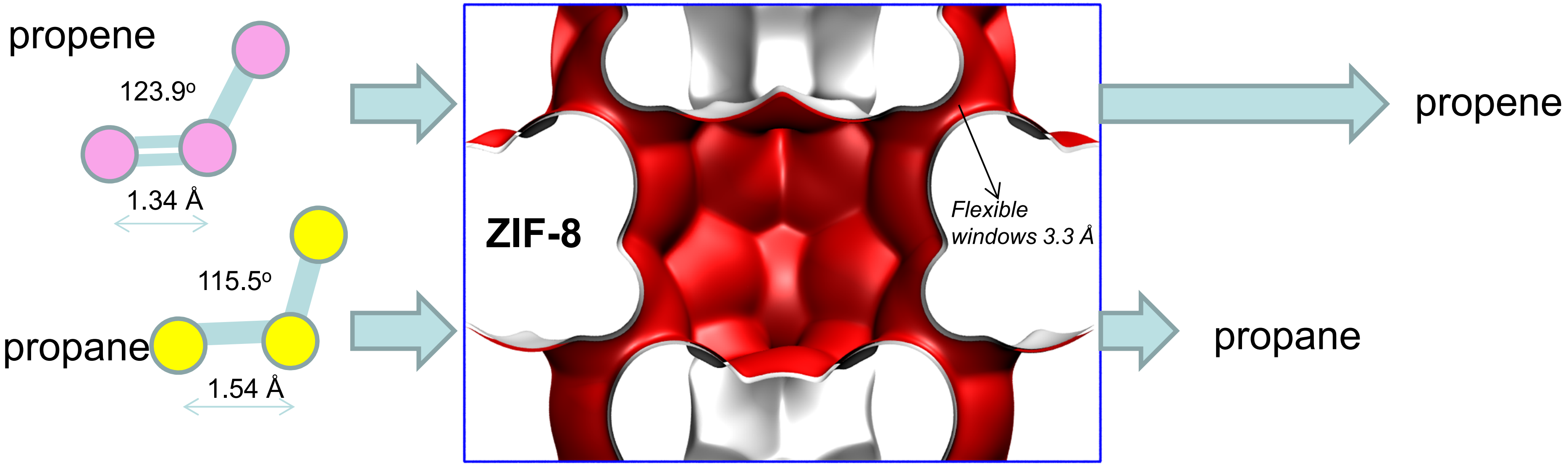

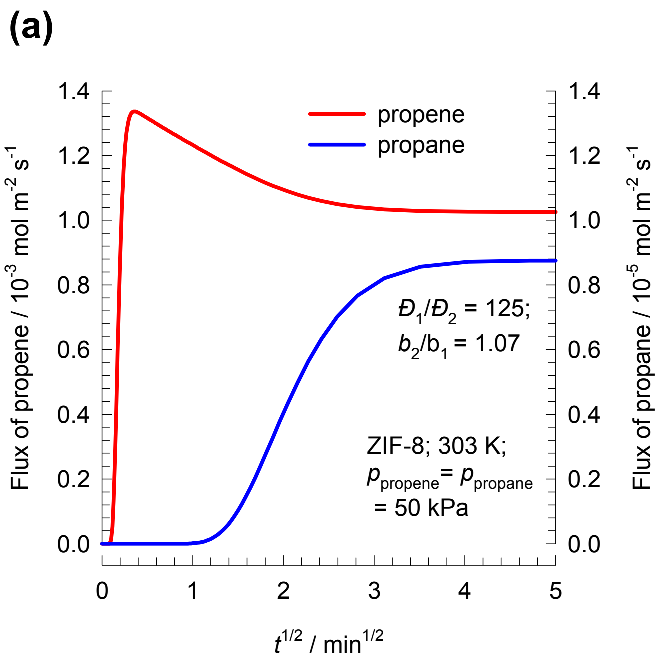

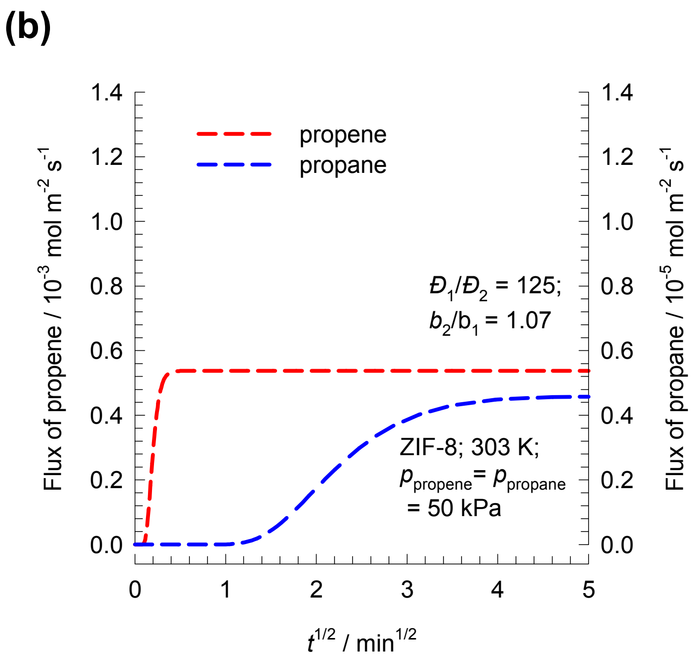

CH_4/n-C_4H_{10} permeation: MFI membrane

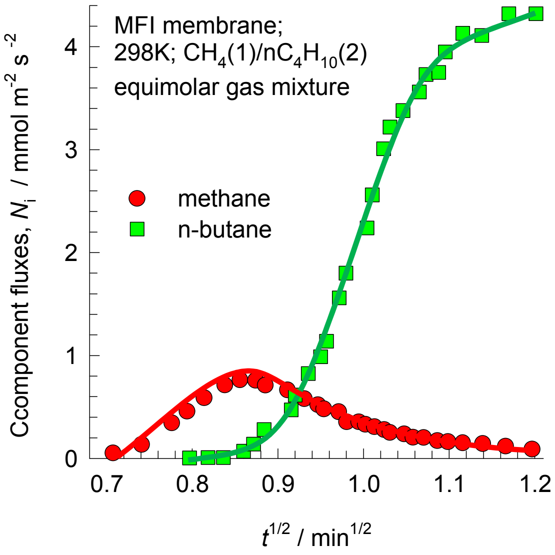

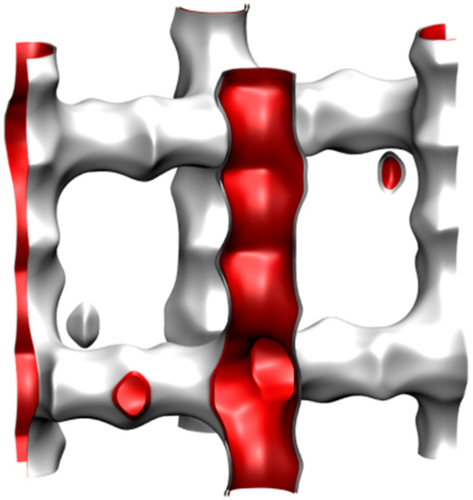

MFI membrane

ESI Fig. 124

MFI transient permeation of linear alkanes

(a)

MFI; 300 K;
$CH_4(1)/C_2H_6(2)/C_3H_8(3)/nC_4H_{10}(4)$;
$p_{10} = p_{20} = p_{30}$ =30 kPa; p_{40} = 10 kPa

M-S model:
with thermodynamic coupling;
no correlations accounted for

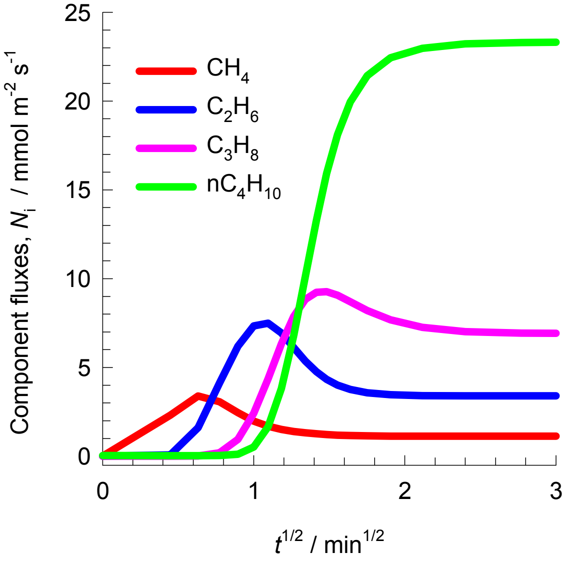

(b)

MFI; 300 K;
$CH_4(1)/C_2H_6(2)/C_3H_8(3)/nC_4H_{10}(4)$;
$p_{10} = p_{20} = p_{30}$ =30 kPa; p_{40} = 10 kPa

M-S model:
no thermodynamic coupling;
no correlations accounted for

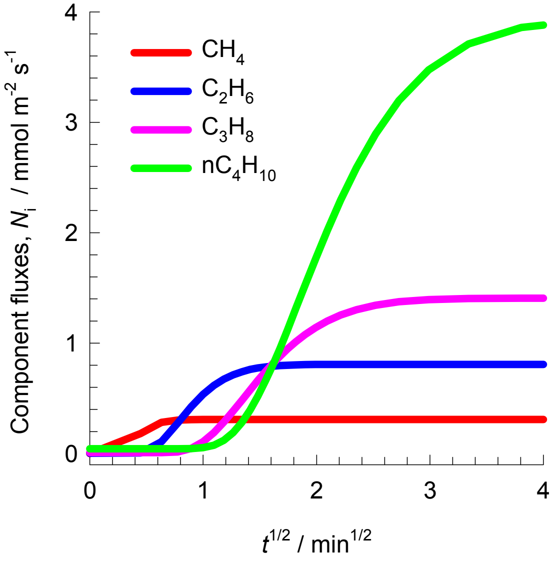

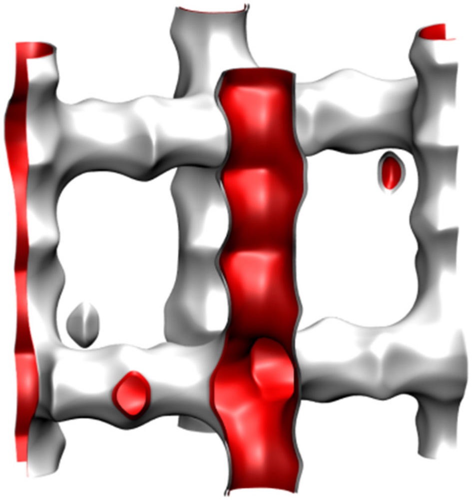

MFI membrane

MFI H_2/n-C_4H_{10} transient mixture permeation

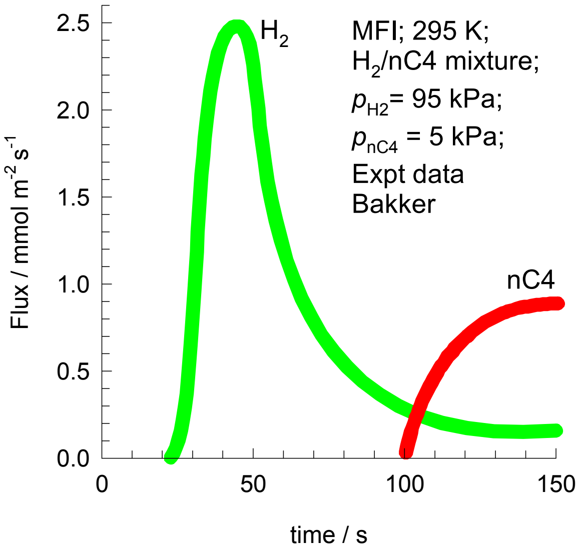

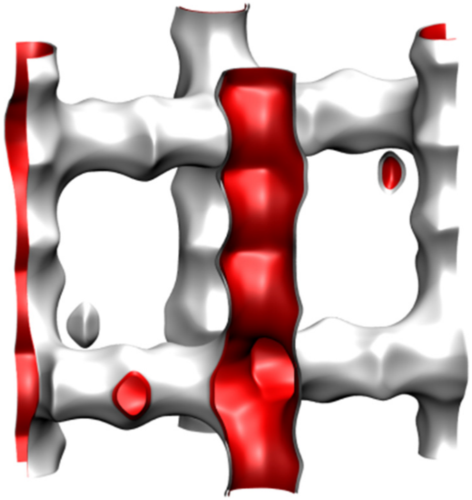

MFI membrane

ESI Fig. 126

MFI transient nC6/2MP, nC6/22MB mixture permeation

(a)

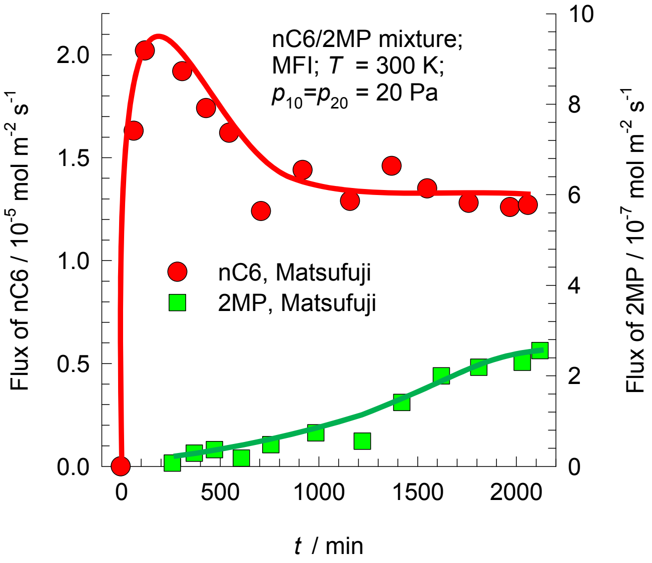

(b)

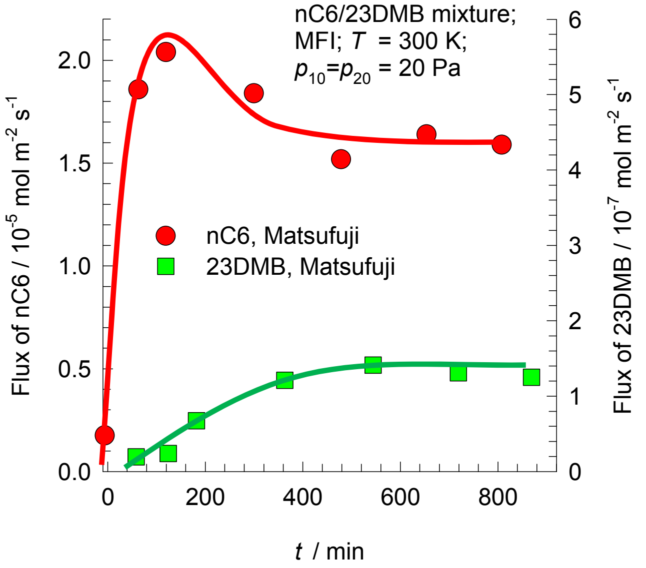

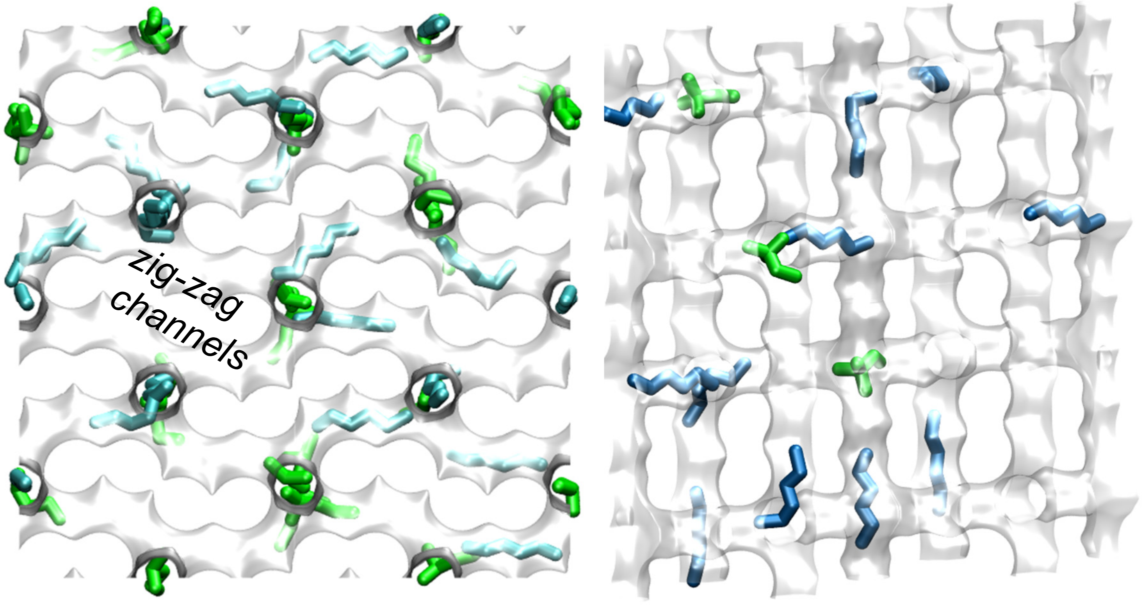

MFI transient xylene isomers mixture permeation

(a)

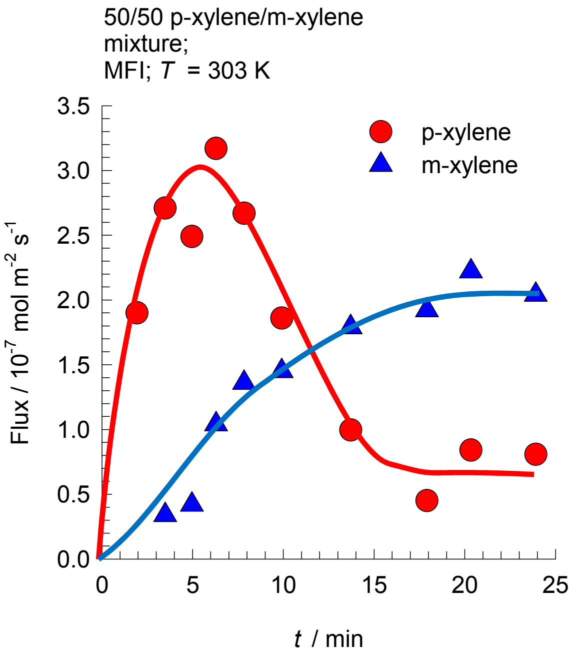

(b)

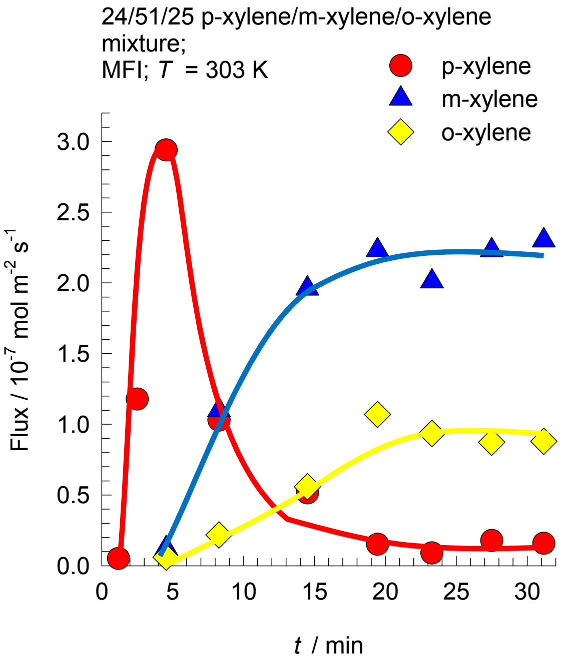

o-xylene is preferentially
located at the intersections
of MFI

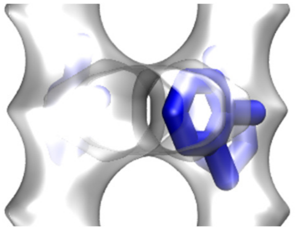

m-xylene is preferentially
located at the intersections
of MFI

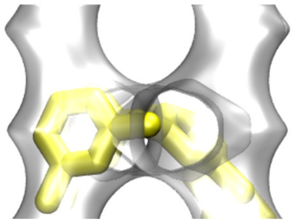

p-xylene can locate along
the channels MFI

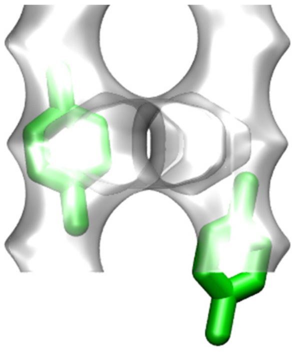

ESI Fig. 128

MFI transient benzene/p-xylene mixture permeation

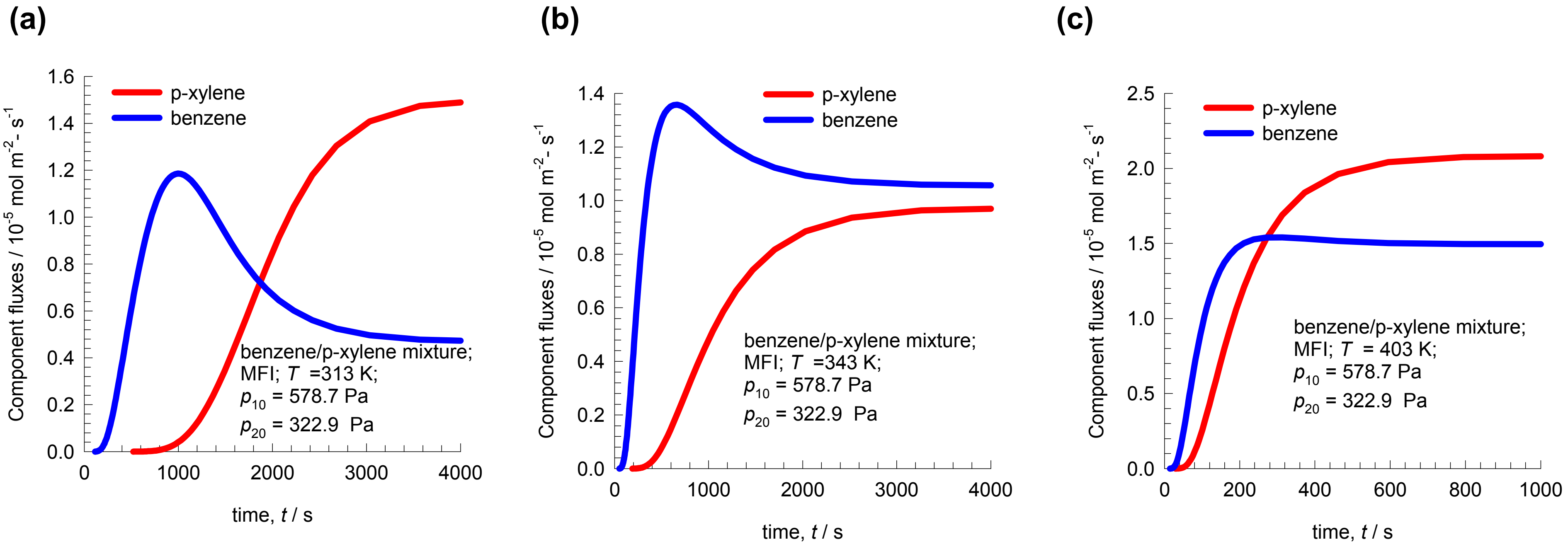

p-xylene

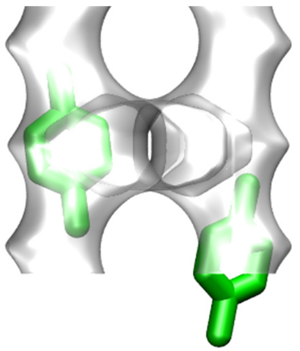

benzene